Dynamic Modeling of Magnetic Components for Circuit Simulation of Power Electronic Systems

THÈSE N^{O} 8801 (2018)

PRÉSENTÉE LE 17 AOÛT 2018
À LA FACULTÉ DES SCIENCES ET TECHNIQUES DE L'INGÉNIEUR
LABORATOIRE D'ÉLECTRONIQUE DE PUISSANCE
PROGRAMME DOCTORAL EN GÉNIE ÉLECTRIQUE

ÉCOLE POLYTECHNIQUE FÉDÉRALE DE LAUSANNE

POUR L'OBTENTION DU GRADE DE DOCTEUR ÈS SCIENCES

PAR

Min LUO

acceptée sur proposition du jury:

Dr S.-R. Cherkaoui, président du jury
Prof. D. Dujic, Dr J. Allmeling, directeurs de thèse
Prof. J. Biela, rapporteur
Dr B. Wunsch, rapporteur
Dr A. Rufer, rapporteur

ÉCOLE POLYTECHNIQUE
FÉDÉRALE DE LAUSANNE
Suisse
2018

École Polytechnique Fédérale de Lausanne
Power Electronics Laboratory
Station 11
1015 Lausanne, Switzerland

`http://pel.epfl.ch`

"All models are wrong, but some are useful"
George E. P. Box

Abstract

Magnetic components play an important role in a power electronic converter system. They provide energy buffering, galvanic isolation and voltage ratio conversion and have significant impact on the overall performance of the system regarding power efficiency and dynamic behavior. On the one hand, the increasing demand for higher power density in the new generation of power converter systems brings new challenges to magnetic component design. On the other hand, the optimization of the whole power converter system including component selection and control design requires a good understanding of the magnetic components. Conventionally, magnetic design and system behavior evaluation rarely take into account the non-idealities of the magnetic components, so that the performance of the final hardware may differ substantially from the expectation.

For this reason, improved models of magnetic components to be used in time-domain circuit simulation are desired. Magnetic circuits based on the permeance-capacitance analogy opens a new direction for modeling magnetic components, because magnetic non-idealities can be incorporated intuitively and the models are simple enough to be seamlessly integrated into system-level simulations. In this thesis, improved models of magnetic components are developed using the permeance-capacitance based magnetic circuits.

In order to evaluate the core losses of a magnetic component, models of the frequency-independent hysteresis effect are proposed for commonly used core materials. Several variations of the Preisach model are used to accommodate different shapes of hysteresis loops. The models are valid over a wide range of field strength amplitude. They are valid for arbitrary excitations such as sinusoidal wave and PWM with DC bias.

The magnetic circuit models are extended to cover frequency-dependent core losses. Two major loss mechanisms – relaxation effect and eddy current effect – are combined with the static hysteresis models, by introducing resistive components into the magnetic circuit. The relaxation effect model typically applies to ferrite materials under intermittent PWM excitation. The eddy current effect occurs in metal based cores, where the material conductivity contributes to the core loss with increasing excitation frequency. Both frequency-dependent and frequency-independent losses are physically present in the circuit model.

Besides the main fluxes within the magnetic core, the leakage fluxes though the air have a considerable influence on the system behavior. The leakage flux coupling in multi-winding transformers leads to unbalances in the electrical circuit of complex power converter systems. The last part of the thesis presents a model for unbalanced leakage flux coupling in the permeance-capacitance based magnetic circuit, which intuitively reflects the impact of the winding placement on the unbalances in the electrical circuit.

The models of magnetic components proposed in this work can be flexibly extended for a wide variety of core geometries and connected to arbitrary external electrical circuits consisting of switching devices and other passive components. The core losses and the unbalances due to leakage flux coupling can be evaluated under dynamic operation without any prior assumptions regarding the frequency spectrum and the magnitude of the excitation. The proposed models help to accurately simulate power converter systems under normal and unexpected operating conditions.

Keywords modeling, magnetic, permeance-capacitance analogy, magnetic circuit, circuit simulation

Kurzfassung

Magnetische Komponenten spielen eine wichtige Rolle in einem leistungselektronischen Systems. Sie fungieren als Energiespeicher, als galvanische Trennung und Spannungswandler und haben wesentlichen Einfluss auf die Leistungsfähigkeit des Systems bezüglich Wirkungsgrad und dynamisches Verhaltens. Das Verlangen nach höherer Leistungsdichte führt einerseits zu neuen Herausforderungen an die Auslegung der magnetischen Komponenten. Andererseits muss das Verhalten der magnetischen Komponenten eingehend verstanden werden, damit das gesamte leistungselektronische System mitsamt der Regelung optimiert werden kann. Üblicherweise werden beim magnetischen Design und der Bewertung des Systemverhaltens die Nichtidealitäten magnetischer Komponenten vernachlässigt, so dass die Leistungsfähigkeit der endgültigen Hardware stark von den Erwartungen abweichen kann.

Aus diesem Grund besteht ein Bedürfnis nach verbesserten Modellen für magnetische Komponenten für Systemsimulationen im Zeitbereich. Die auf der Permeanz-Kapazitäts-Analogie basierte magnetische Schaltung eröffnet neue Wege zur Modellierung magnetischer Komponenten. Magnetische Nichtidealitäten können auf anschauliche Weise integriert werden, und die Verbindung zum Modell der elektrische Schaltung gestaltet sich nahtlos. In dieser Dissertation werden verbesserte Modelle für magnetische Komponenten mit Permeanz-Kapazitäts-basierten magnetischen Schaltungen entwickelt.

Um die Kernverluste einer magnetischen Komponente zu ermitteln, werden Modelle für den frequenzunabhängigen Hysterese-Effekt für übliche Kernmaterialien vorgestellt. Mehrere Variationen des Preisach-Modells werden benutzt, um die unterschiedliche geformten Hystereseschleifen abzubilden. Die Gültigkeit der Modelle erstreckt sich über einen weiten Amplitudenbereich der magnetischen Feldstärke. Die Modelle sind gültig für beliebige Anregungen wie Sinusform und PWM mit Gleichanteil.

Die magnetischen Modelle werden erweitert, um frequenzabhängige Kernverluste abzudecken. Die beiden vorwiegenden Verlustmechanismen Relaxation und Wirbelstrom werden mit dem statischen Hysteresemodell kombiniert, indem Widerstände in die magnetische Schaltung eingefügt werden. Die Relaxation tritt vor allem in Ferritmaterialien bei Unterbrechungen in PWM-Anregung auf. Wirbelströme dagegen treten in metallischen Kernen auf, bei denen die Leitfähigkeit des Kernmaterials bei zunehmender Frequenz zu den Kernverluste beiträgt. Sowohl die frequenzabhängigen als auch die frequenzunabhängigen Verluste treten im Schaltungsmodell als physikalische Grössen zutage.

Neben dem Hauptfluss im magnetischen Kern beeinflussen die Streuflüsse durch die Luft massgeblich das Systemverhalten. Die Kopplung der Streuflüsse in Transformatoren mit mehreren Wicklungen führt zu Unsymmetrien in der elektrischen Schaltung eines komplexen Konvertersystems. Der abschliessende Teil der Arbeit präsentiert daher ein Modell für unsymmetrische Streuflusskopplung in einer Permeanz-Kapaziäts-basierten magnetischen Schaltung. Diese reflektiert auf verständliche Weise den Einfluss der Wicklungspositionen auf die Unsymmetrien in der elektrischen Schaltung.

Die in dieser Arbeit vorgeschlagenen Modelle magnetischer Komponenten können flexibel an eine breite Palette von Kerngeometrien angepasst werden. Sie können beliebig mit externen Stromkreisen verbunden werden, die aus Schalterkomponenten und anderen passive Bauteilen bestehen können. Die Kernverluste und die Unsymmetrien in der Streuflusskopplung können im dynamischen Betrieb ermittelt werden, ohne vorhergehende Annahmen über das Frequenzspektrum und die Amplitude der Anregung zu treffen. Die vorgeschlagenen Modelle helfen, Konvertersysteme unter normalen und unerwarteten Betriebsbedingungen genau zu simulieren.

Stichworte Modellierung, magnetisch, Permanz-Kapazitäts-Analogie, magnetische Schaltung, Schaltungsimulation

Acknowledgments

"Learning without reasoning leads to confusion, thinking without learning is wasted effort."
Confucius

The academic journey finally comes to the end and the last four years as PhD student were eventful and unforgettable. I would like to express my sincere gratitude to Prof. Drazen Dujic for his patient instruction and continuous encouragement. I appreciate his valuable advices coming out of the his previous experience in industry, which led me to the research goals in a straightforward way. His efficient target-oriented style in carrying out research activities and organizing materials impressed me deeply and this will guide me throughout the future professional life. Also thank you very much for the prompt replies to all my questions, even after office time and during vacation.

Doing the PhD in a technical company is a rare opportunity, which allowed me to do research targeting on the practical needs. I would like to give great appreciation to my co-supervisor Dr. Jost Allmeling from Plexim GmbH, who has initiated this challenging PhD topic and provided me with great support both technically and financially during the whole period. I enjoy very much the relaxed and motivating atmosphere that Jost created in the office, which made my PhD research a joyful journey. Also I would like to appreciate Mr. Orhan Toker from Plexim GmbH for his continuous effort in maintaining the cooperation with the university throughout the PhD study, and for his demonstration on the art of making a presentation.

Part of this thesis was carried out within the frame of the ECPE Joint Research Program, I would like to thank ECPE for bridging the research results to the industrial partners.

I'm grateful to the members of the examination committee, Dr. Sidi-Rachid Cherkaoui from the DSEL at EPFL, Prof. Alfred Rufer from EPFL, Prof. Jürgen Biela from the HPE at ETHZ and Dr. Bernhard Wunsch from the ABB Corporate Research Center in Baden-Dättwil for their kindness to evaluate this thesis.

Thanks to all the PEL colleagues for supporting me to carry out the experimental tests: Roland Wetter, Alex Christe, Yan-kim Tran... Without the help of them I could hardly finish during the limited time windows in Lausanne, as an external lab member living in Zürich two hundreds kilometers away.

My sincere thanks also goes to the all the Plexim colleagues especially the application engineer team: Niklaus Felderer and Felix Prausse for relieving me from my company duties during the final phase of this thesis.

Finally I would like to say thank you to my parents, who have been on my side all the time.

Zürich, May 2018

List of Abbreviations

CDF	cummulative distribution function
CHB	cascaded H-bridge converter
CWH	composite waveform hypothesis
EMC	electromagnetic compatibility
EMF	electromotive force
FE	finite element
FEM	finite element method
HFT	high frequency transformer
HV	high voltage
iGSE	improved generalised Steinmetz equation
iiGSE	improved-improved generalised Steinmetz equation
LFT	line frequency transformer
MFT	medium frequency transformer
MMF	magnetomotive force
MV	medium voltage
PCB	printed circuit board
PDF	probability distribution function
PWM	pulse-width modulation
SE	Steinmetz equation
SiFe	silicon steel
SMPS	switch-mode power supply
TDM	terminal-duality model

VSI	voltage source inverter

List of Symbols

A	cross section area
B_r	remanence flux density
B	magnetic flux density
F	magnetomotive force
H	magnetic field strength
I	current
J	current density
L_m	magnetization inductance
L_σ	leakage inductance
N	turns number
P_loss	power loss
R_m	magnetic resistance
R	electrical resistance
V	voltage
W_p	primary winding
W_s	secondary winding
$\Delta\Phi$	phase delay
Φ	magnetic flux
ϵ	error
$\mathscr{A}$	magnetic potential
$\mathscr{P}$	permeance
$\mathscr{R}$	magnetic reluctance
μ_{rm0}	vacuum permeability
μ	permeability
f_sw	switchging frequency
f	frequency
h	height or thickness
l	magnetic path length
w	width

Contents

1

Introduction

People have been aware of the existence of electricity since the earliest civilizations, from the sound and flash released during thunder and lightning, from the shock generated by electric rays and cat fish, and from the "magic" that rods of amber attracts feathers if rubbed with cat's fur. Firstly identified as a nature source by the Arabs, electricity still remains as an intellectual curiosity for over thousand year until Otto von Guericke invented a primitive form of electrostatic generator around 1663, claiming the start of people's history in harnessing electricity. Alessandro Volta's battery of 1800, made from alternating layers of zinc and copper, provided scientists with a more reliable source of electrical energy [1]. Nevertheless, electricity could not be supplied without interrupt of exchanging the empty cells. The development of nearly all kinds of modern technologies would never have become possible without a sustainable electric power source, and the key to it was "Magnetism".

People's utilization of magnetism has begun much earlier than electricity, as the ancient Chinese conceived the first compasses in the Han dynasty between 300 and 200 BC, which facilitated the exploration of oceans and continents. However, magnetism had never been related to the generation of electric power until Michael Faraday discovered the operating principle of electromagnetic generators in the years of 1831-1832, which is recognized as the famous Faraday's law explaining that an electromotive force is generated in an electrical conductor which encircles a varying magnetic flux. As the basis of the electromagnetism theory was further developed by Andre-Marie Ampere, Hans Christian Ørsted and James Clerk Maxwell, various kinds of practical direct current (DC) generators and alternative current (AC) generators came to the world. Being the first magnetic component in a power system, the initial generator, made uninterrupted power supply possible.

The increasing demand of electricity gave rise to initial electrical power grids, where the generators and load devices are interconnected. However, two obstacles existed at that time. Firstly, devices having different rated voltages required specialised generators with their own separate lines. Street lights, electric motors in factories, power for streetcars and lights in homes are examples of the different voltage requirements. Secondly, thanks to the development of transportation technology, the living territory of human-beings expanded dramatically so that electric power generated at one place had to be transmitted to the load hundreds of kilometers away. However, longer distances led to increased resistive loss and voltage drop on the load side, which required higher voltages. To overcome the two obstacles, magnetic components, again, became the solution. Shortly after Faraday's discovery of inductance, scientists discovered if two insulated inductors were placed side by side, the magnetic field from the first coil still affected the secondary coil. This discovery led to the invention of primitive transformers. There were many early trials of building transformers, such as those by Charles F. Brush of Ohio, Sebastian Ziani de Ferranti of England, and Otto Blathy and Karoly Zipernowski of Hungary [2]. It wasn't until the mid-1880s, however, that the first commercially-used transformer was built by William Stanley, who was working under George Westinghouse. Stanley

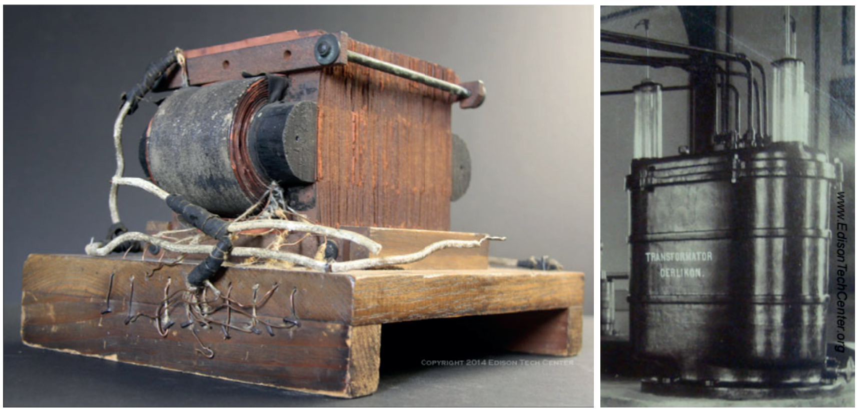

(a) **(b)**

Figure 1.1 (a) Original Stanley prototype transformer at the Berkshire Museum; (b) Dobrovolsky's three phase transformer used on the Lauffen to Frankfurt demonstration line. [2]

made a transformer that was easy to construct and wind to form a core of E-shaped laminates in step-up and step-down variations. This version was inexpensive to produce and easy to adjust. Stanley's version was first used in Barrington, MA, for the electrification of the downtown area using an advanced AC power system. In the few years following, Albert Schmid improved this design by extending the E-shaped laminates to meet at a central projection [2]. Shortly after that the first three-phase transformer was built by Mikhail Dolivo-Dobrovolsky in Germany, whose subsequent improvements can be seen everywhere in the electrical power grids nowadays.

Although AC system won the dominant position against DC in the competition between Nikola Tesla and Thomas Edison, there is still considerable percentage of DC electric loads, which also have different rated voltages. The demand on conversion between AC and DC systems or DC systems with different rated voltages gave rise to the technology of power electronics. The development of power electronic industry came together with magnetic components: The discontinuous switching property of the power electronic converters produces all kinds of distortion and ripple on the current, which are undesired from both AC and DC side. This effect made another family of magnetic components - inductive filters, inevitably become indispensable part in any power electronic converter, for suppression of the distortion and ripple, as the ones applied in nearly all kinds of voltage source inverters (VSI) as shown in **Fig. 1.4a**. The first inductor coil was invented by Reverend Nicholas Calland of Ireland [1]. The earliest version of the inductor consisted of a coil with two terminals at the ends which stored energy inside a magnetic field when a current was flowing. As the electric load devices become even more sensitive to the power quality, the inductive filter technology went through huge innovation in terms of structure and material.

Within power electronic converters, also the transformers have been unleashed from its conventional sinusoidal line-frequency applications. As the technology of high-speed switching devices like MOSFET and IGBT became mature, transformers were introduced into DC to DC converters like resonant- or dual active bridge converters, to provide galvanic isolation as well as achieve wide voltage transformation ratio (**Fig. 1.4c**). Transformers are now transferring electric power in form of square wave voltages at several kilo-Hertz to hundreds of kilo-Hertz, allowing the overall size of the converter system to be significantly reduced.

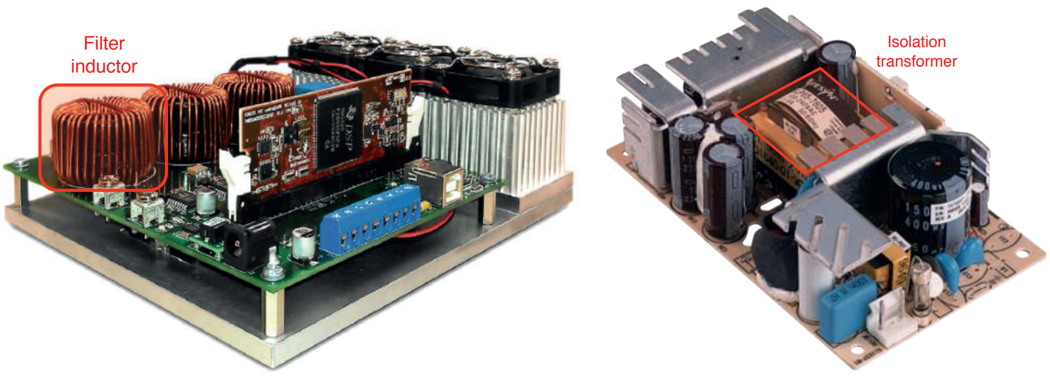

(a) (b)

Figure 1.2 (a) Inductor filter in a VSI. [3] (b) Isolation transformer in a DC-DC converter. [4]

In the recent decades, the increasing interest in the fields of variable speed drive, renewable energy generation, electrical mobility, microgrids and DC-grids has significantly added up to the volume of electric power exchange. The electric power is transmitted between systems with significantly different voltages and frequencies, which requires huge amount of power electronic converters with their considerable number of magnetic components. The rapidly increased production of soft-magnetic materials for industry applications is shown in **Tab. 1.1**, and new magnetic core materials are continuously announced. The noticable percentage of volume that magnetic components occupied, and power loss that magnetic components generate within the whole power electronic converter, become important optimisation target in industry and in academic research, especially as energy efficiency and power density of the power converters are drawing increasing attention nowadays.

Table 1.1 Amount of soft-magnetic materials produced for industry applications [5]

Year / Tons	GO FeSi	FeSi6.5	FeSiB	FeSiBNbCu	Ferrite
1995	750'000	0	20'000	0	180000
2005	1500'000	1'200	60'000	2'000	250'000
2010	1600'000	2'000	100'000	4'000	350'000

1.1 Common types of magnetic component

The main functionalities of magnetic components in power electronic converter systems can be summarized as:

- Voltage transformation
- Galvanic isolation
- Filtering of current ripple

In this section, common types of magnetic component in power electronic converter systems are introduced, in terms of operating condition and construction.

1.1.1 Line frequency transformers (LFT)

In grid-connected power electronic converters, the line frequency transformers interface the sinusoidal voltages of different amplitude between the power grid and the converter output. They transfer the electrical power from the converters to the grid (e.g. solar and wind inverters) or vice-versa (e.g. charging station of E-vehicle and industrial drives), as depicted in **Fig. 1.3** for different applications.

Due to the low frequency operation from 16.7 Hz in railway applications, 50/60 Hz in utilities and up to 400 Hz in aircraft board networks, low frequency core materials like silicon steel are usually

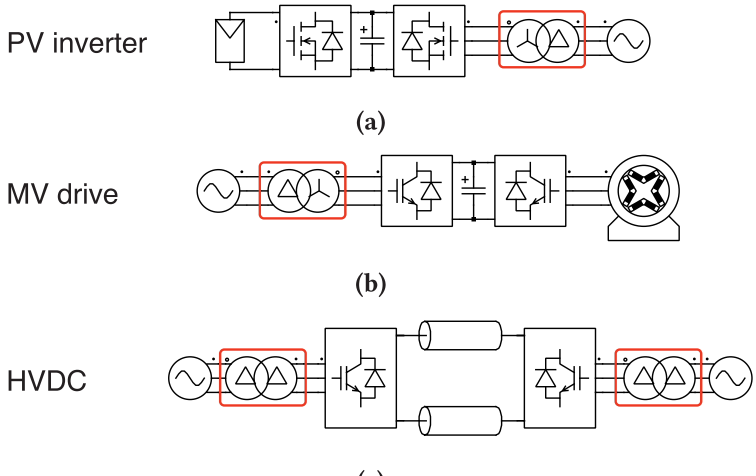

(a) (b) (c)

Figure 1.3 Typical applications of LFT in power electronic systems (a) Low voltage; (b) Medium voltage; (c) High voltage.

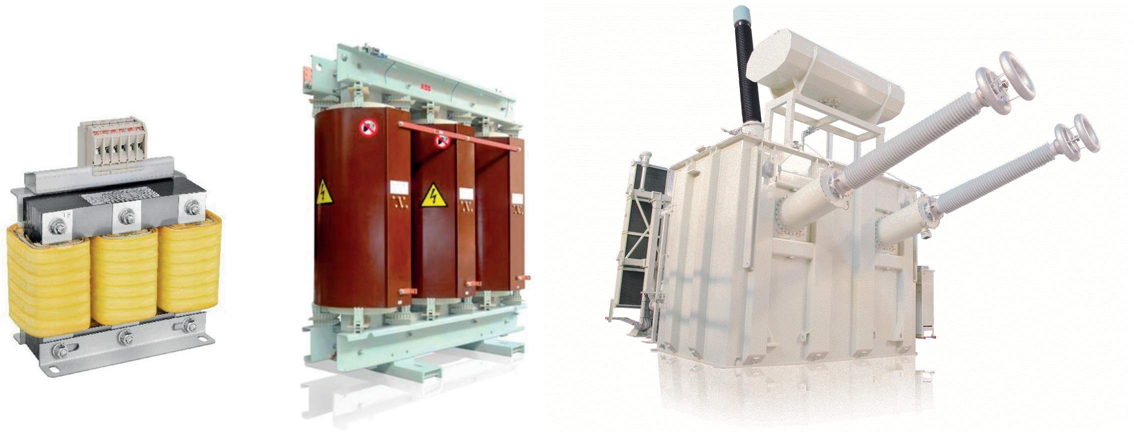

(a) (b) (c)

Figure 1.4 Typical layout of line frequency transformers (a) Low voltage (LV) application [6]; (b) Medium voltage (MV) application[7]; (c) High voltage (HV) application (single phase for HVDC-light) [8].

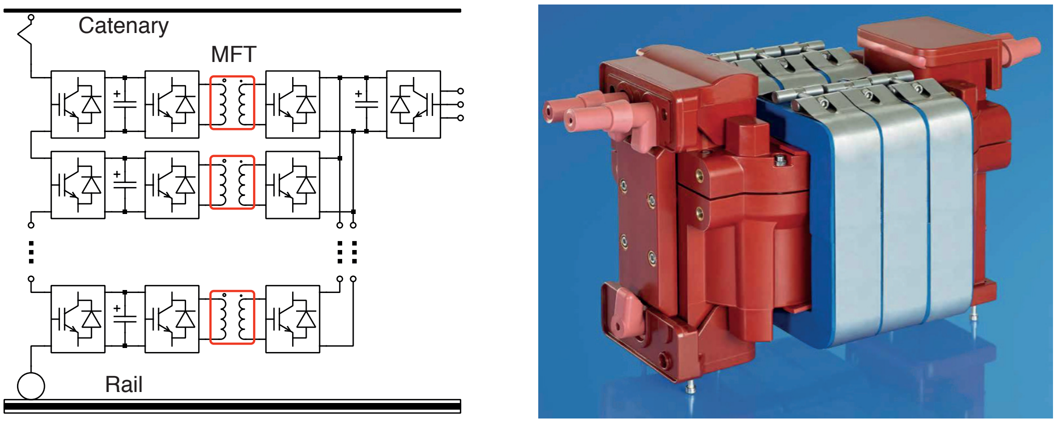

(a)

(b)

Figure 1.5 (a) MFT in solid state transformer for railway application; (b) MFT product from STS [9].

adopted. The silicon steel (SiFe) is produced in form of laminates and stacked together to construct the magnetic core. The windings are composed of solid copper wires in most cases.

1.1.2 Medium frequency (MFT) and high frequency (HFT) transformers

Medium frequency and high frequency transformers are widely employed in DC-DC converters with galvanic isolation, which experience square wave (PWM) excitation generated by the adjacent power electronics circuit. MFTs are usually found in medium voltage, high power applications like power electronic transformers for traction converters, as shown in **Fig. 1.5a**. The grid voltage is first rectified to DC, and then converted into another DC voltage for the drive inverters using DC-DC converters with MFT. In practice, MFTs are usually composed of powdered cores or taped cores of high frequency materials like ferrite, amorphous alloy and nanocrystalline, while the windings are usually realized as wound tube or litz wires.

HFTs are mostly adopted in low voltage switched mode power supplies (SMPSs), like the full bridge phase shifted converter and flyback converter shown in **Fig. 1.6a**. The magnetic core has a form and material as that of MFT but is of smaller size. The winding can be realized in wounded type using litz wire or film wire (**Fig. 1.6b**). In order to reduce the overall height, PCB-integrated planar transformers are also becoming popular (**Fig. 1.6c**).

1.1.3 Filter inductors

Filter inductors can be found in nearly all DC-DC and DC-AC converters for smoothing of the current ripple. In the winding of this type of magnetic components, usually a low frequency sinusoidal current or a static DC current is superimposed by a medium or high frequency ripple, for example in a grid-connected voltage source inverter or a buck converter as shown in **Fig. 1.7a**. The core material, core structure and the winding configuration are similar to that of the MFT and HFT, some different realizations are depicted in **Fig. 1.7b** and **Fig. 1.7c**.

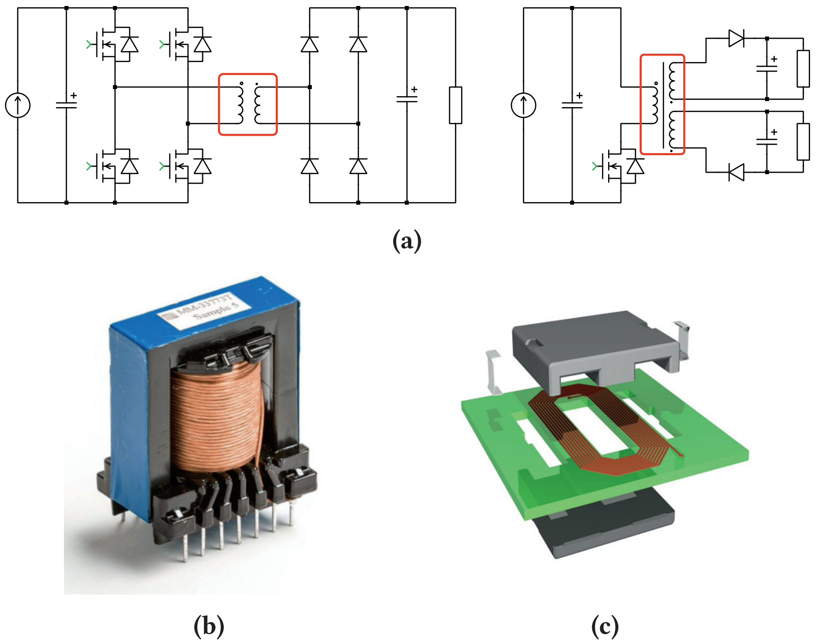

(a) (b) (c)

Figure 1.6 (a) Typical applications of HFT in power electronic systems like full bridge phase shifted converter and flyback converter; (b) HFT with wounded winding [10]; (c) HFT with PCB integrated winding [11].

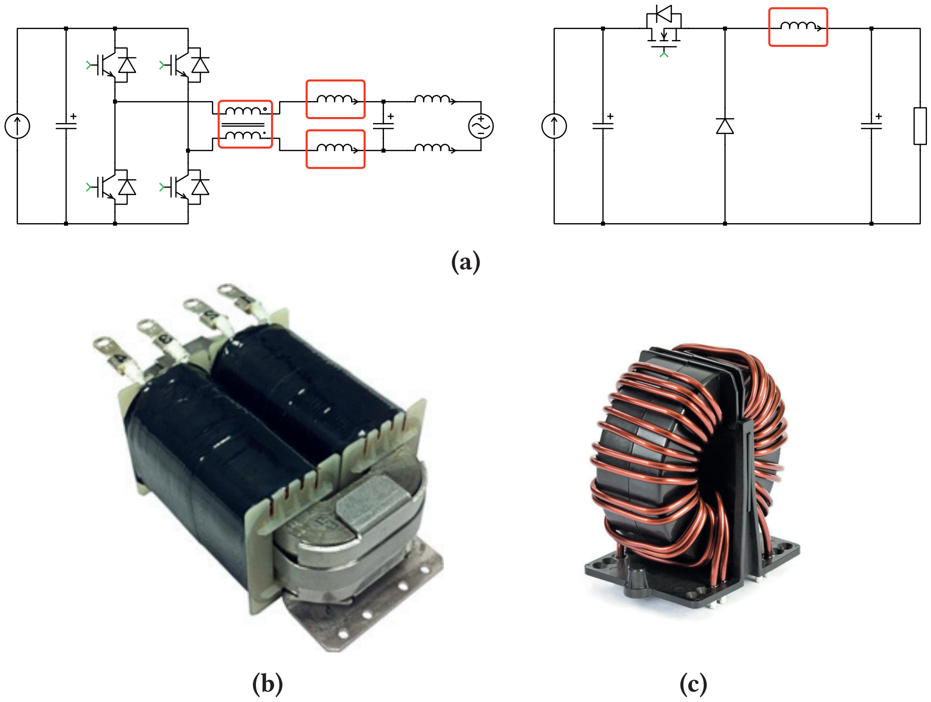

(a) (b) (c)

Figure 1.7 (a) Typical applications of filter inductors in power electronic systems like VSI and buck converter; (b) Filter using gapped U-shape core [12]; (c) Common-mode filter using un-gapped toroidal core [13].

1.2 Motivations for magnetic modeling

During the design phase of a power converter system, system-level time-domain circuit simulation is commonly carried out by engineers to pre-evaluate the overall performance and determine design parameters, prior to the construction of the hardware prototype. The dynamic electrical behavior, power efficiency as well as thermal performance of the complete converter system are mostly of concern, while simplified models are usually sufficient for the individual components (e.g. power semiconductor switches). Regarding the magnetic components, simplified models in form of linear inductor or ideal transformers are commonly applied. In reality however, magnetic components do exhibit non-ideal behavior like the nonlinear characteristic of the core material and the unbalance from leakage flux coupling, which interacts with the rest of the systems. If non-idealities are neglected and the hardware prototype is constructed using the design parameters determined from the simulation result, the performance obtained from experimental test measurement may be considerably different from expected.

Detailed magnetic models are employed during the design process of individual magnetic components. For example, models based on finite element method (FEM) are used to investigate the magnetic field distribution so as to adjust core geometry and winding placement, while models based on empiric formulae like Steinmetz equation are taken to estimate the core loss. However, these models are of too high complexity to be integrated into a system-level simulation environment. Moreover, the physics behind these models are usually obscure and unintuitive for power electronic engineers who are not research deeply in the area of magnetics.

Considering the fact that system-level circuit simulation also helps engineers to better understand the system behavior in relation to the properties of single components, improved models of magnetic component are desired.

1.3 Objectives

The improved model proposed in this thesis uses a permeance-capacitance based magnetic circuit, which on one side has the potential to represent the magnetic structure in a higher level of detail than the electrical equivalence, and on the other side provides a seamless interface to the system-level circuit simulation environment. If the model is properly organized, the simulation can be sufficiently efficient and accurate. Among the magnetic phenomena that power electronic engineers concern about, this thesis focuses on the modeling of two from them: core loss and leakage flux coupling.

1.3.1 Core loss

Core loss of magnetic components is directly related to the overall efficiency of the power electronic system. It is dissipated as heat into the core volume and leads to temperature rise, which could change the $B-H$ characteristic of the material (e.g. lower saturation flux density) and thus the behavior of the magnetic component. Therefore the cooling system needs to be properly sized. According to the definition made by [14], core loss is a combined effect of different physical mechanisms, which can be divided into three groups:

- Hysteresis loss
- Eddy current loss
- Relaxation loss

Hysteresis loss arises from the core material characteristic, and takes place due to irreversible rotation of magnetization or movement of domain-walls. The hysteresis effect is frequency independent, but in reality is always accompanied by the frequency dependent eddy current effect and relaxation effect. The eddy current effect is the result of the material conductivity, which mostly take place in metal-based core materials like silicon steel. The relaxation effect can be observed when the thermal equilibrium of a magnetic system is suddenly altered by some external force and the reestablishment of a new thermal equilibrium happens progressively [14]. During operation, all three mechanisms occur at the same time, so that the magnetic component exhibits obvious nonlinearity in the converter system. The generation of core loss is a coupled effect between the magnetic component and its adjacent circuitry, which need to be captured by the proposed model.

1.3.2 Leakage coupling

The leakage inductance of transformers is related to the magnetic flux flowing through the air or insulation medium, which has a linear magnetic characteristic. It significantly affects the dynamic behavior of the converter system, and must be taken into account during control design. Conventionally, leakage effect is simply represented by series inductor connected to an ideal transformer model in system-level simulation environment. For simple transformer structures with two or three windings, the inductance value can be easily obtained either using empiric formulae available with the designed geometry as input, or by conducting short-circuit test on the constructed magnetic component (even when the remaining hardware is missing). In multi winding structures, however, the complex leakage flux coupling leads to unbalanced short circuit impedance between the windings, depending on the winding placement. For system-level simulations, the simplified representation may result in considerable error.

1.4 Outline

Following this chapter of introduction, a overview of the existing modeling approaches for magnetic components is provided in **Chap. 2**. The advantages of the permeance-capacitance based magnetic circuit, which is taken as fundamental of the models proposed in this thesis, are highlighted. The following part of the thesis is organized in four blocks:

In the first block, a multi-functional magnetic test setup constructed in the frame of this thesis is presented in **Chap. 3**. The test setup is used for model parametrization and verification purposes. The hardware structure and main functionalities are described in details. At the end of the chapter, demonstrative experimental results are provided.

In the second block, the models of frequency independent core loss (hysteresis effect) in permeance-capacitance based magnetic circuit are proposed. Different approaches are applied to different core materials, whose mathematical formulation and the procedure of parametrization are presented. The corresponding results from experimental test are compared to the simulation in each chapter for verification.

- **Chap. 4** presents the model for ferrite materials, which combines the classical Preisach model together with a reversible component. Making use of the logistic distribution function for the classical Preisach model and a new form for the reversible component, the proposed model is able to reproduce both the large limiting loop and small minor loops.

- **Chap. 5** adopts a variation of the classical Preisach model, called product model, for silicon steel materials with wide hysteresis loops. This variation has been tailored to the permeance-capacitance based magnetic circuit. Hysteresis loops in a wide range of field strength amplitude can be captured with good accuracy.

- **Chap. 6** presents a model for core materials with irregular shapes of hysteresis loops such as amorphous and nanocrystalline alloy, which can hardly be reproduced by classical Preisach model using explicit distribution functions. A special formulation of the classical Preisach model is derived, which only requires an expression of the limiting's loops ascending branch.

In the third block, the core loss model is extended to capture the frequency dependent core losses. **Chap. 7** and **Chap. 8** covers different loss mechanisms, and the corresponding experimental verifications are provided:

- **Chap. 7** focuses on modeling the relaxation effect, which has been observed in ferrite cores under PWM excitation with zero-voltage periods and strongly asymmetrical duty cycles. By introducing an additional magnetic resistance and permeance block into the frequency independent model from **Chap. 4**, the extra loss arising from magnetic relaxation can be physically reflected in the circuit model.

- **Chap. 8** presents a model for the eddy current effect in silicon steel materials. The model combines the static hysteresis model from **Chap. 5** with virtual resistive loops in the electrical circuit, so that the frequency dependent core loss due to material conductivity can be captured.

In the fourth block, the models of leakage flux coupling in multi-winding magnetic structures are introduced, aiming to capture their influence on the time domain behavior of the power converter system. Experimental verifications are carried out with short-circuit tests and in connection with diode rectifiers.

- **Chap. 9** presents the fundamental modeling approach, taking a single phase prototype transformer as a starting point. An analytical explanation is provided for the physical origin of the unbalanced short-circuit impedance, using a permeance-capacitance based magnetic circuit. The model structure and the procedure of parametrization are elaborated.

- **Chap. 10** extends the fundamental approach from **Chap. 9** to three-phase phase-shift transformers in commercial MV drive applications. The influence of coupling between different phases, the geometrical misalignment and the extra spacing between windings due to dielectric consideration are additionally considered.

Finally in **Chap. 11**, the modeling approaches proposed in this thesis are summarized. An outlook for the future researches in dynamic modeling of magnetic components is proposed.

1.5 Contribution and publications

Taking the permeance-capacitor based magnetic circuit as the fundamental platform, the major contribution of this thesis is the extension of magnetic components models for phenomena that are commonly considered during power converter designs:

- Models for frequency independent core losses are introduced for commonly used magnetic core materials, which exhibit significantly different shapes of static hysteresis loops.
- Models for frequency dependent core losses including magnetic relaxation and eddy current are presented, also taking into account the frequency independent static hysteresis.
- Models for leakage flux coupling in multi-winding magnetic structures are proposed, aiming to capture the corresponding unbalances in the operation of power converters.

All of the proposed models can be seamlessly integrated into system-level time-domain simulation of power electronic converters. Taking advantage of the proposed model, power electronic designers are able to evaluate the system performance during the design phase more conveniently and accurately. The simulation result can be taken as a reference to improve the magnetic component itself, to adapt the selection of other electrical components and to parametrize the control loop.

The scientific papers published in conjunction with this thesis are listed in below:

Journal papers:

- M. Luo, D. Dujic and J. Allmeling, "Modeling frequency dependent core loss of ferrite materials using permeance-capacitance analogy for system-level circuit simulations", *IEEE Transactions on Power Electronics (early access)*, 2018.
- M. Luo, D. Dujic and J. Allmeling, "Leakage flux modeling of medium-voltage phase-shift transformers for system-level simulations", *IEEE Transactions on Power Electronics (early access)*, 2018.
- M. Luo, D. Dujic and J. Allmeling, "Modeling frequency independent hysteresis of ferrite core materials using permeance-capacitance analogy for system-level circuit simulations", *IEEE Transactions on Power Electronics (early access)*, 2018.
- M. Luo, D. Dujic and J. Allmeling, "Leakage flux modeling of multi-winding transformers for system-level simulations", *IEEE Transactions on Power Electronics*, vol. 33, no. 3, pp. 2471-2483, Mar. 2018.

Conference papers:

- M. Luo, D. Dujic and J. Allmeling, "Test setup for characterisation of biased magnetic hysteresis loops in power electronic applications", *in 2018 International Power Electronics Conference (IPEC-Niigata 2018 ECCE-Asia)*, May. 2018, pp. 422-427.
- M. Luo, D. Dujic and J. Allmeling, "Permeance based modeling of magnetic hysteresis with inclusion of eddy current effect", *in 2018 IEEE Applied Power Electronics Conference and Exposition (APEC)*, Mar. 2018, pp. 1764-1771.

- M. Luo, D. Dujic and J. Allmeling, "Modelling hysteresis of soft core materials using permeance-capacitance analogy for transient circuit simulations", *in 2017 19th European Conference on Power Electronics and Applications (EPE'17 ECCE-Europe)*, Sept. 2017, pp. 1-10.
- M. Luo, D. Dujic and J. Allmeling, "Leakage flux modelling of multi-winding transformer using permeance magnetic circuit", *in 2016 IEEE Applied Power Electronics Conference and Exposition (APEC)*, Mar. 2016, pp. 1108-1114.
- M. Luo, D. Dujic, "Permeance based modelling of the core corners considering magnetic material nonlinearity", *in 41st Annual Conference of the IEEE Industrial Electronics Society (IECON2015)*, Nov. 2015, pp. 950-955.

2

Modeling approaches - Overview

This chapter provides an overview of commonly used modeling approaches for magnetic components, which can be combined with electrical circuit simulation.

2.1 Electrical equivalent circuit

Conventionally, for system-level circuit simulation, the magnetic components are modeled directly in the electrical circuit. The effect of magnetic energy storage in the flux paths is represented by inductors. The inductor voltage is equal to the derivative of the current scaled by the inductance value.

$$V = L \cdot \frac{dI}{dt} \tag{2.1}$$

For complex structure with more than two electrical windings, coupled inductors can be used. The relation between the winding currents and voltages are governed by

$$\begin{bmatrix} V_1 \\ V_2 \\ \ldots \\ V_n \end{bmatrix} = \begin{bmatrix} L_{11} & M_{12} & \ldots & M_{1n} \\ M_{21} & L_{22} & \ldots & M_{2n} \\ \ldots & \ldots & \ldots & \ldots \\ M_{n1} & M_{n2} & \ldots & L_{nn} \end{bmatrix} \cdot \begin{bmatrix} dI_1/dt \\ dI_2/dt \\ \ldots \\ dI_n/dt \end{bmatrix} \tag{2.2}$$

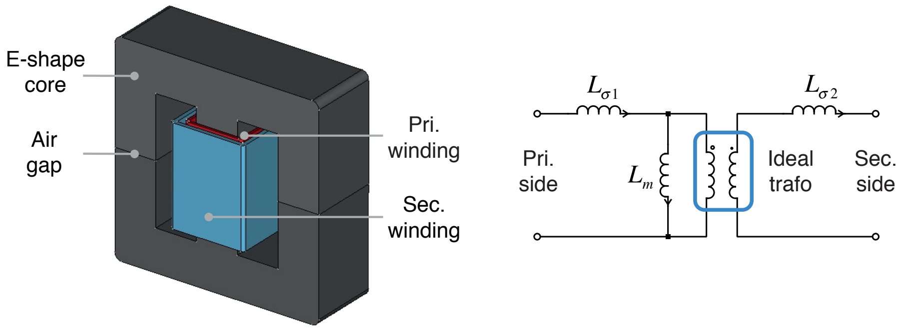

Figure 2.1 Transformer implementation as electrical equivalent circuit

Using coupled inductors, magnetic components can be implemented in any circuit simulators since only electrical components are required. This approach is most commonly used for representing standard magnetic components [15]. A typical two-winding transformer results in a 2 × 2 inductance matrix, which can be equivalently converted into a combination of an ideal transformer and single inductors, as shown in **Fig. 2.1**. Among the inductors, $L_{\sigma 1}$ and $L_{\sigma 2}$ cover the leakage flux, while L_{m} represents the non-linear magnetization inductance.

However, the equivalent circuit bears little resemblance to the physical structure of the magnetic component. Firstly, the magnetization inductance L_{m} hardly reflects the core geometry and material. Secondly, in order to cover the flux coupling in complex magnetic components such as multiple-winding transformers, the equivalent circuit can be difficult to derive and unintuitive to understand. In addition, equivalent circuits based on inductors are impossible to derive for non-planar magnetic components [16].

2.2 Finite element method

The finite element method (FEM) is able to represent the core geometry and flux coupling in a sufficiently detailed level. The physical basis of FEM is the Maxwell field-equations. Introducing a vector potential $\vec{\mathscr{A}}$, which is defined as $\vec{B} = rot\vec{\mathscr{A}}$, the field-equation can be reformulated as

$$\nabla \times \frac{1}{\mu} \nabla \times \vec{\mathscr{A}} + \kappa \frac{\partial \vec{\mathscr{A}}}{\partial t} = \vec{J} \tag{2.3}$$

where κ is the conductivity of the material and $\vec{J}$ is the external current density. The dielectric term $\partial\vec{D}/\partial t$ in the original field-equation is neglected, because the contribution of the displacement current density is negligible in magnetic cores. If observed in a two-dimensional system, under the assumption that the gradient of all variables along the z axis (perpendicular to the $x - y$ plane) are zero, the equation becomes

$$\frac{\partial}{\partial x}(\frac{1}{\mu}\frac{\partial \mathscr{A}}{\partial x}) + \frac{\partial}{\partial y}(\frac{1}{\mu}\frac{\partial \mathscr{A}}{\partial y}) - \kappa \frac{\partial \mathscr{A}}{\partial t} = -J_{\mathrm{s}} \tag{2.4}$$

where $\mathscr{A}$ is the length of the vector potential and J_{s} is the external current density respectively, both of which are aligned with the z direction (perpendicular to the x-y plane).

Solving the field problems using FEM begins with dividing the analysis area into small areas, or in other words“finite elements” (FE). The finer the partitioning, the more accurate the results can be expected. The vector potential $\vec{\mathscr{A}}$ of any arbitrary position inside each FE is represented via interpolation of the adjacent node values [17]. Taking a triangle FE with three nodes as example, the interpolation is expressed as

$$\mathscr{A}(x, y) = \alpha_1 \mathscr{A}_1 + \alpha_2 \mathscr{A}_2 + \alpha_3 \mathscr{A}_3 \tag{2.5}$$

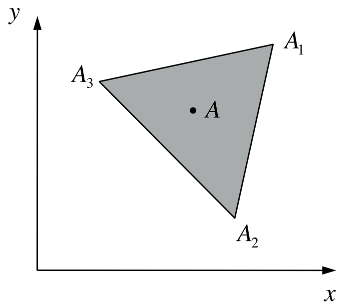

Figure 2.2 A triangle element as fundamental of FEM

where α_{k} is called the shape-function, which is defined as a linear function of the x and y coordinate values:

$$\alpha_{\mathrm{k}} = a_{\mathrm{k}} + b_{\mathrm{k}} x + c_{\mathrm{k}} y \tag{2.6}$$

The constant coefficients a_{k}, b_{k} and c_{k} are chosen such that

$$\alpha_{\mathrm{k}}(x = x_{\mathrm{k}},\ y = y_{\mathrm{k}}) = 1\ , \quad \text{for } k = 1,\ 2,\ 3 \tag{2.7}$$

$$\alpha_k(x = x_{\mathrm{i}},\ y = y_{\mathrm{i}}) = 0\ , \quad \text{for } i \neq k \tag{2.8}$$

The shape function formulation above is not only valid for the vector potential $\mathscr{A}$, but also for the other physical variables like J_s. Special attention need to be paid that each node may belong to several FEs, such that for each FE there will be one corresponding form function. Using Galerkin's method, the differential equation can be transformed into an integral form, which is applied to each FE [18].

$$\iint \Big[\frac{1}{\mu}\Big(\frac{\partial \alpha_{\mathrm{k}}}{\partial x}\frac{\partial \mathscr{A}}{\partial x} + \frac{\partial \alpha_{\mathrm{k}}}{\partial y}\frac{\partial \mathscr{A}}{\partial y}\Big) + \kappa\,\alpha_{\mathrm{k}}\frac{\partial \mathscr{A}}{\partial t} - \alpha_{\mathrm{k}} J_{\mathrm{s}}\Big]\,dxdy = 0 \tag{2.9}$$

where the index α_k is the shape-function of node k in the FE concerned and κ the conductivity assumed to be homogeneous within the FE. Substituting $\mathscr{A}$ with the interpolation form yields

$$\iint \Big\{\frac{1}{\mu}\Big[\frac{\partial \alpha_{\mathrm{k}}}{\partial x}\frac{\partial}{\partial x}\Big(\sum_{j=1}^{3}\alpha_{\mathrm{j}}\mathscr{A}_{\mathrm{j}}\Big) + \frac{\partial \alpha_{\mathrm{k}}}{\partial y}\frac{\partial}{\partial y}\Big(\sum_{j=1}^{3}\alpha_{\mathrm{j}}\mathscr{A}_{\mathrm{j}}\Big)\Big] + \kappa\,\alpha_{\mathrm{k}}\frac{\partial \mathscr{A}}{\partial t} - \alpha_k J_{\mathrm{s}}\Big\}\,dxdy = 0 \tag{2.10}$$

Applying equation (2.10) FE by FE along with their attached nodes yields the matrix form below

$$[K]\,\{\mathscr{A}(t)\} + [C]\,\Big\{\frac{\partial \mathscr{A}(t)}{\partial t}\Big\} - [Q]\,\{J_{\mathrm{s}}\} = \{0\} \tag{2.11}$$

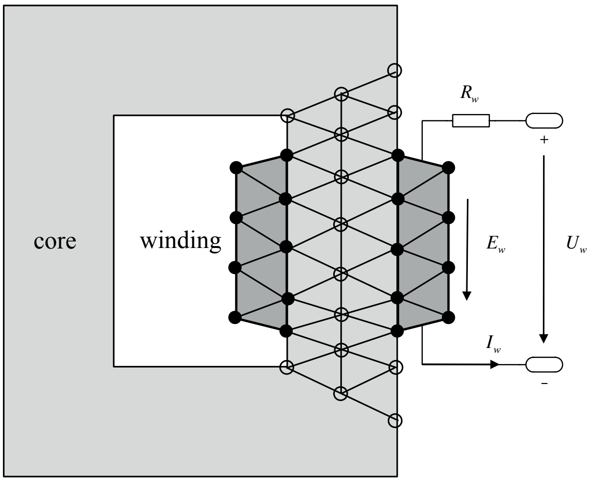

Figure 2.3 Interface between FEM and circuit model

Please note that the length of the array $\{\mathscr{A}\}$ is equal to the number of nodes, while that of $\{J\}$ is equal to number of FEs, under the assumption that current density is homogeneously distributed within each FE. In the case of a linear system, all the elements of the matrix $[K]$ are constant, so that the equation system can be solved by any well-known methods. However if saturation effects need to be taken into account, $[K]$ becomes a nonlinear function of $\{\mathscr{A}\}$, and the numerical algorithms like Newton-Raphson-Iteration have to be adopted, which could potentially increase the simulation time dramatically.

In order to incorporate the field equations into a circuit simulation environment, a simple electrical equivalent circuit for the winding is introduced. As a simple example, one single-winding inductor has been depicted in **Fig. 2.3**. The resistance of the winding is represented by a lumped resistor R_k.

For convenience, the nodes in the FEM model are divided into core nodes (circles in **Fig. 2.3**) denoted by index c and winding nodes (solid points in **Fig. 2.3**) denoted by index w. Similarly, the FEs are also divided into core FEs (bright area) with index c' and winding FEs (dark area in **Fig. 2.3**) with index w'. The FEM equations can be rearranged as

$$\begin{bmatrix} K_{\mathrm{cc}} & K_{\mathrm{cw}} \\ K_{\mathrm{wc}} & K_{\mathrm{ww}} \end{bmatrix} \begin{Bmatrix} \mathscr{A}_{\mathrm{c}} \\ \mathscr{A}_{\mathrm{w}} \end{Bmatrix} + \begin{bmatrix} C_{\mathrm{cc}} & C_{\mathrm{cw}} \\ C_{\mathrm{wc}} & C_{\mathrm{ww}} \end{bmatrix} \begin{Bmatrix} \dfrac{\partial \mathscr{A}_{\mathrm{c}}}{\partial t} \\ \dfrac{\partial \mathscr{A}_{\mathrm{w}}}{\partial t} \end{Bmatrix} - \begin{bmatrix} Q_{\mathrm{c'c'}} & Q_{\mathrm{c'w'}} \\ Q_{\mathrm{w'c'}} & Q_{\mathrm{w'w'}} \end{bmatrix} \begin{Bmatrix} J_{\mathrm{c'}} \\ J_{\mathrm{w'}} \end{Bmatrix} = 0 \tag{2.12}$$

After the separation of core and winding FEs, $\{Q_{\mathrm{w'c'}}\}$ and $\{Q_{\mathrm{c'w'}}\}$ become zero. Since the nodes in the core area have no influence on the FEs in the winding area according to the definition in **Fig. 2.3**, $\{K_{\mathrm{wc}}\}$ and $\{C_{\mathrm{wc}}\}$ should be zero. Also due to the absence of external excitation in the core area, $\{J_{\mathrm{c'}}\}$ is 0. Moreover if the eddy currents in the winding conductor can be neglected, $\{C_{\mathrm{ww}}\}$ becomes zero as well.

$$\begin{bmatrix} K_{\mathrm{cc}} & K_{\mathrm{cw}} \\ 0 & K_{\mathrm{ww}} \end{bmatrix} \begin{Bmatrix} \mathscr{A}_{\mathrm{c}} \\ \mathscr{A}_{\mathrm{w}} \end{Bmatrix} + \begin{bmatrix} C_{\mathrm{cc}} & C_{\mathrm{cw}} \\ 0 & 0 \end{bmatrix} \begin{Bmatrix} \dfrac{\partial \mathscr{A}_{\mathrm{c}}}{\partial t} \\ \dfrac{\partial \mathscr{A}_{\mathrm{w}}}{\partial t} \end{Bmatrix} - \begin{bmatrix} Q_{\mathrm{c'c'}} & 0 \\ 0 & Q_{\mathrm{w'w'}} \end{bmatrix} \begin{Bmatrix} 0 \\ J_{\mathrm{w'}} \end{Bmatrix} = 0 \tag{2.13}$$

Under the assumption of a homogeneous distribution among all the winding FEs, all elements in $\left\{ J_{\mathrm{w'}} \right\}$ can be calculated with the lumped current I_{w} flowing in the electrical circuit divided by the cross-section area of a single turn.

$$J_{\mathrm{w'}} = \frac{N_{\mathrm{w}}\, I_{\mathrm{w}}}{S_{\mathrm{w}}} \tag{2.14}$$

Substituting equation (2.14) into (2.13), and separating the matrixes, (2.13) yields:

$$\begin{bmatrix} K_{\mathrm{cc}} & K_{\mathrm{cw}} \end{bmatrix} \begin{Bmatrix} \mathscr{A}_{\mathrm{c}} \\ \mathscr{A}_{\mathrm{w}} \end{Bmatrix} + \begin{bmatrix} C_{\mathrm{cc}} & C_{\mathrm{cw}} \end{bmatrix} \begin{Bmatrix} \dfrac{\partial \mathscr{A}_{\mathrm{c}}}{\partial t} \\ \dfrac{\partial \mathscr{A}_{\mathrm{w}}}{\partial t} \end{Bmatrix} = 0 \tag{2.15}$$

$$\begin{bmatrix} K_{\mathrm{ww}} \end{bmatrix} \left\{ \mathscr{A}_{\mathrm{w}} \right\} - \begin{bmatrix} Q_{\mathrm{w'w'}} \end{bmatrix} \begin{Bmatrix} \dfrac{N_{\mathrm{w}} I_{\mathrm{w}}}{S_{\mathrm{w}}} \end{Bmatrix} = 0 \tag{2.16}$$

In order to interface the FEM model into a system level circuit simulation, the back EMF E_{w} induced in the coil winding provides the bridge, as has been described by the work of [19].

$$E_{\mathrm{w}} = \frac{N_{\mathrm{w}}\, l_{\mathrm{z}}}{S_{\mathrm{w}}} \iint\limits_{S_{\mathrm{w}}} \frac{\partial \mathscr{A}}{\partial t}\, dS \tag{2.17}$$

In the equation above, N_{w} is the turns number and S_{w} is the total cross-section area of the winding. l_{z} is the thickness of the FEM model in z direction. Substituting the shape function formulation yields

$$E_{\mathrm{w}} = \left\{ F \right\}^{T} \begin{Bmatrix} \dfrac{\partial \mathscr{A}_{\mathrm{w}}}{\partial t} \end{Bmatrix} \tag{2.18}$$

where $\left\{ F \right\}^{T}$ is a row vector. The equation in the electrical equivalent circuit is given as

$$U_{\mathrm{w}} = E_{\mathrm{w}} + R_{\mathrm{w}}\, I_{\mathrm{w}} \tag{2.19}$$

In the time domain, the state variables $\left\{\mathscr{A}_\mathrm{c}\right\}$, $\left\{\mathscr{A}_\mathrm{w}\right\}$ of the current and future sample points can be related by their derivatives, for example using implicit Backward-Euler algorithm with the step size Δt.

$$\begin{Bmatrix}\mathscr{A}_\mathrm{c}\\ \mathscr{A}_\mathrm{w}\end{Bmatrix}_{\mathrm{n+1}} = \begin{Bmatrix}\mathscr{A}_\mathrm{c}\\ \mathscr{A}_\mathrm{w}\end{Bmatrix}_{\mathrm{n}} + \Delta t \begin{Bmatrix}\dfrac{\partial \mathscr{A}_\mathrm{c}}{\partial t}\\ \dfrac{\partial \mathscr{A}_\mathrm{w}}{\partial t}\end{Bmatrix}_{\mathrm{n+1}} \tag{2.20}$$

Substituting the derivative term of (2.20) into (2.15), (2.16) and (2.18), together with (2.18), the FEM model can be combined into a larger circuit model. With $\left\{\mathscr{A}_\mathrm{c}\right\}_\mathrm{n}$ and $\left\{\mathscr{A}_\mathrm{w}\right\}_\mathrm{n}$ given, $\left\{\mathscr{A}_\mathrm{c}\right\}_\mathrm{n+1}$ and $\left\{\mathscr{A}_\mathrm{w}\right\}_\mathrm{n+1}$ can be solved.

$$\begin{bmatrix}K_\mathrm{cc} + \dfrac{1}{\Delta t}C_\mathrm{cc} & K_\mathrm{cw} + \dfrac{1}{\Delta t}C_\mathrm{cw}\end{bmatrix} \begin{Bmatrix}\mathscr{A}_\mathrm{c}\\ \mathscr{A}_\mathrm{w}\end{Bmatrix}_{\mathrm{n+1}} - \begin{bmatrix}\dfrac{1}{\Delta t}C_\mathrm{cc} & \dfrac{1}{\Delta t}C_\mathrm{cw}\end{bmatrix} \begin{Bmatrix}\mathscr{A}_\mathrm{c}\\ \mathscr{A}_\mathrm{w}\end{Bmatrix}_{\mathrm{n}} = 0 \tag{2.21}$$

$$\begin{bmatrix}K_\mathrm{ww}\end{bmatrix} \left\{\mathscr{A}_\mathrm{w}\right\}_\mathrm{n+1} - \begin{bmatrix}Q_\mathrm{w'w'}\end{bmatrix} \begin{Bmatrix}\dfrac{N_\mathrm{w} I_\mathrm{w,n+1}}{S_\mathrm{w}}\end{Bmatrix} = 0 \tag{2.22}$$

$$E_\mathrm{w,n+1} = \frac{1}{\Delta t}\left\{F\right\}^T \left\{\mathscr{A}_\mathrm{w}\right\}_\mathrm{n+1} - \frac{1}{\Delta t}\left\{F\right\}^T \left\{\mathscr{A}_\mathrm{w}\right\}_\mathrm{n} \tag{2.23}$$

$$U_\mathrm{w,n+1} = E_\mathrm{w,n+1} + R_\mathrm{w}\, I_\mathrm{w,n+1} \tag{2.24}$$

The method introduced above can be extremely time consuming, due to the huge number of FE nodes required to achieve sufficient accurary. Moreover, should nonlinear effects of the magnetic material be taken into account, $\{\mathscr{A}_\mathrm{w}\}$, $\{\mathscr{A}_\mathrm{c}\}$, I_w as well as the external circuit need to be solved all together simultaneously via Newton-Ralphson iteration, according to the work of [20].

2.2.1 Magnetic equivalent circuit: Resistance-reluctance analogy

If the detail of magnetic field distribution in the core is not of concern, the magnetic device can be represented in a lumped way using a magnetic circuit. The conventional approach to model magnetic structures with equivalent magnetic circuits is the reluctance-resistance analogy. As a basic constructional element, the reluctance element $\mathscr{R}$ represents the complete core or one part of the

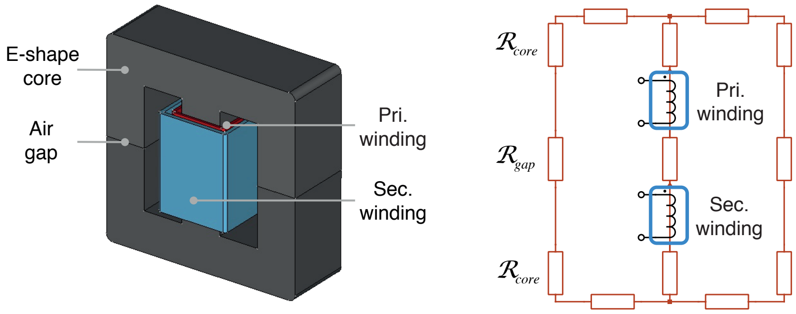

Figure 2.4 Three leg transformer core represented by reluctances

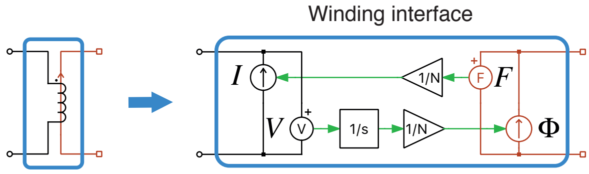

Figure 2.5 Interface in reluctance approach

it. Its value is determined by the geometry including the equivalent magnetic path length l and the cross-section area $\mathscr{A}$, together with the material characteristics reflected by the permeability μ.

$$\mathscr{R} = \frac{1}{\mu} \cdot \frac{l}{A} \tag{2.25}$$

The geometric structure of an E-shape transformer core can be partitioned into several parts, each of which has a specific cross-section area and can thus be represented by one lumped reluctance, as depicted in **Fig. 2.4**. Instead of analyzing the field strength H and the flux density B, the magnetomotive force (MMF) F as the line integration of H along the flux path, and the magnetic flux Φ as teh surface integration of B with the the cross-section area, are considered. In the reluctance-resistance based magnetic circuit, F is regarded as the across-variable (similar to electrical voltage) and Φ as the flow-variable (similar to electrical current). The circuit behaviour of a magnetic reluctance is given by the equation in below, as described by the work of [15].

$$F = \mathscr{R} \cdot \Phi \tag{2.26}$$

In order to link the electrical circuits and magnetic circuits together, the windings of the transformer or inductor serve as the interface. The flux linked by a certain winding is the time-integration of the terminal voltage divided by the turns number N, while the magnetomotive force F is equal to the turns number multiplied by the electrical current. Following this rule, the interface between the magnetic circuit and electrical circuit can be established as shown in **Fig. 2.5**, where the flux (as integration of the winding voltage) presents as a “magnetic” current source in the magnetic circuit, while the “magnetic” voltage (MMF) is reflected by a current source in the electrical circuit.

If the core geometry is properly partitioned and the material characteristics of the magnetic material are clearly defined, this lumped model can be sufficiently intuitive and accurate. Since F and Φ in the magnetic circuit behave similarly to an electrical circuit following Kirchhoff's law, the dimension of the problem has been strongly reduced compared to the FEM approach and therefore requires significantly less computational effort. However, if nonlinearity needs to be taken into account, the permeability μ will be nonlinear function of F (μ is usually defined as $\mu(H)$, and $H = F/l$). This leads to algebraic loop, so that a Newton-Ralphson iteration must be used, which can be time-consuming. Moreover, the integrator between the electrical voltage measurement and flux source indicates that the magnetic energy is stored locally in the individual winding, which in reality, is not the case.

2.2.2 Magnetic equivalent circuit: Permeance-capacitance analogy

To avoid the Newton-Ralphson iteration while solving nonlinear problem in the magnetic circuit and reduce the computational effort, the capacitor-permeance approach has been proposed by the author of [16]. Instead of reluctances, the core is represented by permeances, the value of which is the reciprocal of reluctance.

$$\mathscr{P} = \mu \cdot \frac{A}{l} \tag{2.27}$$

If the time derivative of flux $d\Phi/dt$ (or $\dot{\Phi}$) is taken as the flow-variable in the magnetic circuit, and the magnetomotive force F still as the across-variable, the permeance can be handled similarly to a

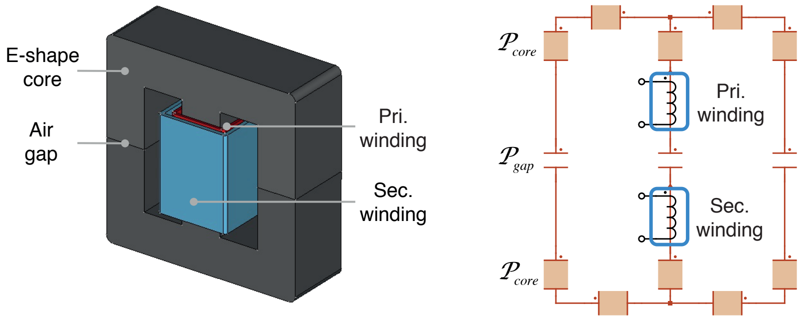

Figure 2.6 Three leg transformer core represent by permeances

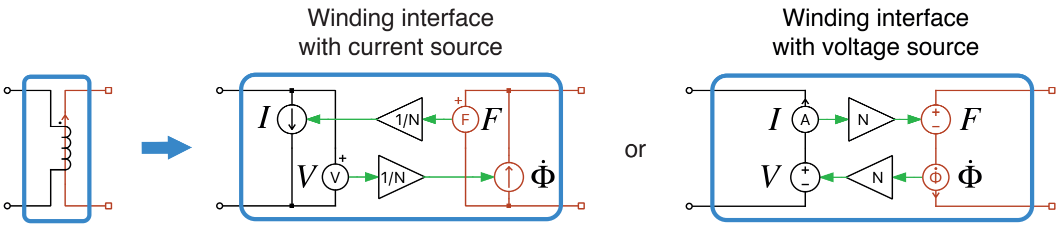

Figure 2.7 Interface in permeance approach

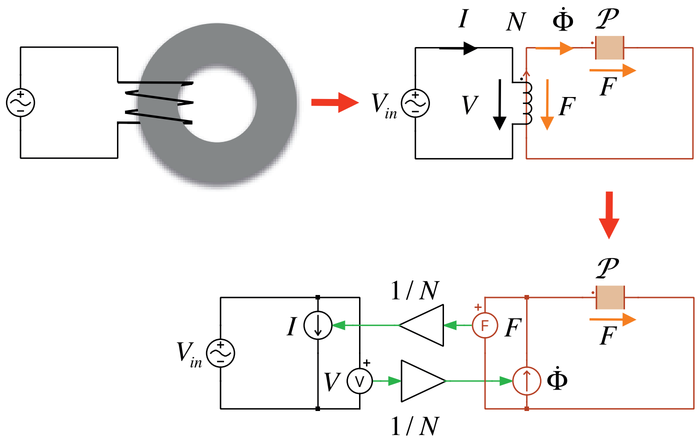

Figure 2.8 Demonstration of a simple inductor model using permeance magnetic circuit and gyrator interface

capacitor. The governing circuit equation thus becomes:

$$\dot{\Phi} = \mathscr{P} \cdot \frac{dF}{dt} \tag{2.28}$$

The model of a two-winding transformer is shown in **Fig. 2.6**. The gyrator structure is used for the winding interface. In one way, the terminal voltage in the electrical circuit is directly introduced into the magnetic circuit as a “magnetic” current ($\dot{\Phi}$) and the “magnetic” voltage (MMF denoted by F) back into electrical circuit as a electrical current, via a linear gain $1/N$. In the other way, the electrical current is translated into a “magnetic” voltage (MMF denoted by F) and the “magnetic” current into a electrical voltage, via a linear gain N. Both realization of a gyrator structure are shown in **Fig. 10.4**. The integrator in the winding interface of the reluctance approach is eliminated here, instead the magnetic energy is stored in the permeances, or in other words, in the magnetic field of the core.

In order to demonstrate the basic modeling approach, a simple inductor excited by a voltage source is taken as an example as shown in **Fig. 2.8**. The circuit model is established including the magnetic permeance $\mathscr{P}$ representing the toroidal core, the winding component with turns number N using gyrator structure and the voltage source V_{in}. The MMF of the toroidal core is the integral of the flux rate divided by the permeance value

$$F = \frac{1}{\mathscr{P}} \cdot \int \dot{\Phi} \cdot dt \tag{2.29}$$

Substituting the MMF by the winding current I using the relation $I = F/N$ and substituting the flux rate $\dot{\Phi}$ by the relation $\dot{\Phi} = V$ yields

$$I = \frac{1}{N^2 \cdot \mathscr{P}} \cdot \int V \cdot dt \tag{2.30}$$

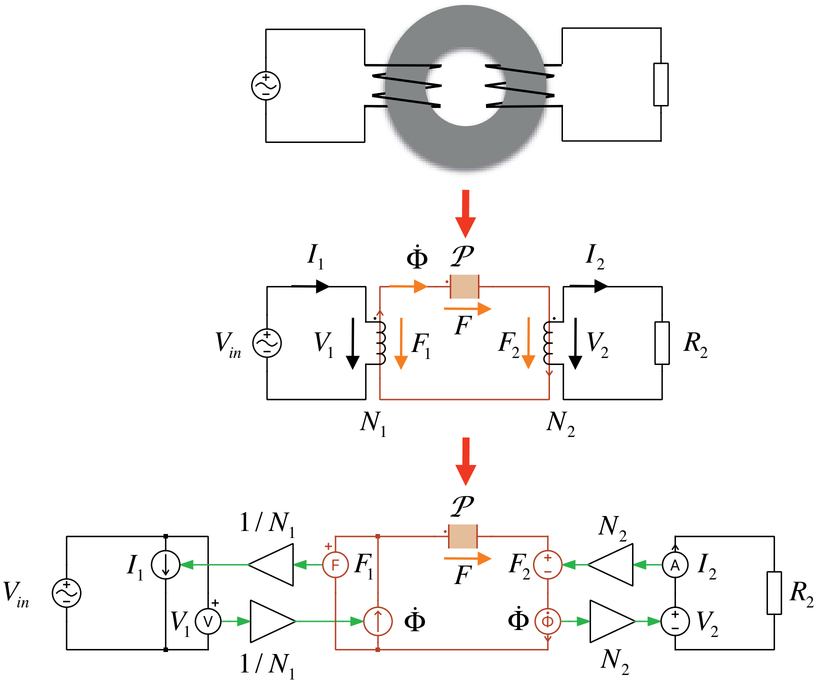

Figure 2.9 Demonstration of a simple transformer model using permeance magnetic circuit and gyrator interface

where the coefficient $N^2\mathscr{P}$ corresponds to the electrical inductance. Further on, the case of magnetic components with multiple windings is demonstrated using a simple ring core transformer as shown in **Fig. 2.9**, where the primary winding (turns number N_1) is supplied by a voltage source V_{in} and the secondary winding (turns number N_2) is loaded by a resistor R_2. Starting from the secondary side, with a induced voltage on the winding terminal the current I_2 appears on the resistor R_2

$$I_2 = V_2/R_2 = \frac{V_1 \cdot N_2/N_1}{R_2} \tag{2.31}$$

On the primary side, the winding current I_1 is equal to the MMF (F_1) divided by the primary winding turns number N_1

$$I_1 = F_1/N_1 \tag{2.32}$$

In the magnetic circuit, the MMF (F_1) is equal to the sum of the MMF on the core permeance $\mathscr{P}$ (F) and that from the secondary winding (F_2)

$$F_1 = F + F_2 = \frac{1}{\mathscr{P}} \cdot \int \dot{\Phi} \cdot dt + N_2 \cdot I_2 = \frac{1}{\mathscr{P}} \cdot \int \frac{V_1}{N_1} \cdot dt + N_2 \cdot I_2 \tag{2.33}$$

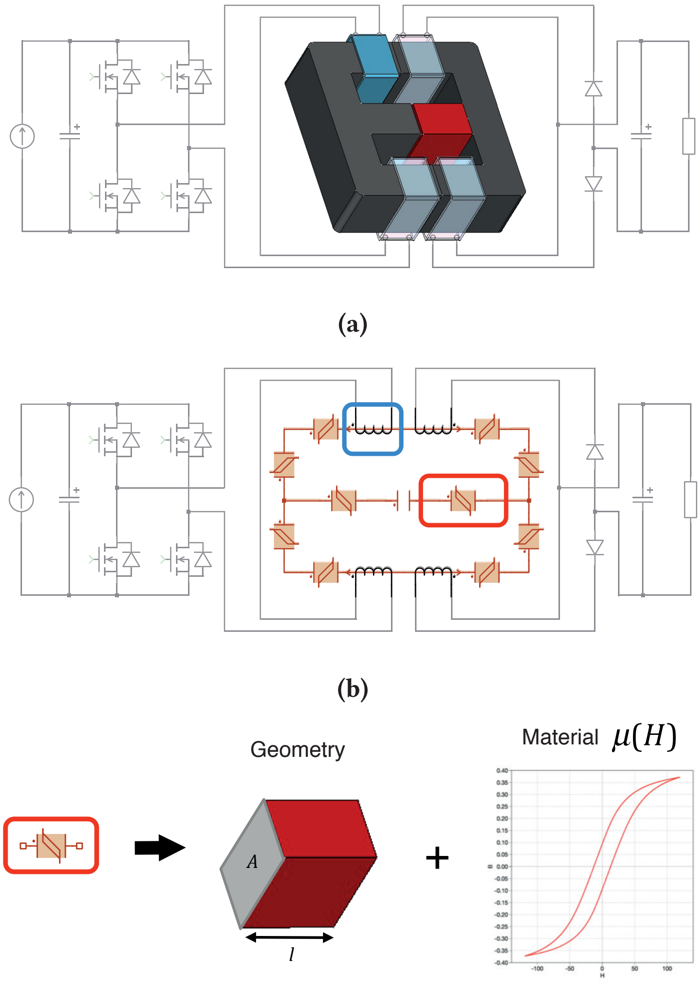

(a)

(b)

(c)

Figure 2.10 Example of permeance-capacitance based magnetic circuit: (a) Integrated magnetic component; (b) Magnetic circuit of the integrated magnetic component; (d) Core block parametrised by geometry and material characteristic.

Substituting equation (2.33) into (2.32) yields

$$I_1 = \frac{1}{N_1^2 \cdot \mathscr{P}} \cdot \int V_1 \cdot dt + \frac{N_2}{N_1} \cdot I_2 \tag{2.34}$$

The first term at the right side of equation (2.34) corresponds to the magnetization current of the transformer and the second term corresponds to the secondary winding load current which is transformed into the primary winding side.

Taking advantage of the permeance-capacitance based magnetic circuit, a complex magnetic structure in a full-bridge phase-shift DC-DC converter can be derived intuitively, as shown in **Fig. 2.10a** and **Fig. 2.10b**. Please note that *F* now becomes a state variable, so that solving the material nonlinearity does not require any numerical iteration. The nonlinearity is modeled by making the permeability $\mu(H)$ a function of the field strength $H = F/l$, as depicted in **Fig. 2.10c**.

Considering the flexibility and potential to easily model the core material nonlinearity, the permeance-capacitance based magnetic circuit is chosen as the fundamental platform of the magnetic component models presented in this thesis.

3

Test setup for core material characterization

The power loss of a core material under arbitrary operation conditions is directly reflected by the magnetization curves on the $B-H$ plane. In order to obtain the $B-H$ characteristic of core samples as input data for model parameter identification as well as for fidelity verification, a multi-functional magnetic characterization test setup has been developed. In this section, the main functionalities of the characterization setup are introduced and preliminary experimental results are presented, which were obtained during functional testing and tuning of various operating modes.

3.1 Objectives

In real power converters, the electrical circuit quantities like voltage (and current) may vary from several volts (amps) up to hundreds of kVs (kAs), depending on their applications. The magnetic field quantities like flux density B and field strength H however, are confined in a much smaller range which is independent of the power rate of the magnetic components, as long as the same core material is applied. This leads to the fact that the core material's $B-H$ characteristic of a large magnetic component designed for high voltage, high current application can be reproduced by a small sample core excited with low voltage and low current. Taking advantage of these circumstances, the test setup is designed to emulate arbitrary operating conditions that a core material experiences in reality, using low voltages and currents.

Four typical operating conditions, common in power electronic systems, can be identified for the magnetic components:

- **Sinusoidal excitation:** In line-frequency transformers which interface voltage source inverter (VSI) to the power grid, especially when the grid is stiff with low internal impedance, the windings are excited by an ideal sinusoidal voltage of low frequency (e.g. 50 Hz). This results in a symmetrical hysteresis loop on the $B-H$ plane, as shown in **Fig. 3.1a**.

- **Asymmetrical PWM excitation with DC bias**: In non-isolated types of DC-DC converters like the Buck converter shown in **Fig. 3.1b**, an asymmetrical PWM excitation with a duty cycle generally different from 50 % is applied, so that the current flowing in the inductive filter winding has a DC-bias. The DC-bias of the winding current directly determines the field strength (H) offset, or in other words, the horizontal position of the hysteresis loop. The vertical position (flux density B) is determined by the previous events in the magnetisation history. A hysteresis loop with an offset on the $B-H$ plane is depicted in **Fig. 3.1b**.

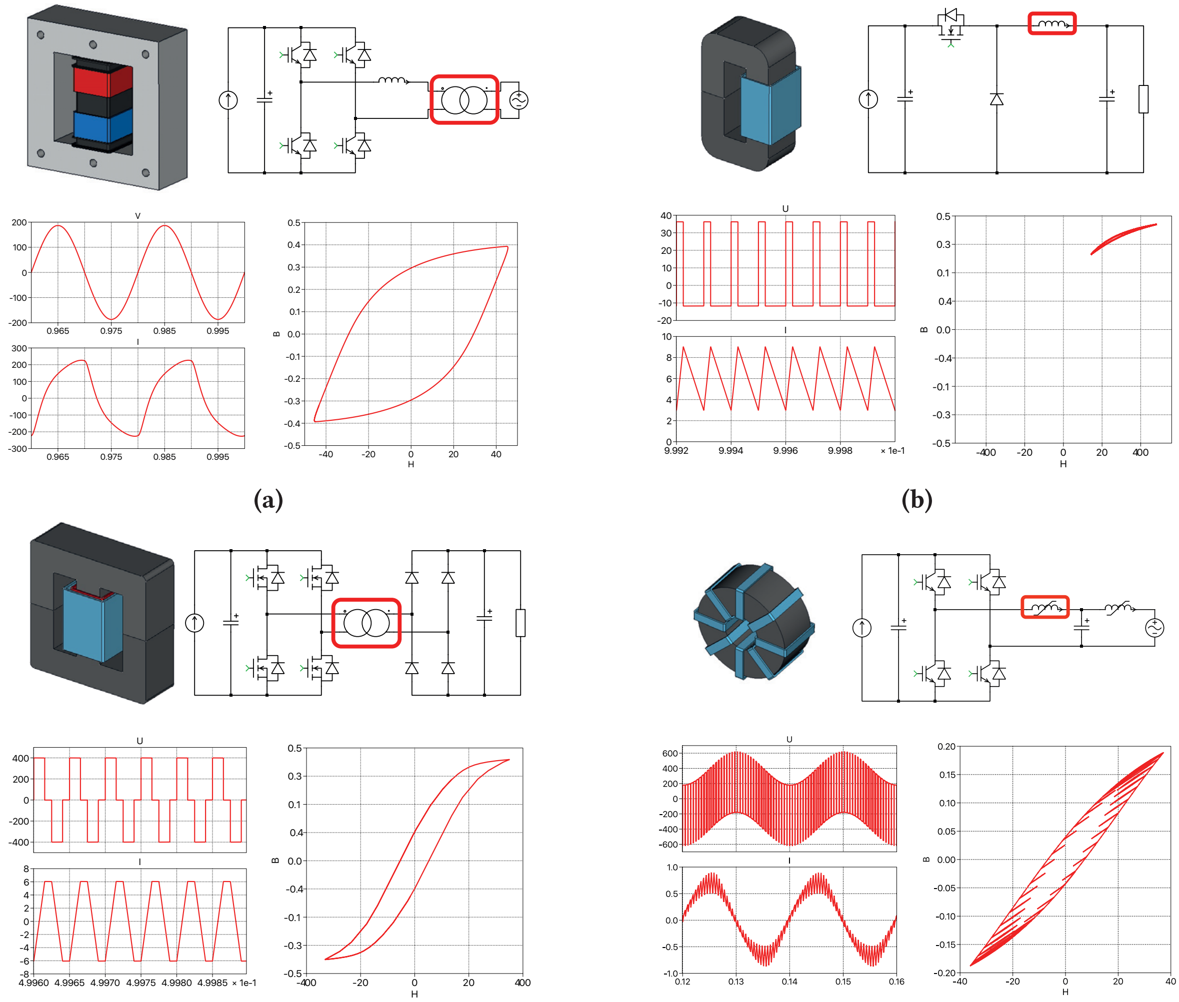

(a) (b) (c) (d)

Figure 3.1 Circuit example, time domain waveforms and $B-H$ characteristic for different operation conditions of magnetic components (a) Line frequency transformer interfacing VSI and power grid (b) Filter inductor in Buck converter with DC-bias (c) Isolation transformer in DC-DC converter with phase-shift modulation (d) Filter inductor in VSI with both sinusoidal and PWM excitation

- **Symmetrical PWM excitation with zero voltage period**: In galvanically isolated DC-DC converters, taking the single active bridge topology depicted in **Fig. 7.1** as an example, the transformer experiences a symmetrical PWM excitation, which results in a symmetrical hysteresis loop on the $B-H$ plane. In order to control the output voltage, a phase shift is introduced to the modulation and a zero-voltage period is present. Different percentage of the zero-voltage period adds up more or less to the core loss, which can be ascribed to the relaxation effect of the core material, as has been discussed in the work of [21].

- **PWM excitation superimposed with sinusoidal component**: In grid connected inverters the inductor filters are excited by both the sinusoidal voltage from the grid side and the pulsed voltage from the power electronic bridge side. With this mixed excitation the current on the inductor winding has both a fundamental component and high frequency ripples, which result in a major hysteresis loop superimposed with small minor loops on the $B-H$ plane, as demonstrated in **Fig. 3.1d**.

Different operating conditions results in hysteresis loops of different shape and offset, the characterization of which can be facilitated using a versatile and flexible test setup. The magnetic test setup proposed in this work is able to reproduce the aforementioned operating conditions for core samples of different materials.

3.2 Hardware description

The hardware of the characterisation setup is designed to have 24 V rated output voltage and 6 A rated output current. The basic idea is derived from the V-I approach proposed by the work of [22]. The circuit schematic and photo of the actual setup are shown in **Fig. 3.2** and **Fig. 3.3a**, including the following elements:

3.2.1 Power stage

The power stage hardware shown in **Fig. 3.4** contains the following functional units. Their positioning on the PCB are marked in **Fig. 3.3b**:

- **The controlled voltage source** V_1 is realized using a power amplifier of type LM3886 with a 2 MHz gain-bandwidth-product and is supplied by ±24 V. The main usage of V_1 is to generate sinusoidal excitation with frequencies up to 10 kHz for major hysteresis loops and can be bypassed by the switch S_1 to ground if unused.

- **The single phase T-type bridge** is composed of three bidirectional switch pairs (Q_{01}&Q_{02}, Q_{11}&Q_{12}, Q_{21}&Q_{22}) to generate PWM excitation of up to 50 kHz. Each of the bidirectional switches contains two MOSFETs of type AO4444 with 80 V blocking voltage and 11 A rated current. Each bidirectional switch is connected to an individually controlled voltage source (V_2,

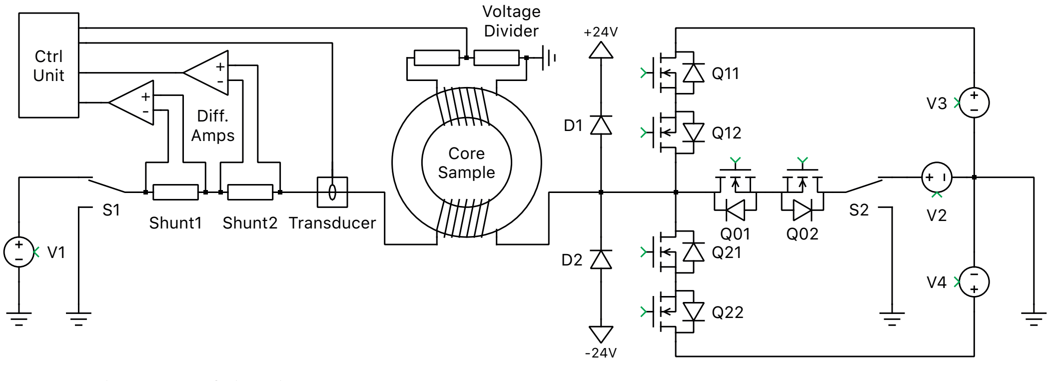

Figure 3.2 Schematic of the characterisation setup

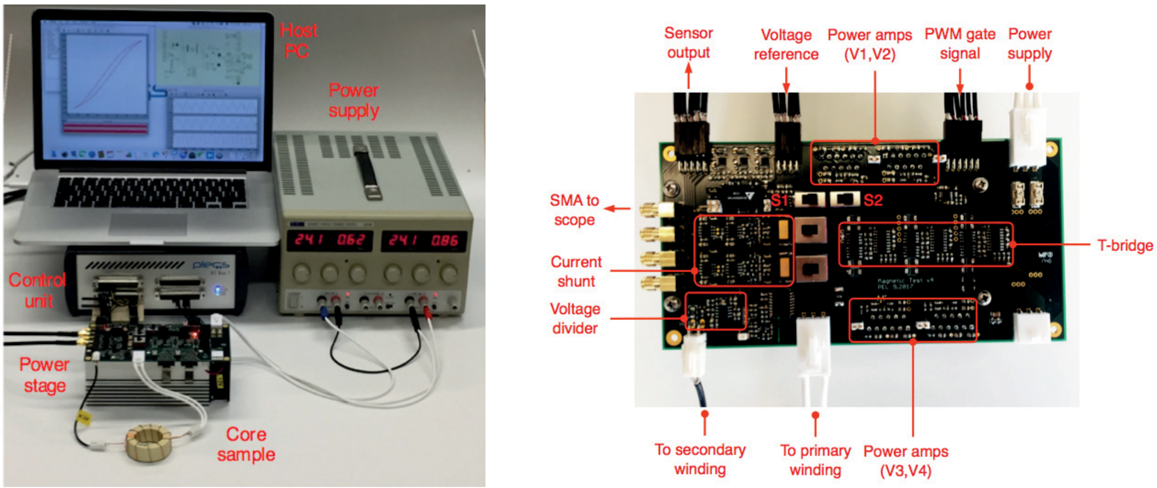

(a) (b)

Figure 3.3 (a) Complete configuration of the characterisation setup including the power stage, core sample, power supply, control unit (PLECS RT-Box) and host PC (b) Arrangement of main functional units on the power stage PCB

Figure 3.4 Power stage hardware of the characterisation setup

V_3, V_4). They are realized using the same type of power amplifier as V_1. The voltage source V_2 can be bypassed by the switch S_2 to ground. All MOSFETs have individual gate drivers and the two diodes D_1 and D_2 are mounted for free-wheeling of the inductive current during the switching dead-time.

- **The current measurement** is realized using low-inductance shunt resistors, taking advantage of their good accuracy and nearly zero phase-delay, which are sensitive enough for measuring the core loss. The voltage drop of the shunt resistor is sensed and amplified using differential instrumentation amplifiers of type AD8429. Two sets of shunt resistors with different resistance are mounted to achieve higher resolutions, both can be bypassed by switches.

  Besides the shunt resistors, another low resolution Hall-type current transducer of type ACS710 is installed on the primary side for fault detection. In combination with a simple logic circuit, all power amplifiers will be muted (output 0 V) if the circuit current exceeds the protection threshold, which can be externally configured for the ACS710 chip.

- **The voltage measurement** is realized using a low capacitance resistive voltage divider. The scaled voltage is amplified by an operational amplifier of type THS4062. An analog integrator is also implemented using another op-amp, which integrates the measured voltage to estimate the flux-rate. Accurate calculation of the flux rate waveform, so as to obtain the flux density (B) waveform, should be achieved by post-processing the voltage measurement in a digital way.

3.2.2 Core Sample

Following the V-I approach for magnetic material characterisation, the core sample should be equipped with two windings as shown in **Fig. 3.2**. The primary winding is excited by the power stage and the secondary winding is left open for voltage measurement. In order to minimise the leakage flux coupling through the air, the secondary winding should be wound as tightly as possible on the core sample. The turns number of the winding should be adapted to the desired filed strength and flux density range on the $B - H$ plane.

3.2.3 Control unit

One PLECS RT-Box is deployed as a control unit for the characterisation setup, which is graphically operated on a host PC using PLECS software environment. The update step size is $2\mu s$ for both data acquisition, processing and the control algorithm.

Four of the 16 available analog output channels of the control unit provide the reference voltage for the power amplifiers. Three out of the 16 analog input channels are connected to the amplification output of the current and voltage measurements, which are converted to field strength (H) and flux density (B) inside the control unit using the equations

$$H = \frac{N_1 \cdot I}{l} \tag{3.1}$$

$$B = \frac{\int V \cdot dt}{N_2 \cdot A} \tag{3.2}$$

where the cross section area A and the equivalent magnetic path length l are geometry-related parameters of the core sample, while N_1 and N_2 are turns numbers of the primary and secondary winding. For gate signal generation of the T-bridge, six of the 32 available digital output channels of the control unit are used.

3.3 Operation modes and control

The proposed characterization setup can be operated in the following four modes, which emulate several typical operating conditions of magnetic components in a power electronics system:

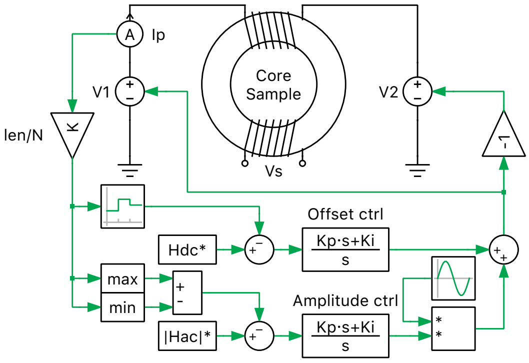

Figure 3.5 Equivalent circuit and control loop for the sinusoidal operation mode

3.3.1 Sinusoidal mode

In this operation mode, a sinusoidal voltage reference of the desired amplitude and frequency is provided to the power amplifiers V_1 and V_2. The switches S_1 and S_2 connect V_1 and V_2 with the test circuit, while the bidirectional switch pair $Q_{01}\&Q_{02}$ is closed as well. In order to configure the desired field strength amplitude $|H_{ac}|^*$ and the DC offset H_{dc} of the hysteresis loop, a simple closed-loop control algorithm is applied. The measured circuit current is converted into field strength using equation (3.1) and processed by an averaging filter of the AC period and a peak value calculator to obtain the offset and amplitude. These two values are subtracted from the references and fed into two PI type controllers. The output of the amplitude controller is multiplied by a sinusoidal signal of the desired excitation frequency with unity amplitude and added to the output of the offset controller, to be used as the reference voltage of the two power amplifiers. Please note that the reference voltages for V_1 and V_2 are opposite in polarity, extending the excitation voltage range on the core sample to ±48 V, which can be necessary to achieve the desired field strength amplitude at relatively high frequencies. The equivalent circuit of this operation mode as well as the control loop is shown in **Fig. 3.5**.

3.3.2 Duty-cycle PWM mode

In this operation mode, the bidirectional switch pairs $Q_{11}\&Q_{12}$ and $Q_{21}\&Q_{22}$ are driven by PWM gate signals of desired duty cycle d and switching frequency, while $Q_{01}\&Q_{02}$ are deactivated. DC voltage references are provided to the power amplifiers V_3 and V_4. Their values should comply with the equation below:

$$V_3 \cdot d = -V_4 \cdot (1 - d) \tag{3.3}$$

The power amplifier V_1 is also active in this operation mode and connected to the circuit via the switch S_1, its output voltage needs to be adjusted by the control unit in order to achieve the desired DC offset for the field strength H. A control structure similar to the sinusoidal mode is adopted here, the equivalent circuit schematic together with the control loop is illustrated in **Fig. 3.6a**. Please

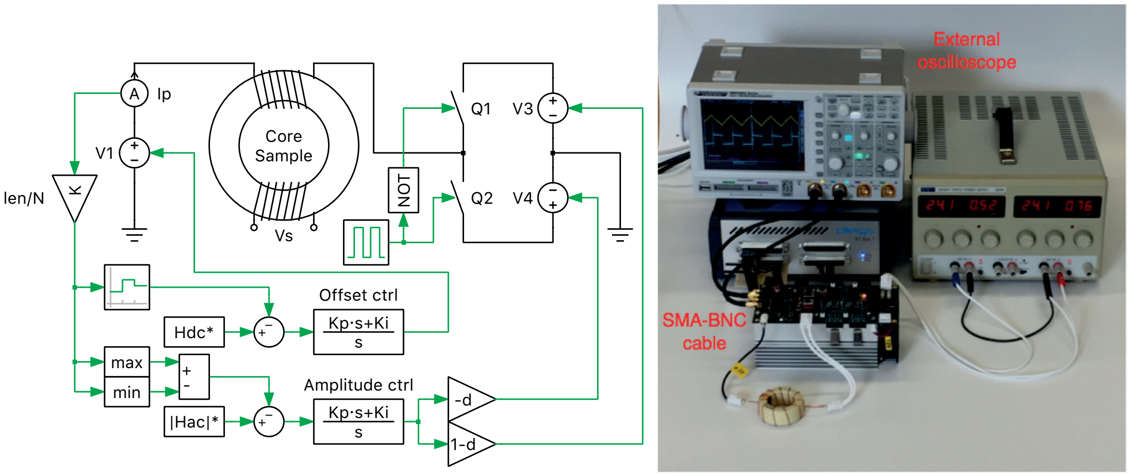

(a) **(b)**

Figure 3.6 (a) Equivalent circuit and control loop for the duty-cycle PWM operation mode; (b) Test configuration for high frequency PWM

note that the PWM generation needs to be synchronized with the execution time step of the control algorithm. For PWM frequencies above 10 kHz, the 2 μs execution step size of the control unit can no longer provide sufficiently high resolution to capture the current peak value. In this case, the measurement signal should be sent to a external hardware scope via the SMA connector at the left hand side of the PCB, while the amplitude and offset need to be manually adjusted.

3.3.3 Phase-shift PWM mode

In this operation mode, all of the bidirectional switch pairs are driven by PWM gate signals to emulate phase-shifted PWM with a zero-voltage period. DC voltage references with opposite polarities are provided to the power amplifiers V_3 and V_4, while the switch S_2 bypasses the power amplifier V_2

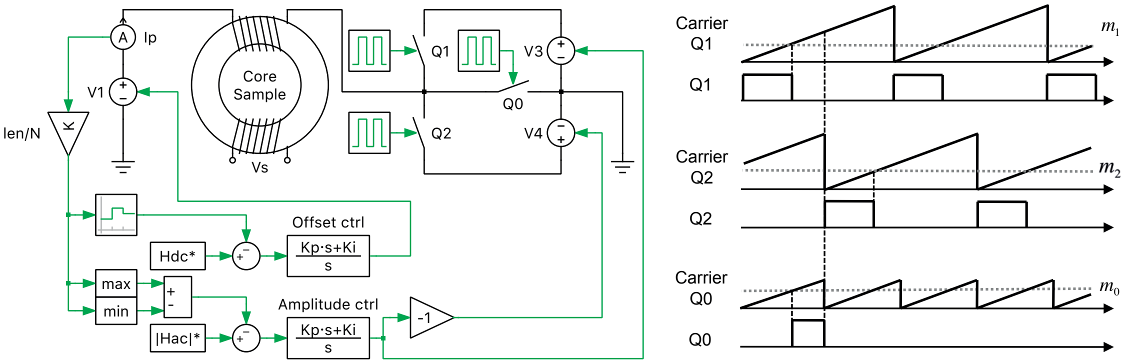

(a) **(b)**

Figure 3.7 (a) Equivalent circuit and control loop for the phase-shift PWM operation mode; (b) PWM generation scheme

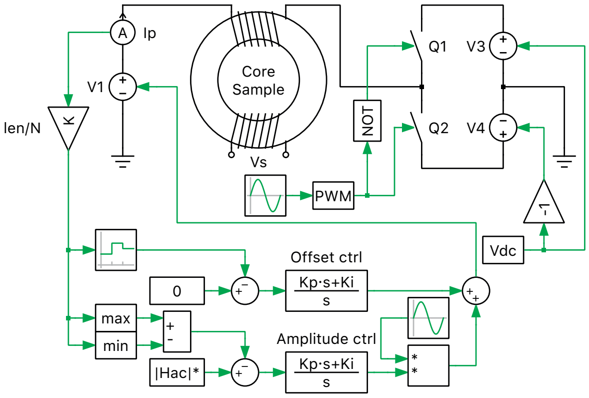

Figure 3.8 Equivalent circuit and control loop of the sinusoidal PWM mode

and connects the branch of $Q_{01}\&Q_{02}$ to ground. The sawtooth carrier based PWM generation is illustrated in **Fig. 3.7b**: The carrier waves of $Q_{11}\&Q_{12}$ and $Q_{21}\&Q_{22}$ are phase-shifted by 50 % from each other, while the carrier wave of $Q_{01}\&Q_{02}$ has double the frequency. Again, closed-loop control can be used here to obtain the desired field strength amplitude and DC offset. The equivalent circuit schematic together with the control loop are shown in **Fig. 3.7a**.

3.3.4 Sinusoidal PWM mode

For the purpose of emulating the operating condition of filter inductors in a single-phase grid-connected inverter, this operation mode provides both sinusoidal and PWM excitation. The power amplifier V_1 is responsible for generating a sinusoidal excitation voltage and compensating the DC offset of the AC current. The bidirectional switch pairs $Q_{11}\&Q_{12}$ and $Q_{11}\&Q_{12}$ are driven by a PWM gate signal with sinusoidal wave as the modulation index, and the power amplifiers V_3 and V_4 output DC voltages with the same amplitude but opposite polarity. To avoid over current, the reference for V_3 and V_4 is set to zero at the beginning of the test. After the the closed-loop control reaches the desired field strength amplitude via adjusting the output of V_1, the reference for V_3 and V_4 can slowly be raised manually until the desired current ripple is obtained. The PWM carrier should be synchronized with the execution step of the control unit, so that a phase-shift of the current ripple remains fixed with respect to the fundamental frequency sinusoidal component. The simplified circuit schematic and control loop are shown in **Fig. 3.8**.

3.4 Test results

To demonstrate the capabilities of the test setup, samples of test results obtained in all four operation modes are presented below.

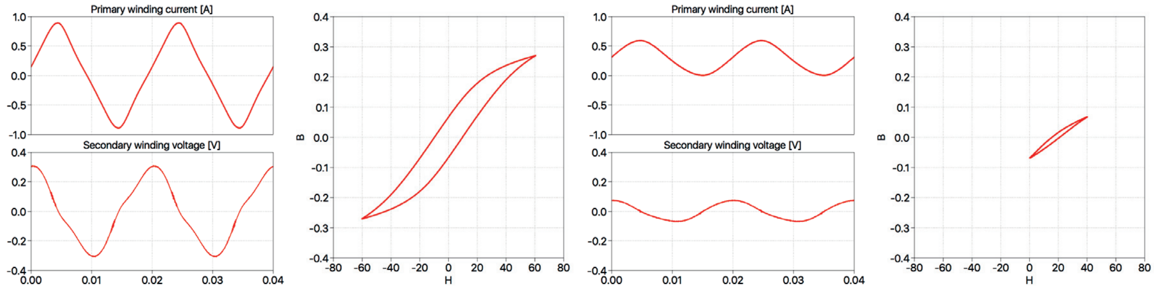

(a) (b) (c) (d)

Figure 3.9 Test result in sinusoidal mode: Symmetrical hysteresis loop (a) Time domain waveforms (b) $B - H$ characteristic; Biased hysteresis loop (c) Time domain waveforms (d) $B - H$ characteristic

3.4.1 Sinusoidal mode

The test result of the sinusoidal mode is gathered using the toroidal core "R 87.0 x 54.3 x 13.5" from EPCOS of ferrite material N87. The measured time domain primary current and secondary voltage waveform as well as the $B-H$ characteristic of a symmetrical hysteresis loop under $50Hz$ are presented in **Fig. 3.9a** and **Fig. 3.9b**. With the closed-loop control, the amplitude of the hysteresis loop can be accurately located at H_{ac} = 60 A/m with zero DC offset. In **Fig. 3.9c** and **Fig. 3.9d** the biased hysteresis loops of AC amplitude H_{dc} = 20 A/m and DC offset H_{dc} = 20 A/m are displayed. Due to the voltage drop on the circuit resistance (shunt, winding...) which is proportional to the circuit current, the measured secondary winding voltage shows harmonic components rather than an ideal sinusoidal wave when the material approaches saturation.

3.4.2 Duty-cycle PWM mode

The test result of the duty-cycle PWM mode is also obtained using the toroidal core "R 87.0 x 54.3 x 13.5" from EPCOS of ferrite material N87. The time domain waveform as well as $B - H$ characteristic with duty-cycle d = 0.2 and 10 kHz switching frequency are presented in **Fig. 3.10a** and **Fig. 3.10b**. With the same AC amplitude H_{ac} = 20 A/m and an additional DC offset of H_{dc} = 20 A/m as before

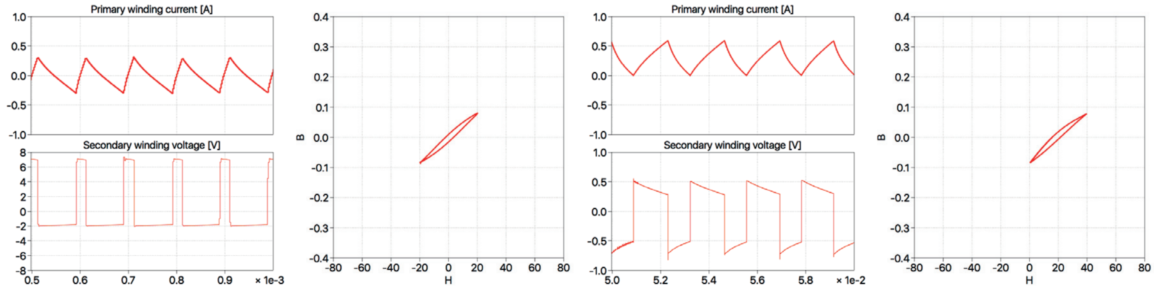

(a) (b) (c) (d)

Figure 3.10 Test result in duty-cycle PWM mode: Symmetrical hysteresis loop (a) Time domain waveforms (b) $B - H$ characteristic; Biased hysteresis loop (c) Time domain waveforms (d) $B - H$ characteristic and configured by the control unit, the test result with a duty-cycle $d = 0.6$ and a 400 Hz switching frequency can be seen in **Fig. 3.10c** and **Fig. 3.10d**. Due to the voltage drop on the circuit resistance (shunt, winding...) which is proportional to the circuit current, the shape of the secondary voltage is not an ideal square-wave.

3.4.3 Phase-shift PWM mode

The test result of the phase-shift PWM mode is gathered taking the toroidal core “R 41.8 x 26.2 x 12.5” from EPCOS with ferrite material N87 as a sample. The PWM signal is generated at 20 kHz. At this frequency, the voltage reference of the power amplifiers V_3 and V_4 are adjusted manually to set the desired AC amplitude, while the voltage V_1 is used to guarantee zero DC-offset. The measurement outputs of the primary winding current and the secondary winding voltage are now connected to an external oscilloscope with 500 MHz bandwidth, in order to correctly capture high-frequency components like the peak point of the primary current and the rising (falling) edge of the secondary voltage. In **Fig. 3.11a** and **Fig. 3.11b**, the test result from a PWM excitation without a zero-voltage period is presented, the voltage reference of V_3 and V_4 are adjusted to make the AC amplitude of the hysteresis equal to $H_{ac} = 25$ A/m. The test result with 60 % zero-voltage period is shown in **Fig. 3.11c** and **Fig. 3.11d**, where a higher voltage output from V_3 and V_4 is required to achieve the same AC amplitude $H_{ac} = 25$ A/m. An obvious difference can be observed on the shape of the hysteresis curve between **Fig. 3.11b** and **Fig. 3.11d** near the peak field strength, which results in a power loss difference and can be ascribed to the relaxation effect of the core material.

3.4.4 Sinusoidal PWM mode

The test result of the sinusoidal PWM mode is obtained with the toroidal core “R 41.8 x 26.2 x 12.5” from EPCOS with ferrite material N87. The PWM gate signal is generated at 2 kHz frequency with a modulation index equal to 0, which results in a constant PWM duty cycle of 0.5. The DC voltage reference of the power amplifiers V_3 and V_4 are configured to be ±0.24 V, and the 50 Hz AC reference of V_1 regulates the AC amplitude of the hysteresis loop to $H_{ac} = 60$ A/m. The time domain current and voltage waveforms are shown in **Fig. 3.12a**. The $B - H$ characteristic displayed in **Fig. 3.12b** results in a large symmetrical major hysteresis loop from the 50 Hz excitation of V_1 superimposed

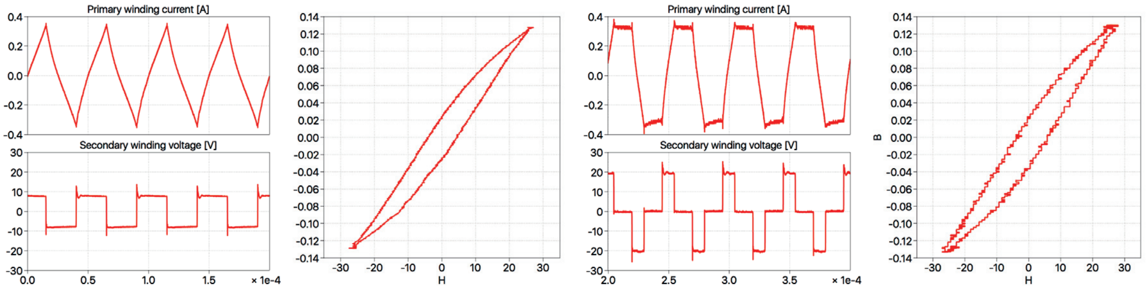

(a) (b) (c) (d)

Figure 3.11 Test result in duty-cycle PWM mode: Without zero voltage period (a) Time domain waveforms (b) $B - H$ characteristic; With zero voltage period (c) Time domain waveforms (d) $B - H$ characteristic

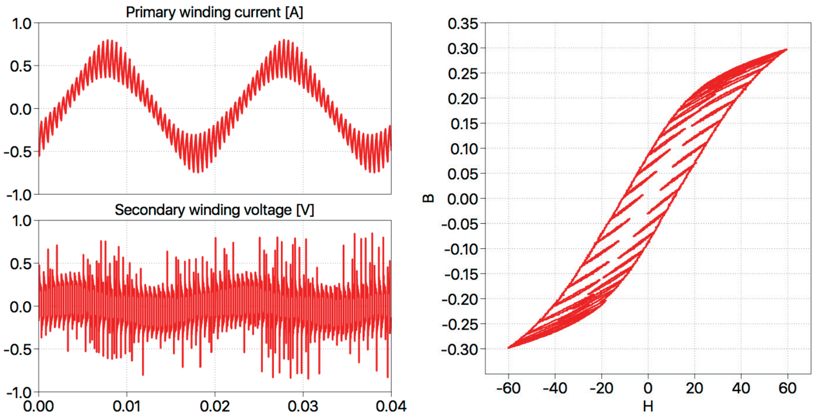

(a) **(b)**

Figure 3.12 Test result in sinusoidal PWM mode: (a) Time domain waveforms (b) $B - H$ characteristic

with small biased minor loops from the the PWM excitation.

3.5 Summary

The developed test setup facilitates the characterization of various core materials. It can be flexibly configured to emulate different operating conditions in typical power electronic applications. The measurement results obtained from the test setup serve for parameter identification and for fidelity verification of the proposed simulation models.

4

Model of hysteresis for ferrite materials

Ferrite materials are widely used to produce magnetic cores for inductive filters and isolation transformers in power electronic converters. In comparison to ferromagnetic materials like amorphous alloy and nanocrystalline, ferrite materials have significantly lower conductivity so that the frequency-independent magnetic hysteresis effect usually dominates the core loss. Due to the fact that magnetic hysteresis contributes to the nonlinearity of the magnetic component's inductance, which interacts with the remaining part of the power electronic system, the hysteresis loss is essentially a coupled effect. In order to predict the behavior of the magnetic component during design phase, an accurate time-domain hysteresis model is desired that can be easily integrated into the system-level circuit environment and simulated in a fully coupled way.

4.1 Literature review

The permeance-capacitance analogy approach, which was proposed in the work of [16], provides a practical way to integrate magnetic components seamlessly with system-level simulation. The benefit of modeling complex magnetic structures using the permeance-capacitance approach has been demonstrated by the authors of [23]. The authors of [15] have introduced this approach in a commercial system-level simulation tool for power electronics. Further on, this approach has been applied in the work of[24], [25] to capture different magnetic phenomena. In this thesis, the permeance-capacitor approach is also chosen as fundamental principle for modeling.

For time-domain simulation of frequency-independent magnetic hysteresis, the Preisach model has been recognized as a flexible approach especially regarding its ability to capture minor loops [26]. According to the formulation of the scalar Preisach model, the magnetic hysteresis is subdivided into many small independent particles [27], called hysterons. Each square-loop hysteron $\gamma(U, V)$ switches between −1 and +1 at a unique set of transition boundaries U and V, depending on the applied field strength H as well as its history, as illustrated in **Fig. 4.1**. The flux density B is expressed

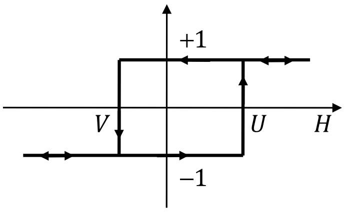

Figure 4.1 Single hysteron $\gamma(U, V)$ of Preisach Model.

as the weighted summation of all hysterons using a probability distribution function (PDF) $p(U, V)$, or in other words, Everett integration. In the case of soft magnetic materials like ferrite, the two-dimensional distribution function $p(U, V)$ can be expressed as the product of two one-dimensional PDFs, considering the fact that the probability of a hysteron switching in one direction is essentially independent of that switching in the opposite direction [28].

$$B = \iint p(U, V) \cdot \gamma(U, V) \cdot dUdV = \iint p_\mathrm{s}(U) \cdot p_\mathrm{s}(-V) \cdot \gamma(U, V) \cdot dUdV \tag{4.1}$$

The authors of [29] proposed the Cauchy-Lorentz PDF for the distribution function p_s, which was further applied by the work of [30], [31] and [32] for modeling soft magnetic materials. A parameter identification scheme using genetic algorithm has been presented in [33]. Taking advantage of the feature that the Cauchy-Lorentz PDF has closed-form integral, the differential permeability $\mu = dB/dH$ can be analytically calculated, so that the Preisach model could be applied directly to the permeance-capacitor magnetic circuit model in the work of [15]. In the existing publications, the Preisach model with the Cauchy-Lorentz PDF has only been verified for metal based material like silicon steel. For ferrites however, Cauchy-Lorentz PDF will result in a considerable error on both the equivalent permeability and the per-cycle energy loss, which will be discussed in a later section of this thesis. To improve the accuracy, other PDFs shall be adopted.

In the work of [34], the authors have developed an approach to numerically construct the PDF using experimentally measured symmetrical hysteresis loops, after discretizing $p(U, V)$ with homogeneous grids on the (U, V) plane and assuming that inside each grid $p(U, V)$ is constant. This approach is potentially able to capture the hysteresis of arbitrary materials including ferrites, but may produce a significant numerical error in practice, as has been discussed and improved in [35]. In order to achieve an acceptable resolution, a large number of hysteresis loops needs to be measured, which is in many cases impractical from engineering point of view. [36] has introduced a discrimination function in order to reduce the number of loops necessarily to be measured. Nevertheless, a Preisach model calculating the Everett integration of the discretized form of $p(U, V)$ could be too complicated and inefficient during time-domain simulation.

The authors of [37], [38] and [39] have explored that all the magnetization curve of the Preisach model following the formulation in equation (4.1) can be derived from the descending curve of only one measured limiting hysteresis loop (with the highest amplitude of concern), without the need of analytically identifying the PDF. Making use of this feature, symmetrical hysteresis loops with relatively large amplitude (larger than 50% of the limiting loop) have been modeled with good accuracy in the work of [40], [41] and [42] for ferrite materials. Hysteresis loops with low amplitudes (e.g. 20% of the limiting loop), however, were not explicitly verified and no technique was specifically proposed to control the accuracy there. With the desire to use the Preisach model for arbitrary operating conditions, the accuracy control of minor hysteresis loops requires further improvement.

It has been discussed in [43] that reversible magnetization is also present in soft magnetic materials which cannot be captured by the classical Preisach model. Therefore the hysteresis model should be composed of a irreversible component using the classical Preisach model and a reversible component. The reversible component is essentially a single-lined $B - H$ characteristic, for which the inverse trigonometric (arctan) function proposed by [44] and hyperbolic cotangen (coth) function by [45], [46] have been adopted by [32] and [42]. This work will still follow this methodology, but a new fitting function is chosen for the reversible component, which provides additional degrees of freedom so that the equivalent permeability can be controlled better.

Aiming to improve the accuracy of simulating the hysteresis effect of ferrite materials in system-level time-domain simulation, this thesis combines the following aspects, it distinguishes itself from the other previous publications:

- A Logistic probability distribution function is adopted for the irreversible component modeled by classical Preisach model to better approximate the per-cycle hysteresis energy loss of ferrite materials. The comparison to the Cauchy-Lorentz PDF is provided in this chapter.
- A improved parametrization process is introduced for the irreversible component to control the accuracy of the per-cycle energy loss for both the symmetrical large limiting loop and the small minor loops.
- A new form of reversible magnetization curve is proposed to accurately model the equivalent permeability of a hysteresis loop over a wide amplitude range.
- The improved modeling approach is seamlessly incorporated into the permeance-capacitor based magnetic circuit for system level simulations.

This chapter is organized as follows: **Sec. 4.2** provides the implementation details of the classical Preisach model in the permeance-capacitance magnetic circuit, as an elaboration of the corresponding part from [15]. **Sec. 4.3** demonstrates the proposed modeling approach together with the procedure for parameter identification. Afterwards in **Sec. 4.4**, the fidelity of the model while simulating different ferrite materials is evaluated with the magnetic characterization setup (**Chap. 3**) and compared with the Preisach model using the Cauchy-Lorentz PDF. In **Sec. 4.5** and **Sec. 4.6**, the ability of the proposed model for representing temperature dependency and various geometries is evaluated. Further in **Sec. 4.7** the performance of the model in a simulation environment for power electronic circuits is demonstrated and evaluated.

4.2 Classical Preisach Model

In this section, the realization of the classical Preisach model for magnetic hysteresis in permeance-capacitance based magnetic circuit is elaborated, as an extension of the corresponding part presented in [15]. Let us recall that in the magnetic circuit, we have the combination of the through variable (the derivative of the magnetic flux $\dot{\Phi}$) and the across variable (magnetomotive force F). The relation between $\dot{\Phi}$ and F at a single permeance block is governed by

$$\dot{\Phi} = \mathscr{P} \cdot \frac{dF}{dt} \tag{4.2}$$

The permeance value $\mathscr{P}$ in the equation above is calculated using the geometry and material characteristic

$$\mathscr{P} = \mu \cdot \frac{A}{l} \tag{4.3}$$

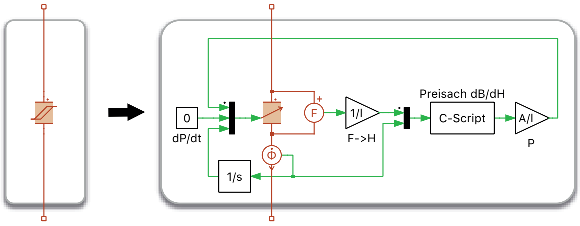

Figure 4.2 Structure of the permeance block with hysteresis behaviour using the classical Preisach model

where A is the cross section area and l is the magnetic path length. The $B-H$ characteristic of the material is reflected by the permeability μ, as illustrated in **Fig. 2.10c**. By adapting the geometrical parameters, the same permeance block can be taken as basic building block to construct other magnetic structures.

Should the material nonlinearity (e.g. magnetic hysteresis) be considered, μ will depend on the field strength H. The internal structure of a permeance block with hysteresis behavior is shown in **Fig. 4.2**. The magnetomotive force F across the variable permeance component is measured and divided by the magnetic path length l, yielding the field strength H.

The classical Preisach model following the formulation of [28] can be implemented with a C-Script that takes H as well as the flux rate $\dot{\Phi}$ as input variables. The C-Script outputs the instantaneous differential permeability $\mu(H) = dB/dH$, which is multiplied by the geometry factor A/l and provided to the variable permeance block. The calculation of $\mu(H)$ during the simulation is explained in below:

- *Virgin curve:* Let us assume that the time-domain simulation initiates from the completely demagnetized state: The boundary between the positive- (S_+) and negative area (S_-) of the Preisach plane lays on $U = -V$, such that the flux density B calculated using equation (4.1) is equal to zero, as depicted on the right hand side of **Fig. 4.3a**. Under positive excitation (e.g. with a positive voltage applied to the winding of the magnetic component so that $\dot{\Phi} > 0$) the operating point on the $B-H$ plane moves along the virgin curve. The flux density B is calculated as Everett integration following equation (4.1).

$$B(H) = \iint_{S_+} p_\mathrm{S}(U) \cdot p_\mathrm{S}(-V) \cdot dU\,dV - \iint_{S_-} p_\mathrm{S}(U) \cdot p_\mathrm{S}(-V) \cdot dU\,dV \tag{4.4}$$

On the $B-H$ plane, the instantaneous differential permeability μ, or in other words, the slope of the $B-H$ curve, is graphically depicted on the left hand side of **Fig. 4.3a** and given as

$$\mu_\mathrm{vir}(H) = 2 \cdot p_\mathrm{S}(H) \cdot \int_{-H}^{+H} p_\mathrm{S}(-V) \cdot dV = 2 \cdot p_\mathrm{S}(H) \cdot \Big(C_\mathrm{S}(+H) - C_\mathrm{S}(-H) \Big) \tag{4.5}$$

The integral term in (4.5) turns out to be closed-form if the probability distribution function p_S can be analytically integrated with a cumulative distribution function (CDF) C_S, as is the case with the Cauchy-Lorentz PDF, which has been used in the existing publications [29], [30], [31] and [32]. If μ can be written in an explicit form, it can be directly substituted into equation (4.3) and used to the permeance core block of the magnetic circuit.

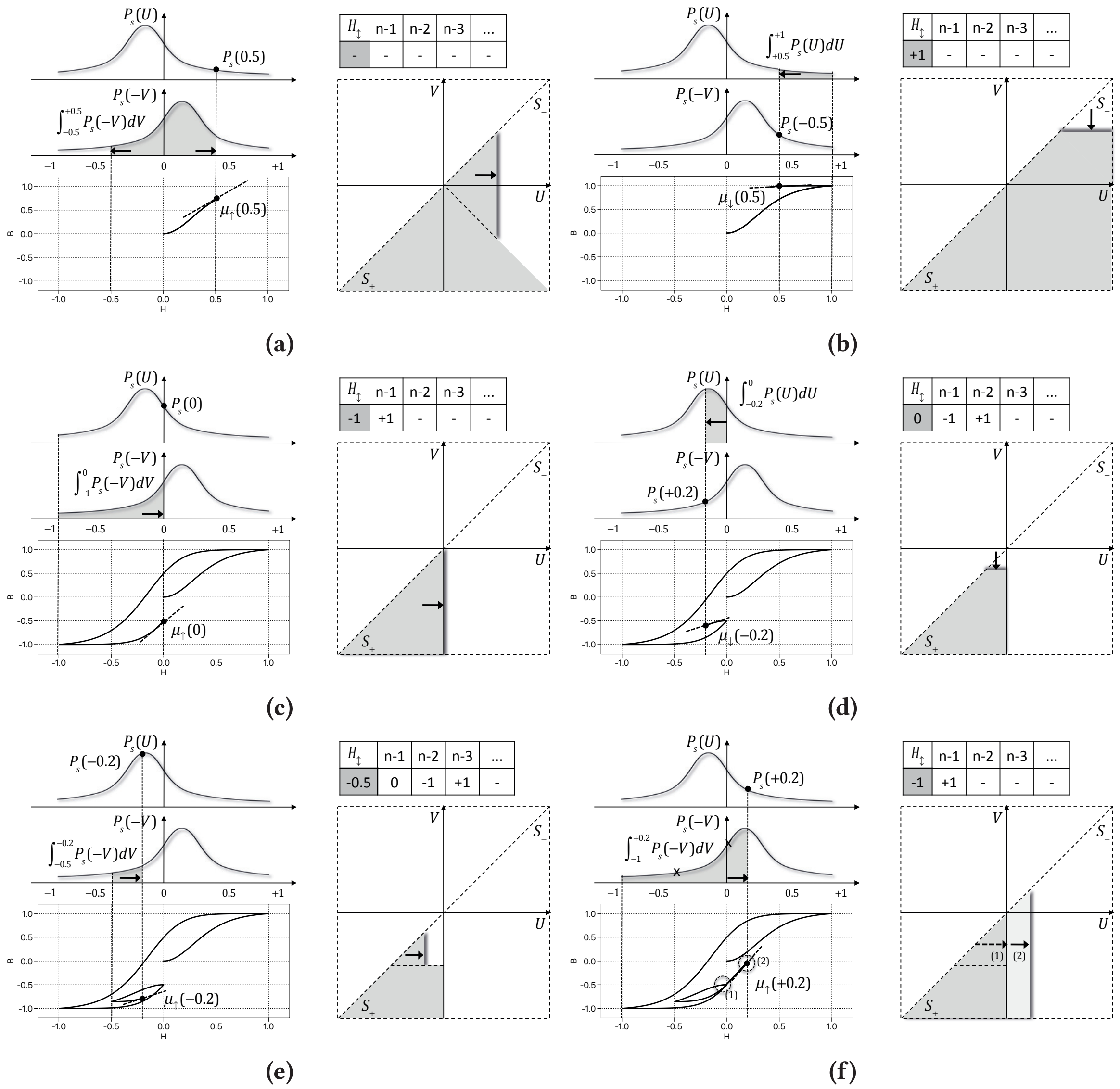

(a) **(b)** **(c)** **(d)** **(e)** **(f)**

Figure 4.3 Calculation of the permeability and the area separation of the Everett integral: (a) on the virgin curve; (b) on the descending curve after reaching the positive peak; (c) on the ascending curve after reaching the negative peak; (d) on the descending curve in an asymmetrical minor loop; (e) on the ascending curve in an asymmetrical minor loop; (f) on the ascending curve after exiting the minor loop.

- *Descending curve:* Assuming that when H reaches the positive peak (p.u. +1), the external excitation changes the polarity. Afterwards, the boundary between the areas S_+ and S_- should move in the direction indicated on the right side of **Fig. 4.3b**. This polarity change is detected by the C-Script via examing the sign of the second input $\dot{\Phi}$ (time derivative of the flux Φ) and the first field strength extremity +1 is pushed into a stack structure as shown on the top-right of **Fig. 4.3b**. From this time point on, μ is calculated using the equation below with extremity

$H_{\updownarrow} = +1$.

$$\mu_{\downarrow}(H) = 2 \cdot p_{\mathrm{s}}(-H) \cdot \int_{H}^{H_{\updownarrow}} p_{\mathrm{s}}(U) \cdot dU = 2 \cdot p_{\mathrm{s}}(-H) \cdot \Big(C_{\mathrm{s}}(H_{\updownarrow}) - C_{\mathrm{s}}(H) \Big) \tag{4.6}$$

- *Ascending curve:* The external excitation becomes positive after H reaches the negative peak (p.u. -1) as shown in **Fig. 4.3c**. The negative peak is memorized in the stack of extremities and the actual $H_{\updownarrow}$ becomes -1, while the previous extremity $+1$ is shifted to a deeper level. The permeability on the ascending curve is given as

$$\mu_{\uparrow}(H) = 2 \cdot p_{\mathrm{s}}(H) \cdot \int_{H_{\updownarrow}}^{H} p_{\mathrm{s}}(-V) \cdot dV = 2 \cdot p_{\mathrm{s}}(H) \cdot \Big(C_{\mathrm{s}}(H) - C_{\mathrm{s}}(H_{\updownarrow}) \Big) \tag{4.7}$$

- *Minor loop:* The external excitation switches its polarity to negative at $H = 0$ on the ascending curve, so that a minor hysteresis loop is initiated (**Fig. 4.3d**). At the very moment, $H_{\updownarrow}$ becomes 0 while the previous two extremities -1 and $+1$ are shifted one level deeper in the stack. The permeability on the descending curve of the minor loop has the same form as equation (4.6), except for the integral limit $H_{\updownarrow} = 0$. Afterwards, let's assume that the ascending curve of the minor loop begins at $H = -0.5$ where $H_{\updownarrow}$ becomes -0.5 (**Fig. 4.3e**). Before H reaches the second last extremity ($H = 0$) there are four values in total $(-0.5, 0, -1, +1)$ stored in the stack, and μ is retained following equation (4.7) with $H_{\updownarrow} = -0.5$.

- *Exit from Minor loop:* At the moment when H just tends to exceed the second last extremity ($H = 0$), the operation point is exactly located on the position where the minor loop has been initiated previously (point (1) in **Fig. 4.3f**). At this point, the last two extremities -0.5 and 0 are erased from the stack. From then on, the operating point travels along the ascending curve with $H_{\updownarrow} = -1$, as if the minor loop had never happened (point (2) in **Fig. 4.3f**). This deletion feature of Preisach model corresponds to the characteristic of ferrite material, which will be verified by the experimental result in a later section of this work.

4.3 Proposed Model

Depending on the applications and their corresponding design considerations, the core material of a magnetic component may operate at different ranges of field strength on the $B - H$ plane, which result in hysteresis loop of different sizes. In oder to predict the hysteresis loss of the magnetic core during the design phase for arbitrary applications, to optimize the design parameters, a model valid for different amplitudes of excitation is required. The main objective of the proposed modeling approach is to achieve good accuracy of simulating magnetic hysteresis in a wide range of amplitudes (both large major- and small minor loops), which is assessed with the following two criteria:

- *Per cycle energy loss:* The area enclosed by the hysteresis loops on the $B - H$ plane.
- *Equivalent permeability:* Slope of the virtual straight line connecting the positive and negative peaks.

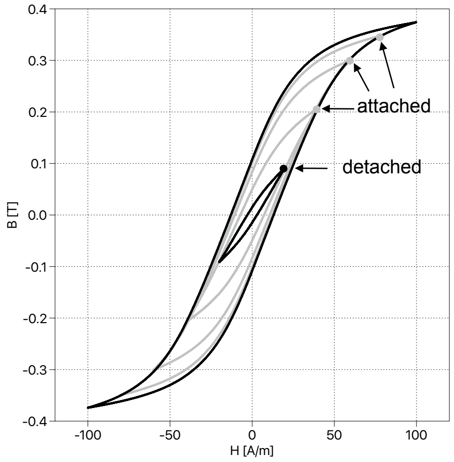

Figure 4.4 Measured hysteresis loops of ferrite material N87 from $H = 100$ A/m to $H = 20$ A/m at 200 Hz

For illustration purposes, the characteristic of ferrite material N87 experimentally measured at 200 Hz is taken as an example. In **Fig. 4.4** the hysteresis loops of different amplitudes are displayed together. We define the one with the largest field strength amplitude $\hat{H}_{100\%}$ (e.g. 100 A/m), which makes the flux density approach saturation, as the "limiting loop". The limiting loop indicates the valid operation range of the model and it is assumed that the hysteresis effect is of concern to the simulation only inside this range. Inside the limiting loop, one can realize that peaks of the other loops with relatively large amplitudes $40\% \cdot \hat{H}_{100\%}$ ~ $80\% \cdot \hat{H}_{100\%}$ (40 A/m ~ 80 A/m) almost touch the lower boundary of the limiting loop. This phenomenon has also been observed with other ferrite materials, which indicates that if a simulation model is able to reproduce the lower boundary of the limiting loop, the smaller ones can be also well presented, at least in terms of the equivalent permeability. However this theory does not apply to minor hysteresis loops with very low amplitudes, say $20\% \cdot \hat{H}_{100\%}$ (20 A/m), whose peaks obviously deviate from the lower boundary of the limiting loop.

In the approach proposed in this thesis, only one limiting hysteresis loop (**Fig. 4.5a**) and one symmetrical minor hysteresis loop (**Fig. 4.5c**) are required to be experimentally measured as input data, and the model is parametrized to approximate these two loops. We suppose the hysteresis loops with amplitudes between the measured limiting loop and the minor loops can be automatically fitted thanks to the physical-based intrinsic property of the Preisach model, which will be verified in a later section by experimental tests.

Following the method proposed by [43], in this work we also construct the hysteresis model as the summation of an irreversible component and a reversible component, which is graphically illustrated in **Fig. 4.5b** and **Fig. 4.5d** for the limiting loop and a minor loop, respectively. Please note that the same classical Preisach model is applied for the irreversible component, and the reversible component in **Fig. 4.5d** is just one part of the same curve in **Fig. 4.5b** within the field strength range $[-H_{20\%}, +H_{20\%}]$. The formulation and parameter identification of the two components are introduced in the following subsections.

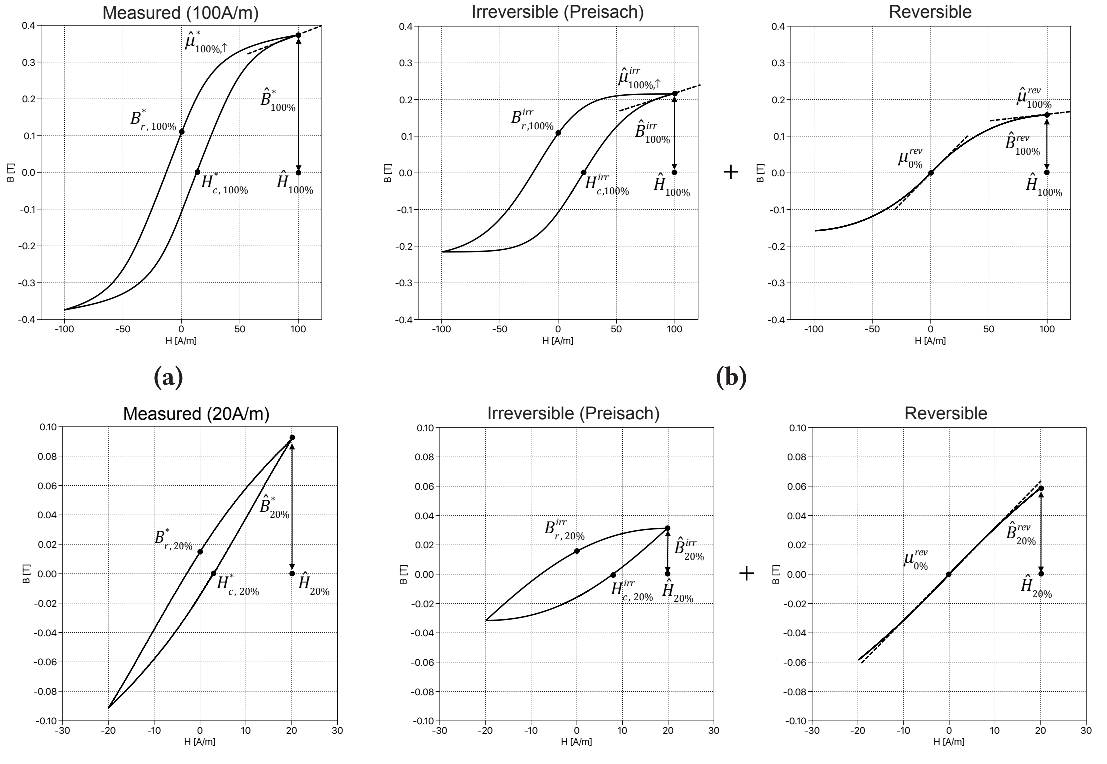

(a) **(b)**

(c) **(d)**

Figure 4.5 (a) Measured limiting hysteresis loop with amplitude $H_{100\%} = 100$ A/m (b) Hysteresis model composed of irreversible- and reversible component with amplitude $H_{100\%} = 100$ A/m (c) Measured limiting hysteresis loop with amplitude $H_{20\%} = 20\% \cdot H_{100\%} = 20$ A/m (b) Hysteresis model composed of irreversible- and reversible component with amplitude $H_{20\%} = 20\% \cdot H_{100\%} = 20$ A/m

4.3.1 Determination of the irreversible component

Contrary to the existing publications, the “logistic” probability distribution function is adopted for the irreversible component, which is represented by the classical Preisach model. The generalized form of the logistic PDF can be expressed as

$$p_s(H) = K \cdot \frac{e^{-(H-H_0)\cdot\sigma}}{(1+e^{-(H-H_0)\cdot\sigma})^2} \tag{4.8}$$

where K, H_0 and σ are parameters to be determined. Similar to the Cauchy-Lorentz PDF which has been chosen by the existing publications, the logistic PDF can be integrated analytically. The cumulative distribution function (CDF) of logistic PDF is given as

$$C_s(H) = \frac{K \cdot \sigma}{1+e^{-(H-H_0)\cdot\sigma}} \tag{4.9}$$

In this way, the permeability μ can be calculated in a closed-form (equations (4.5) - (4.7)). Due to the fact that the reversible component has zero remanence, the remanent flux density of the simulated irreversible component ($B^{irr}_{\mathrm{r},100\%}$ in **Fig. 4.5b** and $B^{irr}_{\mathrm{r},20\%}$ in **Fig. 4.5d**) must be equal to that of the measurement.

$$\begin{cases} B^{irr}_{\mathrm{r},100\%} \overset{\Delta}{=} B^{*}_{\mathrm{r},100\%} \\ B^{irr}_{\mathrm{r},20\%} \overset{\Delta}{=} B^{*}_{\mathrm{r},20\%} \end{cases} \tag{4.10}$$

where $B^{*}_{\mathrm{r},100\%}$ and $B^{*}_{\mathrm{r},20\%}$ are the remanence flux density of the measured limiting- and minor loops, as has been highlighted in **Fig. 4.5a** and **Fig. 4.5c**. Any values from experimental measurement in this work are denoted with superscript "*". As has been explored by the authors of [47], the remanence flux density of Preisach using independent PDF can be explicitly expressed as

$$B^{irr}_{\mathrm{r},100\%} = \int_{0}^{\hat{H}_{100\%}} p_{\mathrm{s}}(U)dU \int_{-\hat{H}_{100\%}}^{0} p_{\mathrm{s}}(-V)dV = \Big(C_{\mathrm{s}}(\hat{H}_{100\%}) - C_{\mathrm{s}}(0)\Big)^{2} \overset{\Delta}{=} B^{*}_{\mathrm{r},100\%} \tag{4.11}$$

The equation above is also valid for the symmetrical minor loop:

$$B^{irr}_{\mathrm{r},20\%} = \int_{0}^{\hat{H}_{20\%}} p_{\mathrm{s}}(U)dU \int_{-\hat{H}_{20\%}}^{0} p_{\mathrm{s}}(-V)dV = \Big(C_{\mathrm{s}}(\hat{H}_{20\%}) - C_{\mathrm{s}}(0)\Big)^{2} \overset{\Delta}{=} B^{*}_{\mathrm{r},20\%} \tag{4.12}$$

Different from the metal-based materials, since ferrite materials do not experience field-annealing treatment during the manufacturing process, it is reasonable to assume symmetrical nature for the PDF of classical Preisach model. Therefore the bias parameter H_0 of the irreversible part (equation (4.8) and (4.9)) is chosen to be zero in this work if not mentioned otherwise, which makes the PDF symmetrical around the vertical axis. The remaining two parameters K and σ can be fully determined via solving the two equations (4.11) and (4.12). Due to nonlinearity, commonly used iteration method like Newton-Raphson must be used. Please note that the per-cycle energy loss is determined by the irreversible component.

4.3.2 Determination of the reversible component

After the Preisach model parameters of the irreversible component (classical Preisach model) are identified, the reversible component is parametrized to make the sum of the two components match the peak point as the measured limiting loop and minor loop, or in other words, to adjust the equivalent permeability. Instead of arctan and coth proposed by the existing publications, a new form of "Sigmoid" function is proposed in this work, in order to shape the reversible component with more degrees of freedom. The reversible $B^{rev}(H)$ is constructed as the integration of a shifted arctan function, and the flux density for $H \geq 0$ is governed by the equation below.

$$B^{rev}(H) = \int_0^H \Big(F \cdot \arctan((H_1 - x)\cdot\alpha) + D\Big)dx = -F/\alpha \cdot \Big((H_1 - H)\cdot\alpha\cdot atan((H_1 - H)\cdot\alpha)$$
$$- 0.5ln(1 + (H_1 - H)^2 \cdot \alpha^2)\Big) + F\alpha \cdot \Big(H_1 \cdot \alpha \cdot atan(H_1 \cdot \alpha) + 0.5ln(1 + H_1^2 \cdot \alpha^2)\Big) + D \cdot H \quad (4.13)$$

The permeability $\mu^{rev}(H)$ to be provided to the permeance block in the magnetic circuit is the derivative of equation (4.13) with respect to the field strength H, or in other words, the shifted arctan function itself.

$$\mu^{rev}(H) = F \cdot \arctan((H_1 - H)\cdot\alpha) + D \quad (4.14)$$

In the operation range with field strength $H < 0$, the mirroring function of equations (4.13) and (4.14) with respect to the origin of the $B - H$ plane are applied. The parameter α is preliminary configured to be 0.01 and can be adjusted to improve the permeability accuracy, which will be described later in sub**Sec. 4.3.3**. The identification of the other three parameters H_1, F and D is described as follows:

In the Preisach model, the symmetry of the irreversible component's PDF (due to the parameter configuration $H_0 = 0$) leads to a peak flux density $\hat{B}^{irr}_{100\%}$ of the simulated limiting loop that is two times the remanence flux density $B^{irr}_{\mathrm{r},100\%}$ (equal to $B^{*}_{\mathrm{r},100\%}$) after the parameter identification described in **Sec. 4.3.1**.

$$\hat{B}^{irr}_{100\%} = 2 \cdot B_{\mathrm{r},100\%} \overset{\Delta}{=} 2 \cdot B^{*}_{\mathrm{r},100\%} \quad (4.15)$$

Therefore the peak flux density of the reversible component at $\hat{H}_{100\%}$ can be extracted from the measured peak flux density of the limiting loop using

$$\hat{B}^{rev}_{100\%} = B^{*}_{100\%} - \hat{B}^{irr}_{100\%} = B^{*}_{100\%} - 2 \cdot B^{*}_{\mathrm{r},100\%} \quad (4.16)$$

As has been observed at the beginning of **Sec. 4.3**, the peak of the relatively large minor loops touch the lower boundary of the limiting loop. In order to make the simulated lower boundary of the limiting loop match that from the measurement, the permeability of the reversible component at $\hat{H}_{100\%}$ ($\hat{\mu}^{rev}_{100\%}$ in **Fig. 4.5b**) should be adjusted as well. This is done by subtracting the permeability of the irreversible component model from the measured one:

$$\hat{\mu}^{rev}_{100\%} = \hat{\mu}^{*}_{100\%} - \hat{\mu}^{irr}_{100\%} = \hat{\mu}^{*}_{100\%} - p_{\mathrm{s}}(\hat{H}_{100\%})\Big(C_{\mathrm{s}}(\hat{H}_{100\%}) - C_{\mathrm{s}}(-\hat{H}_{100\%})\Big) \quad (4.17)$$

In the case of the minor symmetrical loop with field strength amplitude $\hat{H}_{20\%} = 20\% \cdot \hat{H}_{100\%}$, the irreversible component described by the Preisach model is calculated using solely the part of the PDF inside the range $[-\hat{H}_{20\%}, +\hat{H}_{20\%}]$. With the previous assumption $H_0 = 0$, this part of the PDF is also symmetrical with respect to the origin so that the relation described in equation (4.15) is valid here as well.

$$\hat{B}^{irr}_{20\%} = 2 \cdot B_{\mathrm{r},20\%} \overset{\Delta}{=} 2 \cdot B^{*}_{\mathrm{r},20\%} \tag{4.18}$$

If the reversible component can be considered a linear function close to the origin as depicted in **Fig. 4.5d**, the initial permeability of the reversible component can be obtained by subtracting $\hat{B}^{irr}_{20\%}$ from the peak flux density of the measured minor loop and dividing it by $\hat{H}_{20\%}$.

$$\mu^{rev}_{0\%} = (\hat{B}_{20\%} - \hat{B}^{irr}_{20\%})/\hat{H}_{20\%} = (\hat{B}^{*}_{20\%} - 2 \cdot B^{*}_{\mathrm{r},20\%})/\hat{H}_{20\%} \tag{4.19}$$

Up to this stage, with the parameter α provided, the other three parameters H_1, F and D of the reversible component can be determined by solving the three equations (4.16), (4.17) and (4.19), and substituting $\hat{B}^{rev}_{100\%}$, $\hat{\mu}^{rev}_{100\%}$ and $\mu^{rev}_{0\%}$ with the expression from equations (4.13) and (4.14). Newton-Raphson iteration is adopted for the parameter identification. Initial values should be provided to guarantee convergence.

$$H_1^{(0)} = \frac{\hat{B}^{rev}_{100\%} - \hat{H}_{100\%} \cdot \hat{\mu}^{rev}_{100\%}}{\mu^{rev}_{0\%} - \hat{\mu}^{rev}_{100\%}} \quad K^{(0)} = \frac{\mu^{rev}_{0\%} - \hat{\mu}^{rev}_{100\%}}{v_1 - v_2} \quad D^{(0)} = \frac{\mu^{rev}_{0\%} \cdot v_2 - \hat{\mu}^{rev}_{100\%} \cdot v_1}{v_2 - v_1} \tag{4.20}$$

where $\hat{B}^{rev}_{100\%}$, $\hat{\mu}^{rev}_{100\%}$ and $\mu^{rev}_{0\%}$ are given by the right hand side of equations (4.16), (4.17) and (4.19), respectively, while v_1 and v_2 are provided below.

$$v_1 = \arctan\left(H_1^{(0)} \cdot \alpha\right) \tag{4.21}$$

$$v_2 = \arctan\left((H_1^{(0)} - \hat{H}_{100\%}) \cdot \alpha\right) \tag{4.22}$$

4.3.3 Final adjustment

For the sake of further controlling the simulated lower boundary of the limiting loop to approach that from the measurement, which intrinsically determines the peak point of the other minor loops with amplitudes close to the limiting loop (as has been discussed in **Fig. 4.4**), the parameter α can be adjusted.

The goal is to make the simulated flux density $B_{50\%}$ at $H = 0.5 \cdot \hat{H}_{100\%}$ be equal to that of the limiting loop's ascending curve. The parameter α determines the curvature of the reversible component such that the flux density $B^{rev}_{50\%}$ at $H = 0.5 \cdot \hat{H}_{100\%}$ on the reversible component can be adjusted by changing

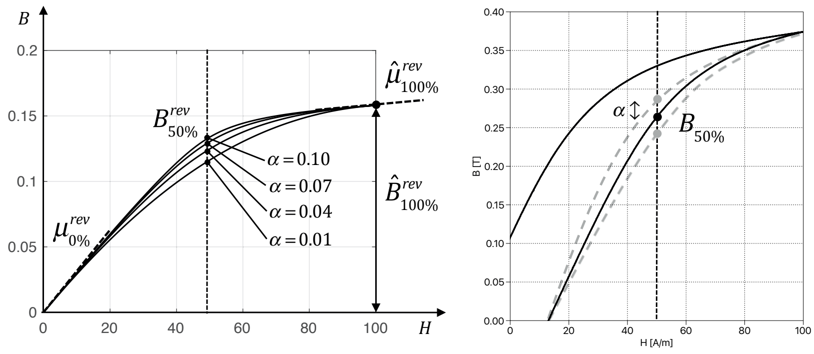

(a) (b)

Figure 4.6 (a) Influence of the model parameter α on the curvature of the irreversible component (b) Influence of the model parameter α on the lower bondary of the limiting hysteresis loop after summing up the reversible- and irreversible component together

α, as demonstrated in **Fig. 4.6a**. In **Fig. 4.6a**, the Newton-Raphson iteration described in **Sec. 4.3.2** should be carried out for any chosen α, so that the point $\hat{B}^{rev}_{100\%}$ and the slopes $\hat{\mu}^{rev}_{100\%}$ and $\mu^{rev}_{0\%}$ remain the same. Please note that at this stage, the irreversible component has been completely determined and its parameters remain unchanged. As a consequence, the change of $B^{rev}_{50\%}$ due to adjustment of α is directly reflected on $B_{50\%}$ which locates on the lower boundary of the simulated limiting loop, as shown in **Fig. 4.6b**. Thanks to the fact that α is monotonously related to $B^{rev}_{50\%}$ ($B^{rev}_{50\%}$ increases with higher α), the adjustment of α can be either conducted manually or automatically by adding another fitting loop on the top of the Newton-Rahphson iteration introduced in **Sec. 4.3.2**.

4.3.4 Model structure

The structure of the proposed combined hysteresis model in a permeance-capacitance based magnetic circuit is shown in **Fig. 4.7**. Two variable core blocks are connected in parallel, to account for the irreversible component and reversible component. The permeance value of the two core blocks are calculated in two separate C-Scripts and scaled with the geometric coefficient A/l. The equivalent permeance of the whole hysteresis core block is essentially the sum of the individual permeances,

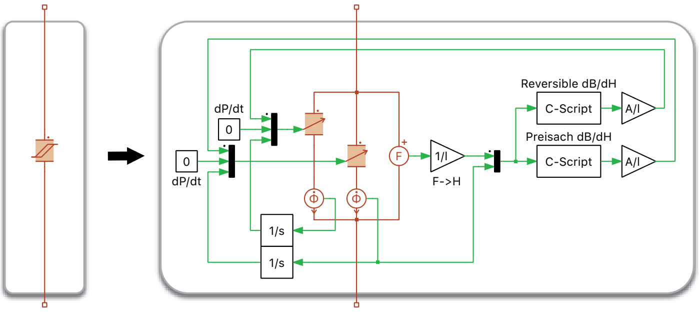

Figure 4.7 Model structure of the permeance block using proposed model

which are provided to the first input of the variable core blocks.

$$\mathscr{P}(H) = \mu^{irr}(H) \cdot \frac{A}{l} + \mu^{rev}(H) \cdot \frac{A}{l} \tag{4.23}$$

Since differential permeability has been used throughout this work, the second input of the variable core blocks $d\mathscr{P}/dt$ can be provided by a constant zero, as has been discussed in [15]. The third input of the variable core blocks accepts the flux density of the irreversible- and reversible components, which are obtained from integral of the flux rate $\dot{\Phi}$, in order to make the simulation solver comply with Kirchhoff's junction law for the magnetic circuit.

4.4 Verification in continuous circuit

For validation of the proposed modeling approach, the characterization setup is configured to sinusoidal operation mode to measure the hysteresis loop of the core materials. As this chapter focuses on the frequency independent hysteresis effect without eddy current and residual effects, the power amplifier's output voltage has been configured to a low frequency 200 Hz sinusoidal wave. If not mentioned, all tests have been conducted at room temperature of 25°C.

The simulation model (top of **Fig. 4.8**) is implemented in the system-level simulation software PLECS for power electronics. The hysteresis core block represents the core sample, whose geometric parameters A and l are configured using the values from the datasheet, while the material characteristic is modeled and parametrized using the approach introduced in **Sec. 4.3**. The power amplifiers V_1 and V_2 which are activated in this operation mode are modeled as an ideal sinusoidal AC voltage source connected in series to the equivalent resistance (including the shunt resistor for current measurement and parasitics, measured in DC condition). All components are configured to match the test bench hardware.

The ferrite material N87 from TDK is taken as the first verification case, where the toroidal core of size code "R 41.8 x 26.2 x 12.5" is taken as a sample, the turns number of primary and secondary windings are identical and equal to 8. For the parameter identification process which has been described in the **Sec. 4.3**, the limiting hysteresis loop with amplitude $\hat{H}_{100\%}$ = 100 A/m and a symmetrical minor loop with amplitude $\hat{H}_{20\%}$ are measured. Please note that the parameters of the model will remain the same in the other verification cases. In **Fig. 4.9a** and **Fig. 4.9b**, the simulated hysteresis loop as well as the time domain waveform of the primary winding current and secondary winding voltage at different field strength amplitudes (20 A/m ~100 A/m) are compared to the experimental measurement.

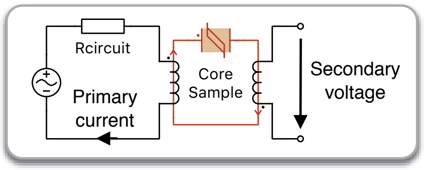

Figure 4.8 Simulation model of the test setup

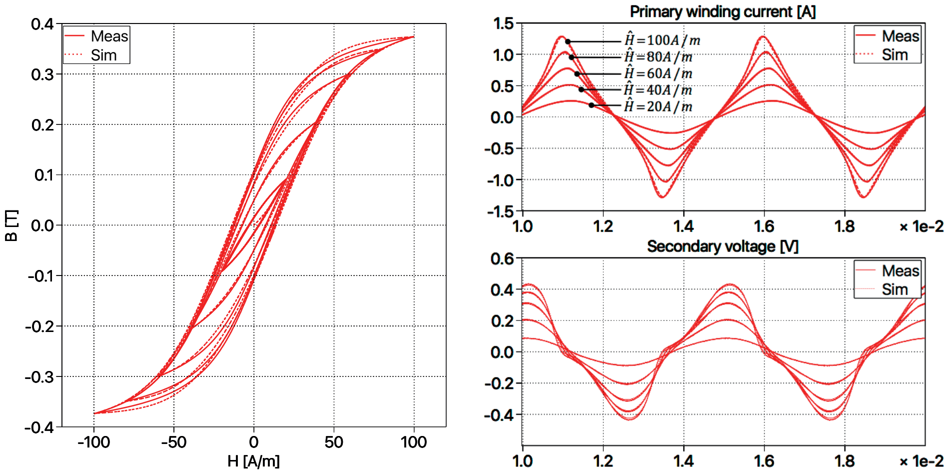

(a) (b)

Figure 4.9 Comparison between measurement and simulation of Ferrite N87 at different field strength amplitudes (a) Hysteresis loop (b) Time-domain primary winding current and secondary voltage

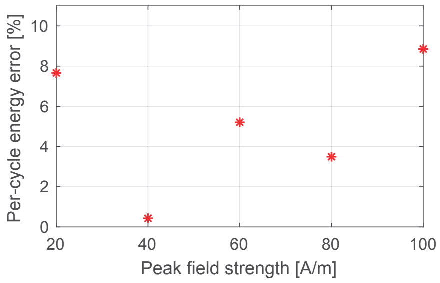

Figure 4.10 Percentage error of the simulated per-cycle energy loss from simulation of ferrite N87

Although an ideal sinusoidal voltage is generated on the power amplifier output, the measured primary winding current is heavily distorted, due to the presence of nonlinear hysteresis effect. The proposed simulation model is able to approximate the hysteresis loop on the $B - H$ plane and the time domain waveform well. Especially on the secondary voltage waveform in **Fig. 4.9b**, due to the voltage drop on the circuit resistance as a coupled effect from the distorted circuit current, the secondary open-circuit voltage includes harmonic components that are captured by the model. In **Fig. 4.9a**, the peak point of the hysteresis loops is nearly congruent with the measurement, so that the error of the equivalent permeability is maintained below 1%. The per-cycle energy loss has been measured and simulated by integrating the product of the time domain voltage and current waves for one AC period (equivalent to the enclosed area of the $B - H$ loop). The error between simulation and measurement are illustrated in **Fig. 4.10**. The maximum error of 8.9% is present at the limiting hysteresis loop of high amplitude $\hat{H}_{100\%} = 100$ A/m.

If the irreversible component (classical Preisach model) is calculated using the Cauchy-Lorentz PDF with parameters identified following the same procedure described in **Sec. 4.3.1**, the hysteresis loops with field strength amplitudes of 100 A/m (limiting loop) and 60 A/m are compared to the measurement in **Fig. 4.11a** and **Fig. 4.11b**:

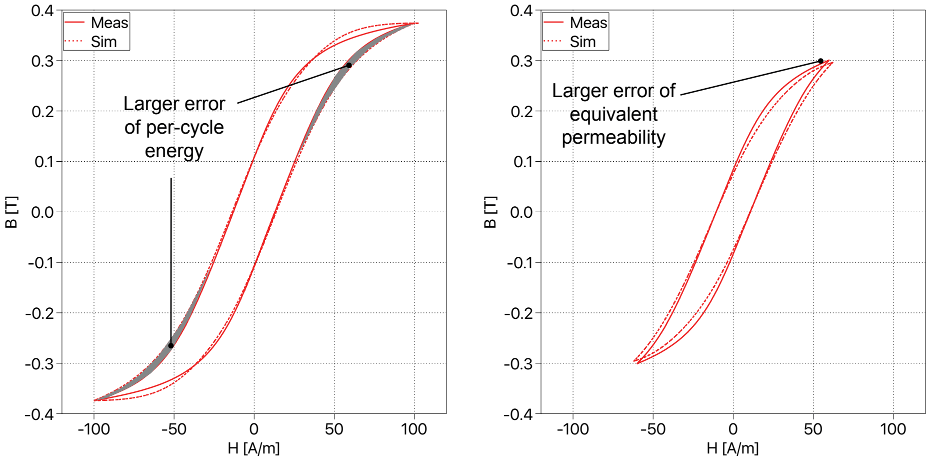

(a) **(b)**

Figure 4.11 Comparison between measurement and simulation of Ferrite N87 using Cauchy-Lorentz PDF (a) Hysteresis loop at $\hat{H}_{100\%} = 100$ A/m (b) Hysteresis loop at $\hat{H}_{60\%} = 60$ A/m

In **Fig. 4.11a**, the simulated limiting loop (at $\hat{H}_{100\%} = 100$ A/m) using the Cauchy-Lorentz PDF exhibits significantly higher per-cycle energy loss, in comparison to the one using the logistic PDF (**Fig. 4.9a**). The excessive energy loss is indicated by the highlighted loop area difference (gray color). The error compared to the measurement is 11.5%, which is higher than that obtained using the logistic PDF (8.9%). The reason can be ascribed to the simulated differential permeability on the top of a ascending branch. The models using the logistic and Cauchy-Lorentz PDF are compared in **Fig. 4.12a** regarding the simulated irreversible component of the limiting loop (that of the right-hand side variable permeance block in **Fig. 4.7**). Higher permeability $\hat{\mu}^{irr}_{\uparrow,100\%}$ is present on the model using Cauchy-Lorentz PDF, which leads to large enclosed area on the $B-H$ plane and thus higher per-cycle energy loss.

One should recall that in the parameter identification procedure from **Sec. 4.3.1** the irreversible component is configured to approximate the remanent flux density of the limiting loop and that of a low amplitude minor loop, so that $B^{irr}_{r,100\%} = B^{*}_{r,100\%}$ and $B^{irr}_{r,20\%} = B^{*}_{r,20\%}$. To generalize the statement that $\hat{\mu}^{irr}_{\uparrow,100\%}$ using Cauchy-Lorentz PDF is higher than that using Logistic PDF, we fit the parameters of the irreversible component such that the remanent flux density of the limiting loop $B^{irr}_{r,100\%}$ is still equal to the measurement, while that of the low amplitude minor loop $B^{irr}_{r,20\%}$ is fitted targeting different values. The resulting permeability $\hat{\mu}^{irr}_{\uparrow,100\%}$ from the model using two PDFs is compared in **Fig. 4.12b**. Independently of $B^{irr}_{r,20\%}$, the permeability $\hat{\mu}^{irr}_{\uparrow,100\%}$ from the model using Cauchy-Lorentz PDF is always higher than that using Logistic PDF, which leads to higher per-cycle energy loss in simulation.

Moreover in the case of N87 material, since the irreversible permeability $\hat{\mu}^{irr}_{\uparrow,100\%}$ calculated using Cauchy-Lorentz PDF is already higher than the permeability $\hat{\mu}^{*}_{\uparrow,100\%}$ from the measurement (in **Fig. 4.5a**), no positive permeability of the reversible component can be found to fulfill the criteria defined in the equation (4.17). Thus, the lower boundary of the ascending curve of the model deviates from the measurement, which make the equivalent permeability of the minor loops (with amplitudes slightly lower than the limiting loop) to be less accurate. This is highlighted in **Fig. 4.11b** on the hysteresis loop with field strength amplitude $\hat{H}_{60\%} = 60$ A/m. This permeability discrepancy together with the coupling from the circuit (e.g. voltage drop on the circuit resistance), adds to the error of per-cycle energy loss.

In a next step, the proposed model is verified on the 3C81 material from Ferroxcube, the core sample of shape code "TX 51 / 32 / 19" is taken, while the turns number of both primary and secondary windings are 10. The parameters are identified based on the limiting hysteresis loop with amplitude $\hat{H}_{100\%} = 100$ A/m and a symmetrical minor loop with amplitude $\hat{H}_{20\%} = 20$ A/m. The comparison between simulation and measurement is presented in **Fig. 4.13a** and **Fig. 4.13b**. A significantly different shape of the hysteresis loop compared to N87 is present here and the proposed model is still

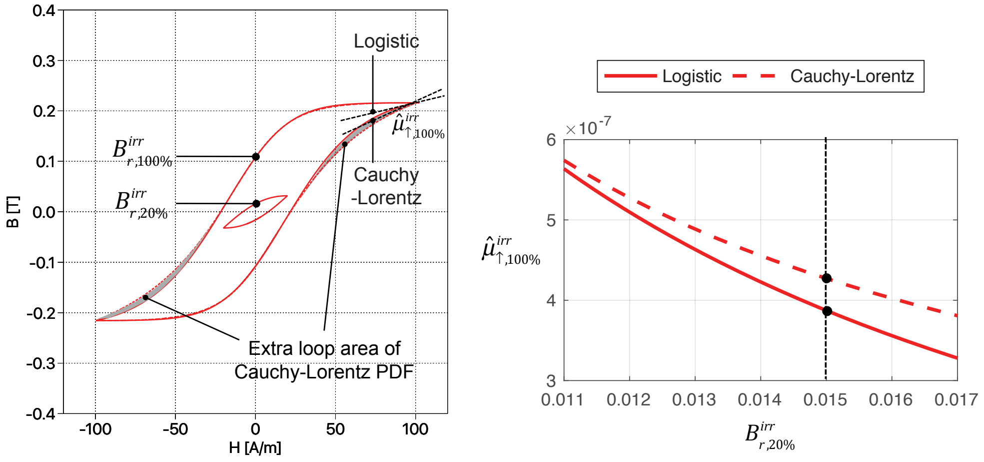

(a) (b)

Figure 4.12 Comparison of irreversible component between Preisach model using two different PDFs (a) Irreversible component with field strength amplitude $\hat{H}_{100\%} = \mathbf{100}$ A/m (b) Permeability on the top of the ascending branch of a limiting loop with model parameters fitted to fixed $B^{irr}_{\mathrm{r},100\%}$ and varying $B^{irr}_{\mathrm{r},20\%}$

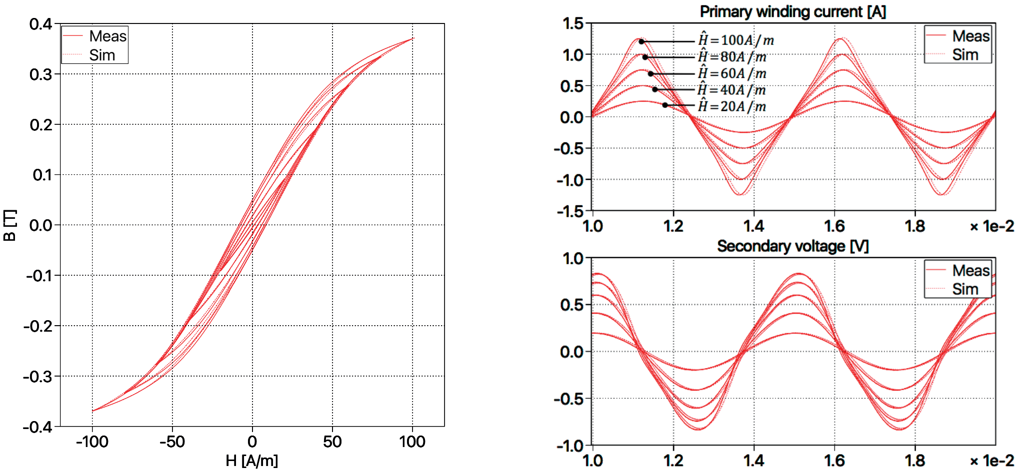

(a) (b)

Figure 4.13 Comparison between measurement and simulation of Ferrite 3C81 at different field strength amplitudes (a) Hysteresis loop (b) Time-domain primary winding current and secondary voltage

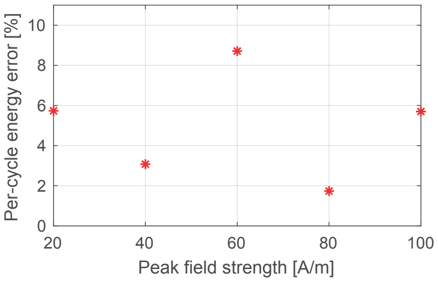

Figure 4.14 Percentage error of the simulated per-cycle energy loss from simulation of ferrite 3C81

able to approximate the measurement well. Again the error of equivalent permeability is negligible, as in the case of N87, thanks to the proposed formulation of the reversible component. The maximum error of per-cycle energy loss is 8.7% at $\hat{H}_{60\%} = 60\ \mathrm{A/m}$, while the error of all the other loops are under 8%.

The third material chosen for verification is 3F3 from Ferroxcube and the core sample is "TX 36 / 23 / 15", the turns number of both primary and secondary windings are 8. The parameters are also

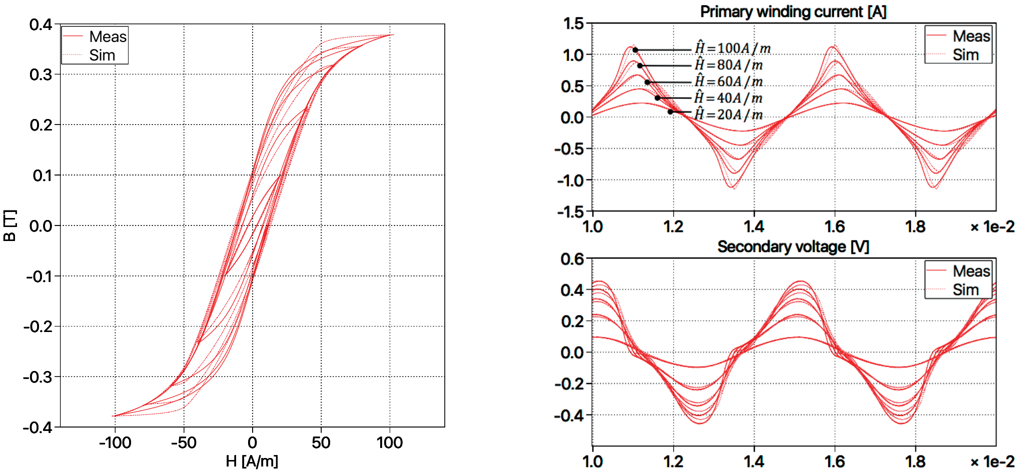

(a) (b)

Figure 4.15 Comparison between measurement and simulation of Ferrite 3F3 at different field strength amplitudes (a) Hysteresis loop (b) Time-domain primary winding current and secondary voltage

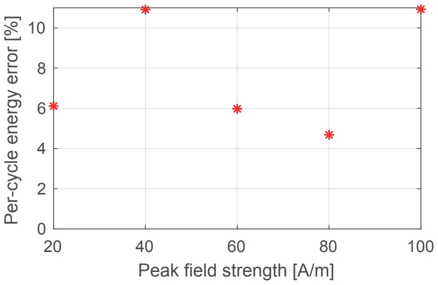

Figure 4.16 Percentage error of the simulated per-cycle energy loss from simulation of ferrite 3F3

identified based on the limiting hysteresis loop with amplitude $\hat{H}_{100\%}$ = 100 A/m and a symmetrical minor loop with amplitude $\hat{H}_{20\%}$ = 20 A/m. Again in **Fig. 4.15a** and **Fig. 4.15b**, the comparison between simulation and measurement is presented. Larger shape discrepancy than the previous two materials can be observed in **Fig. 4.15a** at high field strength amplitudes (e.g. 100 A/m), due to the larger curvature of the 3F3 hysteresis loop, while the accuracy of equivalent permeability is still well controlled thanks to the good approximation of the limiting loop's lower boundary. The error of per-cycle energy loss is illustrated in **Fig. 4.16**, the maximum value 10.9% occurs on the limiting loop with field amplitude $\hat{H}_{100\%}$ = 100 A/m.

4.5 Verification at increased temperatures

The $B-H$ characteristic of ferrite materials exhibits obvious dependency on temperature. Preliminary experimental tests have been carried out at increased temperature. For the measurement under different temperatures, the constant temperature oven of type DJ250 from Digitronic is used, which has forced convection. The characterisation setup combined with the oven is shown in **Fig. 4.17**. The core sample is placed inside the oven, the primary and secondary winding of which are connected to the power stage outside. In order to avoid noise on the measured secondary voltage, grounded coaxial cable with surge impedance 50Ω is used.

The measured hysteresis loop of the ferrite material $N87$ with 200 Hz sinusoidal excitation under 25°C and 100°C are compared in **Fig. 4.18a**. In comparison to 25°C, the flux density of the hysteresis loop under 100°C is significantly lower at the same peak field strength $\hat{H}_{100\%}$ = 100 A/m, which indicates deeper saturation and results in lower equivalent permeability. The remanence flux density as well as the coercitive field strength become smaller so that the per-cycle energy loss is reduced. The simulated hysteresis loops of ferrite N87 under 100°C temperature at different field strength amplitudes are compared to that from the measurement. Please note that in order to better fit the narrower shape and the deeper saturation of the hysteresis loop at high temperature, the bias parameter H_0 of the logistic distribution function in equation (4.8) has been manually adjusted to be a non-zero value of 25 A/m, while the identification process of all the other parameters described in **Sec. 4.3** remains the same. The corresponding percentage error of the per-cycle energy loss is indicated in **Fig. 4.19**.

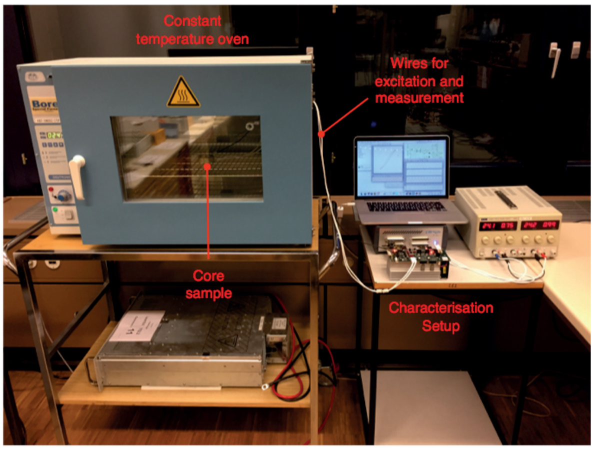

Figure 4.17 Test setup with core sample heated by the constant temperature oven

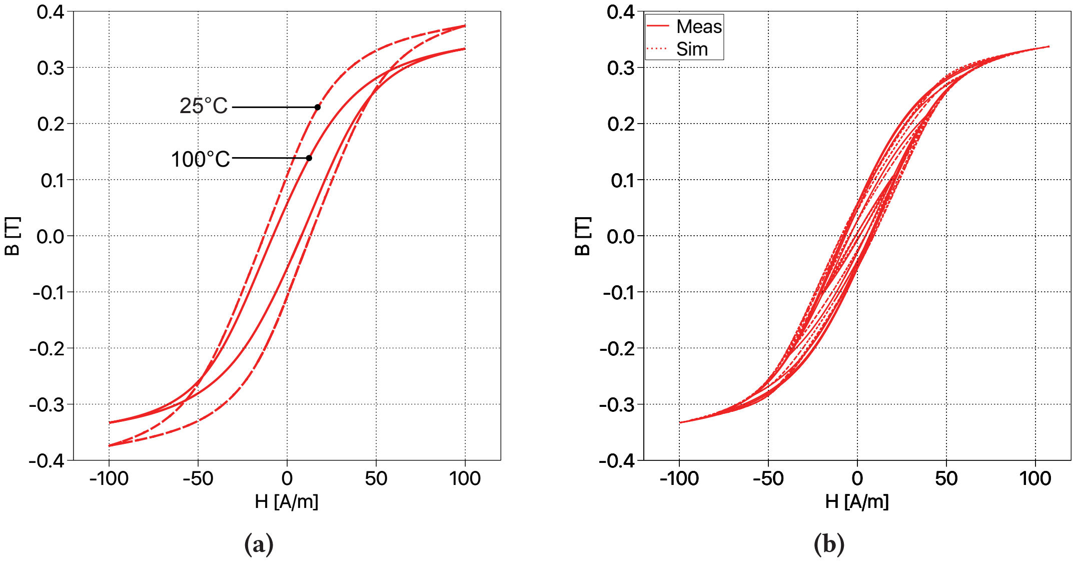

Figure 4.18 (a) Measured hysteresis loop under 25°C and 100°C temperature at field strength amplitude 100 A/m (b) Comparison between measured- and simulated hysteresis loop of Ferrite N87 under 100°C temperature at different field strength amplitudes

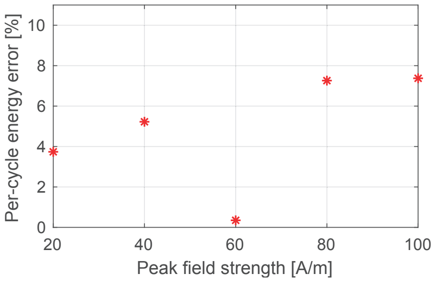

Figure 4.19 Percentage error of the simulated per-cycle energy loss from simulation of ferrite N87 under 100°C temperature

4.6 Verification for complex core geometry

After the material-related parameters of the core block are identified, one can configure geometrical parameters and connect multiple core blocks together, in order to model cores of arbitrary shape. For verification, a prototype transformer has been constructed using an E-core from EPCOS of size “E80/38/20” and material N87, as shown in **Fig. 4.20a**. An air gap of 0.075 mm has been introduced in each of the limbs. Two windings are installed on the side limb, the lower one with $N_1 = 15$ turns is supplied by the power amplifier output of the test bench, while the upper one with $N_2 = 10$ turns is left open and its voltage is measured. The magnetic circuit model of the prototype transformer is shown in **Fig. 4.20b**. Hysteresis core blocks using the proposed model for N87 have been adopted to construct the magnetic flux path inside the E-core. The geometry-related parameters (A and l) are configured according to the size of the center and side limbs. The three air gaps are represented by linear permeance blocks. In **Fig. 4.21a** the simulated primary winding current and the secondary

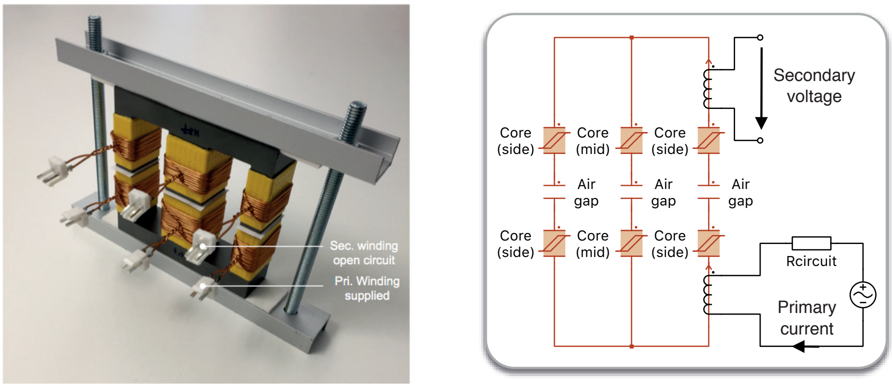

(a) **(b)**

Figure 4.20 Verification case of an E-core transformer with one winding on the side limb supplied and voltage of another on the same limb measured (a) Photo of the E-core transformer (b) Simulation model of the E-core transformer

winding voltage are compared between experimental measurement and simulation: The simulation model is able to reproduce the measurement with a minor error. The waveforms in this verification case have significantly low harmonic content. This is due to the presence of the air gap, which reduces the contribution from the nonlinear hysteresis effect of the transformer core. The core loss here can be calculated by multiplying the primary winding current and the secondary winding voltage divided by the turns ratio (N_1/N_2). This yields 0.0025 W for measurement and 0.0028 W for simulation, corresponding to an error of 12%. In **Fig. 4.21b**, the magnetic flux Φ (in Henry) of the side limb and magneto motive force F (in A) generated by the primary winding ($F = I \cdot N_1$) are plotted together reflecting the combined behavior of the linear air gap and nonlinear core material. Again, the proposed model is able to match the measurement well.

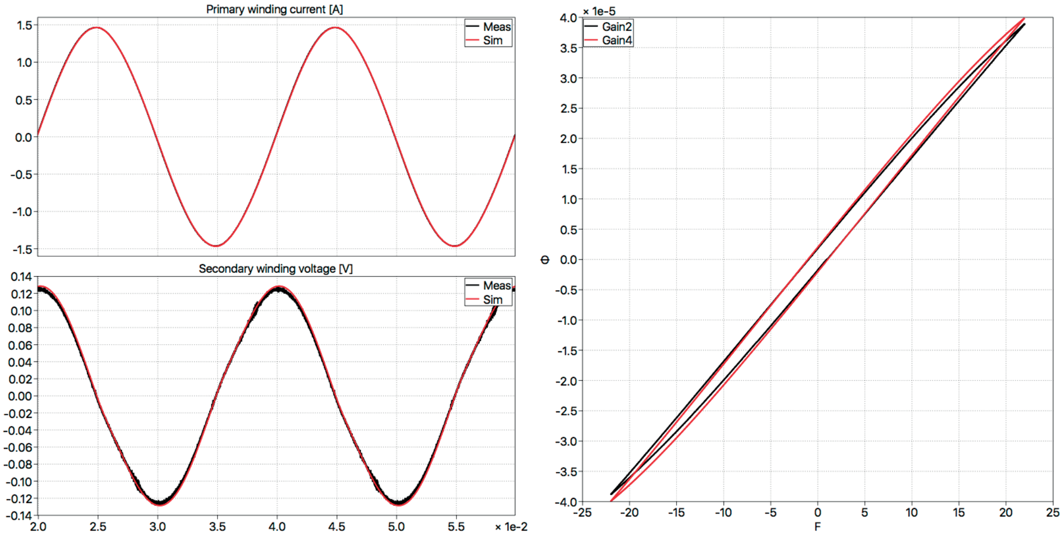

(a) **(b)**

Figure 4.21 Comparison between measurement and simulation of E-core transformer (a) Primary winding current and secondary winding voltage (b) $\Phi - F$ plot

4.7 Verification in power electronic circuits

In this section, the application of the proposed model in power electronic circuit is demonstrated. The characterization is configured to duty-cycle PWM or sinusoidal PWM mode. The same core sample of N87 ferrite from the last section is used, which is equipped with two windings of 8 turns each. The circuit simulation model is established according to the corresponding operation mode of the test setup, as shown in **Fig. 4.22**, including the AC voltage source representing the output of the left-hand side power amplifier, the circuit resistance of 0.4Ω (measured under DC condition) and the MOSFET bridge supplied by two DC sources.

The first scheme is intended to imitate the ferrite material's operation in an isolation transformer of a DC-DC converter. The left-hand side power amplifier is muted (zero voltage output), while the right-hand side MOSFET bridge is operated at 5 kHz switching frequency and 50% duty cycle, generating a square wave excitation voltage. In this operating condition, the frequency dependent residual effect is negligible. The DC side voltage is configured to different values, which set the peak field strength of the material to $100A/m$, $60A/m$ and $20A/m$. The simulated $B-H$ characteristic and time domain primary current as well as secondary voltage waveform are compared to the measurement. Due to

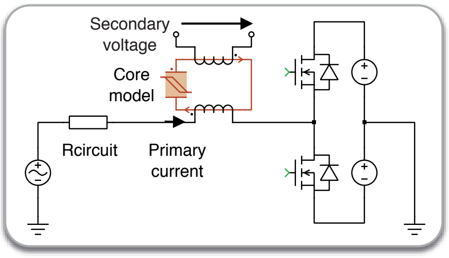

Figure 4.22 Simulation model of the test setup in duty-cycle PWM and sinusoidal PWM mode

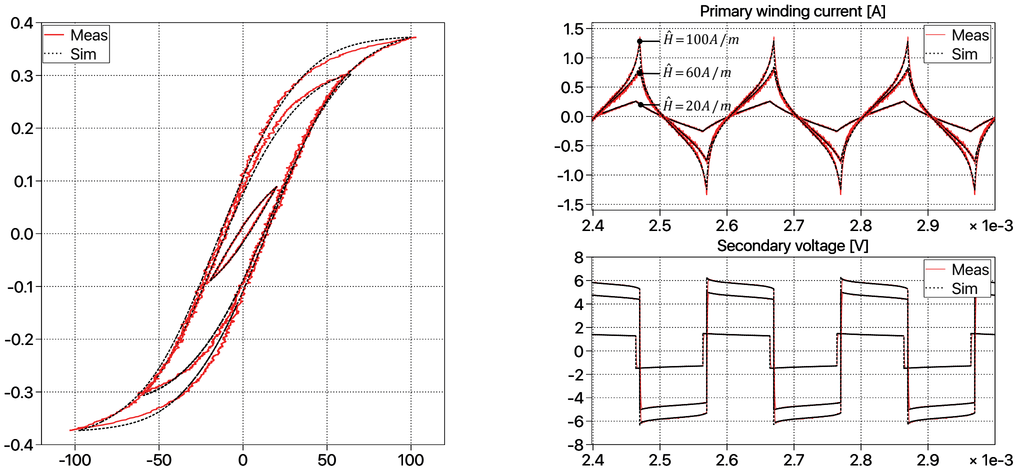

(a) (b)

Figure 4.23 Comparison between measurement and simulation of Ferrite N87 in power electronic circuit with 50% PWM modulation index: (a) Hysteresis loop; (b) Time-domain primary winding current and secondary voltage.

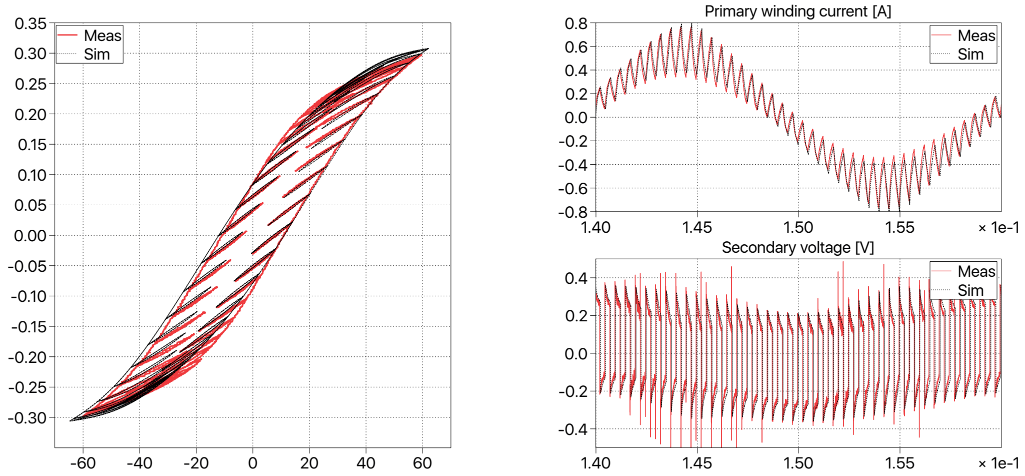

(a) **(b)**

Figure 4.24 Comparison between measurement and simulation of Ferrite N87 in power electronic circuit with sinusoidal and 50% PWM modulation index: (a) Hysteresis loop; (b) Time-domain primary winding current and secondary voltage.

the material nonlinearity together with the coupling of the circuit resistance, the primary current has obvious harmonic component rather than a ideal triangular wave while the secondary voltage is not ideal square wave, all these effects have been well captured by the proposed model. Since the frequency dependent effect is negligible in this case, the per-cycle energy loss is mainly determined by the peak field strength, and the error of the per cycle energy loss remains approximately the same value as in the corresponding cases of the last section (**Fig. 4.10**).

The second scheme imitates the condition where the ferrite material is used for filter inductors in a voltage source inverter. The left-hand side power amplifier generates a 50 Hz sinusoidal voltage and the right-hand side MOSFET bridge generates a PWM voltage. A sinusoidal voltage with $0.24\,V$ amplitude and 50 Hz frequency is generated by the left-hand side power amplifier. The MOSFET bridge is operated at medium switching frequency of 2 kHz with a 50 % duty cycle and DC voltage of 0.24 V.

The simulated hysteresis loop on the $B-H$ plane and the time-domain primary current and secondary open circuit voltage are compared in **Fig. 4.24a** and **Fig. 4.24b**. The proposed model is able to reproduce the ripple current and pulsed voltage with good accuracy, while the influence of the circuit resistance has been reflected in a fully coupled way. The sinusoidal voltage of the left-hand side power amplifier contributes to the large hysteresis loop, while the right-hand side MOSFET bridge generates the small minor loops. It is to be noted that the minor loops close themselves, which corresponds to the deletion property of the Preisach model as has been discussed in **Sec. 4.2**. Both loops are well captured by the proposed model and the error of energy loss per 50 Hz cycle (including that from both large major- and small minor loops) is 5 %. Please note that there are not only symmetrical but also asymmetrical hysteresis loops present in this verification scheme. The asymmetrical hysteresis loops are not explicitly controlled during the model parameter identification, nevertheless they are generated by the simulation model as acceptable approximation of the measurement, thanks to the physics-based intrinsic property of the Preisach model.

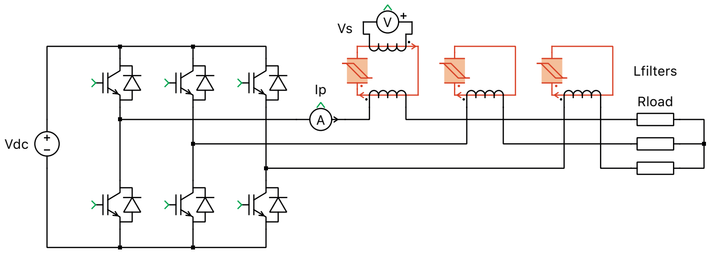

Figure 4.25 Schematic of the verification setup with a three phase VSI.

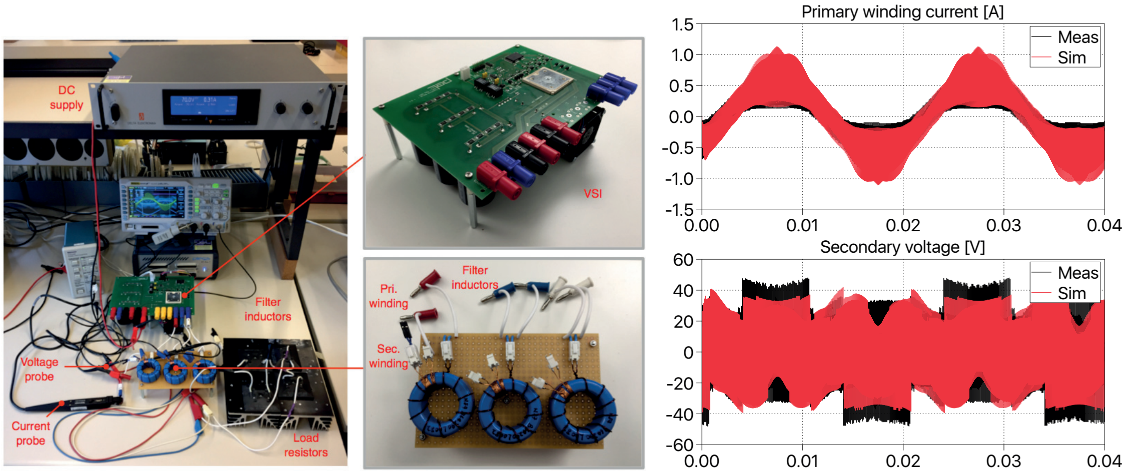

(a) **(b)**

Figure 4.26 (a) Hardware of the verification setup with a three phase VSI; (b) Comparison between the measured and simulated time domain waveforms at the filter inductor in a three-phase VSI (two AC cycles).

In the third scheme, the model is verified using a three phase two-level voltage source inverter. The circuit schematic and hardware realization of the experimental setup are shown in **Fig. 4.25** and **Fig. 4.26a**. The input of the VSI is supplied with a 50 V DC voltage source. The output is connected to three load resistors of 22 Ω and filtered by three filter inductors. Each of the three filter inductors is composed of a toroidal core of ferrite material N87 (shape code “R 50.0 x 30.0 x 20.0”) and a winding of 10 turns, which result in an equivalent inductance of 446 μH. To obtain the core loss following the V-I approach, a secondary winding of 10 turns is also installed on the inductor and left open for voltage measurement. The IGBT full bridge is driven by 10 kHz PWM, the modulation signal has 50 Hz fundamental frequency with 50 % peak modulation index.

The simulated time domain primary winding current and secondary winding voltage as well as the $B-H$ characteristic of the filter inductor in phase A are compared to the measurement in **Fig. 4.26b**, **Fig. 4.27** and **Fig. 4.28**. The simulation model is able to reproduce the current ripple and corresponding voltage impulses. The energy loss per 50 Hz AC cycle is obtained by integrating the product of the primary winding current and secondary voltage for both the measurement and simulation, the error between the two is 10.2 %. The simulated hysteresis loops near zero AC current with zero bias (**Fig. 4.28b**) matches the measurement well, thanks to the parametrization scheme presented in **Sec. 4.3**. The hysteresis loops close to the AC current peak with maximum DC bias (**Fig. 4.28b**) exhibit shape-differences to the measurement, which needs improvement in the future.

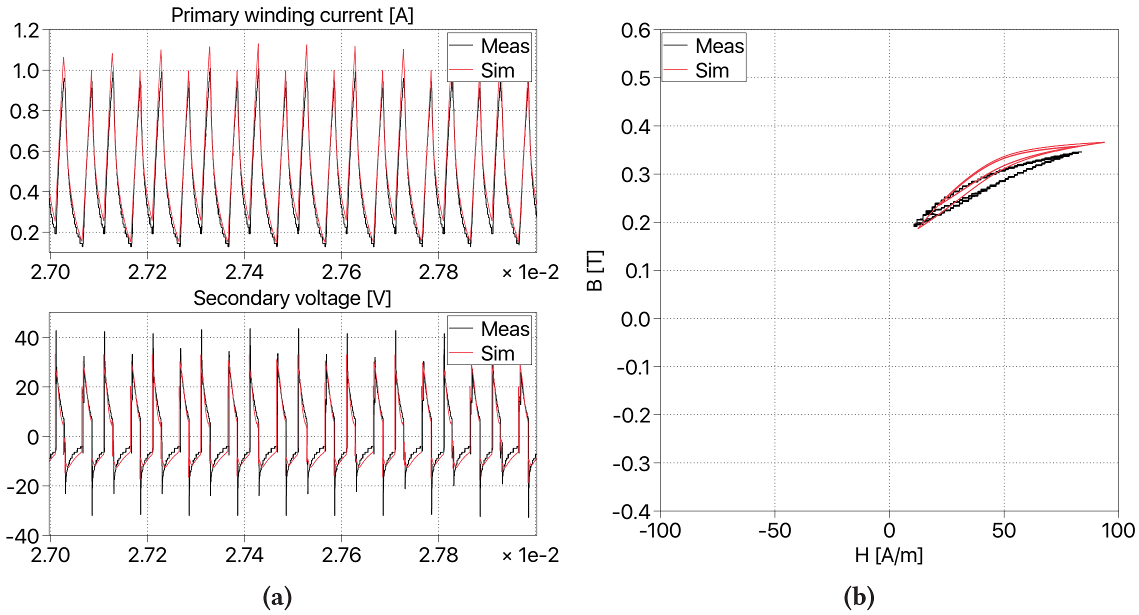

Figure 4.27 Comparison between measurement and simulation of filter inductor in three-phase VSI: (a) Time domain waveform at AC current peak; (b) $B-H$ characteristic at AC current peak.

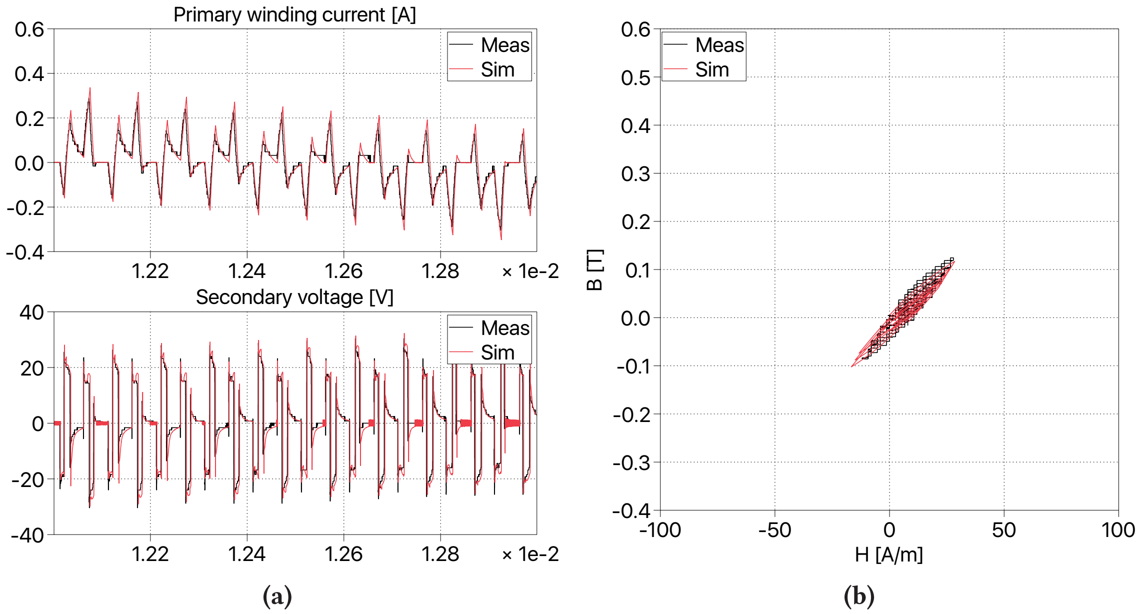

Figure 4.28 Comparison between measurement and simulation of filter inductor in three-phase VSI: (a) Time domain waveform zoomed-in area at zero AC current; (b) $B-H$ characteristic at zero AC current.

4.8 Summary

This chapter proposed an improved model for the frequency independent hysteresis effect of ferrite materials, using a permeance-capacitor analogy based magnetic circuit which can be seamlessly integrated into system-level time domain simulations. By applying the logistic probability distribution function to the Preisach model of the irreversible magnetization together with a newly constructed form of $B - H$ function for the reversible magnetization, the accuracy of the simulated per-cycle energy loss and the equivalent permeability of hysteresis loops with wide range of amplitudes can be controlled with good accuracy. The proposed approach of modeling has been verified with ferrite materials of different hysteresis loop shapes, the fidelity has been evaluated by integrating the model into circuit simulation environments in a fully coupled way.

5

Model of hysteresis for silicon steel

As power semiconductors with even higher switching frequency are continuously developed, core materials for high frequency operating conditions, like ferrite and nanocrystalline are gradually taking the place of iron based alloys (typically grain oriented silicon steel) for magnetic components in many power electronic applications. However, in some fields like medium voltage drives or high power line commutated converters with medium or low switching frequencies excitation, silicon steel is still dominated in production of transformers or filter inductors due to its low cost and high mechanical robustness. This chapter presents the product Preisach model in permeance-capacitance based magnetic circuit for silicon steel material.

5.1 Literature review

In comparison to the high frequency materials like ferrite, silicon steel has significantly larger hysteresis losses which is reflected on the wide $B-H$ loops. This feature is not only present at medium frequencies where the eddy current effect is observable, but also at low frequencies where the frequency independent magnetic hysteresis effect dominates. **Fig. 5.1** shows the difference between silicon steel and territes in experimental measurements.

The fundamental structure combining a classical Preisach model with a reversible component has been used to model the time-domain hysteresis behavior of silicon steel material in many existing publications like [29], [30] and [31]. The fidelity has been evaluated on large limiting hysteresis loops (or with amplitudes close to the limiting loop), based on which the models are parametrized. However, no verification has been carried out on both limiting loop and significantly smaller minor loops (e.g. with field strength amplitude equal to 20% of the limiting loop). In the following section, it is demonstrated that the formulation of a classical Preisach model in combination with a reversible component is not sufficient to represent the $B-H$ characteristic of silicon steel material over a wide range of field strength amplitudes:

Two hysteresis loops from experimental measurements of silicon steel laminate M330/35 with a large amplitude $\hat{H}_{100\%} = 100\,\mathrm{A/m}$ and a small amplitude $\hat{H}_{20\%} = 20\,\mathrm{A/m}$ are depicted in **Fig. 5.2a**. They are obtained under 25 Hz sinusoidal excitation so that the frequency-dependent eddy current effect can be neglected. The remanence flux densities of these two loops are denoted as $B^{*}_{\mathrm{r},100\%}$ and $B^{*}_{\mathrm{r},20\%}$. As discussed in the **Sec. 4.3**, the irreversible part of the hysteresis model (classical Preisach model) should be parametrized to reproduce the remanence flux density, in order to accurately capture the per-cycle energy loss. Using equations (4.11) and (4.12), the remanence flux density $B_{\mathrm{r},100\%^{\mathrm{irr}}}$ and

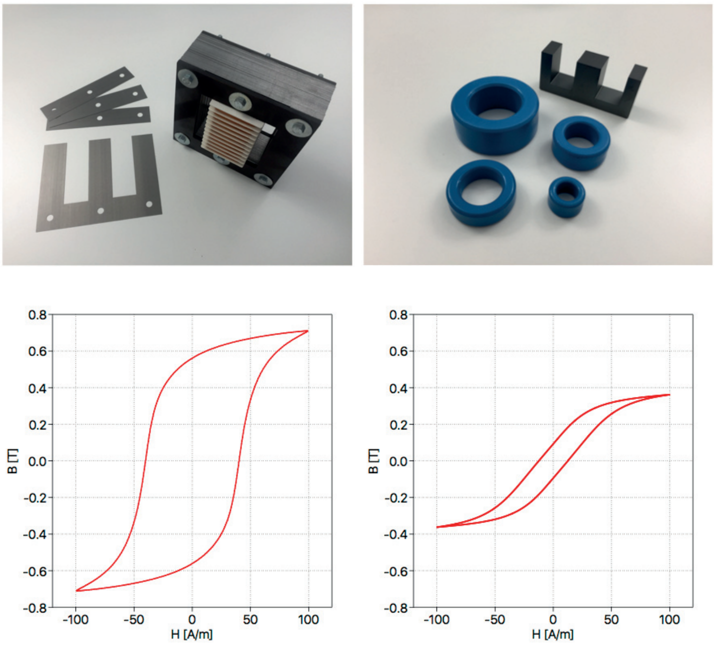

(a) **(b)**

Figure 5.1 $B-H$ characteristic comparison under $50Hz$ excitation of (a) Silicon steel; (b) Ferrite.

$B^{\text{irr}}_{\text{r},20\%}$ of the classical Preisach model is given by:

$$B^{irr}_{\text{r},100\%} = \Big(C_\text{s}(\hat{H}_{100\%}) - C_\text{s}(0)\Big)^2 \tag{5.1}$$

$$B^{irr}_{\text{r},20\%} = \Big(C_\text{s}(\hat{H}_{20\%}) - C_\text{s}(0)\Big)^2 \tag{5.2}$$

Following the formulation presented in **Sec. 4.2**, the differential permeability $\mu^{\text{irr}}_{0\%,\downarrow 100}$ and $\mu^{\text{irr}}_{0\%,\downarrow 20}$ of the irreversible component at the remanence point are given by:

$$\mu^{\text{irr}}_{0\%,\downarrow 100} = 2 \cdot p_\text{s}(0) \cdot \int_0^{\hat{H}_{100\%}} p_\text{s}(U) \cdot dU = 2 \cdot p_\text{s}(0) \cdot \Big(C_\text{s}(\hat{H}_{100\%}) - C_\text{s}(0)\Big) \tag{5.3}$$

$$\mu^{\text{irr}}_{0\%,\downarrow 20} = 2 \cdot p_\text{s}(0) \cdot \int_0^{\hat{H}_{20\%}} p_\text{s}(U) \cdot dU = 2 \cdot p_\text{s}(0) \cdot \Big(C_\text{s}(\hat{H}_{20\%}) - C_\text{s}(0)\Big) \tag{5.4}$$

Combining equations (5.1), (5.2), (5.3) and (5.4) leads to the relation in below:

$$\sqrt{\frac{B^{irr}_{\text{r},100\%}}{B^{irr}_{\text{r},20\%}}} = \frac{\mu^{\text{irr}}_{0\%,\downarrow 100}}{\mu^{\text{irr}}_{0\%,\downarrow 20}} = \frac{\mu_{0\%,\downarrow 100} - \mu^{\text{rev}}_{0\%}}{\mu_{0\%,\downarrow 20} - \mu^{\text{rev}}_{0\%}} \tag{5.5}$$

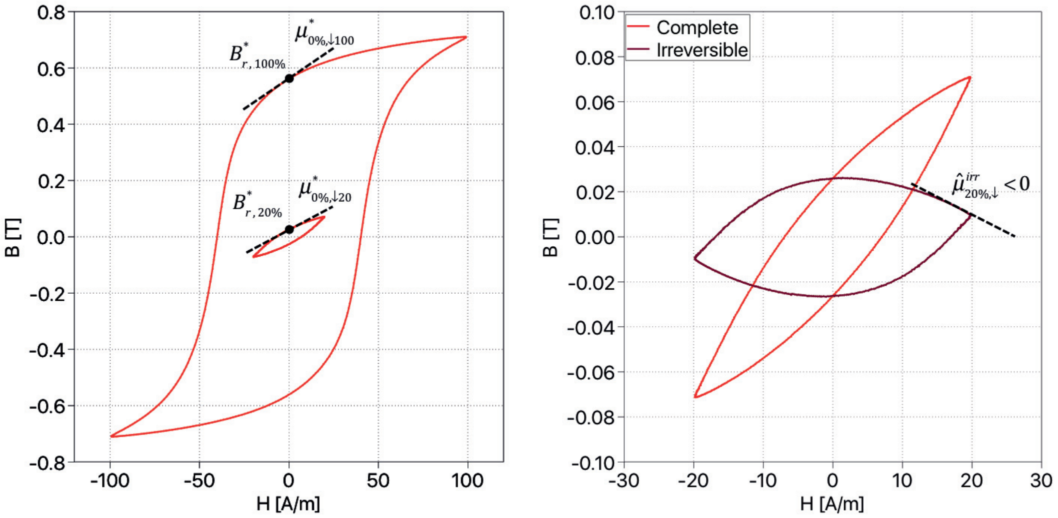

(a) **(b)**

Figure 5.2 (a) Measured hysteresis loops with peak field strength $\hat{H}_{100\%} = 100$ A/m and $\hat{H}_{20\%} = 20$ A/m (b) Hysteresis loop with peak field strength $\hat{H}_{20\%} = 20$ A/m and the irreversible component with the calculated reversible permeability $\mu^{\text{rev}}_{0\%}$ subtracted

where $\mu_{0\%,\downarrow 100}$ and $\mu_{0\%,\downarrow 20}$ are the differential permeabilities of the complete hysteresis model (sum of irreversible- and reversible components) at the remanence point, while $\mu^{\text{rev}}_{0\%}$ is the permeability of the reversible component. If we substitute $B^{\text{irr}}_{\text{r},20\%}$, $B^{\text{irr}}_{\text{r},100\%}$, $\mu_{0\%,\downarrow 100}$ and $\mu_{0\%,\downarrow 20}$ with the values from the experimental measurement (values with superscript "*" in **Fig. 5.2a**), the required reversible permeability at $H = 0$ can be explicitly calculated as $\mu^{\text{rev}}_{0\%} = 3.1 \cdot 10^{-3}$. Assuming that the reversible component is linear in the small field strength range $[-\hat{H}_{20\%}, +\hat{H}_{20\%}]$, the desired irreversible component of the hysteresis loop with peak field strength $\hat{H}_{20\%}$ can be obtained by subtracting the $B-H$ characteristic $B^{\text{rev}}(H) = \mu^{\text{rev}}_{0\%} \cdot H$ from the measurement, as demonstrated in **Fig. 5.2b**. However, the descending permeability $\hat{\mu}^{irr}_{20\%,\downarrow}$ of the irreversible hysteresis loop at the peak point (marked in **Fig. 5.2b**) becomes negative. Considering the fact that the classical Preisach model introduced in **Sec. 4.2** always result in $\hat{\mu}^{irr}_{20\%,\downarrow}$ equal to zero, this shape of the desired irreversible component cannot be represented by the classical Preisach model with acceptable accuracy.

The problem can be ascribed to the fact that the material permeability does not only depend on the field strength but also on the flux density. This dependency is obvious in materials with relatively wide hysteresis loops. Besides the classical Preisach model's mismatch on the symmetrical hysteresis loop, this flux density dependency is also reflected on the congruency violation of minor loops and has been discussed in the work of [28]. In order to capture the flux density dependency of hard materials like recording media, an extension of the classical Preisach model called *Moving Preisach model* has been proposed in [28]. For soft materials (e.g. silicon steel) in power electronic applications, the authors of [48] has proposed a *Product Preisach model.*

This thesis adopts the product Preisach model for modeling static hysteresis of silicon steel material. This chapter is organized as follows: The realization in a permeance-capacitance based magnetic circuit for silicon steel material is proposed in **Sec. 5.2**. Experimental verification including the comparison to the classical Preisach model are presented in **Sec. 5.3**.

5.2 Proposed model

5.2.1 Model structure

The structure of the proposed product Preisach model in the permeance-capacitance based magnetic circuit is shown in **Fig. 5.3**. The C-script block “Preisach” implements the classical Preisach model. Different from the model of ferrite materials introduced in **Chap. 4**, the Cauchy-Lorentz PDF proposed by [29] and has been widely applied for silicon steel material in plenty of existing publications is adopted. The generalized form of the Cauchy -Lorentz PDF is expressed as

$$p_s(H) = K \cdot \frac{1}{1 + \Big((H - H_0) \cdot \sigma\Big)^2} \tag{5.6}$$

The corresponding CDF is given by

$$C_s(H) = K/\sigma \cdot \arctan\Big((H - H_0) \cdot \sigma\Big) \tag{5.7}$$

The parameter K is set to 1 in the C-script. During the simulation, two output signals are calculated by the C-Script block:

- The instantaneous permeability following the expression of equations (4.5) ~ (4.7) for different operating points, denoted as μ'^{irr}.
- The instantaneous flux density by numerically integrating the equations (4.5) ~ (4.7) for field strength H, denoted as B'^{irr}

B'^{irr} is provided to the input of a function block Pct. On the “virtual” limiting loop generated by the C-Script, the peak flux density at the field strength $\hat{H}_{100\%}$ can be pre-calculated by numerically integrating the equation (4.5) in the range $[0, \hat{H}_{100\%}]$ before the start of simulation, denoted as $\hat{B}'^{\text{irr}}_{100\%}$. Please note that $\hat{B}'^{\text{irr}}_{100\%}$ remains a constant value during the simulation, provided that the model

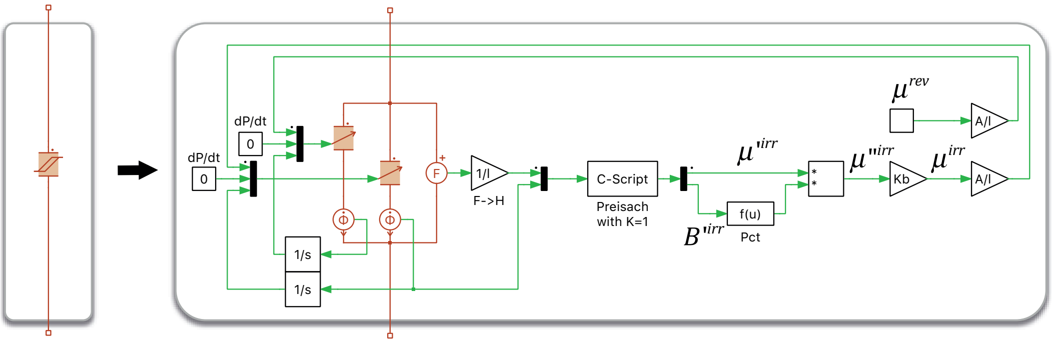

Figure 5.3 Model structure of the permeance block using proposed product Preisach model.

parameters H_0 and σ are identified prior to the simulation. With $\hat{B}'^{\mathrm{irr}}_{100\%}$ given, the output of the function block Pct is generated according to

$$Pct(\hat{B}'^{\mathrm{irr}}) = e^{k_{pct}\cdot(B'^{\mathrm{irr}}/\hat{B}'^{\mathrm{irr}}_{100\%}-1)} \tag{5.8}$$

where the coefficient k_{pct} is a model parameter, the identification of which is introduced later in this chapter. Multiplying Pct with μ'^{irr} yields a new permeability μ''^{irr}.

$$\mu''^{\mathrm{irr}}(H, \hat{B}'^{\mathrm{irr}}) = \mu'^{\mathrm{irr}}(H) \cdot Pct(\hat{B}'^{\mathrm{irr}}) \tag{5.9}$$

Numerically integrating again equation (5.9) in the range $[0, \hat{H}_{100\%}]$ prior to the simulation, with equation (4.5) and the instantaneous $\hat{B}'^{\mathrm{irr}}$ substituted, yields $\hat{B}''^{\mathrm{irr}}_{100\%}$. $\hat{B}''^{\mathrm{irr}}_{100\%}$ is also a constant, if the model parameters H_0, σ and k_{pct} are given. The ultimate irreversible permeability μ^{irr} is μ''^{irr} scaled by a constant factor, given by

$$\mu^{\mathrm{irr}}(H, \hat{B}'^{\mathrm{irr}}) = \mu''^{\mathrm{irr}}(H, \hat{B}'^{\mathrm{irr}}) \cdot \hat{B}^{irr*}_{100\%}/\hat{B}''^{\mathrm{irr}}_{100\%} \tag{5.10}$$

where $\hat{B}^{irr*}_{100\%}$ is the peak flux density of the limiting hysteresis loop's irreversible component extracted from the measurement. Considering the dominant hysteresis effect of silicon steel material, the reversible permeability can be assumed to be a linear function with constant permeability μ^{rev}. Thus $\hat{B}^{irr*}_{100\%}$ is obtained by simply subtracting the reversible flux density from $\hat{B}^{*}_{100\%}$, given by

$$\hat{B}^{irr*}_{100\%} = \hat{B}^{*}_{100\%} - \mu^{\mathrm{rev}} \cdot \hat{H}_{100\%} \tag{5.11}$$

5.2.2 Parametrisation

For parametrization of the proposed model, three hysteresis loops as shown in **Fig. 5.4** are required from experimental measurement, including:

- A symmetrical limiting loop with the highest peak field strength $\hat{H}_{100\%}$
- A symmetrical minor hysteresis loop with 20% of the limiting loop's peak field strength, that is $\hat{H}_{20\%} = 0.2 \cdot \hat{H}_{100\%}$
- Another symmetrical minor hysteresis loop with 50% of the limiting loop's peak field strength, that is $\hat{H}_{50\%} = 0.5 \cdot \hat{H}_{100\%}$

The peak flux density $\hat{B}^{*}_{100\%}$ can be read directly from the measured limiting loop. The constant reversible permeability is assigned the value of the descending permeability on the limiting loop's peak, that is $\mu^{\mathrm{rev}} = \hat{\mu}^{*}_{100\%\downarrow}$. Making use of the known values $\hat{B}^{*}_{100\%}$ and μ^{rev}, the target irreversible peak flux density $\hat{B}^{irr*}_{100\%}$ can be obtained following equation (5.11). The remaining three model parameters H_0, σ and k_{pct} are determined to fit three values from the measurement:

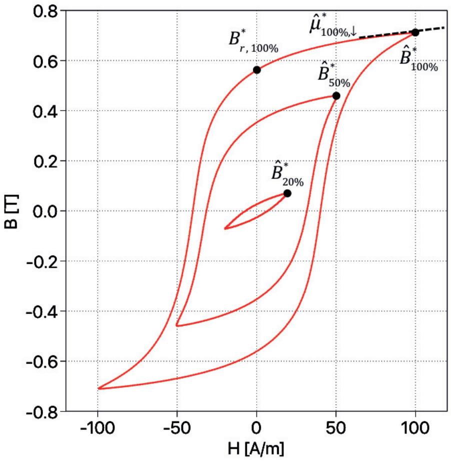

Figure 5.4 Required hysteresis loops from measurement parametrization of the produce Preisach model

- Peak flux density $\hat{B}^*_{20\%}$ of the 20% hysteresis loop. $\hat{B}_{20\%}$ of the model is obtained by numerically integrating equation (5.10) on the virgin curve plus the reversible component $\mu^{\mathrm{rev}} \cdot \hat{H}_{20\%}$.
- Peak flux density $\hat{B}^*_{50\%}$ of the 50% hysteresis loop. $\hat{B}_{50\%}$ of the model is obtained by numerically integrating equation (5.10) on the virgin curve plus the reversible component $\mu^{\mathrm{rev}} \cdot \hat{H}_{50\%}$.
- Remanence flux density $B^*_{\mathrm{r},100\%}$ of the limiting hysteresis loop. $B_{\mathrm{r},100\%}$ of the model is obtained by numerically integrating equation (5.10) on the virgin curve from zero up to $\hat{H}_{100\%}$ and back to $H = 0$.

A two-loop fitting process is conducted, as demonstrated in **Fig. 5.5**. The outer loop iterates the

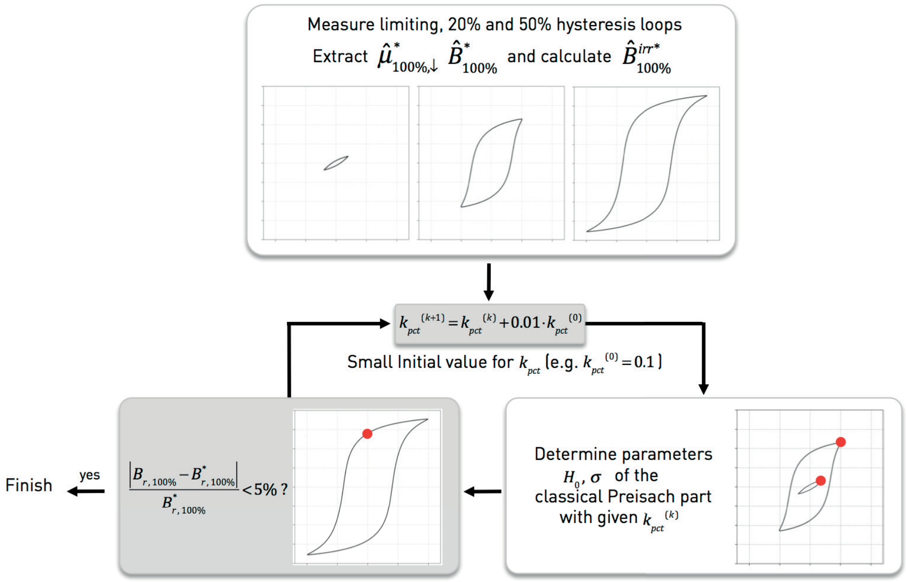

Figure 5.5 Parametrization of the proposed model in a two-loop structure, where the outer loop iterates k_{pct} of the product term and the inner loop iterates H_0 and σ of the classical Preisach part.

parameter k_{pct} of the produce term aiming to fit the remanence flux density $B_{\mathrm{r},100\%}{}^*$, while the inner loop iterates H_0 and σ of the classical Preisach model to fit the two peak flux densities $\hat{B}^*_{20\%}$ and $\hat{B}^*_{50\%}$. Since the objective values $\hat{B}_{20\%}$, $\hat{B}_{50\%}$ and $B_{\mathrm{r},100\%}$ do not have analytical form, but instead, are determined using numerical integration, implicit gradient-based or evolutionary algorithm are adopted. In this thesis the "fminsearch" fitting algorithm provided by MATLAB (referred as unconstrained nonlinear optimization) is chosen.

5.3 Verification

For verification purposes, 15 pieces of square laminates made of silicon steel M330/35 are pressed together creating the core sample for the study, as shown in **Fig. 5.6a**. One primary and one secondary winding with the same turns number $N_1 = N_2 = 30$ are installed. The core sample is connected to the test setup introduced in **Chap. 3**, which is operated in sinusoidal excitation mode with 25 Hz excitation frequency. The simulation model established in the system level simulation software PLECS includes the core sample using the proposed magnetic circuit as shown in **Fig. 5.6b**. A controlled

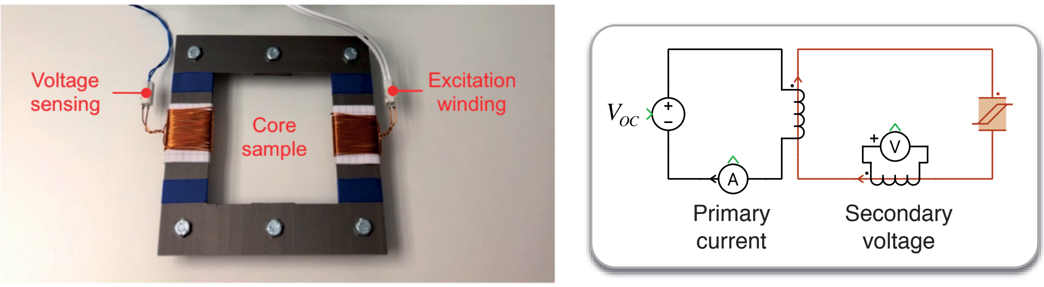

(a) **(b)**

Figure 5.6 (a) Core sample made of stacked laminates; (b) Simulation model.

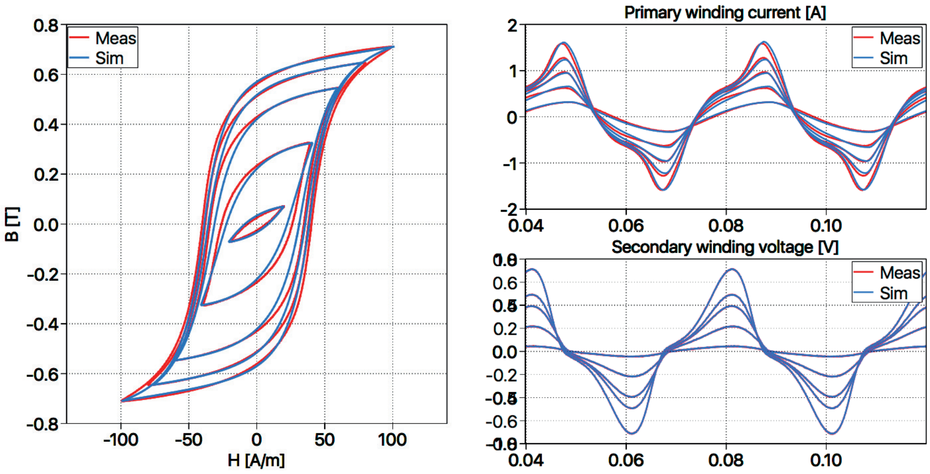

(a) **(b)**

Figure 5.7 Comparison between measurement and simulation of silicon steel M330 lamination at different field strength amplitudes (a) Hysteresis loop (b) Time-domain primary winding current and secondary voltage

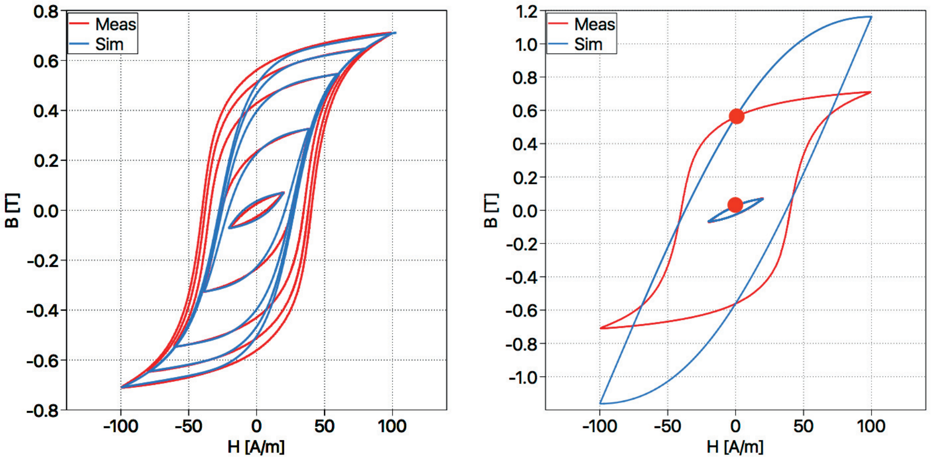

(a) (b)

Figure 5.8 Hysteresis loop without the product term in model (a) Parametrized to fit $\hat{B}_{20\%}$ and $\hat{B}_{50\%}$ (b) Parametrized following the scheme proposed in **Chap. 4**

voltage source is fed by measured secondary voltage value multiplied by a factor N_1/N_2, which is equal to the excitation voltage on the primary winding with the voltage drop on the winding- and circuit resistance excluded. All components are configured to be same as the test bench hardware. For parametrization, the hysteresis loop with peak field strength $\hat{H}_{100\%}$ = 100 A/m is chosen as the limiting loop.

In **Fig. 5.7a**, the $B-H$ loops of different amplitudes are compared between measurement and the parametrized model, good match has been achieved. A comparison is also carried out in the corresponding time domain waveform of the primary winding current, again the proposed model is able to reproduce the measurement with good accuracy.

To prove the necessity of introducing the product term, comparitive verifications are carried out. If the product term is not included in the model by configuring the parameter k_{pct} of equation (5.8) equal to zero, while the parameters H_0 and σ of the classical Preisach model are identified to fit $\hat{B}^*_{20\%}$ and $\hat{B}^*_{50\%}$, the simulated hysteresis loops exhibit significant error in comparison to the measurement, especially on the remanence flux density, as demonstrated in **Fig. 5.8a**.

Otherwise if the model is parametrized following the scheme described in the **Chap. 4**, although the remanence flux density of the limiting- and minor loops can be accurately captured, the shape of the limiting loop, is considerable different than that from the measurement, as shown in **Fig. 5.8b**. The problem is that the peak flux density of the irreversible component is already higher than that of the measured limiting loop, therefore no reversible component with positive peak flux density can be found.

5.4 Summary

By introducing a product term into the classical Preisach model, the frequency-independent hysteresis effect of silicon steel material can be accurately captured in the permeance-capacitance based magnetic circuit over a wide range of excitation amplitudes. The model for the frequency-dependent eddy current effect, extended from the static hysteresis model, is presented in the future **Chap. 8**.

6

Model of hysteresis for selected materials

Besides ferrite and silicon steel materials which have been commonly used since middle of 20^{th} *century, new metal based materials like amorphous and nanocrystalline alloys are becoming popular in power electronic applications, due to their higher saturation flux density compared to ferrite and lower core loss compared to silicon steel. In this chapter, a special form of Preisach model representation is adopted for these materials in a permeance-capacitance based magnetic circuit.*

6.1 Literature review

Some materials exhibit significantly different shapes of $B-H$ characteristic as ferrite materials, as shown in **Fig. 6.1**, which can hardly be reproduced by a Preisach model with distribution function in explicit form. The authors of [37], [38] and [39] have demonstrated that all magnetization curves of the Preisach model following the formulation defined by equation (4.1) can be derived from the ascending

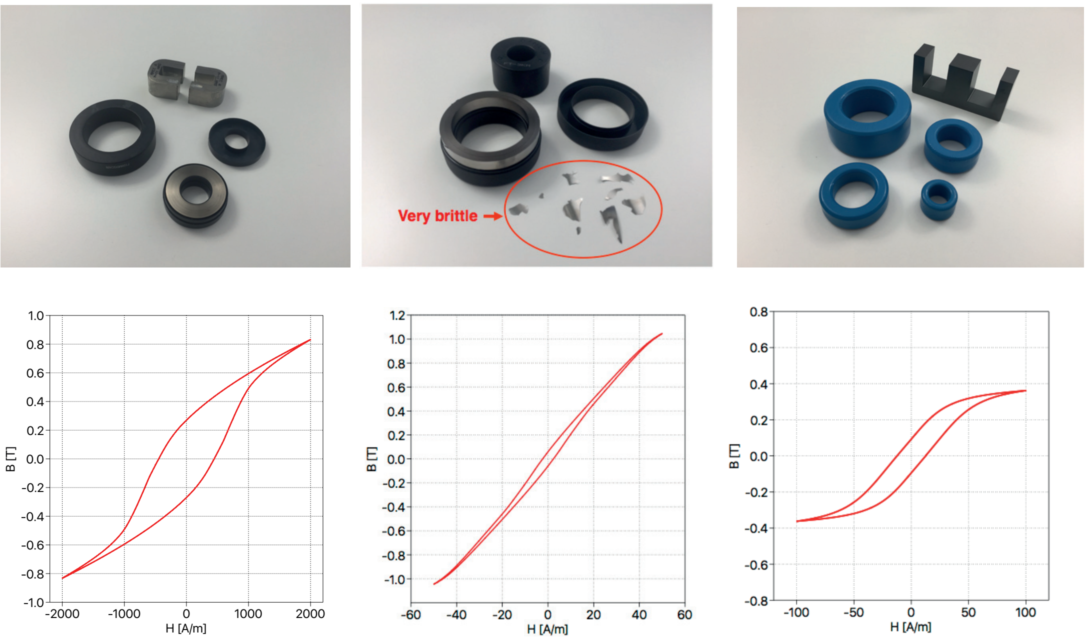

(a) (b) (c)

Figure 6.1 $B-H$ characteristic comparison under $50Hz$ excitation of (a) Amorphous; (b) Nanocrystalline; (c) Ferrite.

curve of only one measured limiting hysteresis loop (with the highest amplitude of concern), without the need of analytically identifying the PDF. Making use of this property, symmetrical hysteresis loops with relatively large amplitude (typically larger than 50 % of the limiting loop) have been modeled with good accuracy in the work of [40], [41] and [42] for ferrite materials. In this chapter, the basic idea of this approach is applied to the permeance-capacitance based magnetic circuit, in order to model the materials with irregular shape of hysteresis loop which cannot be represented by a classical Preisach model using an explicit form of distribution function.

This chapter is organized as follows: The realization in a permeance-capacitance based magnetic circuit using the explicit representation is introduced in **Sec. 6.2**, together with the method of parameter identification. Experimental verification of the proposed model for different materials are presented in **Sec. 6.3**.

6.2 Proposed model

6.2.1 Model structure

The only information needed for the proposed model is the $B-H$ characteristic of a symmetrical limiting hysteresis loop's ascending branch, denoted as $B_u(H)$. Using the classical Preisach model, $B_{\mathrm{u}}(H)$ at a given field strength H is calculated by the Everett integration, following the equation (4.4). The integral can be decomposed into several areas $S_1 \sim S_5$, as demonstrated in **Fig. 6.2a** and expressed in equation (6.1). The signs "+" and "-" indicate that the corresponding area belongs to S_+ and S_- in equation 4.4, respectively.

$$B_{\mathrm{u}}(H) = \iint p_{\mathrm{s}}(U) \cdot p_{\mathrm{s}}(-V) \cdot \gamma(U,V) \cdot dU dV = Intg(S_1) + Intg(S_2) - Intg(S_3) - Intg(S_4) - Intg(S_5) \quad (6.1)$$

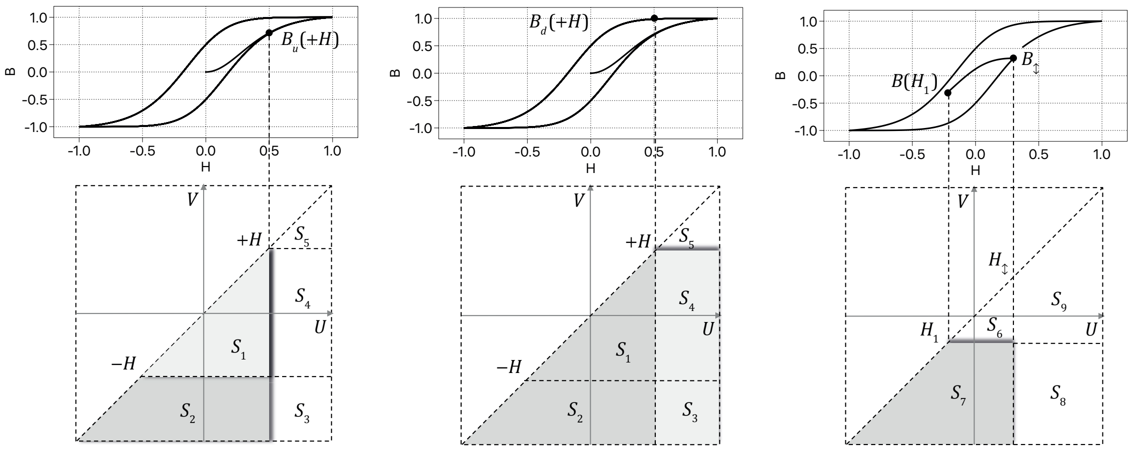

(a) **(b)** **(c)**

Figure 6.2 Everett integration of (a) ascending branch of the limiting loop (b) descending branch of the limiting loop (c) descending branch of a minor loop where the term $Intg(S_k)$ stands for the integration of the PDF in the area with index k.

$$Intg(S_k) = \iint_{S_k} p_s(U) \cdot p_s(-V) \cdot \gamma(U,V) \cdot dUdV \tag{6.2}$$

Making use of the PDF's axial symmetry about the axis $U = -V$, or in other words $p_s(U) \cdot p_s(-V) = p_s(-V) \cdot p_s(U)$), the area integration of S_2 cancels that of the summation $(S_4 + S_5)$, so that equation (6.1) is reduced to

$$B_u(H) = Intg(S_1) - Intg(S_3) \tag{6.3}$$

Taking advantage of the same symmetry, $Intg(S_3)$ can be expressed as

$$Intg(S_3) = \left(\int_H^{\hat{H}_{100\%}} p_s(x)dx \right)^2 \tag{6.4}$$

We can denote the integration term inside the parenthesis as $F(H)$, that is

$$F(H) = \int_H^{\hat{H}_{100\%}} p_s(x)dx \tag{6.5}$$

If we also assume that the distribution function p_s is symmetrical about zero, $Intg(S_1)$ becomes

$$Intg(S_1) = 0.5 \cdot \left(\int_{-H}^{\hat{H}_{100\%}} p_s(x)dx - \int_H^{\hat{H}_{100\%}} p_s(x)dx \right)^2 = 0.5 \cdot \Big(F(-H) - F(H) \Big)^2 \tag{6.6}$$

Substituting equations (6.4) and (6.6) into (6.3), yields

$$B_u(H) = 0.5 \cdot \Big(F(-H) - F(H) \Big)^2 - F(H)^2 \tag{6.7}$$

On the descending branch of the limiting loop, the flux density $B_d(H)$ at the same field strength H (**Fig. 6.2b**) is given by equation (6.8). Again the signs "+" and "-" indicate that the corresponding area belongs to S_+ and S_- in equation 4.4.

$$B_d(H) = Intg(S_1) + Intg(S_2) + Intg(S_3) + Intg(S_4) - Intg(S_5) \tag{6.8}$$

Subtracting equation (6.8) from (6.1) and making use of the PDF's symmetry, results in

$$B_{\mathrm{u}}(H) - B_{\mathrm{d}}(H) = 2 \cdot (Intg(S_3) + Intg(S_4)) = 2 \cdot \int_{H}^{\hat{H}_{100\%}} p_{\mathrm{s}}(x)dx \cdot \int_{-H}^{\hat{H}_{100\%}} p_{\mathrm{s}}(x)dx = 2 \cdot F(H) \cdot F(-H) \quad (6.9)$$

Combing equation (6.7) and (6.9), $F(H)$ can be solved analytically as

$$F(H) = \frac{1}{\sqrt{2}} \cdot \sqrt{-B_{\mathrm{d}}(H) - B_{\mathrm{u}}(H) + \sqrt{2 \cdot B_{\mathrm{d}}(H)^2 + 2 \cdot B_{\mathrm{u}}(H)^2}} \quad (6.10)$$

With the expression of $F(H)$, the flux density on an arbitrary operating point on the $B - H$ plane can be calculated explicitly. Taking the minor loop initiated from the turning point $(H_{\updownarrow}, B_{\updownarrow})$ (see **Fig. 6.2c**) as an example, the flux density $B(H_1)$ on the descending branch at an arbitrary field strength H_1 is given by

$$B(H_1) = B_{\updownarrow} - 2 \cdot Intg(S_6) \quad (6.11)$$

where $B_{\updownarrow}$ is a known historic value (stored in the stack structure introduced in **Sec. 4.2**) while the integration term $Intg(S_6)$ can be obtained as follows: Using a similar formulation of equations (6.1) and (6.8), the flux density of the limiting loop's ascending branch at the field strength $H_{\updownarrow}$ is given by

$$B_{\mathrm{u}}(H_{\updownarrow}) = Intg(S_6) + Intg(S_7) - Intg(S_8) - Intg(S_9) \quad (6.12)$$

while the flux density of the limiting loop's descending branch at H_1 is given by

$$B_{\mathrm{d}}(H_1) = -Intg(S_6) + Intg(S_7) + Intg(S_8) - Intg(S_9) \quad (6.13)$$

Subtracting equation (6.13) from (6.12) yields

$$Intg(S_6) = 0.5 \cdot \Big(B_{\mathrm{u}}(H_{\updownarrow}) - B_{\mathrm{d}}(H_1)\Big) + Intg(S_8) = 0.5 \cdot \Big(B_{\mathrm{u}}(H_{\updownarrow}) - B_{\mathrm{d}}(H_1)\Big) + F(H_{\updownarrow}) \cdot F(-H_1) \quad (6.14)$$

Up to this stage, if we substitute the equation (6.14) into (6.11) and replace $F(H)$ by the expression of (6.10), the flux density at any arbitrary field strength H_1 with given historical turning point $(H_{\updownarrow}, B_{\updownarrow})$ can be explicitly calculated from the expression of $B_{\mathrm{u}}(H)$ and $B_{\mathrm{d}}(H)$. Please note that B_{d} is the mirrored function of B_{u} with respect to the origin of the $B - H$ plane. Therefore, only the expression for $B_{\mathrm{u}}(H)$ is needed, while $B_{\mathrm{d}}(H)$ can be replaced with

$$B_{\mathrm{d}}(H) = -B_{\mathrm{u}}(-H) \quad (6.15)$$

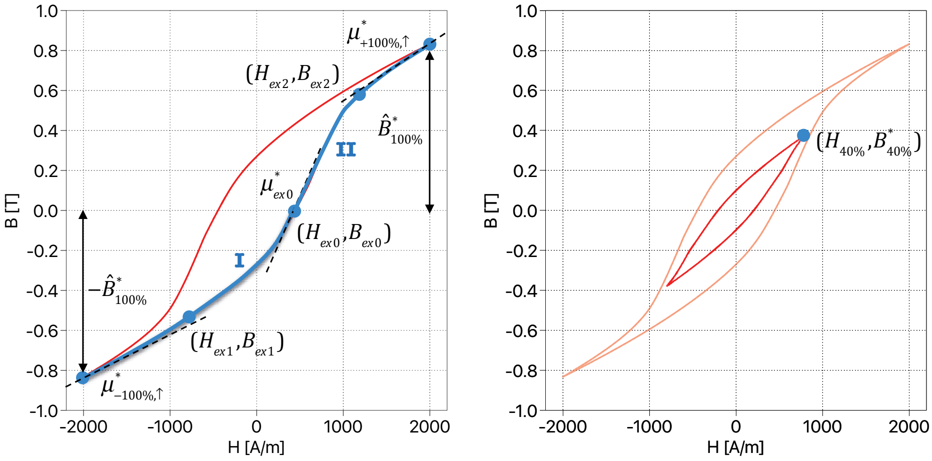

(a) **(b)**

Figure 6.3 (a) Splitting of the ascending branch into two parts. (b) Peak flux density of a 40% minor loop.

6.2.2 Realization and parametrization

An explicit expression of the ascending branch $B_\mathrm{u}(H)$ with sufficient degree of freedom is required. For this purpose, the ascending branch B_u is split into two parts at an additional point $(H_\mathrm{ex0}, B_\mathrm{ex0})$, denoted as part “I” (left hand side) and part “II” (right hand side), as demonstrated in **Fig. 6.3a**. The additional point (H_{ex0}, B_{ex0}) should be chosen as the one with the highest differential permeability on the ascending branch. Both parts are described using equation (4.13) from **Sec. 4.3** and shifted by $(H_\mathrm{ex}, B_\mathrm{ex})$ on the $B-H$ plane. The four parameters (H_1, F, D, α) of both parts are configured separately. For parametrization, six values are required to be extracted from the measured ascending branch of the limiting loop as marked in **Fig. 6.3a**:

- Peak flux density $\hat{B}^*_{100\%}$ (or $-\hat{B}^*_{100\%}$) at $\hat{H}_{100\%}$ (or $-\hat{H}_{100\%}$)
- Differential permeability $\mu^*_{+100\%,\uparrow}$ at the positive peak field strength $\hat{H}_{100\%}$
- Differential permeability $\mu^*_{-100\%,\uparrow}$ at the negative peak field strength $-\hat{H}_{100\%}$
- Differential permeability μ^*_{ex0} on the additional point (H_{ex0}, B_{ex0})
- Flux density B^*_ex1 at field strength $H_\mathrm{ex1} = 0.5 \cdot (H_\mathrm{ex0} - \hat{H}_{100\%})$
- Flux density B^*_ex2 at field strength $H_\mathrm{ex2} = 0.5 \cdot (H_\mathrm{ex0} + \hat{H}_{100\%})$

The parameters (H_1, F, D, α) of part I are fitted to reproduce the four measured values ($-\hat{B}^*_{100\%}$, $\mu^*_{-100\%,\uparrow}$, μ^*_{ex0}, B^*_ex1), following the same procedure introduced in the **Sec. 4.3** (for the reversible component), while those of part II are fitted to reproduce ($+\hat{B}^*_{100\%}$, $\mu^*_{+100\%,\uparrow}$, μ^*_{ex0}, B^*_ex2).

In order to adjust the peak flux density of minor loops, the model is also split into one irreversible and one reversible component. The reversible component is defined to be a linear function

$$B^\mathrm{rev}(H) = \mu_\mathrm{rev} \cdot H \tag{6.16}$$

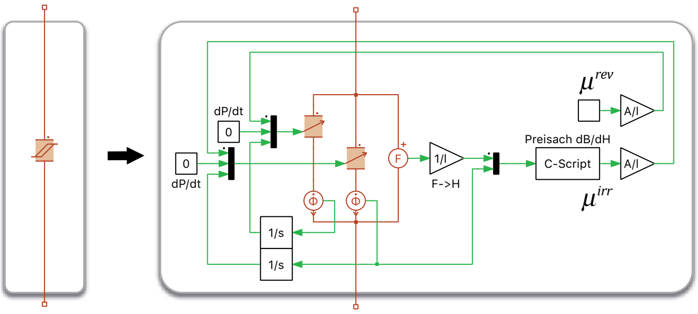

Figure 6.4 Model structure of the permeance block using proposed Preisach model for hysteresis loops with irregular shape.

The irreversible component of the ascending limiting loop is thus given as

$$B_{\mathrm{u}}^{\mathrm{irr}}(H) = B_{\mathrm{u}}(H) - B^{\mathrm{rev}}(H) \tag{6.17}$$

For the calculation of any minor loops inside the limiting hysteresis loop, $B_{\mathrm{u}}^{\mathrm{irr}}(H)$ instead of $B_{\mathrm{u}}(H)$ is applied to the formula defined by equation (6.11). The linear permeability μ_{rev} of the reversible component is adjusted to let the model's peak flux density of a symmetrical minor loop within the range $[-\hat{H}_{40\%}, +\hat{H}_{40\%}]$ equal to $\hat{B}^{*}_{40\%}$ from the measurement, as demonstrated in **Fig. 6.3b**. Please note that unlike the model for ferrite material proposed in **Sec. 4.3**, the per-cycle energy loss of the small minor loop is not explicitly controlled. The accuracy relies on the physics-based intrincity of the Preisach model, which is only guaranteed for minor loops with amplitude close to the limiting loop, e.g. the one with 40 % field strength amplitude.

During the simulation in a permeance-capacitance based magnetic circuit, the derivative of equation (6.11) with respect to the field strength should be calculated to obtain the instantaneous differential permeability, which is also an closed-form expression. The resulting model structure is demonstrated in **Fig. 6.4**.

6.3 Verification

The verification of the proposed model is carried out using the test setup introduced in **Chap. 3** operating in sinusoidal excitation mode. The circuit simulation model is established shown in **Fig. 6.5**, where the voltage source is controlled by the measured secondary voltage value multiplied with a factor N_1/N_2. In the first experiment, the amorphous material 2605SA1from Metglas is chosen, and the core sample with code "MP4010MDGC" is taken for parametrization and verification. The primary winding has $N_1 = 60$ turns and the secondary $N_2 = 30$ turns. The excitation frequency is configured as 50 Hz so that the frequency dependent effect is negligible. The large hysteresis loop with peak field strength $\hat{H}_{100\%} = 2000$ A/m is defined as the limiting loop. The additional point is chosen at $H_{\mathrm{ex0}} = 447$ A/m and $B_{\mathrm{ex0}} = 0$. The simulated $B - H$ characteristic of the hysteresis loops with peak field strength 100%, 70%, 40% of $\hat{H}_{100\%}$ and their corresponding time domain waveform are compared to the measurement in **Fig. 6.6a** and **Fig. 6.6b**, respectively. The proposed simulation model is able

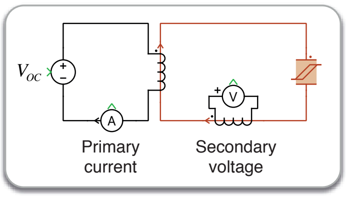

Figure 6.5 Circuit simulation model for verification emulating the test setup.

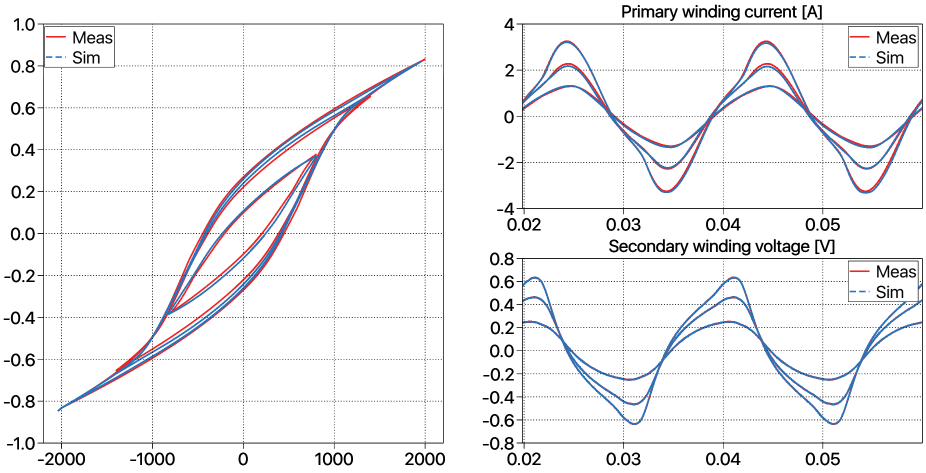

(a) **(b)**

Figure 6.6 Comparison between measurement and simulation of amorphous alloy 2605SA1 at different field strength amplitudes (a) Hysteresis loop (b) Time-domain primary winding current and secondary voltage

to reproduce the measurement with good accuracy, and the maximum error of the per-cycle energy loss is 13.5%.

In the second experiment, the nanocrystalline material Vitroperm 500F from Vacuumschmelze (VAC) is chosen and the toroidal core with code “160-W758” is taken as a sample. The turns numbers of the primary- and secondary winding are both 12. The large hysteresis loop with peak field strength $\hat{H}_{100\%}$ = 50 A/m is defined as the limiting loop. The additional point at H_{ex0} = 10 A/m and B_{ex0} = 0.2T is taken as the splitting point for piece-wise parametrization. The simulated $B - H$ characteristic and the time domain waveform are compared to measurement in **Fig. 6.7**. The nanocrystalline material 500F has quite good linearity on the $B - H$ characteristic in the range of interest, so that only slight harmonic distortion can be observed from the time domain primary winding current waveform. Also this material exhibits a significantly narrower hysteresis loop and thus leads to lower per-cycle energy loss, in comparison to the materials discussed before. The shape of the simulated hysteresis loop matches the measurement well. However, due to the extremely narrow hysteresis loop, the simulated per-cycle energy loss is very sensitive to the model parameters. The resulted maximum error of per-cycle energy loss among all simulated loops is 25%.

Please note that this proposed approach can be also applied to the materials (ferrite, silicon steel) discussed in the previous chapters. However, due to the relatively complex mathematical formulation, the simulation of the model requires significantly higher computational effort and thus leads to slower simulation speed in comparison to the regular classical Preisach representation using explicit PDF.

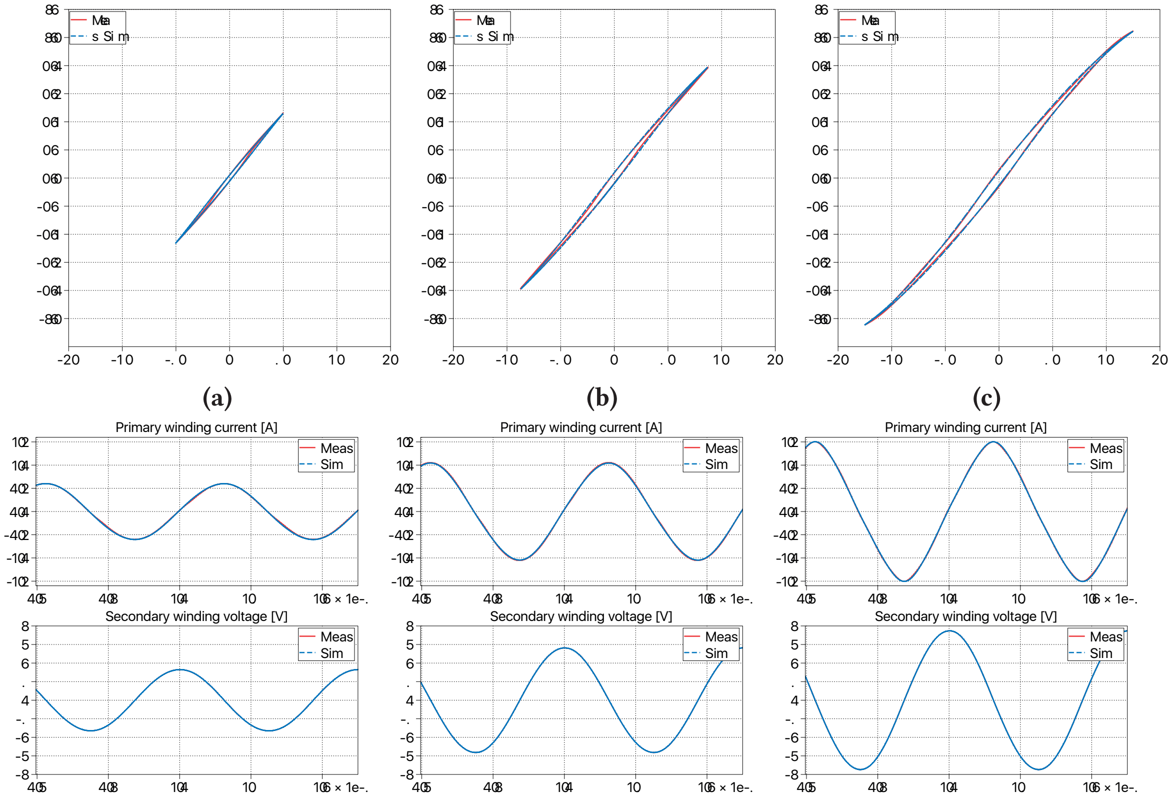

(a) (b) (c)

(d) (e) (f)

Figure 6.7 Comparison between measurement and simulation of nanocrystalline 500F at different field strength amplitudes: Hysteresis loop (a) with $\hat{H}_{100\%} = 20\,\mathrm{A/m}$; (b) with $\hat{H}_{70\%} = 35\,\mathrm{A/m}$; (c) with $\hat{H}_{100\%} = 50\,\mathrm{A/m}$ as well as time-domain primary winding current and secondary voltage for (d) with $\hat{H}_{100\%} = 20\,\mathrm{A/m}$; (e) with $\hat{H}_{70\%} = 35\,\mathrm{A/m}$; (f) with $\hat{H}_{100\%} = 50\,\mathrm{A/m}$

6.4 Summary

In this chapter, a variation of the classical Preisach model has been introduced to the permeance-capacitance based magnetic circuit. Using this approach, materials with irregular shape of $B - H$ characteristic, which can hardly be represented using an explicit formula of distribution function, can be modeled with good accuracy.

7

Model of relaxation effect for ferrite materials

The core loss of magnetic materials can be separated into three parts according to [14]:

- *Hysteresis loss: Frequency independent effect related to the material nonlinearity.*
- *Eddy current loss: Frequency dependent effect related to the material conductivity.*
- *Relaxation loss: Frequency dependent effect related to other physical mechanisms.*

Due to the low electrical conductivity, eddy currents which obviously occur in metal-based core materials (e.g. silicon steel) are negligible in ferrites, so that the core loss is dominated by the frequency independent hysteresis effect in most operating conditions of power converters. However, in high frequency (e.g. $> 20kHz$*) applications under certain modulation schemes, the core loss of ferrite materials do exhibit strong frequency and rate of change dependencies that cannot be ascribed to eddy currents but to the relaxation effect. This chapter proposes a model for the relaxation effect in permeance-capacitance based magnetic circuit.*

7.1 Literature review

In practice, the core loss is usually estimated using empirical formulas based on Steinmetz equation (SE), whose parameters are extracted from experimental measurements under sinusoidal excitation. The authors of [49] proposed an improved form of Steinmetz equation (iGSE) to generalize it to non-sinusoidal excitations, as is the case in power electronic applications. In the work of [50], the authors have observed that with phase-shift modulation (e.g. in the case of galvanically isolated type of DC-DC converters shown in **Fig. 7.1**) where a zero-voltage period is present, and with strongly asymmetrical PWM with duty-cycle far away from 50%, the core loss increases significantly in comparison to the case of 50% symmetrical PWM. In the aforementioned modulation schemes, the authors of [21] have demonstrated that the improved form proposed by [49] still significantly underestimates the core loss. Aiming to reduce the error, an additional term has been added to the iGSE, resulting in an improved-improved generalized Steinmetz equation (iiGSE). Alternatively, the approach based on the composite waveform hypothesis (CWH) proposed by [50] was further developed by [51]. Physically, this considerable relaxation loss under high switching frequency PWM excitation with a zero-voltage period or a strongly asymmetrical duty cycle, takes place if the thermal equilibrium of a magnetic system is suddenly altered by some external force and the reestablishment of a new thermal equilibrium happens progressively, as introduced in the work of [14]. More detailed analysis of the relaxation effect can be found in [52].

Although the continuously improved empirical equations proposed by the existing publications

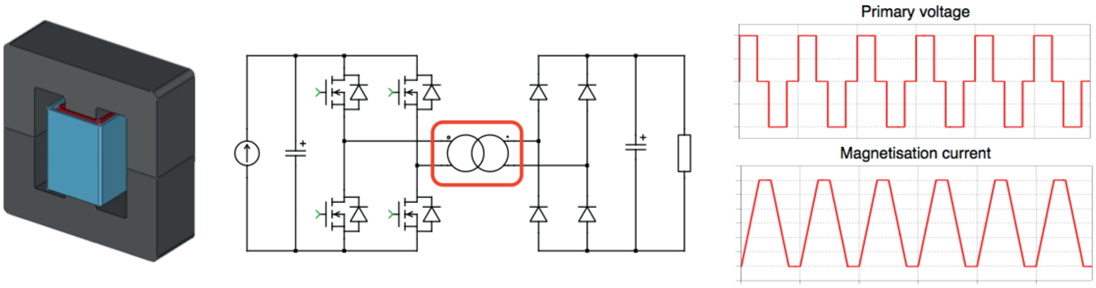

Figure 7.1 Isolation transformer in DC-DC converter with phase-shift modulation as well as the typical operational waveforms of primary voltage and magnetization current.

provide even better accuracy in core loss estimation, the physics behind are still obscure and unintuitive for power electronic engineers without a profound knowledge in the area of magnetics. To help engineers with understanding the physical interaction between the components and evaluating the dynamic behavior of the whole system, time-domain circuit simulation is commonly used in the design phase of power converters. The empirical equations, however, are difficult to incorporate in the circuit simulation environment. In order to reflect the core loss's impact on the dynamic behavior of the converter system, the authors of [53] managed to implement iGSE directly in a SPICE-type circuit simulator using a variable resistor, which yielded good accuracy in various operating conditions. However the loss mechanism still remains a black box having the same transparency level as the empirical equation, where all the three loss components (hysteresis, eddy current, relaxation) are mixed together.

To provide a clear insight into the loss mechanism, it is desired to handle the loss components separately in the simulation environment. Frequency independent hysteresis loss can be exclusively represented in time domain by a classical Preisach model in a flexible way [26]. In the work of [42] and [54], the classical Preisach model is extended in circuit simulations for the static hysteresis effect of ferrite materials, where good accuracy was achieved for various excitation amplitudes. Beside using the Preisach model for frequency independent hysteresis, the other two loss components - eddy current and residual effect are incorporated by the authors of [40] by introducing two resistive components. However the model was only verified under symmetrical PWM excitation without a zero-voltage period, where the relaxation loss hardly has a visible impact while the eddy current loss is intrinsically negligible in ferrite materials. The authors of [55] modeled the relaxation effect explicitly using a third-order circuit model, the similar model structure was also applied later by [56], while the frequency independent hysteresis effect was not taken into account and the model has been verified in the frequency domain rather than time domain.

Aiming to provide a model which is sufficiently accurate to capture the total core loss of ferrite materials, and is clear and intuitive in terms of the individual loss mechanism, the modeling approach proposed in this chapter differs from the existing publications in the following aspects:

- The frequency dependent relaxation effect is specifically modeled. An explicit way of parametrization from measurement results is presented.
- The frequency independent hysteresis effect is also individually covered using the Preisach model, and combined in the same circuit structure.

- The total core loss is physically present in the circuit model, while the mechanism of individual loss components (hysteresis, relaxation) can be investigated separately.

- The permeance-capacitor based magnetic circuit proposed by [16] and further adopted in **Chap. 4** is chosen as the fundamental platform, which has a seamless interface to electrical circuit. In the permeance magnetic circuit, the relaxation effect can be explained in a intuitive way. This will be presented in the following sections.

In **Sec. 7.2**, the experimental result of an operating condition, where both frequency independent hysteresis and frequency dependent relaxation effect are visible, is presented. In **Sec. 7.3**, referring to the experimental result, the fundamental model structure and physical origins of the frequency dependent relaxation effect is interpreted by means of a permeance-magnetic circuit, as a starting point for the modeling. The parametrization process of the proposed model for ferrite material as well as the required measurement data are introduced. In **Sec. 7.4**, the proposed model is verified by experimental tests with different ferrite materials under various operating conditions including switching frequency, duty cycle and zero-voltage period. A summary is provided in **Sec. 7.5**.

7.2 Experimental measurement

7.2.1 Measurement results

To demonstrate the impact of relaxation effect at high switching frequency excitation, comparative measurements have been carried out based on the ferrite material N87 from EPCOS, with the toroidal core of size code “R 20.0 x 10.0 x 7.00” chosen as sample. As temperature dependency is not in the scope of this chapter, all tests for parametrization and verification have been conducted under room temperature of 25°C.

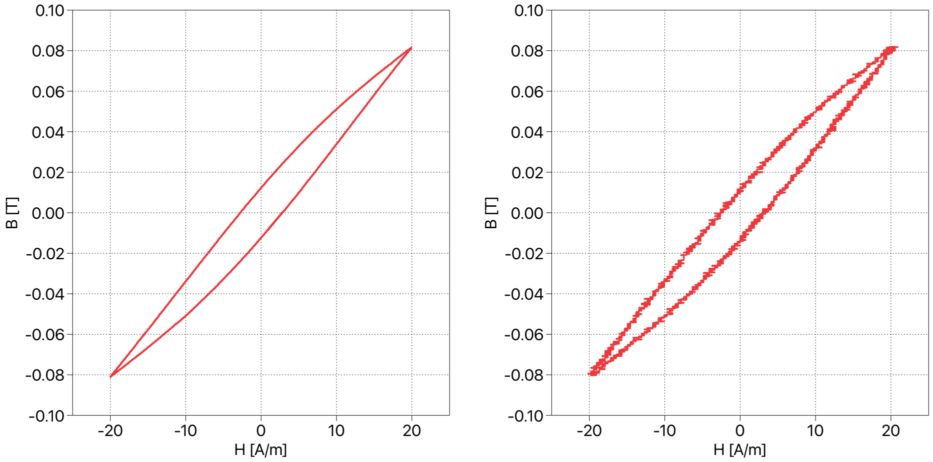

(a) (b)

Figure 7.2 Measured $B - H$ characteristic of ferrite N87 with peak strength $\hat{H} = 20\,\mathrm{A/m}$ excited by: (a) 500 Hz sinusoidal excitation; (b) 50 kHz symmetrical PWM excitation without zero voltage period.

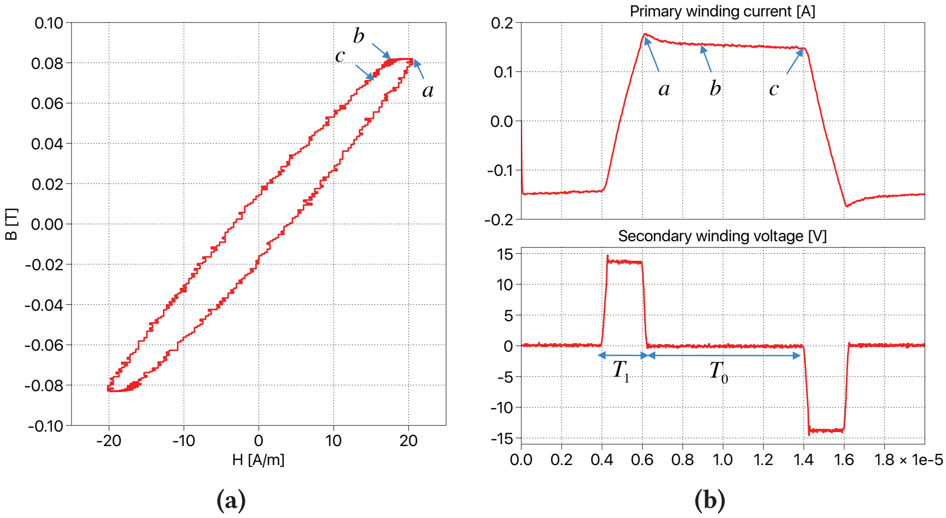

Figure 7.3 Measurement results of ferrite N87 (peak strength $\hat{H}$ = 20 A/m) excited by $50kHz$ symmetrical PWM excitation with zero voltage period of $T_0 = 8\mu s$ (a) $B - H$ characteristic (b) Primary winding current and secondary winding voltage

In the first experiment, the core sample is excited by the test setup proposed in **Chap. 3** operating in sinusoidal excitation mode, the frequency is configured as 500 Hz where the frequency dependent effect is negligible. The amplitude of V_1 is adjusted to generate a $B - H$ loop with a peak field strength $\hat{H}$ = 20 A/m, as shown in **Fig. 7.2a**. In the second experiment, the test setup is reconfigured to provide a 50 kHz symmetrical PWM excitation without zero-voltage period. The output of the voltage sources V_3 and V_4 are provided by the reference signal with the same amplitude but opposite polarity, which is adjusted to generate a $B - H$ loop with peak field strength $\hat{H}$ = 20 A/m, as shown in **Fig. 7.2b** (V_1 is tuned to ensure zero DC bias). Comparing **Fig. 7.2a** and **Fig. 7.2b**, only slight shape differences can be observed, while the per-cycle energy loss (indicated by the loop area) exhibits less than 10% difference. This indicates that the part of frequency independent core loss still dominates in this operating condition, although the switching frequency of 50 kHz is significantly higher than 500 Hz.

In the third experiment, the test setup is operated in phase-shifted PWM mode with a zero voltage period of duration $T_0 = 8\mu s$, the voltage output of V_3 and V_4 are adjusted to ensure that the peak amplitude is still equal to $\hat{H}$ = 20 A/m. The measured $B - H$ characteristic and the time domain primary current and secondary voltage are shown in **Fig. 7.3a** and **Fig. 7.3b**. In comparison to **Fig. 7.2**, a significant larger $B - H$ loop area can be observed especially close to the peak. The flat part between the points "a" and "b" arise from the relaxation effect, where the field strength decreases although nearly zero excitation is applied. This effect has also been observed in the work of [21]. According to the observed phenomenon, a basic model structure for the relaxation effect using permeance-capacitor based magnetic circuit is derived in the next section.

7.2.2 Discussion of measurement accuracy

During measurement and data post processing, one should pay attention to the influence of the phase error between current and voltage. The authors of [22] have explored that the percentage error of the core loss power can be expressed as:

$$\Delta_{\%} = \tan\left(\Phi_{\mathrm{v-i}}\right) \cdot \Delta\Phi \tag{7.1}$$

where $\Phi_{\mathrm{v-i}}$ is the absolute phase shift between the measured primary winding current and secondary winding voltage under sinusoidal excitation, while $\Delta\Phi$ is the error of the phase shift arising from the measurement system. Equation (7.1) indicates that, the closer to 90° is $\Phi_{\mathrm{v-i}}$, the more sensitive is the percentage error to $\Delta\Phi$. Different modifications on the measurement circuit structure have been proposed by the work of [57], [58] and [59], so as to drag $\Phi_{\mathrm{v-i}}$ away from 90° and thus decrease the sensitivity to $\Delta\Phi$. High excitation frequencies of several or tens of MHz were discussed. The frequency in this chapter (50 kHz), however, is far below that range. Considering that $\Delta\Phi$ is proportional to the excitation frequency [60], the influence of $\Delta\Phi$ is significantly lower in the frequency range of this work. Although with the suggested modifications the core loss power can be measured more accurately, the exact shape of the $B - H$ is no longer available, which, however, is necessary for the model parametrization as well as verification in this thesis. Therefore, the original circuit structure from [22] is continued to be used.

The influence of the phase error in the measurement at low frequency (500 Hz) sinusoidal excitation can be neglected. In the case of 50 kHz PWM excitation, phase error compensation has been applied during post processing. A phase error may exist in both voltage and current measurements:

- Voltage measurement: In the 50 kHz measurement, the large amplitude of the excitation voltage is sufficiently large, so the amplification stage is bypassed. The secondary winding is directly connected to the oscilloscope via shielded axial cable (V_{S} in **Fig. 7.4**), which has the same length as the one for the current measurement, so that the phase delay of the voltage measurement can be neglected.
- Current measurement: According to the datasheet of the ferrite material N87 [61], the per-volume core loss (25 C°) at frequency $f = 50$ kHz and peak-to-peak flux density $\Delta B = 200$ mT (amplitude 100 mT) is 54 kW/m^2, which corresponds to $P_{loss} = 0.08$ W loss power for the core "R 20.0 x 10.0 x 7.00" if multiplied by the core volume. The equivalent phase shift between voltage and current can be calculated as [60]:

  $$\Phi_{\mathrm{v-i}} = \arctan\left(\frac{\left(N_1 \cdot A \cdot 2\pi f \cdot \Delta B/2\sqrt{2}\right)^2}{P_{loss}} \cdot \frac{1}{2\pi f \cdot L}\right) = 84.6^{\circ} \tag{7.2}$$

  where $N_1 = 5$ is the primary winding turns number, A is the cross section area of the core and L the equivalent inductance calculated from the A_L value provided by the manufacturer datasheet [61].

  If we target on $\epsilon_{ph} = \pm 5\%$ phase error in equation (7.1), the allowed uncompensated phase error is ±0.272° at 50 kHz. The first source of the uncompensated phase error is the sample step size of the oscilloscope, which in our case is equal to 10 ns (0.18° for 50 kHz). The second source of the uncompensated phase error arise from the stray inductance of the shunt resistor. The manufacturer of the 0.1Ω shunt resistor [62] specifies that the stray inductance is typically

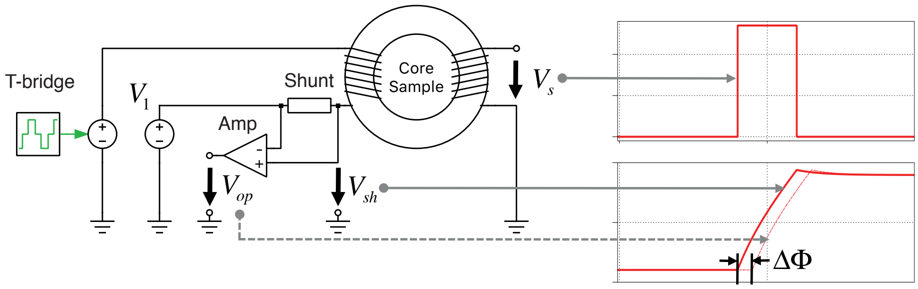

Figure 7.4 Phase error compensation of the differential amplifier output in the current measurement.

0.5 nH, which results in a phase angle of 0.09° at 50 kHz. The sum of the phase error of the oscilloscope and shunt resistor is within the criteria 0.272°.

The differential amplifier aims to filter out EMC noise and eliminate the DC voltage bias of the power amplifier V_1. The phase delay between the voltage drop on the shunt resistor and the differential amplifier's output can be explicitly compensated: As demonstrated in the simplified circuit schematic shown in **Fig. 7.4**, for each measurement, the voltage V_{sh} between the positive terminal of the shunt and ground (with DC bias of V_1) is connected to the oscilloscope using a coaxial cable with the same length as the differential amplifier output V_{op} (without DC bias of V_1). At the moment when the excitation voltage becomes positive from zero, the time difference between the turning point of V_{sh} and that of V_{op} is considered as the phase delay ΔΦ to be compensated (with the uncompensated phase error discussed before). During the data post processing to calculate core loss, the current measurement should be shifted by −ΔΦ. When measuring other materials and cores, compensation is applied in a similar manner.

Besides the phase error, the equipment accuracy also adds up to the measurement error, which can be found in the datasheet of the corresponding components and devices. The major contributions are:

- The shunt resistor has an error of $\epsilon_{sh} = \pm 0.5\,\%$.
- The chip resistor to configure the gain of the differential amplifier has $\epsilon_{amp} = 0.1\,\%$ error.
- The oscilloscope has a measurement error of $\epsilon_{osc} = \pm 2\,\%$.

Combining these three error sources and as well as the phase error together, the system measurement error is expected to be

$$\epsilon_{sys} = (1 + \epsilon_{sh}) \cdot (1 + \epsilon_{amp}) \cdot (1 + \epsilon_{osc}) \cdot (1 + \epsilon_{ph}) - 1 = \pm 7.7\,\% \tag{7.3}$$

7.3 Proposed model

7.3.1 Model behavior

The model for the frequency independent hysteresis effect introduced in **Chap. 4** is taken as a starting point for the modeling approach in this work. The equivalent electric-magnetic circuit of the test setup is shown in **Fig. 7.5a**, which includes the PWM excitation represented by a voltage source, the winding block as interface to the magnetic circuit (**Fig. 10.4**) and the permeance building block modeling the core sample. **Fig. 7.5b** shows the internal structure of the permeance block, which is able to represent a complete magnetic core of simple geometry or a single section of a core with complex geometry. Please note that in **Chap. 4** two variable permeance blocks accounting for irreversible and reversible magnetization are connected in parallel for illustration purpose. Here in this chapter they are structurally merged into one and the differential permeability of the irreversible- and reversible components are summed up as $\mathscr{P}_1(H)$. This is physically equivalent to that in **Chap. 4**.

After the parameters in the formula for calculating $\mathscr{P}_1(H)$ are completely identified using the experimental measurement at low frequency sinusoidal excitation, according to **Chap. 4**, the relaxation effect can be added. In a first step illustrated in **Fig. 7.6**, the permeance block $\mathscr{P}_1$ is split into two permeance blocks in parallel, namely $\mathscr{P}'_1$ and $\mathscr{P}_2$. In this step, it is assumed that the permeance $\mathscr{P}_2$ is constant. In a later **Sec. 7.4.3** a field strength dependent $\mathscr{P}_2$ is proposed to account for different amplitude of excitation.

$$\mathscr{P}'_1(H) = \mathscr{P}_1(H) - \mathscr{P}_2 \tag{7.4}$$

In a second step, a "magnetic" resistor R_m is connected to the branch of $\mathscr{P}_2$. Similar to the behaviour of a electrical resistor, the "magnetic" voltage drop (magneto-motive force MMF F) across R_m is equal to R_m multiplied by the "magnetic" current (flux changing rate $\dot{\Phi} = d\Phi/dt$), governed by the equation:

$$F = R_\mathrm{m} \cdot \dot{\Phi} \tag{7.5}$$

Please note that there is no magnetic resistor placed at the left hand side of the hysteresis permeance, which is present in the structure proposed by **Chap. 8** to account for the eddy current effect. This complies to the fact that we neglect the eddy current effect of ferrite materials, which has negligible contribution to the core loss compared to the relaxation effect and frequency independent hysteresis. It is emphasized that if sufficiently low frequency sinusoidal excitation is applied, R_m has negligible effect and the $B-H$ characteristic of the overall system is equal to that of the original $\mathscr{P}_1$ (since

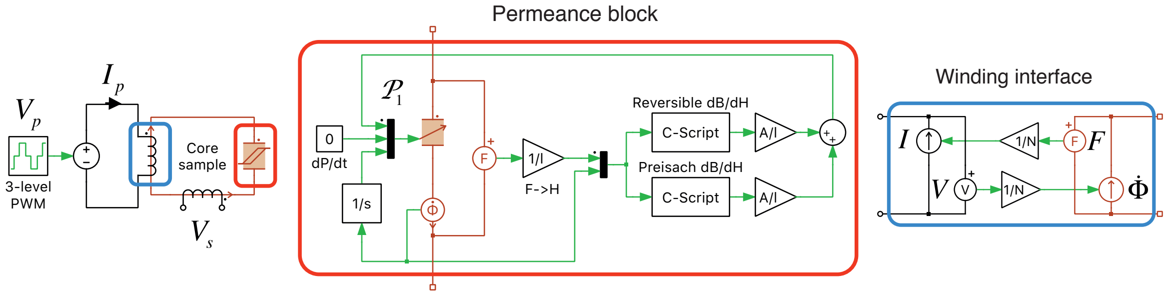

(a) **(b)** **(c)**

Figure 7.5 (a) Simplified model of the test setup including both electrical- and magnetic circuit; (b) Internal structure of the permeance block; (c) Winding interface using gyrator structure.

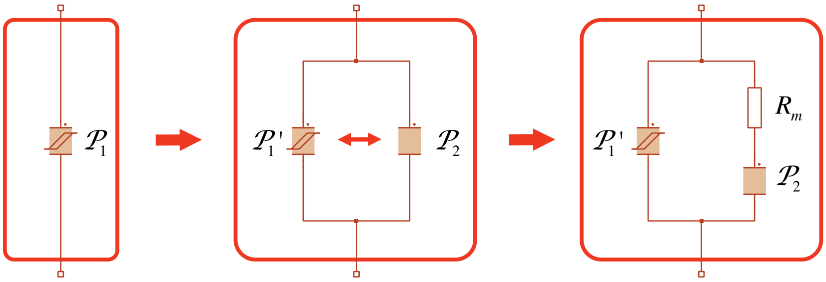

Figure 7.6 Modification of the original hysteresis permeance block to incorporate relaxation effect, where the permeance value of $\mathscr{P}_1'$ is provided by subtracting $\mathscr{P}_2$ from $\mathscr{P}_1$.

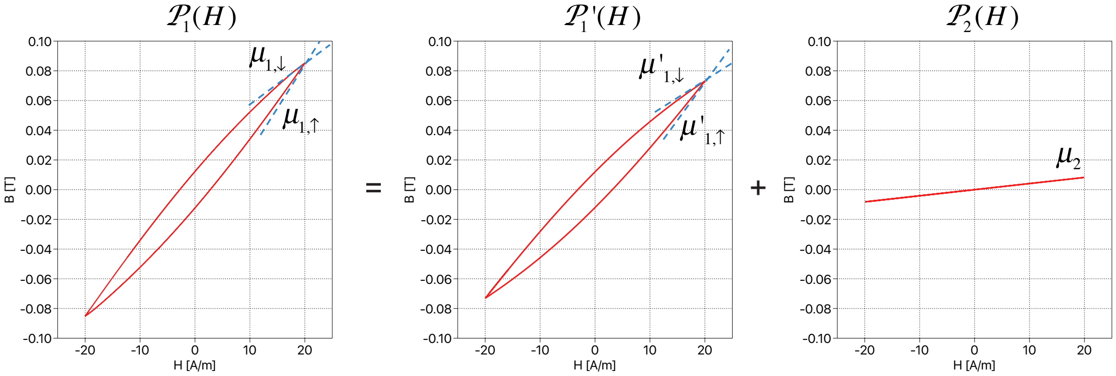

Figure 7.7 Summation of the $B-H$ characteristic of P_1' and P_2 under low frequency excitation

the summation of $\mathscr{P}_1'$ and $\mathscr{P}_2$ is equal to $\mathscr{P}_1$), as the symmetrical loops within the range $[-\hat{H}, +\hat{H}]$ in **Fig. 7.7** demonstrate. If the excitation is performed with high frequency PWM especially when including a zero voltage period, the relaxation effect taking place in reality can be covered by R_m. In the next step, the mechanism of magnetic relaxation is interpreted in the magnetic circuit. We still take the simplified circuit model of the test setup in **Fig. 7.5a** as an example, with the original permeance block proposed in **Chap. 4** extended to the new structure. The circuit resistance and winding resistance are neglected. The time area in which the external excitation (generated via switching the T-shape bridge) varies from positive to negative (including the zero voltage period in between) is analyzed, the DC voltages of V_3 and V_4 are assumed to be tuned (equal to $\pm V_\mathrm{in}$) so that the equivalent field strength is controlled in the range $[-\hat{H}, +\hat{H}]$:

- Period T_1: When the switch pair $Q_{11}\&Q_{12}$ is turned on, positive voltage $+V_\mathrm{in}$ is applied on the primary winding and the circuit current rises, as the interval T_1 in **Fig. 7.8b** demonstrates. In the permeance-capacitor based magnetic circuit, the voltage excitation is translated into a "magnetic" current source (flux rate $\dot{\Phi} = V_\mathrm{in}/N$), which charges the two permeance-capacitors $\mathscr{P}_1'$ and $\mathscr{P}_2$, as shown in **Fig. 7.9a**. The "magnetic" voltage (magneto-motive-force MMF, denoted as F_1) of permeance $\mathscr{P}_1'$ increases, which leads to increased equivalent field strength, as shown in **Fig. 7.8b** (rising interval T_1). The equivalent field strength looking from the excitation source is given by:

$$H = F_1/l \tag{7.6}$$

where l is the equivalent magnetic path length of the core. Under positive excitation, the MMF of $\mathscr{P}_2$ (denoted as F_2) also increases, however in a slower rate due to the existence of the resistor R_m. As a consequence, at the end of period T_1 (point a in **Fig. 7.8a**), $F_{2,0}$ is lower than $F_{1,0}$. The rising rate $\dot{F}_{1,0-} = dF_1/dt(0_-)$ directly before point a is given as

$$\dot{F}_{1,0-} = \frac{l}{(\mu_{1,\uparrow} - \mu_2) \cdot A} \cdot \left(\frac{V_\mathrm{in}}{N} - \frac{F_{1,0} - F_{2,0}}{R_\mathrm{m}}\right) \tag{7.7}$$

In the equation above, A is the cross section area of the core sample and N the primary winding's turns number. $\mu_{1,\uparrow}$ is the ascending permeability of the original frequency-independent model at the peak $H = \hat{H}$ (**Fig. 7.7**). The peak MMF ($F_{1,0}$) as well as the rising rate ($\dot{F}_{1,0-}$) can be determined from the peak primary winding current I_0 and its rising rate $\dot{I}_{0-}$ using the equation

$$F_{1,0} = I_0 \cdot \frac{l}{N}, \quad \dot{F}_{1,0-} = \dot{I}_{0-} \cdot \frac{l}{N} \tag{7.8}$$

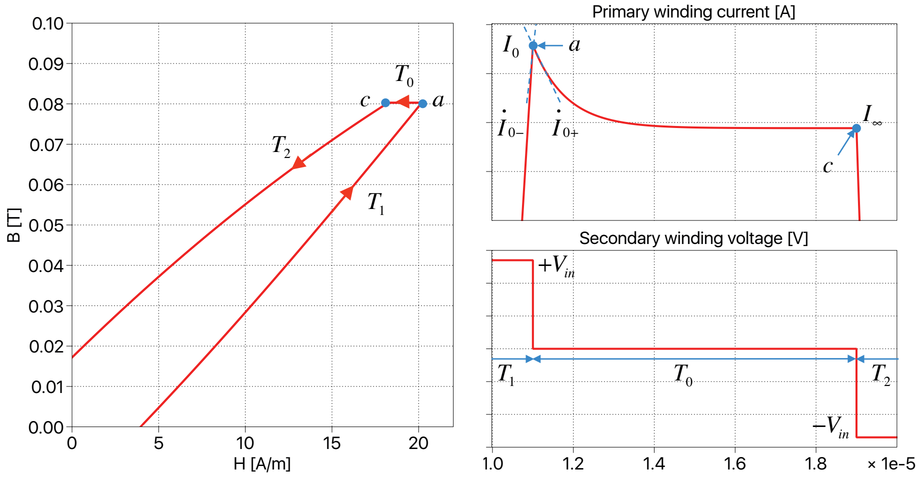

(a) **(b)**

Figure 7.8 Circuit behavior of the proposed model for reproducing the relaxation effect (a) $B-H$ characteristic including a flat part near the peak (from point a to c). (b) Time domain waveform with current descending rapidly at the beginning of the zero-voltage period.

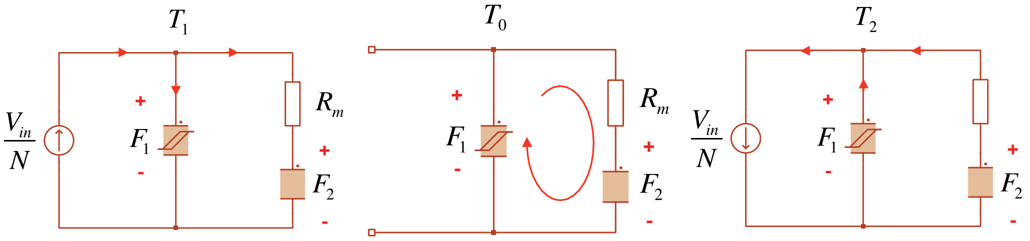

(a) **(b)** **(c)**

Figure 7.9 Equivalent circuit configuration (a) Pos. excitation (b) Zero voltage period (c) Neg. excitation

- Period T_0: After the switch pair $Q_{11}\&Q_{12}$ is turned off and $Q_{01}\&Q_{02}$ turned on, a zero voltage is applied to the primary winding. In the magnetic circuit, this situation corresponds to an open circuit on the winding side, as demonstrated in **Fig. 7.9b**. Starting from point a on, there is only a circulating "magnetic" current (flux rate) flowing in the loop composed of $\mathscr{P}'_1$ and $\mathscr{P}_2$. Due to the higher initial MMF on $\mathscr{P}'_1$, the circulating "magnetic" current charges $\mathscr{P}_2$ and discharges $\mathscr{P}'_1$, the initial value of the MMF's falling rate immediately after the zero-voltage period has started is given by:

  $$\dot{F}_{1,0+} = \dot{I}_{0+} \cdot \frac{l}{N} = \frac{l}{(\mu_{1,\downarrow} - \mu_2) \cdot A} \cdot \frac{F_{2,0} - F_{1,0}}{R_\mathrm{m}} \tag{7.9}$$

  $\mu_{1,\downarrow}$ is the descending permeability of the original frequency-independent model at the peak $H = \hat{H}$ (**Fig. 7.7**). Afterwards, on one hand, $\mathscr{P}'_1$ is discharged and F_1 goes down, which is reflected by the decreasing equivalent field strength in **Fig. 7.8a** (from point a to c). Since the flux rate on the external winding side is zero, the equivalent flux density remains unchanged. On the other hand, $\mathscr{P}_2$ is charged, and the MMF of both permeances gradually approach a common value. This behavior complies to the explanation of the relaxation effect provided in [14], that a new thermal equilibrium is gradually achieved where the system has minimum magnetic energy state (the magnetic energy stored in the permeance capacitors is reflected by the MMF). Please note that after the MMF of the two permeances are balanced, the total energy stored is lower than at the beginning of the zero-voltage period, and the energy difference is actually dissipated by the magnetic resistor Rm, which generates extra core loss. After sufficiently long time (e.g. point c in **Fig. 7.8**), following a law similar to series connected electrical capacitors, the balanced MMF F_∞ fullfills the relation below:

  $$\frac{\mu_2 \cdot A}{l} \cdot (F_{2,0} - F_{1,0}) = \frac{\mu_{1,\downarrow} \cdot A}{l} \cdot (F_\infty - F_{1,0}) \tag{7.10}$$

  F_∞ can be derived from the stabilized current I_∞ (denoted in **Fig. 7.8b**) as $F_\infty = I_\infty \cdot N/l$.

- Period T_2: Negative voltage appears on the primary winding when the switch pair $Q_{21}\&Q_{22}$ is turned on at point c in **Fig. 7.8b**. This corresponds to a flux rate source in the magnetic circuit flowing in opposite direction compared to that in the period T_1, as shown in **Fig. 7.9c**. From then on, both field strength and flux density decrease rapidly as shown in **Fig. 7.8a**. After this negative voltage period there is another zero-voltage interval T_0 coming and the situation is similar as discussed before, however with the relaxation effect observable at the negative peak $-\hat{H}$.

7.3.2 Parameter identification

Up to this stage, if we substitute the slopes $\dot{I}_{0-}$, $\dot{I}_{0-}$ and the peak current I_0, the stabilized current I_∞ with the corresponding values from the measurement results (e.g. that in **Fig. 7.3b**), and the permeability $\mu_{1,\downarrow}$ and $\mu_{1,\uparrow}$ with the measured values under low frequency sinusoidal excitation (with the same peak field strength), the equations (7.7), (7.9) and (7.10) can be solved for R_m, μ_2 and $F_{2,0}$. Thus all parameters of the extended model can be explicitly determined. With μ_2 and the geometry of the core sample, $\mathscr{P}_2$ is calculated as

$$\mathscr{P}_2 = \frac{\mu_2 \cdot A}{l} \tag{7.11}$$

The measurements for parameter identification must be made with the highest switching frequency and longest zero-voltage period of concern, where the relaxation effect can be observed. In the next section, it is proved that the parametrized model is able to reproduce the material's behavior at any lower switching frequency and shorter zero-voltage period.

Please note that in the real test setup, due to the circuit resistance the current is damped after the active interval of the relaxation effect rather than stabilized on a final value I_∞, as the part between point b and c in **Fig. 7.3b** indicates. The point in time b when the flux starts to decrease can be identified in the measured $B - H$ plot (in **Fig. 7.3a**), which indicates that the active period of the relaxation effect is over. In this case, the current at point b should be considered I_∞ for parameter identification.

7.4 Experimental verification

In this section, several verification schemes for the proposed model are carried out using the test setup introduced in **Chap. 3**. The ferrite material N87 is considered as the first study case with the toroidal core of shape code “R 20.0 x 10.0 x 7.00” as sample. The model is parametrized following the process from **Sec. 7.3.2**, which is composed of two steps:

- The parameters of the frequency independent effect (model proposed in **Chap. 4**) are identified using experimental measurement under sinusoidal excitation of $500Hz$, where frequency dependent effect is negligible.
- The parameters of the relaxation effect ($\mathscr{P}_2$ and R_m) are identified using experimental measurement under 50 kHz PWM excitation with 80% zero-voltage period, where the amplitudes of the DC sources are trimmed to obtain a peak field strength amplitude equal to $\hat{H} = 20\,\mathrm{A/m}$.

The circuit model is established in the system level simulation software PLECS complying to the test setup, with the structure shown in **Fig. 7.5a**. In order to exclude the influence of the circuit resistance of the test setup, the equivalent voltage source connected to the primary winding is fed with the measured secondary voltage multiplied by N_1/N_2, where $N_1 = N_2 = 5$ are the turns number of the primary and secondary winding.

7.4.1 Verification under PWM excitation with different zero-voltage period

In the first group of verification schemes, the fidelity of the proposed model is verified under $f_\mathrm{sw} = 50\,\mathrm{kHz}$ PWM excitation with different percentages of the zero-voltage period (80%, 60%, 20%), while the DC voltage sources are adjusted to maintain the equivalent peak field strength $\hat{H} = 20\,\text{A/m}$. As demonstrated in **Fig. 7.10**, with a decreasing percentage of the zero-voltage period, the flat part near the peak of the $B-H$ loops becomes narrower, which results in decreasing per-cycle energy loss (loop area) and indicates that the contribution from the relaxation effect is reduced. The proposed model is able to reproduce the hysteresis loop with good accuracy. If the corresponding core loss power are compared to measurement in **Fig. 7.11**, the error turns out to be under 5%. The presence of the relaxation effect is also clearly reflected on the time domain waveforms, where the primary winding current decreases rapidly after the zero-voltage period begins, as highlighted with dashed circles. In the simulation model, the frequency independent core loss (magnetic hysteresis loss) can be easily extracted by multiplying F and $\dot{\Phi}$ of the permeance $\mathscr{P}'_1$, integrating over one switching period and scaling by the switching frequency:

$$P_{\text{loss,hyst}} = f_{\text{sw}} \cdot \int_T F \cdot \dot{\Phi} \cdot dt \tag{7.12}$$

Subtracting the frequency independent part from the simulated total loss, the frequency dependent part associated with the relaxation effect can be directly obtained, as demonstrated in **Tab. 7.1**. With decreasing percentage of the zero-voltage period, the frequency dependent core loss is reduced, while the frequency independent one remains the same.

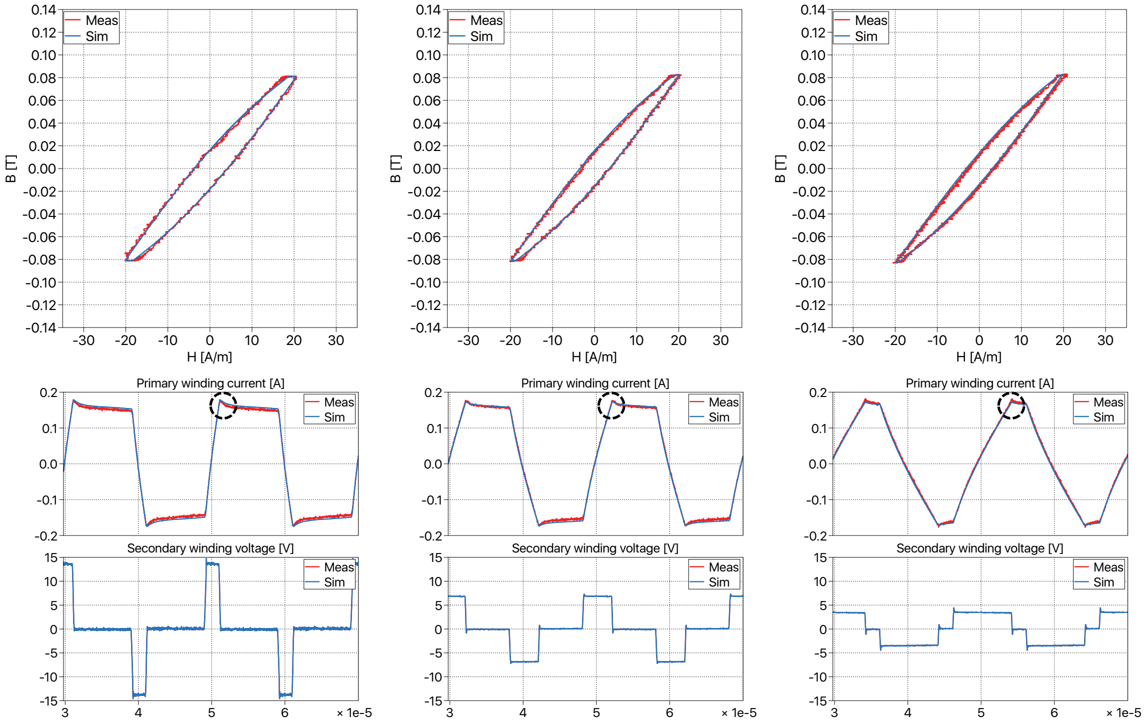

(a) **(b)** **(c)**

Figure 7.10 $B-H$ characteristic and time domain waveform comparison between measurement and simulation under 50 kHz PWM excitation with peak field strength $\hat{H} = 20\,\text{A/m}$ and different percentage of zero-voltage period T_0 (a) 80%; (b) 60%; (c) 20%.

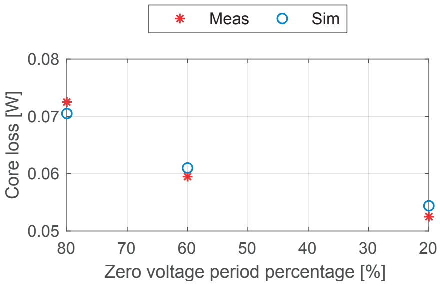

Figure 7.11 Core loss comparison between measurement and simulation under 50 kHz PWM excitation with peak field strength $\hat{H}$ = 20 A/m and different percentage of zero-voltage period T_0

Table 7.1 Loss splitting of the simulation model into frequency independent and dependent parts [W]

T_0 in percentage	80%	60%	20%
Total loss	0.071	0.061	0.054
f_{sw} independent loss	0.045	0.045	0.045
f_{sw} dependent loss	0.026	0.016	0.009

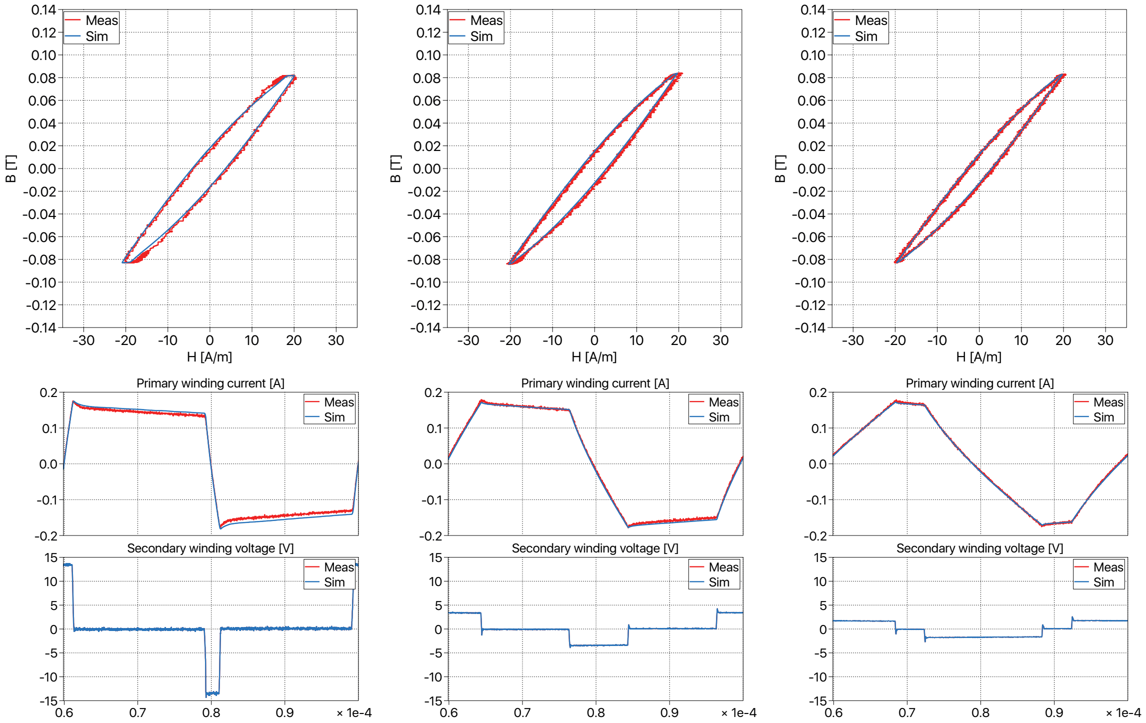

(a) **(b)** **(c)**

Figure 7.12 B–H characteristic and time domain waveform comparison between measurement and simulation under 25 kHz PWM excitation with peak field strength $\hat{H}$ = 20 A/m and different percentage of zero-voltage period T_0 (a) 90%; (b) 60%; (c) 20%.

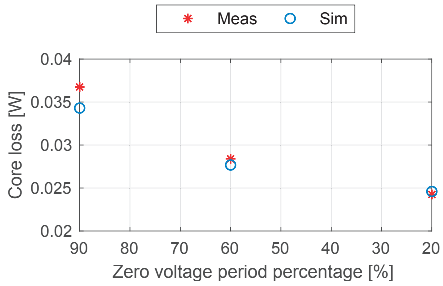

Figure 7.13 Core loss comparison between measurement and simulation under 25 kHz PWM excitation with peak field strength $\hat{H} = 20$ A/m and different percentage of zero-voltage period T_0

Afterwards, the frequency of the PWM excitation is reduced to 25 kHz, while the DC voltage sources are configured so that the equivalent peak field strength remains at $\hat{H} = 20$ A/m. The time domain simulation results from the same model with 90%, 60% and 20% zero-voltage period (longer than that in 50 kHz case) are compared to the measurement in **Fig. 7.12**, while the core loss powers are compared in **Fig. 7.13**. Good match is achieved here as well. One should notice that the hysteresis loop under 25 kHz excitation with 90% zero-voltage period has almost the same shape as that under 50 kHz excitation with 80% zero-voltage period, and the core loss power of the later is twice of the former. This relation indicates that the per-cycle energy losses are the same, which has also been observed by the authors of [21]. This can be ascribed to the fact that the amplitude and duration of the non-zero (positive or negative) voltage excitation are the same in these two cases. Both zero-voltage periods are long enough to find a new thermal equilibrium after the relaxation process (permeance capacitors fully recharged) and the same energy is dissipated.

7.4.2 Verification under PWM excitation with different duty cycle

In multiple existing publications, significantly larger core loss was reported under strongly asymmetrical PWM excitation than that with 50% duty-cycle, which can be ascribed to frequency dependent effect of ferrite materials. In the second group of verification schemes, 50 kHz PWM excitation with different duty cycles $d = 10\%, 20\%, 50\%$ (without zero-voltage period) is applied to the same core sample. The DC voltage sources are configured following the constraint $V_3 = (1 - d) \cdot V_4$, so that symmetrical hysteresis loop with equivalent peak field strength $\hat{H} = 20$ A/m can be obtained. The $B - H$ characteristic and time domain waveforms are compared between simulation result and experimental measurements in **Fig. 7.14**.

In comparison to the result under symmetrical PWM excitation shown in **Fig. 7.14c**, the top-right corner of the $B - H$ loop under 10% duty-cycle PWM in **Fig. 7.14a** is blunter, which adds up to the loop area. This phenomenon arises from the fact that the peak of the positive voltage (V_3) is significantly higher than the negative one (V_4). The situation at the positive-to-negative transition is similar to the positive-to-zero transition under PWM excitation with zero-voltage period, so that relaxation effect is considerably strong. In the case of symmetrical PWM excitation ($d = 50\%$) however, the material is demagnetized with the same rate as it is magnetized, so that relaxation effect has nearly no time to reestablish the new thermal equilibrium. Using the magnetic circuit in **Fig. 7.9**, this can be intuitively interpreted: Although $\mathscr{P}'_1$ is charged to higher F than $\mathscr{P}_2$ after the positive excitation, it is rapidly discharged afterwards and its F sinks towards that of $\mathscr{P}_2$ in such short time that very little energy can be dissipated on R_m. All the aforementioned phenomenons have been captured by the proposed model both qualitatively and quantitatively, good match has been obtained regarding the $B - H$ characteristic and time domain waveform shown in **Fig. 7.14** and the core loss shown in **Fig. 7.15**.

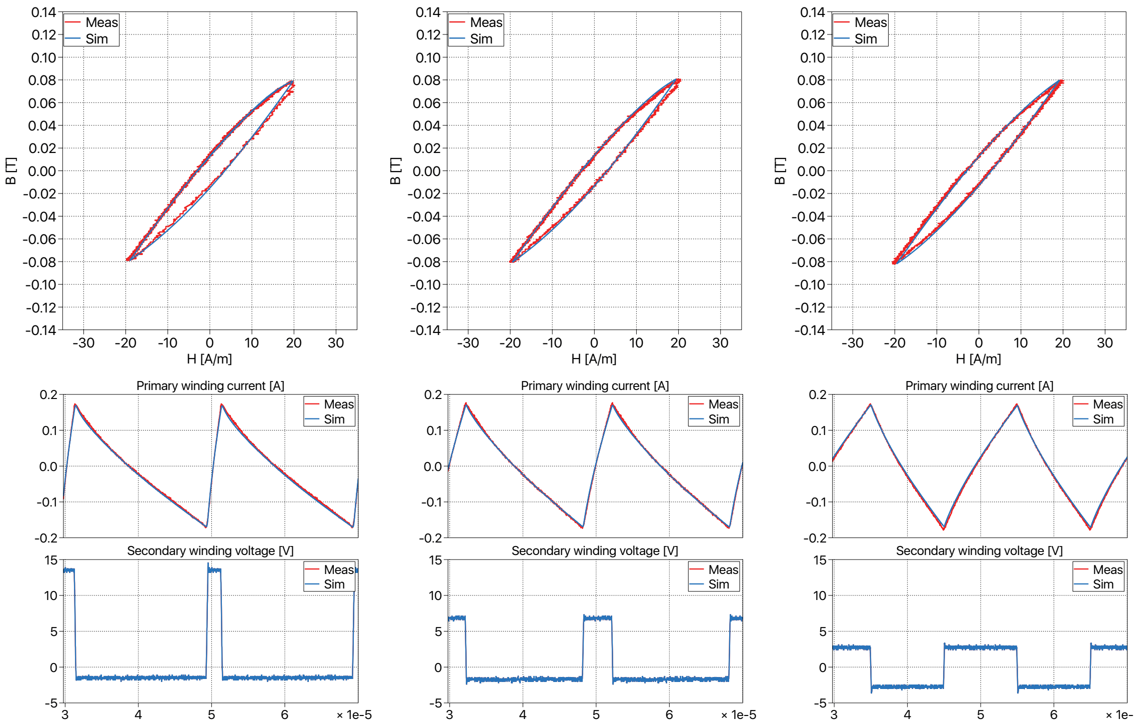

(a) **(b)** **(c)**

Figure 7.14 B–H characteristic and time domain waveform comparison between measurement and simulation under 50 kHz PWM excitation with peak field strength $\hat{H}$ = 20 A/m and different duty cycle (a) 10%; (b) 20%; (c) 50%.

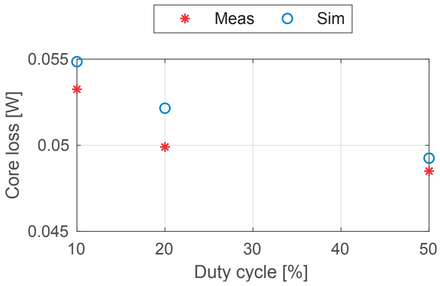

Figure 7.15 Core loss comparison between measurement and simulation under 50 kHz PWM excitation with peak field strength $\hat{H}$ = 20 A/m and different duty cycle

7.4.3 Verification under PWM excitation with a different amplitude

In the third group of verification schemes, the core sample is still excited by 50 kHz PWM excitation with inclusion of a zero-voltage period. The DC voltage sources are configured to generate $B-H$ loops with higher equivalent peak field strength $\hat{H} = 30$ A/m. In this case, the parameters of $\mathscr{P}_2$ and R_m are re-identified making use of the slopes $\dot{I}_{0+}$, $\dot{I}_{0-}$ (see **Fig. 7.8b**) and the currents I_0, I_∞ measured under 80% zero-voltage period as well as the permeability $\mu_{1,\downarrow}$ and $\mu_{1,\uparrow}$ measured under low frequency sinusoidal excitation, with equivalent peak field strength $\hat{H} = 30$ A/m. The simulated $B-H$ loops and the time domain waveforms with different zero-voltage period are compared to the experimental measurements in **Fig. 7.16**. The core loss power is compared in **Fig. 7.17**. Again the proposed model is able to achieve good accuracy.

In order to accommodate the model to arbitrary amplitude of excitation, $\mathscr{P}_2$ and R_m need to be realized as piecewise-linear variables with the value on the supporting points identified by $\dot{I}_{0+}$, $\dot{I}_{0-}$, I_∞, $\mu_{1,\downarrow}$ and $\mu_{1,\uparrow}$ measured under the corresponding amplitudes of excitation (with sufficiently long zero-voltage period). The modified structure of the model is demonstrated in **Fig. 7.18**. The piecewise-linear relation between the equivalent field strength on one side, and the permeance and magnetic resistor values on the other side, are included in the $f(u)$ function block, with the measured MMF of the permeance $\mathscr{P}_1'$ as input.

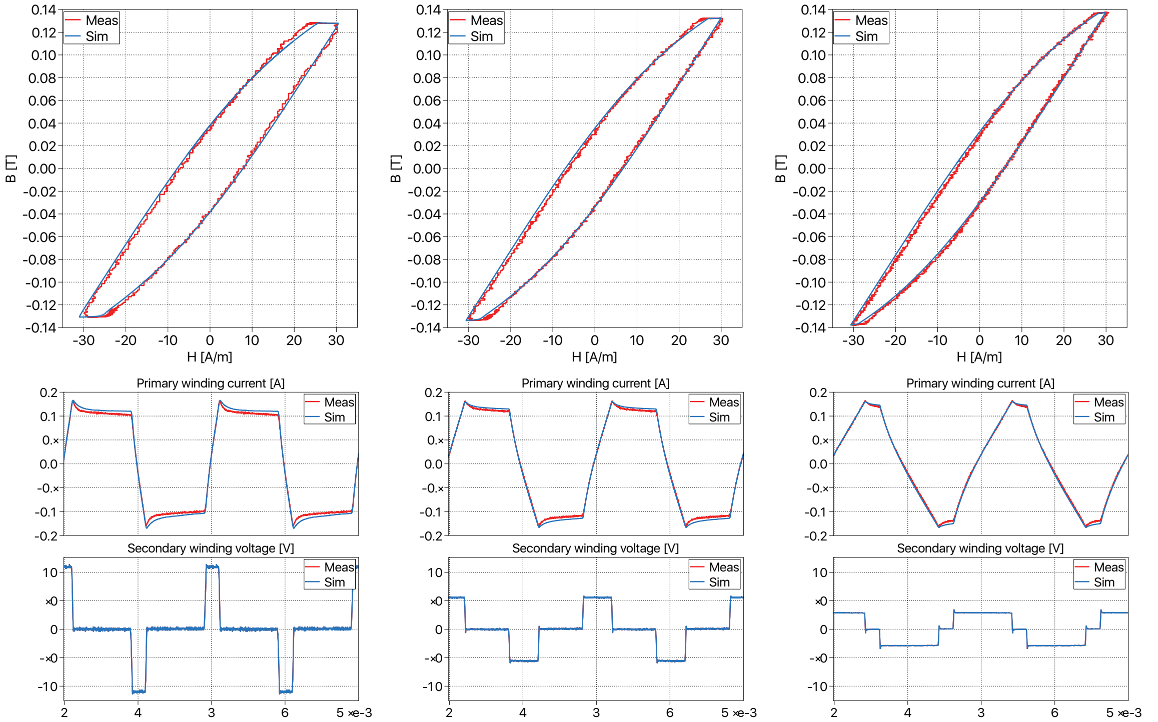

(a) (b) (c)

Figure 7.16 $B-H$ characteristic and time domain waveform comparison between measurement and simulation under 50 kHz PWM excitation with peak field strength $\hat{H} = 30$ A/m and different percentage of zero-voltage period T_0 (a) 80%; (b) 60%; (c) 20%.

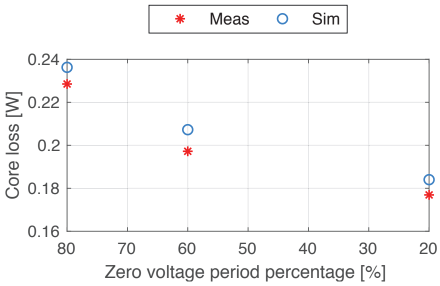

Figure 7.17 Core loss comparison between measurement and simulation under 50 kHz PWM excitation with peak field strength $\hat{H} = 30$ A/m and different percentage of zero-voltage period T_0

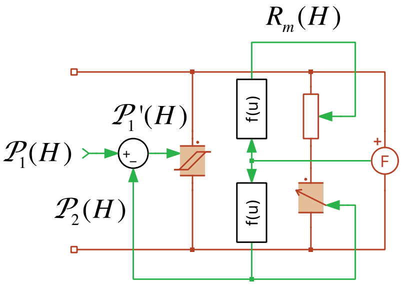

Figure 7.18 Piecewise-linear realization of $\mathscr{P}_2$ and R_m to accommodate arbitrary amplitudes of excitation

7.4.4 Verification under PWM excitation with DC offset

Using the model structure proposed in **Fig. 7.18**, an arbitrary hysteresis loop inside the field strength range $H \subset [-30, +30]$ A/m can be represented, even with DC bias. For verification, a differential component ΔV_dc is introduced into the voltage reference of the power amplifiers V_3 and V_4:

$$V_3 = V_\mathrm{dc} + \Delta V_\mathrm{dc}, \quad V_4 = V_\mathrm{dc} - \Delta V_\mathrm{dc} \tag{7.13}$$

Due to the existence of circuit resistance on the primary side, the differential component ΔV_dc is able to stabilize the hysteresis loop at desired field strength offset. Adjusting both V_dc and ΔV_dc, the biased hysteresis loop in the field strength range $H \subset [0, +30]$ A/m is obtained under different percentages of the zero-voltage period. The simulation result is compared to the measurement in **Fig. 7.19**, where the $B - H$ characteristic exhibits a slight asymmetry which is captured by the simulation model. The core loss comparison in **Fig. 7.20** also provides good match. The trend that with shorter zero voltage period, the core loss decreases, is also valid for the biased loop. Observable discrepancy of the loop shape is present in **Fig. 7.19c**, where the relaxation effect has minor impact and the frequency independent hysteresis loss dominates, due to the fact that the static hysteresis model is not particularly parametrized to account for biased loops. Thanks to the physics-based intrinsity of the Preisach model, acceptable accuracy of the biased loop is still achieved. If should be noted that the flux density of the biased loop depends on the historical pre-magnetization in reality, which cannot explicitly be measured in the existing test setup. Therefore, in the $B - H$ plots of **Fig. 7.19** the B range is displayed centred around zero (as integration of the secondary winding voltage).

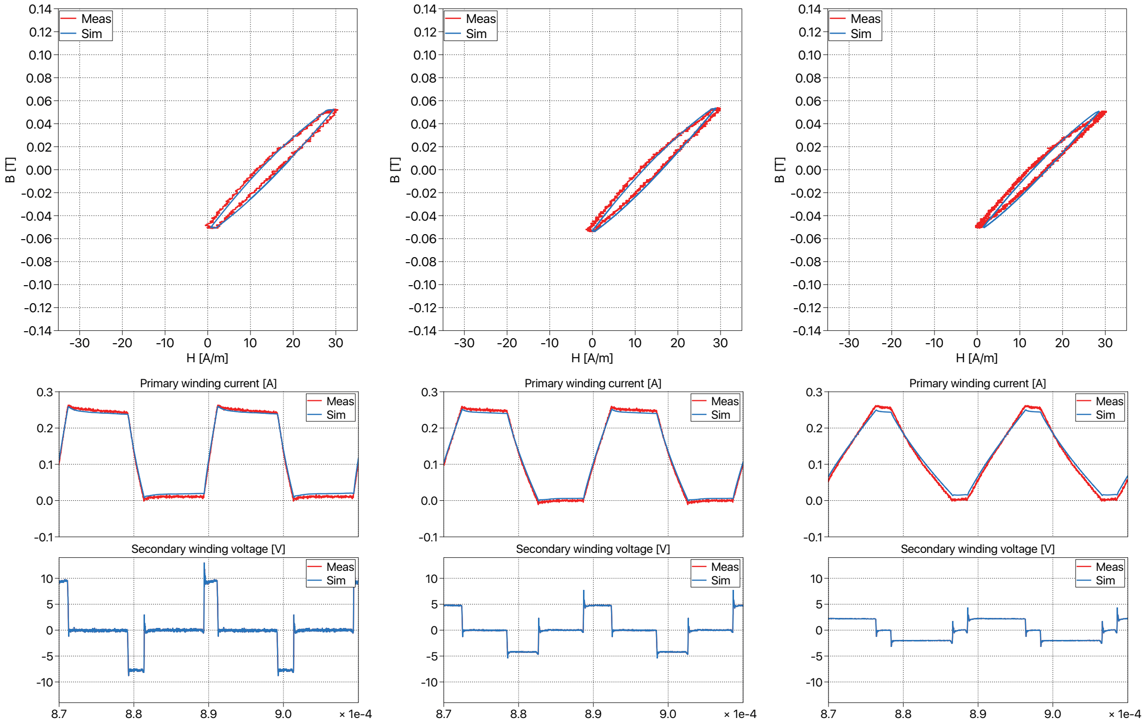

(a) **(b)** **(c)**

Figure 7.19 B–H characteristic and time domain waveform comparison between measurement and simulation under $50kHz$ PWM excitation with biased field strength range $H \subset [0, +30]$ A/m and different percentage of zero-voltage period T_0 (a) 80%; (b) 60%; (c) 20%.

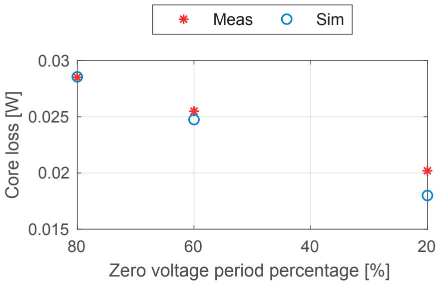

Figure 7.20 Core loss comparison between measurement and simulation under $50kHz$ PWM excitation with biased field strength range $H \subset [0, +30]$ A/m and different percentage of zero-voltage period T_0

7.4.5 Verification on core sample with different geometry

Once the parameters of the frequency-independent hysteresis and the frequency-dependent relaxation effect are identified using one core sample for certain ferrite material, the model can be easily extended to other geometries. Assuming that the core sample for parametrization has cross section area A_1 and equivalent magnetic path length l_1, the permeance $\mathscr{P}'_{1,(2)}$, $\mathscr{P}_{2,(2)}$ and magnetic resistor $\mathcal{R}_{\mathrm{m},(2)}$ of another core with another cross section area A_2 and another equivalent magnetic path length l_2 can

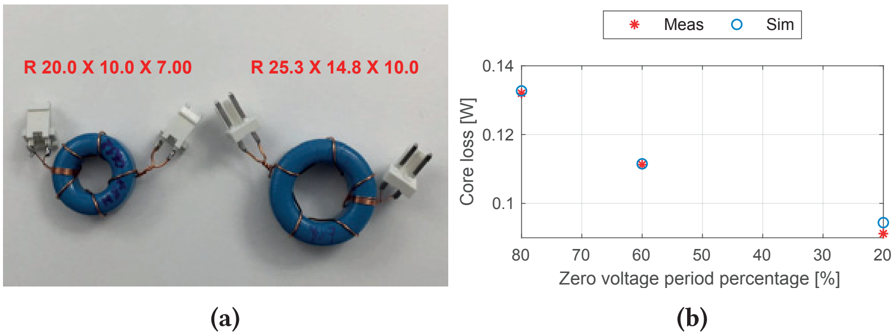

(a) **(b)**

Figure 7.21 (a) Core sample “R 25.3 x 14.8 x 10.0” and “R 20.0 x 10.0 x 7.00” of different geometries; (b) Core loss comparison between measurement and simulation under 50 kHz PWM excitation with peak field strength $\hat{H} = 20$ A/m and different percentage of zero-voltage period T_0, obtained from the core “R 25.3 x 14.8 x 10.0” and “R 20.0 x 10.0 x 7.00”.

be scaled from $\mathscr{P}'_{1,(1)}$, $\mathscr{P}_{2,(1)}$ and $R_{\mathrm{m},(1)}$:

$$\mathscr{P}'_{1,(2)} = \mathscr{P}'_{1,(1)} \cdot \frac{A_2}{A_1} \cdot \frac{l_1}{l_2} \tag{7.14}$$

$$\mathscr{P}_{2,(2)} = \mathscr{P}_{2,(1)} \cdot \frac{A_2}{A_1} \cdot \frac{l_1}{l_2} \tag{7.15}$$

$$R_{\mathrm{m},(2)} = R_{\mathrm{m},(2)} \cdot \frac{A_1}{A_2} \cdot \frac{l_2}{l_1} \tag{7.16}$$

The verification is carried out on the toroidal core with shape code “R 25.3 x 14.8 x 10.0”, the geometry difference compared to the previous core sample “R 20.0 x 10.0 x 7.00” is visible in **Fig. 7.21a**. PWM excitation of 50 kHz switching frequency and different zero-voltage period is applied, while the DC voltage sources are configured to obtain $\hat{H} = 20$ A/m peak equivalent field strength, which is similar to the case presented in **Sec. 7.4.1**. The comparison between simulated and measured core loss power are displayed in **Fig. 7.21b**, where only small errors exist. The scaling can also be applied to the model of a complex core, where separate parts of the core are represented by a circuit of multiple permeances.

The E-core with shape code “E 20/10/6” (product number “B66311G0000X187”) is taken as the next verification case as shown in **Fig. 7.22a**. The circuit is modeled in analogy to the real geometry, as shown in **Fig. 7.22b**. Each of the permeances $\mathscr{P}_{\mathrm{c}1}$ and $\mathscr{P}_{\mathrm{c}2}$ represents a single segment of the core, with the internal structure shown in **Fig. 7.18**. The equivalent geometrical parameters (cross section area and magnetic path length) are calculated following the formula proposed by [63]. All values $\mathscr{P}'_1$, $\mathscr{P}_2$ and R_m for the individual permeances are scaled by the geometry of the corresponding segment of the E-core from the parameters obtained previously for toroidal core with equations (7.14) ~ (7.16)).

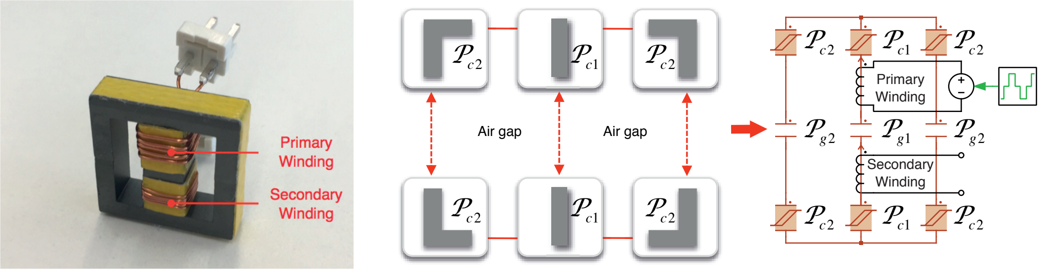

(a) **(b)**

Figure 7.22 (a) E-shape core sample "E 20/10/6"; (b) Simulation model with separate permeances representing middle-, side limbs as well as air gap of the core.

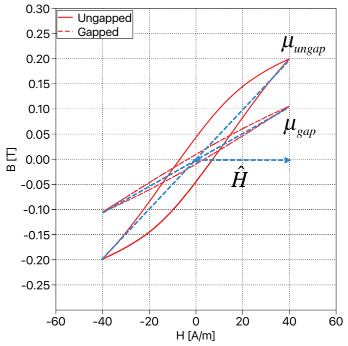

Figure 7.23 $B-H$ characteristic measured from toroidal core without air gap (peak flux density $\hat{B}_{\mathrm{ungap}}$) and E-core with tiny air gap (peak flux density $\hat{B}_{\mathrm{gap}}$), under 500 Hz sinusoidal excitation

Please note that there is no new experimental measurement needed for parametrization of the core pemeances $\mathscr{P}_{\mathrm{c1}}$ and $\mathscr{P}_{\mathrm{c2}}$ as they already include the core material characteristic.

Considering the accuracy limitation of the test setup for measuring gapped cores, where the phase shift $\Phi_{\mathrm{v-i}}$ becomes close to 90° resulting in extremely high $\tan\left(\Phi_{\mathrm{v-i}}\right)$ in equation (7.1), the two E-core parts are tightly pressed together. Nevertheless, tiny air gaps still exist in between, depending on the treatment of the joining surface during the manufacturing process. The length l_{g} of the tiny air gap between the two E-core parts is difficult to measure, but can be estimated using the measured frequency independent $B-H$ characteristic of the E-core and that of the toroidal core: The air gap results in a different shape of the static hysteresis loop obtained under 500 Hz sinusoidal excitation, in comparison to the toroidal core, as demonstrated in **Fig. 7.23**. With the same equivalent peak field strength $\hat{H} = 40$ A/m, the loops of the toroidal core and the E-core exhibit different equivalent permeability μ_{ungap} and μ_{gap} (slope of the virtual straight line connecting the two peaks). l_{g} can be calculated with the equations in below. Please note that the air gap has linear $B-H$ characteristic, so that the permeance obtained in the two equations above remains constant for different operating conditions.

$$l_{\mathrm{g}} = \frac{1}{2} \cdot \mu_0 \cdot l_e \cdot \left(\frac{1}{\mu_{\mathrm{gap}}} - \frac{1}{\mu_{\mathrm{ungap}}} \right) = 4.5\,\mu\mathrm{m} \tag{7.17}$$

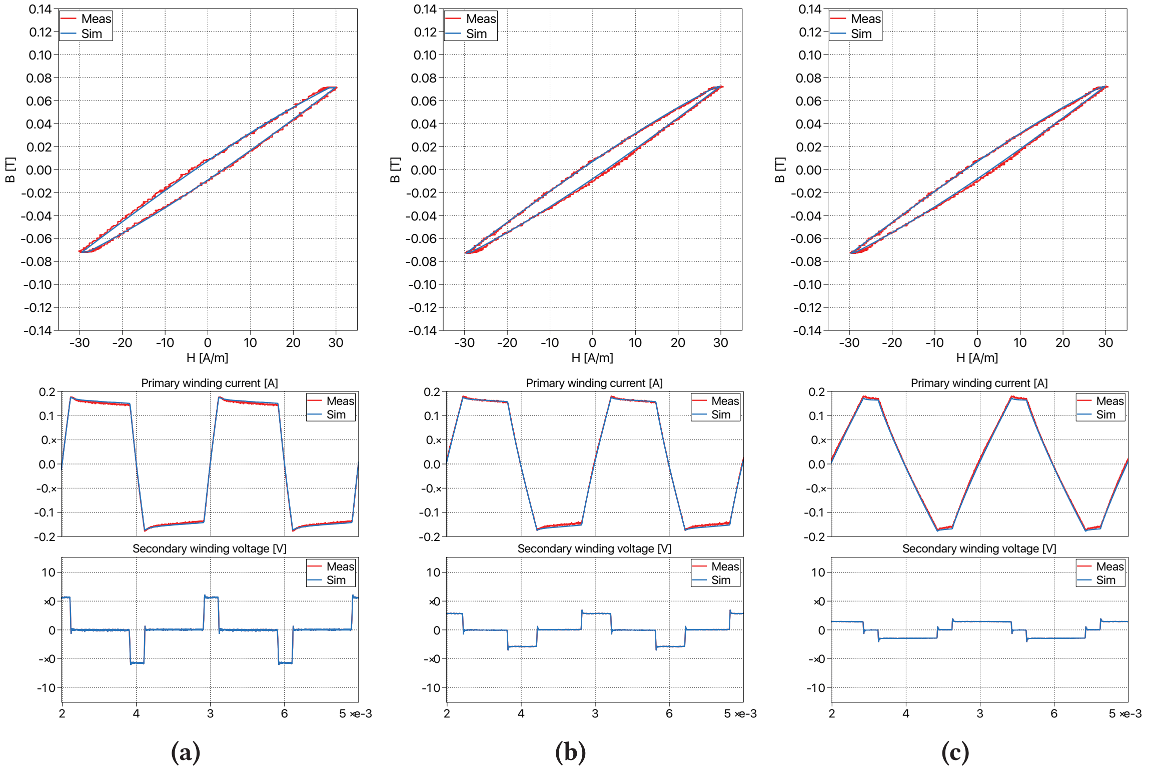

Figure 7.24 $B-H$ characteristic and time domain waveform comparison of E-core "E 20/10/6" between measurement and simulation under $50kHz$ PWM excitation with equivalent peak field strength $\hat{H} = 30A/m$ and different percentage of zero-voltage period T_0 (a) 80%; (b) 60%; (c) 20%.

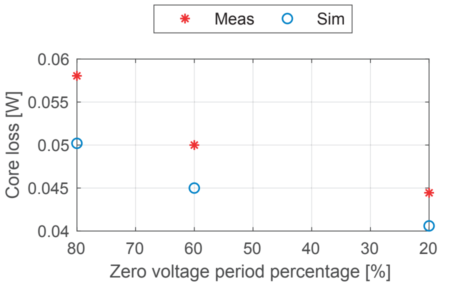

Figure 7.25 Core loss comparison of E-core "E 20/10/6" between measurement and simulation under $50kHz$ PWM excitation with equivalent peak field strength $\hat{H} = 30A/m$ and different percentage of zero-voltage period T_0

l_e is the equivalent magnetic path length of the E-core provided by the datasheet. In the circuit model shown in **Fig. 7.22b**, the air gap on the middle limb is represented by the constant permeance $\mathscr{P}_{\mathrm{g1}}$ and that on the side limbs by $\mathscr{P}_{\mathrm{g2}}$. Please note that $\mathscr{P}_{\mathrm{g1}}$ and $\mathscr{P}_{\mathrm{g2}}$ have the same length l_{g}, while the cross section area are configured to be the same as $\mathscr{P}_{\mathrm{c1}}$ and $\mathscr{P}_{\mathrm{c2}}$.

$$\mathscr{P}_{\mathrm{g1}} = \mu_0 \cdot \frac{A_{c1}}{l_{\mathrm{g}}}, \; \mathscr{P}_{\mathrm{g2}} = \mu_0 \cdot \frac{A_{c2}}{l_{\mathrm{g}}} \tag{7.18}$$

The verification is still carried out under PWM excitation with different durations of the zero-voltage period. The DC voltage output of V_3 and V_4 are configured to generated an unbiased $B-H$ loop with a peak field strength $\hat{H} = 30$ A/m. The time domain waveforms and the $B-H$ characteristic are compared between measurement and simulation in **Fig. 7.24**. Due to the presence of the tiny air gap, the $B-H$ characteristic has a smaller loop area and a less steep slope, in comparison to the toroidal core in **Fig. 7.16**. The influence of the zero-voltage period on the core loss is well reflected by the proposed model with maximum error of 13.5 %, as demonstrated in **Fig. 7.25**. The error is larger than in the case of the toroidal core presented in **Fig. 7.17**, which can be ascribed to the estimation error of the air gap length l_g.

7.4.6 Verification with core sample of different ferrite material

In the last group of verification schemes, the model is verified with another ferrite material N30 from EPCOS. The toroidal core with shape code "R 16.0 X 9.60 X 6.30" is taken as a sample. Again, 50 kHz PWM excitation with different zero-voltage periods is applied to the core sample, in which case the relaxation effect can be obviously observed. The model is parametrized using the measurement with 80% zero-voltage period and equivalent peak field strength $\hat{H} = 20$ A/m. The comparison between simulation and measurement regarding $B-H$ characteristic, time domain waveform and core loss

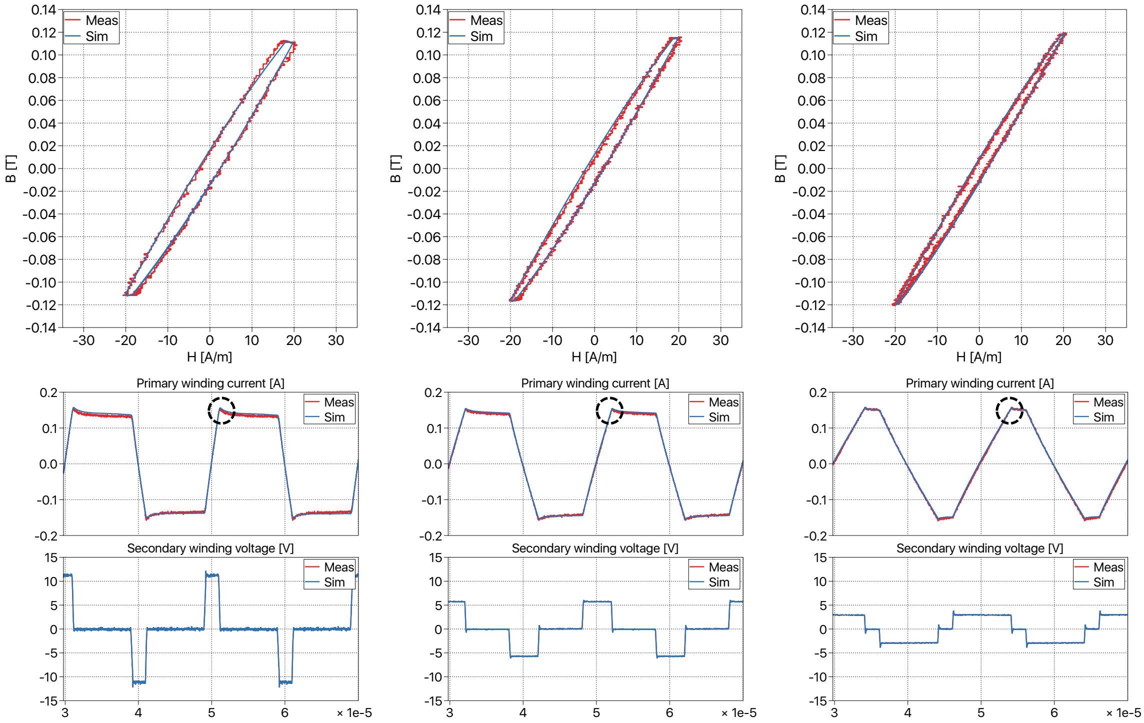

(a) (b) (c)

Figure 7.26 $B-H$ characteristic and time domain waveform comparison between measurement and simulation of ferrite material N30 under 50 kHz PWM excitation with peak field strength $\hat{H} = 20$ A/m and different percentage of zero-voltage period T_0 (a) 80%; (b) 60%; (c) 20%.

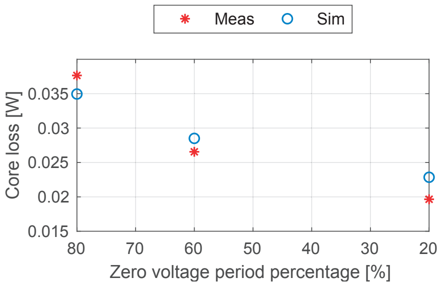

Figure 7.27 Core loss comparison between measurement and simulation of ferrite material N30 under 50 kHz PWM excitation with peak field strength $\hat{H} = 20$ A/m and different percentage of zero-voltage period T_0

power are presented in **Fig. 7.26** and **Fig. 7.27**. In comparison to the ferrite material N87, the $B - H$ loop of N30 exhibits a significantly different shape. Still, good match has been achieved with the proposed model.

7.5 Summary

This chapter proposes a modeling approach for frequency-dependent core loss of ferrite core materials that takes into account both the frequency-independent magnetic hysteresis and the frequency-dependent relaxation effect. The model can be seamlessly integrated into system-level circuit simulations, and can easily be extended for different geometries. The fidelity of the proposed model has been verified under PWM excitations of different switching frequencies, zero voltage-periods and duty-cycles. With the proposed model, power electronic designers are able to get intuitive insight into the magnetic core loss of magnetic components using ferrite materials in relation to the individual operating conditions. Based on the simulation result, improvement or optimization on the magnetic component itself or the power electronic circuitry can be carried out in an efficient way.

8

Model of eddy current for silicon steel

In silicon steel core material, magnetic hysteresis together with eddy currents contribute directly to the nonlinearity and the power loss of the magnetic component during operation. Due to the conductivity of the core material, eddy currents occur under alternating magnetization. In order to investigate their influence on the system behavior, and to adapt the control algorithm and component selection for the power converter, model is desired that is accurate and simple enough to be integrated into a system-level circuit simulation environment.

8.1 Literature review

Electrical equivalent circuit models have been commonly used for system-level simulations. The iron core is usually represented by the Cauer-type equivalent circuits as demonstrated in **Fig. 8.1** [64]. The inductors account for the magnetic flux channel while the resistors for the eddy current loss. Using the electrical equivalent circuit, authors of [65] were able to reproduce the analytical form of the core laminate's frequency response, with the material nonlinearity neglected. In the work of [66] and [67] the authors have taken into account the material nonlinearity and the method of [67] has been extended to a multi-winding structure in [68]. In [66], [67] and [68] the material characteristic is represented by a single-line nonlinear B-H curve, which does not include the power loss from the frequency-independent hysteresis effect of real magnetic materials. The authors of [69] and [40] have included the magnetic hysteresis into the circuit model. However, only a simple core geometry (toroidal core) was considered, which has not been generalized for complex core structures.

Magnetic circuits based on the permeance-capacitance analogy introduced by [16] are able to represent complex core geometries intuitively, and have been proved to be practical for system-level circuit simulation in the work of [23], [15] and [25]. The magnetic hysteresis of soft material can be accurately captured by the Preisach model, as discussed in chapters 4 ~ 6. Thanks to its gyrator structure to interface the electrical part of the model, the magnetic circuit can be simulated in its original form directly. Based on the permeance-capacitance magnetic circuit, the author of [70] has proposed a ladder structure for the eddy current effect, however the core material nonlinearity was not taken

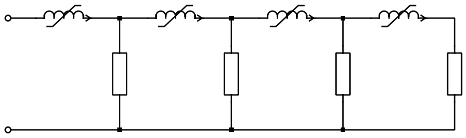

Figure 8.1 Cauer-type electrical equivalent circuits for iron cores including eddy current effect.

into account.

In this chapter, **Sec. 8.2** proposes a core model for time domain system-level simulations, which captures the magnetic hysteresis of the core material together with the eddy current effect. In **Sec. 8.3**, the model validity is verified experimentally under excitation of different amplitudes and frequencies.

8.2 Proposed model

Laminated silicon steel (SiFe) material is taken as a study case, because it has been widely used to construct iron cores like the one of the three-phase transformer shown in **Fig. 8.2a**. The modeling approach uses the magnetic structure shown in **Fig. 8.2b** as an example. The iron core is composed of K identical square laminates which are pressed together and are electrically isolated from each other. The cross section area of each laminate is A and the equivalent magnetic path length (centre line) is l. An electrical winding is bundled on one side of the core.

In order to derive the circuit model, the cross section of one laminate shown in **Fig. 8.3a** is virtually divided into several sub-laminates. In this thesis, considering the thickness of the laminate we were using, six sub-laminates provided a good balance between complexity and accuracy for the modeling purposes. In a linear case, [66] has explored that the error of equivalent impedance with six sub-laminations is below 15 %. It is assumed that the sub-laminates are non-conductive with magnetic fluxes $\Phi_1/2 \sim \Phi_3/2$ pointing perpendicularly to the cross section. Virtual conductive foils are placed around the sub-laminates to represent the conductivity of the core material, which can be modeled as short-circuit resistor loops ($R_1 \sim R_3$). If only one laminate is present ($K = 1$), the magnetic circuit model can be constructed as shown in **Fig. 8.3b**. Each of the three permeances $\mathscr{P}_1 \sim \mathscr{P}_3$ represent one pair of the non-conductive sub-laminates, through which the fluxes $\Phi_1 \sim \Phi_3$ are flowing. $R_1 \sim R_3$ in the electrical circuit correspond to the virtual resistor loops in **Fig. 8.3a**, which are connected to the magnetic circuit via winding block (with turns number $N = 1$) using a gyrator structure. The winding block on the very left of **Fig. 8.3b** represents the real electrical coil.

Geometrically one can assume that all sub-laminates have the same thickness. However recognizing that the flux becomes confined to an increasingly thinner layer near the lamination surface as the

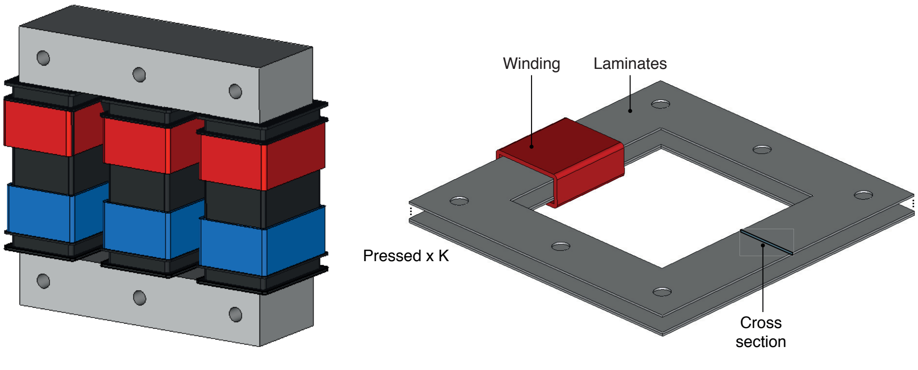

(a) (b)

Figure 8.2 (a) Three-phase transformer using laminated silicon steel; (b) Magnetic structure taken as example for demonstration with pressed laminates and one winding.

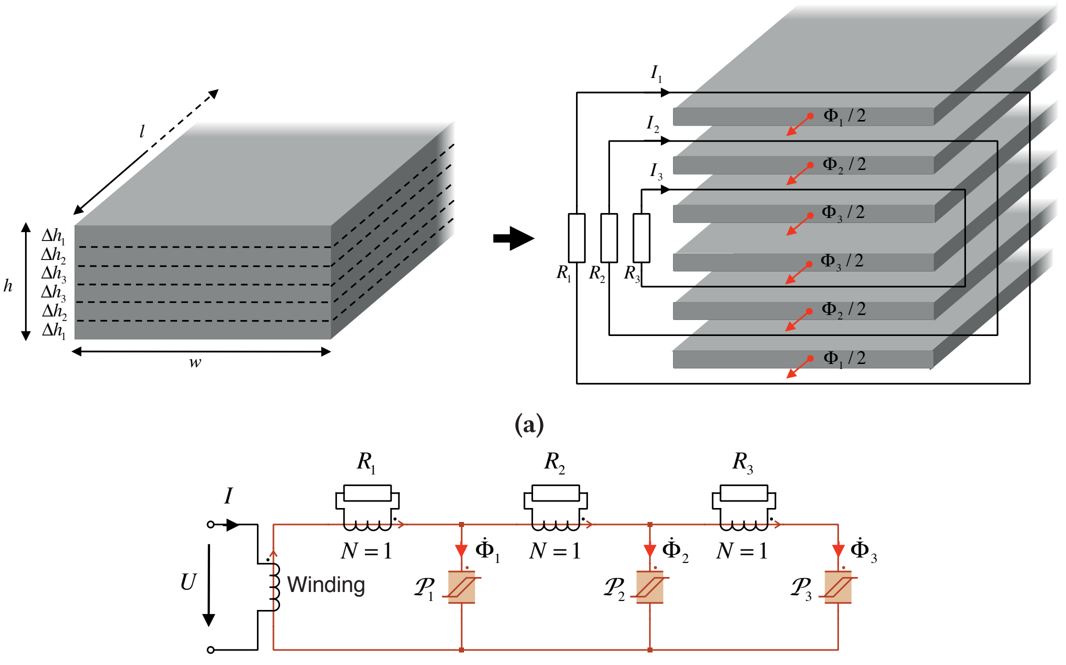

(a)

(b)

Figure 8.3 (a) Cross section of one single laminate virtually divided into non-conductive sub-laminates and resistor loops; (b) Magnetic circuit of one single laminate with three permeances and resistor loops.

frequency increases, nonuniform division proposed by the authors of [66] is adopted in this thesis. The thickness of the sub-laminates is doubled progressively from the surface to the centre of the lamination, that is:

$$\Delta h_{\mathrm{k-1}} = 2 \cdot \Delta h_{\mathrm{k}} \tag{8.1}$$

while the summation of all h_{k} should be equal to the thickness h of the original lamination.

$$\sum \Delta h_{\mathrm{k}} = h \tag{8.2}$$

The nonlinear permeances are modeled following the approach introduced in **Chap. 5**, the nonlinear permeances depending on field strength H are provided as the summation of an irreversible component $\mathscr{P}_{\mathrm{k}}^{irr}$ (using the product Preisach model) and a reversible component $\mathscr{P}_{\mathrm{k}}^{rev}$, scaled by the geometrical parameters of the individual sub-laminates (Δh_{k}, w and l in **Fig. 8.3a**).

$$\mathscr{P}_{\mathrm{k}}(H) = \mathscr{P}_{\mathrm{k}}^{irr} + \mathscr{P}_{\mathrm{k}}^{rev} = \left(\mu^{irr} + \mu^{rev}\right) \cdot \frac{2\Delta h_{\mathrm{k}} w}{l} \tag{8.3}$$

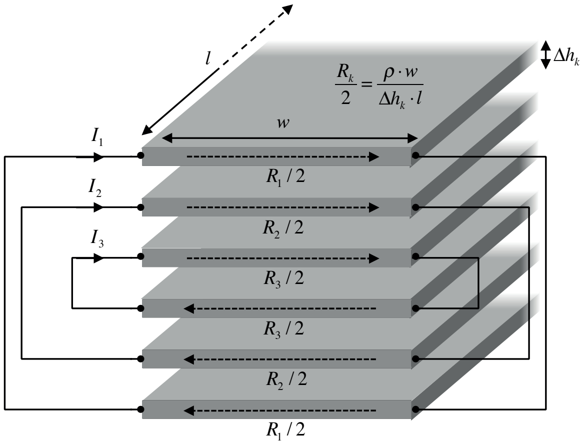

Figure 8.4 Equivalent resistance of the sub-laminates

Please note that the factor 2 in the equation indicates that the permeance in each section of the magnetic circuit includes two sub-laminates. The resistors $R_1 \sim R_3$ are calculated based on the sub-laminates' geometry:

$$R_\mathrm{k} = \frac{2 \cdot \rho \cdot w}{\Delta h_\mathrm{k} \cdot l} \tag{8.4}$$

where ρ is the material's resistivity, which can be obtained from the datasheet from the material manufacturer. Equation (8.4) essentially calculates the equivalent resistance along the horizontal direction using the sub-laminates' geometry with non-zero conductivity, and the factor 2 indicates that the two sub-laminates in the same section are connected in series, as demonstrated in **Fig. 8.4**.

If two or more laminates are pressed together, the circuit model becomes a parallel connection of K times the circuit shown in **Fig. 8.3b**. Merging the parallel items together yields the same structure as in **Fig. 8.3b**, while the thickness Δh_k in equation (4.3) and the resistance R_k should be multiplied by K.

8.3 Experimental verification

For validation of the proposed modeling approach, the test setup from **Chap. 3** is used and the same core sample as in **Chap. 5** (**Fig. 5.6a**) is adopted.

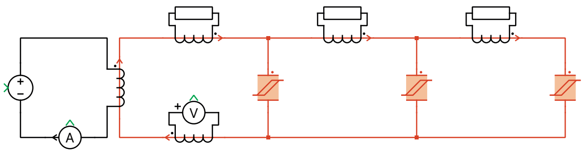

Figure 8.5 Simulation model of the test setup using the proposed approach

The frequency independent permeance model is parametrized following the scheme introduced in **Sec. 5.2**. After that the resistance values R_k in **Fig. 8.3b** are calculated using the equations (8.1), (8.2) and (8.4). Please note that the parameters determined in this stage will remain the same for the verification.

The simulation model established in the system level simulation software PLECS includes the core sample using the proposed magnetic circuit as shown in **Fig. 8.5**. A controlled voltage source is controlled with the measured secondary voltage value multiplied by the factor N_1/N_2. This corresponds to the excitation voltage on the primary winding with the resistive voltage drop on the winding and circuit resistance excluded. All components are configured to be the same as the test bench hardware in each of the following schemes.

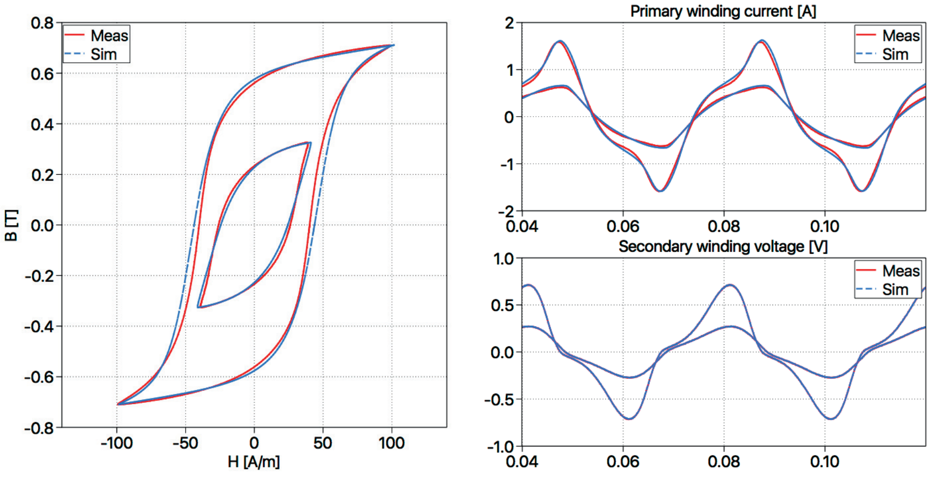

(a) **(b)**

Figure 8.6 Comparison between measurement and simulation under 25Hz sinusoidal excitation with different amplitudes (a) $B-H$ loops; (b) Time domain waveforms.

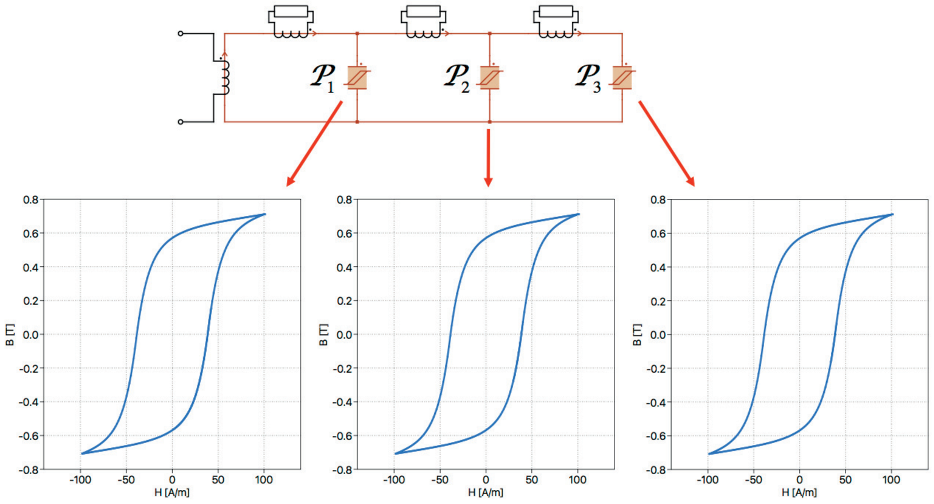

Figure 8.7 Static $B-H$ characteristic of the permeance blocks under 25 Hz sinusoidal excitation (with equivalent peak field strength 100 A/m)

The verification is firstly carried out with low frequency sinusoidal excitation of 25 Hz. In **Fig. 8.6** the simulated B-H loops of different amplitudes as well as the corresponding primary winding current and secondary winding voltage are compared to the measurement. The simulation model is able to accurately reproduce the distorted time domain waveform which reflects the influence of the material's hysteresis nonlinearity. The power loss is calculated via integrating the product of the primary current and the secondary voltage, then average it for one AC period. The maximum error of the simulation results is 3%. In the test case with the equivalent peak field strength 100 A/m, the $B-H$ characteristic of the three permeance blocks $\mathscr{P}_1 \sim \mathscr{P}_3$ are shown in **Fig. 8.7**. They represent the non-conductive sub-laminates depicted in **Fig. 8.3a**. Their nearly identical $B-H$ loops indicates that the flux is homogeneously distributed on the cross-section area of the laminates under low frequency excitation.

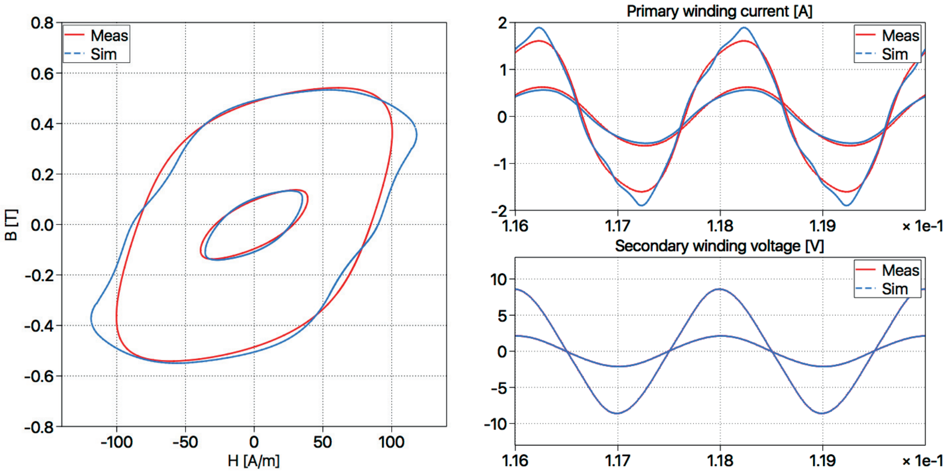

(a) **(b)**

Figure 8.8 Comparison between measurement and simulation under 500 Hz sinusoidal excitation with different amplitudes (a) $B-H$ loops; (b) Time domain waveforms.

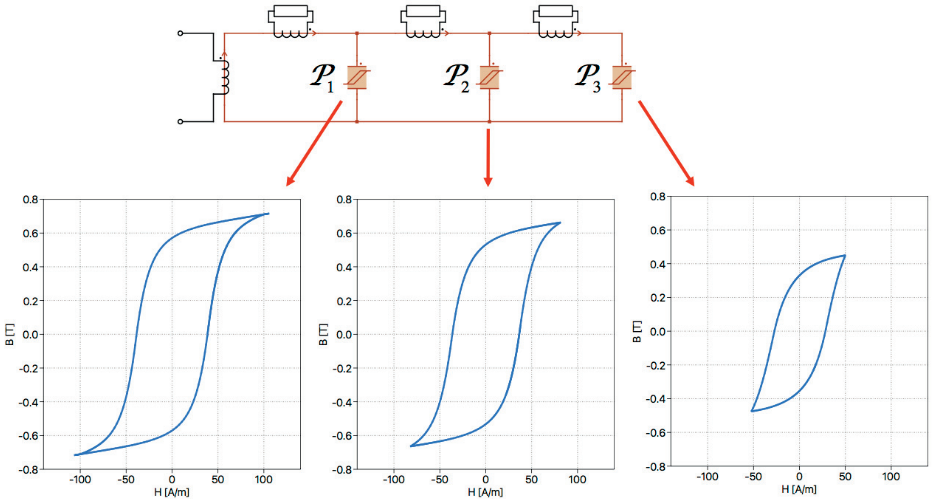

Figure 8.9 Static $B-H$ characteristic of the permeance blocks under 500 Hz sinusoidal excitation (with equivalent peak field strength 100 A/m)

Then in **Fig. 8.8** and **Fig. 8.10** the simulation results at 500 Hz and 1 kHz excitation are compared with the measurement. Again good match is obtained in both the $B-H$ characteristic and the time domain waveforms. The error of the power loss is 4.1% at 500 Hz and 1.7% at 1 kHz. Again in **Fig. 8.9** and **Fig. 8.11** the $B-H$ loops of the permeance blocks $\mathscr{P}_1 \sim \mathscr{P}_3$ are compared. The flux density amplitude reduces from the outer sub-laminates (represented by $\mathscr{P}_1$) towards the inner sub-laminates (represented by $\mathscr{P}_3$). Comparing **Fig. 8.7**, **Fig. 8.9** and **Fig. 8.11** with each other, one can realize that with increasing excitation frequency, the difference between the peak flux density of the three permeances $\mathscr{P}_1$ and $\mathscr{P}_3$ becomes larger. This model behavior corresponds to the theory that the eddy current effect prevents the flux from penetrating into the centre of the laminate. The higher the excitation frequency, the more obvious this effect will be.

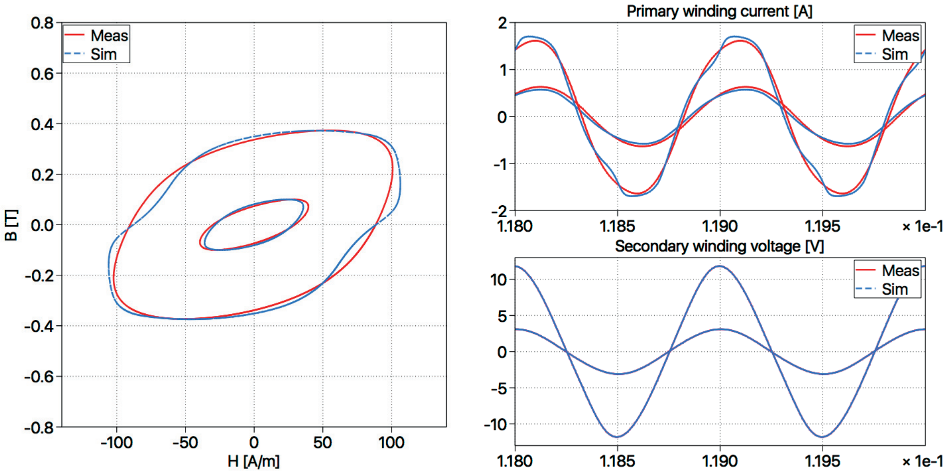

(a) **(b)**

Figure 8.10 Comparison between measurement and simulation under **1** kHz sinusoidal excitation with different amplitudes (a) $B-H$ loops; (b) Time domain waveforms.

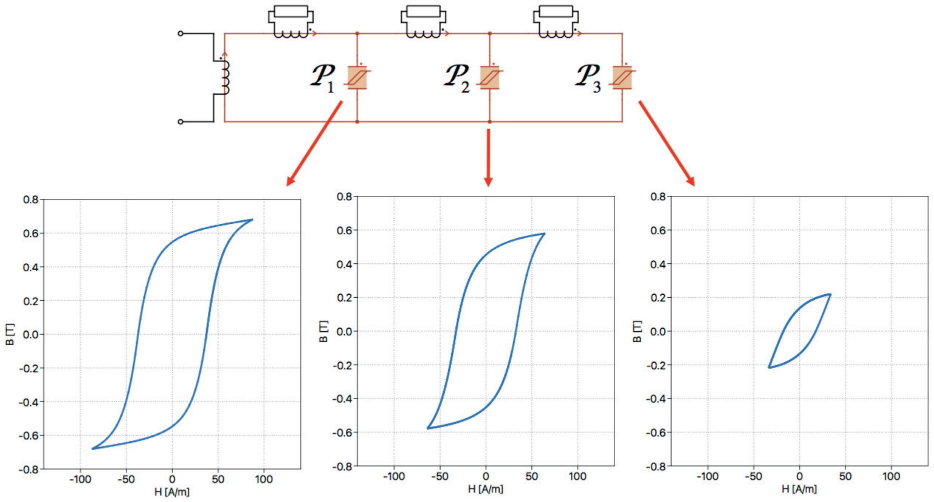

Figure 8.11 Static $B-H$ characteristic of the permeance blocks under **1** kHz sinusoidal excitation (with equivalent peak field strength **100** A/m)

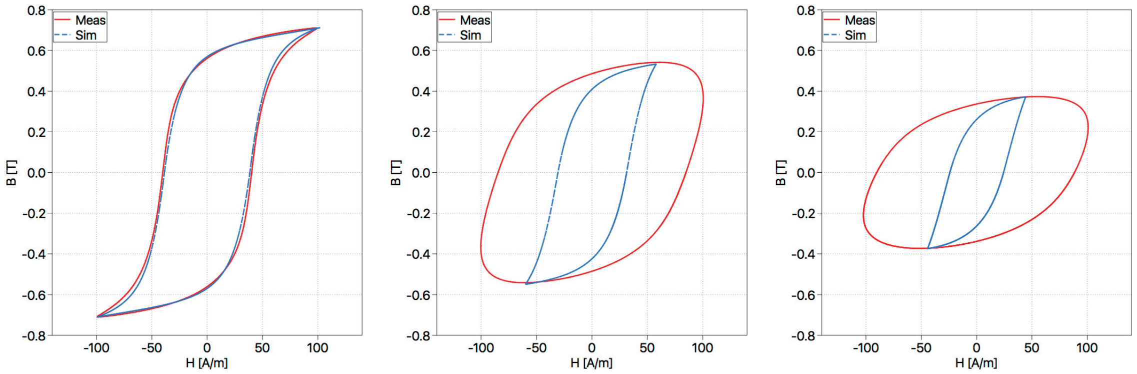

(a) (b) (c)

Figure 8.12 Comparison between measurement and simulation with virtual resistor loops removed from the model under excitation frequency (a) 25 Hz; (b) 500 Hz; (c) 1 kHz.

The power loss from eddy current effect can be directly obtained by summing up the power loss of the three virtual resistors $R_1 \sim R_3$ (voltage multiplied by current and averaged over one AC period). Subtracting the eddy current loss from the total loss yields the static hysteresis losses. The loss-splitting under the three excitation frequencies 25 Hz, 500 Hz and 1 kHz are compared in **Tab. 8.1** (with equivalent peak field strength equal to 100 A/m). With increasing excitation frequency, the percentage of the eddy current increases significantly.

The eddy current effect is neglected if the virtual resistors $R_1 \sim R_3$ are removed from the circuit model. With the same excitation voltage in the test case of three different frequencies are applied to the primary winding (result in equivalent peak field strength equal to 100 A/m), the simulated equivalent $B-H$ loops exhibits large discrepancy compared to the measurement. This mismatch servers especially as the excitation frequency increases as shown in **Fig. 8.12**, which indicates that the eddy current resistors are inevitable for simulating the core losses.

Table 8.1 Splitting of the simulated core loss into static hysteresis and eddy current parts

Excitation frequency	25 Hz	500 Hz	1 kHz
Total loss	0.21 W	6.40 W	8.74 W
Static hysteresis	0.188 W	2.40 W	2.92 W
Eddy current	0.022 W	4.00 W	5.82 W
	10.5 %	62.5 %	66.5 %

Further in **Fig. 8.13** the verification results with 1 kHz PWM excitation (50 % duty cycle) are illustrated. In this verification case, the test setup is operated under 50% duty-cycle PWM mode. Still the proposed model is able to well reproduce the $B-H$ characteristic and the time domain waveforms.

After the model is established and parameterized based on the sample core, the proposed magnetic circuit can be configured for different geometry and taken as a building block to compose iron cores with complex structures. A rudimentary transformer prototype is constructed as shown in **Fig. 8.14a**, with three-limb iron core made of laminates having the same material and thickness as the square core sample. The number of the stacked laminates here is 20. Two windings with turns number

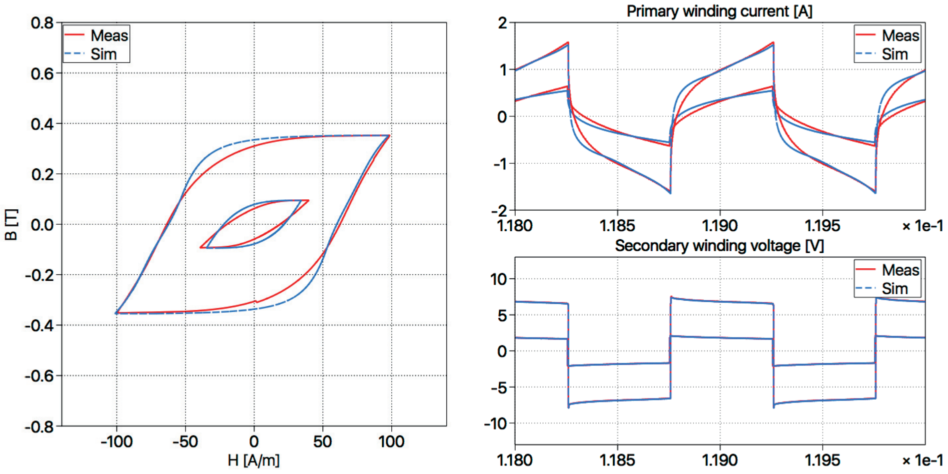

(a) **(b)**

Figure 8.13 Comparison between measurement and simulation under 1 kHz PWM excitation (50 % duty cycle) with different amplitudes (a) $B-H$ loops; (b) Time domain waveforms.

$N_1 = N_2 = 20$ are installed on the middle limb. The magnetic circuit model is composed of three ladder structures (**Fig. 8.5**) in parallel connection, which represent the center limb and the side limbs, as depicted in **Fig. 8.14b**. The two winding components are placed at the corresponding locations. In comparison to the model presented in **Fig. 8.5**, only the geometrical parameters l, w and the stacking number K need to be adapted. Please note that the material related parameters for calculating the nonlinear permeabilities μ^{irr} and μ_{rev}, which have been identified in a previous stage, remain the same.

For verification, the primary winding is supplied by a 500 Hz sinusoidal voltage, while the secondary winding is left open. Similar to the configuration of the magnetic circuit model in **Fig. 7.5a**, the measured secondary winding voltage is multiplied by the factor N_1/N_2 and provided to the controlled voltage source as reference on the primary winding. In **Fig. 8.15** the $B-H$ loops and time domain waveforms are compared between simulation and measurement. After adapting the geometry while

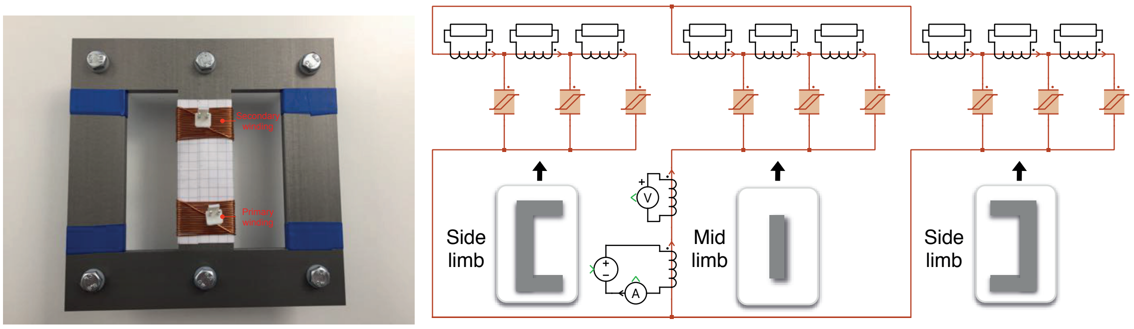

(a) **(b)**

Figure 8.14 Three limb transformer prototype (a) Hardware structure; (b) Magnetic circuit model using proposed approach.

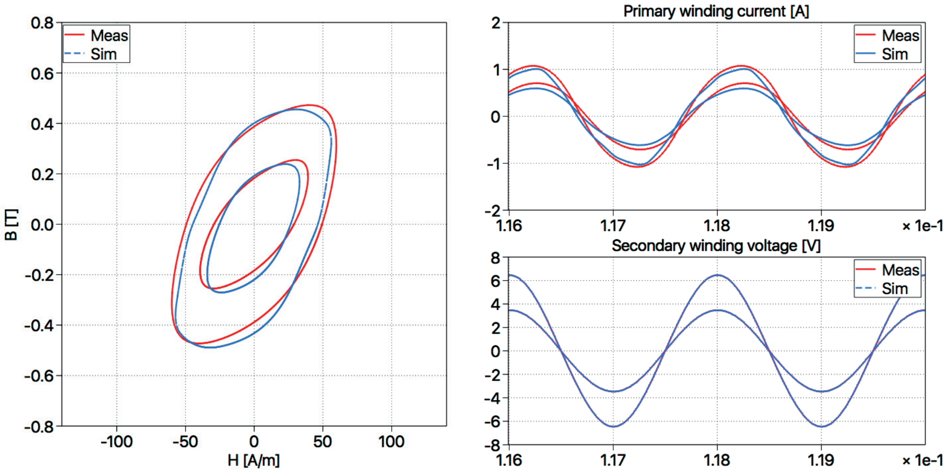

(a) **(b)**

Figure 8.15 Comparison between measurement and simulation of the three limb transformer prototype under $500Hz$ excitation with different amplitudes (a) $B-H$ loops; (b) Time domain waveforms.

using the same material representation, the model with the three limbs is still able to reproduce the measurement with good accuracy. The maximum error of the core loss is 6.2%.

8.4 Summary

This chapter has proposed a core model for time domain system-level simulation using permeance-capacitance based magnetic circuit, which captures the frequency-independent magnetic hysteresis of the material together with the frequency-dependent eddy current effect. Parameters of the model are identified via experimentally measured low frequency limiting loop as well as geometrical parameters. The fidelity of the model has been verified with experimental tests under excitation of different amplitude and frequencies on a sample core. The magnetic circuit can be easily extended to represent complex core geometries, which has been verified in terms of time domain waveform and $B-H$ characteristic.

9

Model of leakage flux for 1-phase multi-winding transformer

Multi-winding transformers have been applied in power electronic converters to interface systems operating on different voltage levels. Placement of the windings leads to unbalances, which are directly reflected in the dynamic behavior of the converter system. To compensate impact of the unbalance by means of component selection or control algorithm, sufficiently accurate transformer model is desired. For system-level simulation, the model should be integrated with power electronic circuit.

9.1 Literature review

In typical multilayer- (**Fig. 9.1a**), multidisk- (Fig. 9.1b) and mixed- (**Fig. 9.1c**) structures, non-identical size and position of the individual windings may lead to different leakage flux coupling, which gives rise to unbalanced short-circuit impedances [71].

Finite element method (FEM) has been widely adopted in modeling the main- and leakage flux distribution. However FEM is not suitable for dynamic simulation combined with complex power electronic circuits, due to its high computational effort and poor convergence in these circumstances. For system-level dynamic simulation, transformers are commonly represented by electrical equivalent circuit using coupled inductors, as has been discussed in **Sec. 2.1**. Coupled-inductor approach requires electric test to identify all the self- and mutual inductance values including the main flux path L_m and leakage flux path L_σ. If more than two windings are present, electric test needs to be enumerated among different short-and open circuit combinations, which can be time consuming and in some cases impractical.

Besides FEM and coupled-inductor, magnetic circuit has become popular nowadays. Firstly, the complexity is much lower than FEM thanks to the lumped representation, while the integration to electrical circuit is nearly seamless. Secondly, magnetic circuit has closer relation to the geometry than coupled-inductor, making it possible to parametrize the flux path directly without any electric tests. In combination with the material characteristic, this methodology have been successfully applied to model the main flux path[55] [72] [67] [73] [74]. However the leakage flux path was not analyzed.

Only a few publications have considered leakage flux path in magnetic circuit, due to the difficulty in parametrization. One of the underlying assumption in magnetic circuit approach is that the fluxes are confined in virtual tubes. Each section of the tube is characterized by the geometry together with material's permeability μ as lumped reluctance or permeance. Parametrization of the main flux path through the iron core is straightforward, since the geometry is determined and directly visible. In

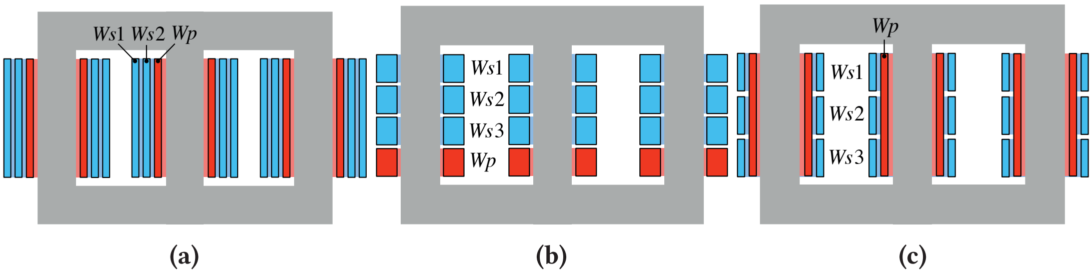

Figure 9.1 Winding arrangements considered in the existing publications, (a) Multilayer; (b) Multidisk; (c) Mixed.

comparison however, the geometry of the leakage flux path through the air is usually not clearly shaped.

In the work of [70] permeances representing leakage flux path has been introduced into the magnetic circuit of transformer with closed pot-type core. Thanks to the special core-structure, geometry of the leakage flux path was well determined, so that parametrization could be done in similar manner as the main flux path. However this type of transformer is not typically adopted in high-power applications. For typical E-core structure, authors of [75] have made a clear classification for leakage flux paths, and parametrized the permeances by geometrical data. However, this approach has been verified only on a single-winding inductor, where no leakage coupling between different windings takes place as in transformers.

For transformers with typical core structure, several publications have successfully modeled the leakage flux path. In the work of [76], a generalized reluctance magnetic circuit including leakage flux path between the windings was presented for complex multi-winding structures. Authors of [77] and [78] have followed this approach for dynamic simulation of different types of transformer. However in all these publications the magnetic circuit served as a intermediate step to derive the terminal-duality model (TDM) introduced by [79], which was essentially electrical equivalent circuit. In TDM the main flux path was represented by shunt-inductors on winding terminals, while the leakage flux path by coupled leakage inductance network in between. Elements of the leakage inductance matrix are linear summation of the short-circuit impedances between certain winding pairs, requiring again large number of electric tests. Especially when the leakage inductance matrix is being composed by measured short circuit impedance, assumption has been made that the inductance of the main flux path is magnitudes higher, which is not always the case in reality. Moreover, since the information about geometry is hardly visible after conversion to TDM model, open-circuit test is still necessary to identify the main inductance on winding terminals and this may make the representation of the material nonlinearity less accurate. As extension to the work done by [76], authors of [80] calculated the short-circuit impedances between winding pairs directly from geometrical data using the method introduced in [81], to get rid of the electric tests. The simulated short-circuit impedance matched well to the experimental measurements from single- and three phase transformers. However the increased error in three-phase case indicates that the 2D formulation of the method from [81] may run into issues, if the part of windings outside the core window area dominates.

The leakage flux models with direct parametrization from geometry are difficult to generalize in terms of accuracy. The ones parametrized from electric test do not include the geometrical information contained in the magnetic circuit, so that large number of measurement is required to cover all

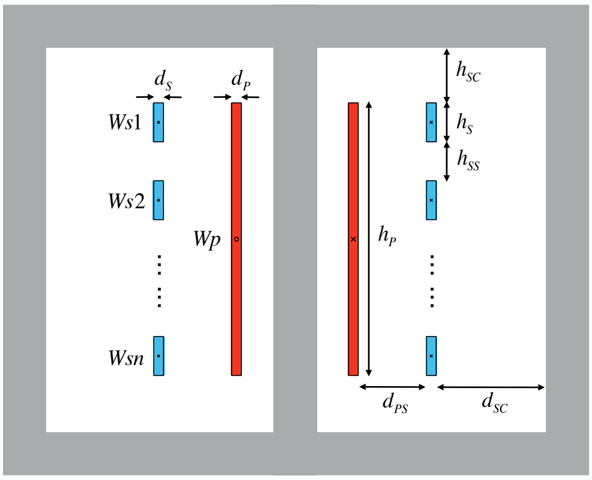

Figure 9.2 Winding arrangement with long primary winding and multiple stacked secondary windings

the possible couplings. This thesis proposes a solution which combines the intuitive geometric information and experimental results from only a few electric measurement together, and is able to achieve good accuracy, as demonstrated in the paper.

In most of the complex transformers, the individual windings do have something geometrically in common, due to consideration of mass production or space utilization. Taking advantage of this repetitive feature, this thesis demonstrates how the leakage flux path model and its parametrization procedure can be simplified, meanwhile demonstrating that the proposed approach of model is able to reproduce the unbalance of short-circuit impedance in reality. The model proposed by this chapter distinguished from the other previous publications via combining the following aspects together:

- Magnetic circuit is directly simulated in its original form, without transformation into electrical equivalent. The main- and leakage flux paths related to the real geometrical structure are contained in the same model and observable during the simulation.
- Main flux path is parametrized directly from geometry. Model of material nonlinearity like hysteresis proposed by in **Chap. 4** ~ **Chap. 6** and corner flux concentration, analyzed in [24], can be potentially incorporated, but are not analyzed in this chapter.
- Leakage flux path is characterized by a few parameters only, identification of which can be done via fitting to only a small number of electric test. The influence of the main flux path has been taken into account, apart from the infinite permeability assumption made in [76].

Typical winding arrangements in **Fig. 9.1a**, **Fig. 9.1b** and **Fig. 9.1c** have been investigated in the existing publications [76], [77], [78] and [80], while the one depicted in **Fig. 9.2** has not been discussed in detail so far, where the height of the inner layer winding spread out the total height of the others. This arrangement is typical for the phase-shift transformers used in multi-pulse rectifier systems, which interface power grid to medium voltage power electronic converters like the cascaded H-bridge patented by Robicon Corporation [82] and widely applied in industry nowadays. Simplified single-phase transformer version of this winding arrangement is taken for the case study presented in this chapter. A low power prototype transformer has been constructed to evaluate fidelity of the proposed modeling's approach. The permeance-capacitor element proposed by [16] and implemented by [15] is chosen to compose the magnetic circuit, considering its capability to apply ordinary differential equation (ODE) solver which is already provided in numerous commercial system-level simulation softwares like Simulink and PLECS.

This chapter is organized as follows. **Sec. 9.2** demonstrates the modeling's approach and the procedure for parameter identification. **Sec. 9.3** provides the verification of the fidelity of the model via different experimental short-circuit tests. Afterwards in **Sec. 9.5**, the fidelity of the model in system-level simulation is further evaluated in combination with power electronic converters.

9.2 Proposed model

The prototype transformer depicted in **Fig. 9.3a** has been taken as study case. This transformer is rated to convert 115 Vrms 400 Hz low voltage to 15.2 Vrms on nine output terminals with nominal power of 180W in total. Each output terminal can be connected to full-bridge rectifier to generate 20V DC voltage as input for switched-mode power supplies. The iron core is stacked by laminations type "EI 150/150" of material "M330-35A", resulting in total thickness of $D_C = 50mm$. There is one primary winding (W_p) with $N_p = 144$ turns on the input side and nine secondary windings ($W_{s1} \dots W_{s9}$) with $N_s = 19$ turns each on the output side. Low window area utilization is configured for this prototype transformer, in order to exaggerate the leakage flux path and resemble the high winding spacing in medium voltage applications due to consideration of insulation. The transformer in medium voltage applications is discussed in **Chap. 10**.

The windings of the prototype transformer have been arranged complying to the structure in **Fig. 9.2**. All dimensional parameters have been listed in **Tab. 9.1**. Typical geometrical repetition and symmetry present in complex transformers has been introduced to the prototype. All secondary windings W_{sk} ($k = 1 \dots 9$) are designed to be the same size, which are allocated along the middle core limb with the same vertical interval in between. Please note that h_{SS} is significantly smaller than the winding's

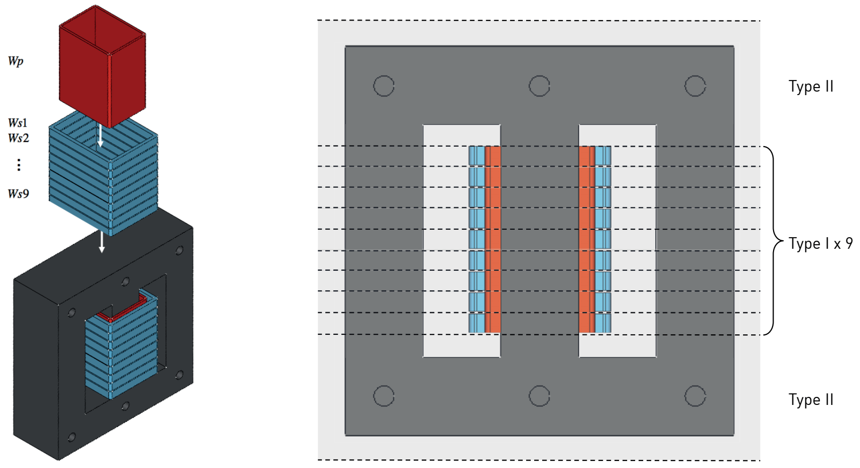

(a) (b)

Figure 9.3 (a) Structure of the prototype transformer with one primary- W_p and nine secondary windings W_{sk} (b) Vertical separation of the transformer's geometry into nine divisions of type I and two of type II

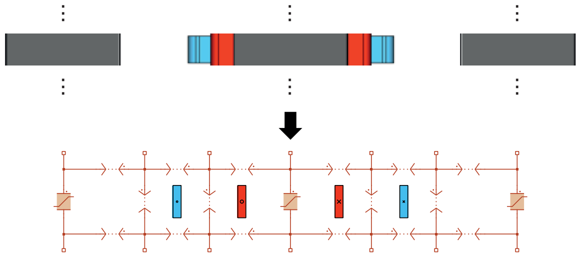

Figure 9.4 Permeance magnetic circuit of the division type I with the flux path of the core and air

dimension. The primary winding W_p is placed inside the secondary winding, whose height is equal to the distance from the top of W_s1 to the bottom of W_s9.

Table 9.1 Dimensional parameters of the prototype transformer in [mm]

Parameter	Value	Parameter	Value
d_P	2	d_SC	18
h_P	71	h_SC	9
d_S	3	d_PS	3
h_S	7	h_SS	1

To derive the magnetic circuit model, the geometry of the transformer is separated into divisions along the vertical axis, as **Fig. 9.3b** demonstrates. Nine divisions of type I have been defined. All of them have the same height equal to $h_\mathrm{DivI} = h_\mathrm{S} + h_\mathrm{SS}$, each one includes one section of the three core limbs, one complete secondary winding, and one section of the primary winding. The turns number of the primary winding section is equal to $N_\mathrm{pDiv} = N_\mathrm{p}/9$. This division can be converted into a magnetic circuit shown in **Fig. 9.4** . The three permeances filled with solid color represent flux path inside the transformer core, while the others represent the leakage flux path through the air. The cross section of the windings are placed schematically in between, according to the real geometry.

Besides that, two divisions of type II representing the rest of the transformer is demonstrated in **Fig. 9.5**, including core yoke and the top and bottom part of the limbs. In comparison to the division type I, since no winding is present in division type II and the permeability of the main flux path inside the core is much more dominant than that of the leakage flux path through the air, and the leakage

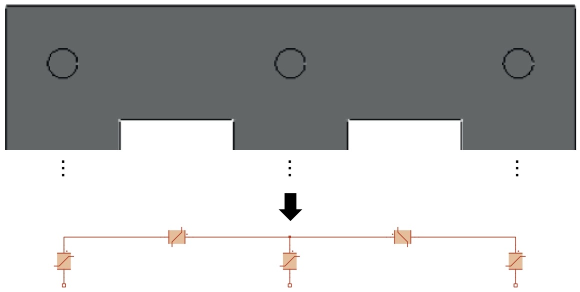

Figure 9.5 Permeance magnetic circuit of the division type II

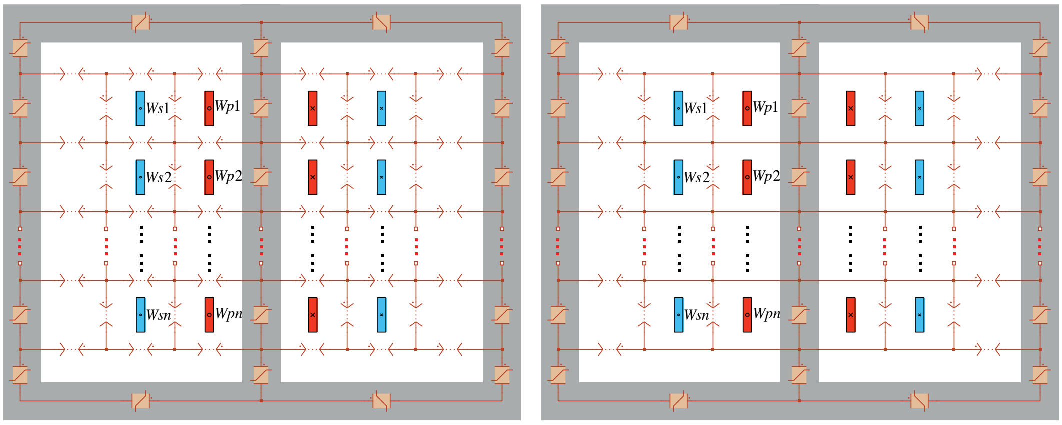

(a) **(b)**

Figure 9.6 Permeance circuit of the transformer with schematically placed windings, (a) Original (b) Simplified

permeances in this type of division can be neglected.

Stacking nine divisions of type I over each other and adding two divisions of type II on the top and bottom, yields the complete magnetic circuit as shown in **Fig. 9.6a**. If all the windings are installed close enough to the middle limb of the transformer core (as is usually the case in practice to reduce leakage inductance), the horizontal leakage permeances above- or below the windings can be assumed to be "magnetically" short circuit, resulting in the structure of **Fig. 9.6b**. The other horizontal permeances stand for the leakage flux paths from middle- towards side limb, while the vertical ones surrounding W_p and W_s for the leakage flux paths looping back to the middle limb. Also one should keep in mind that these permeances account not only for the leakage flux paths inside the core window area, but also the ones exposed outside the middle limb (e.g. fringing field), despite of the 2-D sketches being used for illustration.

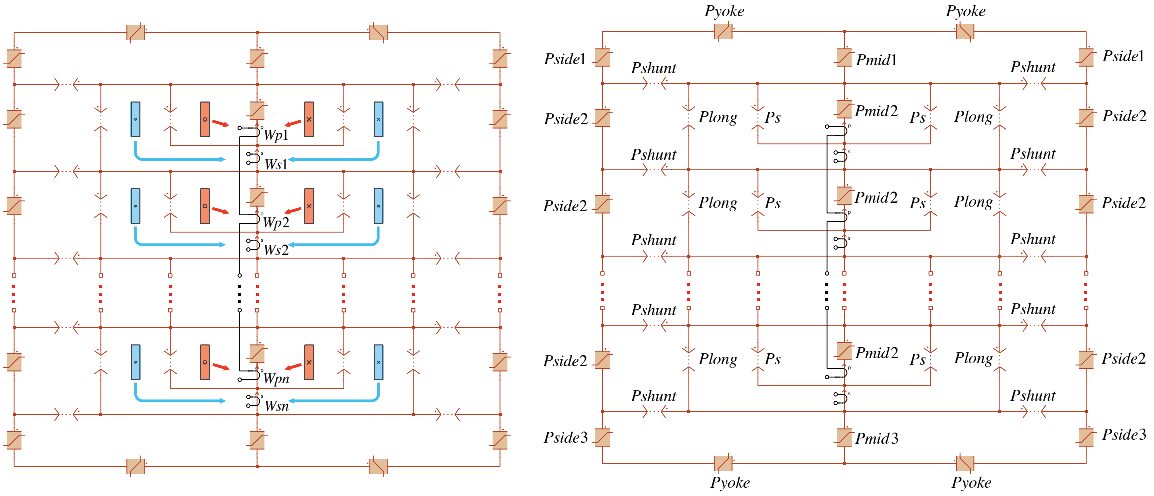

(a) **(b)**

Figure 9.7 (a) Permeance circuit with lumped-winding components to interface electrical circuit (b) Final version of the magnetic circuit model

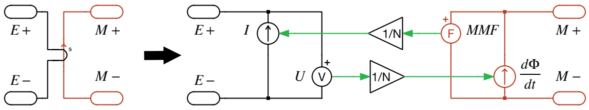

Figure 9.8 Gyrator structure of the lumped-winding component

Afterwards, the schematically depicted windings are converted into lumped-components as demonstrated in **Fig. 9.7a**, which is ready to be directly connected to electrical circuit model. The lumped winding components are implemented using the gyrator structure proposed by [16] and discussed in **Sec. 2.2.2**, which serves as interface between the electrical and magnetic circuit (shown in **Fig. 10.4** again). In one direction, the electrical voltage measured on the winding terminal is divided by the number of turns N and fed into the magnetic circuit as a flux rate source ($d\Phi/dt$). The flux rate source "charges" or "discharges" the magnetic permeances which behave like capacitors (not electrical). In the other direction, the "magnetic voltage" measured on the magnetic terminal (magnetomotive force MMF) is also divided by N and fed into the electrical circuit as electrical current source. Please note that all the primary winding sections are series-connected in the electrical circuit, so that all sections share the same electrical current while the terminal voltage is the summation of all the individual voltages. For this prototype transformer, the final version becomes the structure in **Fig. 9.7b**.

The permeances representing different part of the iron core can be calculated as:

$$\mathscr{P} = \frac{\mu_r \mu_0 A}{l} \tag{9.1}$$

In the equation above, the equivalent cross-section area A and magnetic path length l can be calculated from the core geometry using the formulas introduced in [83]. For the prototype transformer, the length of $\mathscr{P}_{\mathrm{mid2}}$ and $\mathscr{P}_{\mathrm{side2}}$ is equal to $h_{\mathrm{S}} + h_{\mathrm{SS}}$, while that of $\mathscr{P}_{\mathrm{mid1}}$($\mathscr{P}_{\mathrm{mid3}}$) and $\mathscr{P}_{\mathrm{side1}}$($\mathscr{P}_{\mathrm{side3}}$) equal to h_{SC} (geometry parameters see **Fig. 9.2**). The permeance $\mathscr{P}_{\mathrm{yoke}}$ includes both the yoke and corner. Should nonlinearity of the core material be considered, the relative permeance μ_{r} will be a function of the MMF, which is the magnetic "voltage" measured on the individual permeance. In linear case, μ_{r} can be simply configured as a constant.

After the core permeances get determined, only the value of the leakage permeances still remain undefined. Recalling that the nine type I divisions are identical in geometry and the transformer is symmetrical about the middle limb, yields the fact that only three parameters $\mathscr{P}_{\mathrm{s}}$, $\mathscr{P}_{\mathrm{long}}$ and $\mathscr{P}_{\mathrm{shunt}}$ are needed to characterize the whole leakage flux path, which are marked in **Fig. 9.7b**. As has been discussed in the previous section, it is difficult to accurately define the geometry of the leakage flux path through the air, therefore a few short circuit tests are carried out to identify the three unknown parameters, in which one single winding is supplied by voltage source and selected others windings are short-circuited. Instead of enumerating all the supply-short combinations, only five short-circuit test schemes are needed for the parameter identification which carry sufficient information about coupling between the windings. The equivalent inductance looking into the supplied winding is calculated as imaginary part of the measured complex impedance, as listed in **Tab. 10.3**:

After that, the leakage permeance values of the circuit model in **Fig. 9.7b** are fitted to minimize a quadratic objective function, which is the square-summation of the error between the short-

Table 9.2 Test schemes for leakage permeance parameter fitting

	Supply	Short	Fit to
1	W_p	W_s1	$L_\mathrm{k1,Test} = imag(\vec{V}_\mathrm{p}/\vec{I}_\mathrm{p})/(2\pi f)$
2	W_p	W_s5	$L_\mathrm{k2,Test} = imag(\vec{V}_\mathrm{p}/\vec{I}_\mathrm{p})/(2\pi f)$
3	W_s1	W_s2	$L_\mathrm{k3,Test} = imag(\vec{V}_\mathrm{s1}/\vec{I}_\mathrm{s1})/(2\pi f)$
4	W_s1	W_s9	$L_\mathrm{k4,Test} = imag(\vec{V}_\mathrm{s1}/\vec{I}_\mathrm{s1})/(2\pi f)$
5	W_p	All W_ss	$L_\mathrm{k5,Test} = imag(\vec{V}_\mathrm{p}/\vec{I}_\mathrm{p})/(2\pi f)$

circuit inductances from measurement and the one obtained from magnetic circuit simulation of the aforementioned 5 short-circuit schemes, given by the equation in below:

$$f_\mathrm{obj} = \sum_{i=1}^{4} \left(\frac{L_\mathrm{ki,Test} - L_\mathrm{ki,Sim}}{L_\mathrm{ki,Test}}\right)^2 \tag{9.2}$$

One should also note that the resistances of the windings need to be measured (e.g. using LRC-meter) and connected in series with the winding components in electrical circuit part of the model, if resistive part of the windings constitutes relatively large percentage of the short-circuit impedance, which is the case in the low voltage prototype. In case of high power medium voltage transformers however,

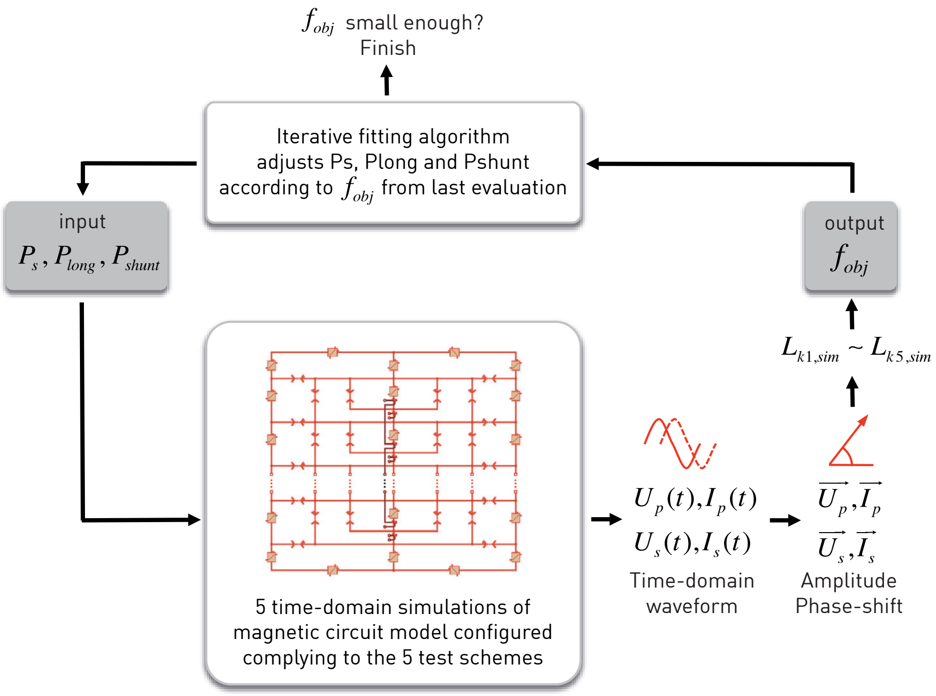

Figure 9.9 Generalized fitting process of the leakage permeance values, where the magnetic circuit model is simulated to for calculating the output of the objective function for the fitting algorithm

inductive part will be much more dominated due to the large spacing between windings, so that accurate parametrization of the winding resistance is not critical. Commonly used gradient based- or evolutionary fitting algorithms can be applied to find out the leakage permeance values, iteratively. Generally the fitting process can be carried out in a way demonstrated in **Fig. 9.9**. On one side, after receiving the leakage permeance values $\mathscr{P}_{\mathrm{s}}$, $\mathscr{P}_{\mathrm{long}}$, $\mathscr{P}_{\mathrm{shunt}}$ provided by the fitting algorithm before each objective function evaluation, five magnetic circuit models of the transformer which are configured complying to each of the five test schemes specified by **Tab. 9.2** are simulated in time-domain, one after each other. The simulated time-domain waveforms of winding voltage and current are transformed to amplitude and phase-angle, so as to calculate the equivalent inductance values and yields the output of the objective function following equation (2). On the other side, the fitting algorithm retrieves the output of objective function from the last evaluation, adjusts the $\mathscr{P}_{\mathrm{s}}$, $\mathscr{P}_{\mathrm{long}}$, $\mathscr{P}_{\mathrm{shunt}}$ values and brings them into the next objective function evaluation.

Initial values need to be assigned in order to make the algorithm better converge, which for the prototype transformer can be calculated in below. In circumstances the fitting algorithm may have difficulty in convergence if $\mathscr{P}_{\mathrm{long0}}$ is exactly equal to zero, instead a small value of e.g. 10^{-9} can be chosen.

$$\mathscr{P}_{\mathrm{s0}} = \frac{\mu_r \mu_0 D_{\mathrm{c}} d_{\mathrm{PS}}}{h_{\mathrm{S}} + h_{\mathrm{SS}}} \tag{9.3}$$

$$\mathscr{P}_{\mathrm{long0}} = 0 \tag{9.4}$$

$$\mathscr{P}_{\mathrm{shunt0}} = \frac{\mu_r \mu_0 D_{\mathrm{c}} (h_{\mathrm{S}} + h_{\mathrm{SS}})}{d_{\mathrm{SC}}} \tag{9.5}$$

Despite of the repetitive structure, thanks to which the whole leakage flux path can be characterized by only three permeance values, strong unbalance of short-circuit impedances will still take place, which will be discussed in the following sections.

9.3 Experimental verification with short circuit test

For verification of the proposed modeling's approach, the aforementioned prototype transformer has been realized in hardware. In order to carry out the five short-circuit schemes for model parameter identification and further schemes for validation, the transformer is connected to a simplified version of the test setup introduced in **Chap. 3**, which operates in sinusoidal excitation mode, as shown in **Fig. 9.10a**.

After the five inductance values listed in **Tab. 9.2** have been obtained, the magnetic circuit models with the structure depicted in **Fig. 9.7b** is built up in the system-level simulation software PLECS (Blockset version) in combination with MATLAB/Simulink. Sinusoidal voltage sources are connected

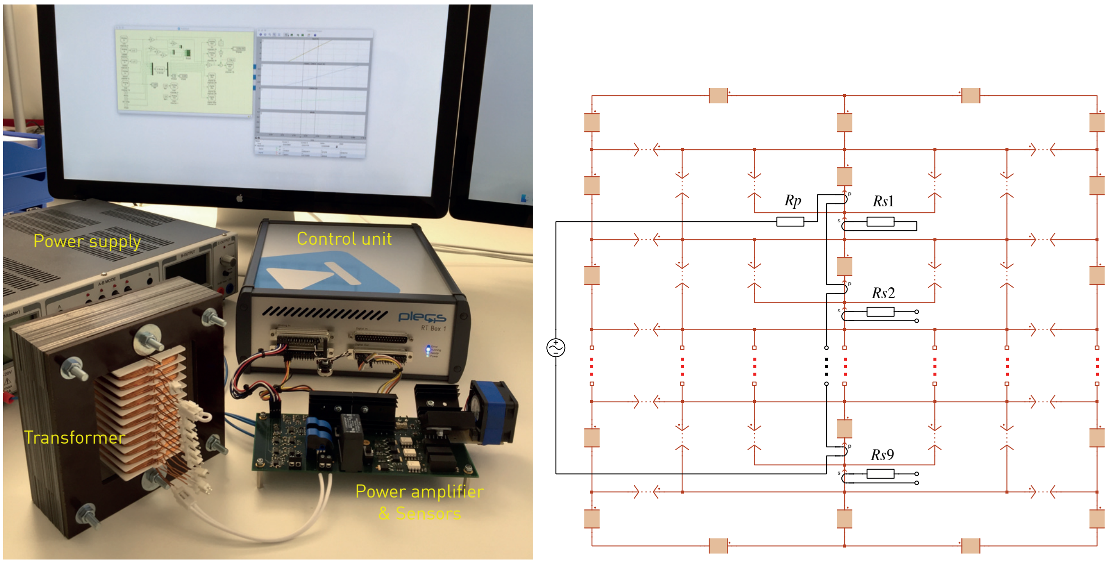

(a) **(b)**

Figure 9.10 (a) Short-circuit test setup for the prototype transformer, with voltage and current on the supplied winding measured (b) Magnetic circuit model in PLECS for parameter fitting and verification

to the winding terminals to emulate the power amplifier output in the test setup. Prior to leakage parameter identification, the permeances representing the iron core have been parametrized directly from geometry and material characteristic. Since the transformer is designed to operate far away from saturation, so that the nonlinearity of the core material has little affect on the measured short-circuit inductances, constant permeability from the data sheet has been assigned to the core permeances. The circuit model which is configured complying to test scheme 1 with primary winding W_p supplied and secondary winding W_s1 shorted is demonstrated in **Fig. 9.10b**, while the ones for the other four test schemes are established in similar way. Also please note that the winding resistances can not be neglected and have been connected to the windings with $R_\mathrm{p} = 0.9\Omega$ and $R_\mathrm{s1}...R_\mathrm{s9} = 0.15\Omega$, considering the fact that the winding resistance is comparable to the measured short-circuit reactance, for example $X_\mathrm{k4,Test} = L_\mathrm{k4,Test} \cdot 2\pi 400 = 0.10\Omega$ is measured from test scheme 4 in **Tab. 9.2**, which is 66% of the secondary winding resistance.

For parameter identification, the “fminsearch” fitting algorithm provided by MATLAB (referred as unconstrained nonlinear optimisation) is adopted. As required by “fminsearch”, a customized objective function has been written using Matlab script which realizes the functionalities listed in below:

- Accept the permeance values ($\mathscr{P}_\mathrm{s}$, $\mathscr{P}_\mathrm{long}$, $\mathscr{P}_\mathrm{shunt}$) as input arguments and assign them to the five magnetic circuit models in PLECS/Simulink via mask variables.

- Simulate the five magnetic circuit models configured complying to each of the five test schemes specified in **Tab. 9.2**, one by one.

- Calculate the equivalent inductance values ($L_\mathrm{k1,Sim}$ ... $L_\mathrm{k5,Sim}$) using the simulated voltage and current from the five models.

- Return the output of objective function calculated following equation (2).

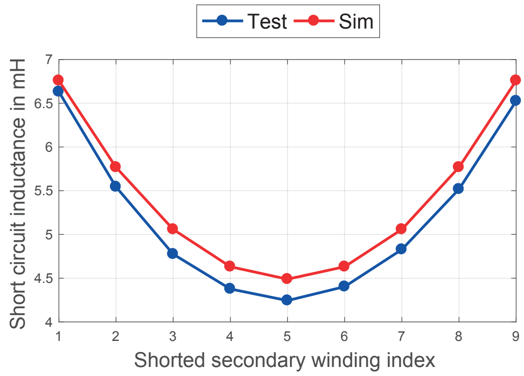

Figure 9.11 Short circuit inductances with W_p supplied and different single W_s shorted

The initial permeance values calculated using equation (3) till (5) and the ones obtained after parameter fitting using “fminsearch” algorithm are compared in **Tab. 10.4**.

Table 9.3 Leakage permeance values fitted to the measurements $[H]$

	$\mathscr{P}_\mathrm{s}$	$\mathscr{P}_\mathrm{long}$	$\mathscr{P}_\mathrm{shunt}$
Initial value	$39 \cdot 10^{-9}$	$1 \cdot 10^{-9}$	$25 \cdot 10^{-9}$
After fitting	$81 \cdot 10^{-9}$	$33 \cdot 10^{-9}$	$32 \cdot 10^{-9}$

In the first group of verification schemes, the primary winding is supplied, meanwhile one single secondary winding is shorted. The short-circuit inductances looking into the primary winding with different secondary windings shorted are compared between measurement and magnetic circuit model in **Fig. 9.11**. Although all the secondary windings have the same geometrical dimension and parameterized by repetitive permeance network, the resulted short-circuit impedances however, are unbalanced, due to difference in vertical position with respect to the primary winding. The U-shape curve reveals the fact that the more centralized the secondary winding is located with respect to the primary winding, the stronger is the coupling and thus the lower the short-circuit inductance will be.

Figure 9.12 Short circuit inductances with W_s1 supplied and one of the other W_ss shorted

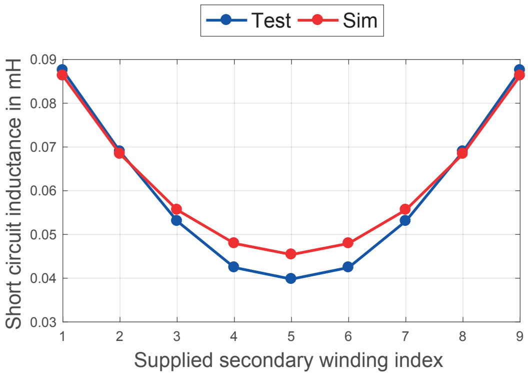

Figure 9.13 Short circuit inductances with W_p shorted and different single W_s supplied

In the second group of verification schemes, the secondary winding $W_{\mathrm{s}1}$ on the very top is supplied, meanwhile another secondary windings is shorted. The resulted inductances looking into $W_{\mathrm{s}1}$ are shown in **Fig. 9.12** with different other secondary windings shorted. From the result comparison one can see that not only the points used for parameter identification (short $W_{\mathrm{s}1}$, $W_{\mathrm{s}5}$ in **Fig. 9.11** and short $W_{\mathrm{s}2}$, $W_{\mathrm{s}9}$ in **Fig. 9.12**), but also the inductance values of the other verification points match quite well between the proposed magnetic circuit model (built in PLECS/Simulink) and test result, with maximum error of 8.3 %.

In the third group of verification schemes, the primary winding is shorted with single secondary winding supplied. The short-circuit inductances looking into the different secondary winding supplied are compared between simulation and test in **Fig. 9.13**. Maximum error of 12.0 % occurs when $W_{\mathrm{s}5}$ is supplied.

In the forth group of verification schemes, one winding (primary or secondary) is supplied with other two shorted at the same time. The short-circuit combination together with the leakage inductance values looking into the supplied windings are listed in **Tab. 9.4** and **Tab. 9.5**. Good match between magnetic circuit model and the measurement is present here as well with maximum error of 5.0 %.

Table 9.4 Leakage inductances [mH] comparison with one winding supplied and other two shorted: I

Supplied	**Shorted**	L_k **Test**	L_k **Sim**	Error
W_p	$W_{\mathrm{s}1}$, $W_{\mathrm{s}2}$	4.03	3.85	4.5 %
$W_{\mathrm{s}1}$	W_p, $W_{\mathrm{s}2}$	0.080	0.076	5.0%
$W_{\mathrm{s}2}$	W_p, $W_{\mathrm{s}1}$	0.058	0.059	1.7%

Table 9.5 Leakage inductances [mH] comparison with one winding supplied and other two shorted: II

Supplied	**Shorted**	L_k **Test**	L_k **Sim**	Error
W_p	$W_{\mathrm{s}1}$, $W_{\mathrm{s}9}$	2.15	2.09	2.8%
$W_{\mathrm{s}1}$	W_p, $W_{\mathrm{s}9}$	0.093	0.095	2.2%
$W_{\mathrm{s}9}$	W_p, $W_{\mathrm{s}1}$	0.093	0.095	2.2%

9.4 Origins of unbalanced leakage flux

In this section, the physical background of the unbalance in magnetic flux coupling, which is reflected by the experimental measurement in **Fig. 9.11** and **Fig. 9.12**, is analyzed using a generalized form of single-phase transformer. As depicted in **Fig. 9.14a**, the single phase transformer is composed of one primary winding W_p which spreads out the middle limb of the iron core, as well as M identical secondary windings $W_{\mathrm{s}1} \sim W_{\mathrm{s}M}$ stacking over each other. The magnetic circuit topology proposed in this chapter is adopted for the analysis as demonstrated in **Fig. 9.14b**. Considering the axis-symmetry of the geometry, the left- and right halves of the original magnetic circuit can be merged together. Following the formulation defined in **Sec. 9.2**, all divisions of the leakage flux path share the same three permeance values $\mathscr{P}_\mathrm{s}$, $\mathscr{P}_\mathrm{long}$ and $\mathscr{P}_\mathrm{shunt}$. The vertical leakage permeances ($\mathscr{P}_\mathrm{s}$, $\mathscr{P}_\mathrm{long}$) surrounding the primary- and secondary windings stand for the leakage paths looping back to the corresponded limb, the flux flowing through $\mathscr{P}_\mathrm{s}$ only links with the primary winding section, while that through $\mathscr{P}_\mathrm{long}$ links the primary- and secondary windings together. The horizontal ones ($\mathscr{P}_\mathrm{shunt}$) stand for the leakage paths between different limbs. If the permeance representing the core limbs ($\mathscr{P}_\mathrm{mid}$ and $\mathscr{P}_\mathrm{side}$ in **Fig. 9.14b**) are significantly larger than that of the leakage ones, they can be replaced by short-circuit lines, as shown in **Fig. 9.14c**. The permeance representing the core yokes ($\mathscr{P}_\mathrm{yoke}$) in **Fig. 9.14c** can be merged with the horizontal permeances $\mathscr{P}_\mathrm{shunt}$ at the top and bottom

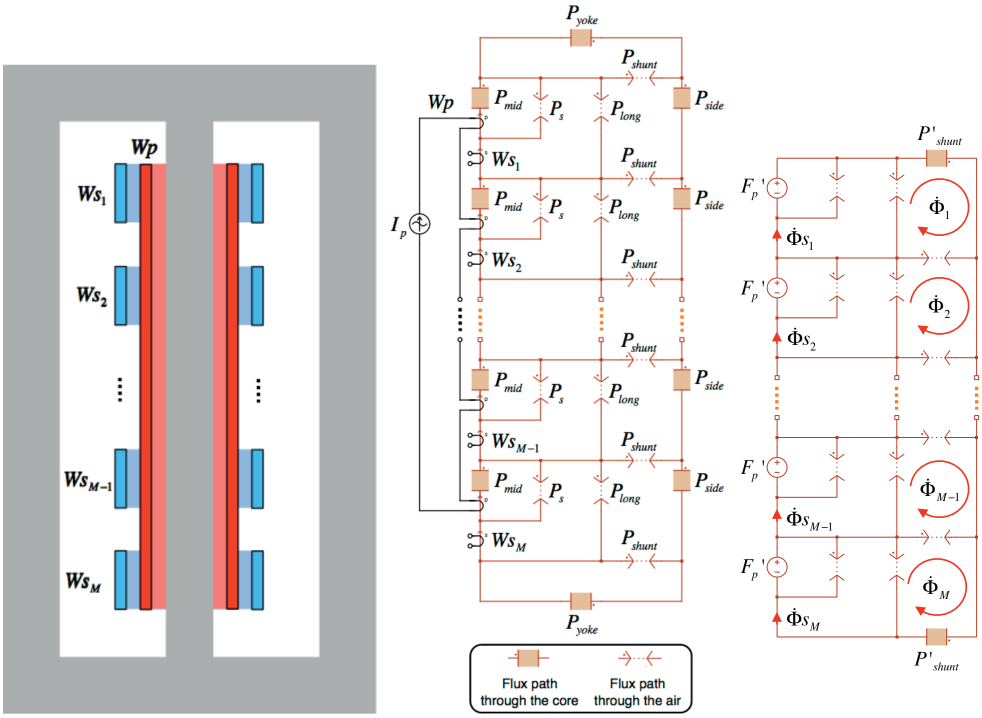

(a) (b) (c)

Figure 9.14 Demonstration of the unbalanced coupling I (a) Single phase transformer with M secondary windings; (b) Magnetic circuit of the transformer with current I_p flowing on the primary winding and all secondary windings are left open; (c) Simplified magnetic circuit where the core limb permeances are neglected and the two yoke permeances are merged into $\mathscr{P}_\mathrm{shunt}$ as $\mathscr{P}'_\mathrm{shunt}$.

of the magnetic circuit, yields the the equivalent permeance $\mathscr{P}'_{\text{shunt}} = \mathscr{P}_{\text{shunt}} + \mathscr{P}_{\text{yoke}}$ in **Fig. 9.14c**. The primary winding has been equally divided into M sections, the effect of an AC current I_{p} flowing on the primary winding can be represented by M identical MMF sources connected in each division, whose value is given by

$$F'_{\text{p}} = I_{\text{p}} \cdot N_{\text{p}}/M \tag{9.6}$$

where N_{p} is the turns number of the primary winding. If the secondary winding are kept open, the induced magnetic flux rate $\dot{\Phi}_{\text{s1}} \sim \dot{\Phi}_{\text{sM}}$ ($d\Phi/dt$) are essentially the "magnetic" current flow on the corresponding branches, as has been highlighted in **Fig. 9.14c**. In order to derive $\dot{\Phi}_{\text{s1}} \sim \dot{\Phi}_{\text{sM}}$, the circulating flux rate $\dot{\Phi}_1 \sim \dot{\Phi}_{\text{M}}$ in each division are firstly calculated. Following the second Kirchhoff's law applied to magnetic circuit, the flux rates in the very top- and very bottom division are given by

$$F'_{\text{p}} = (X'_{\text{shunt}} + X_{\text{shunt}}) \cdot \dot{\Phi}_1 - X_{\text{shunt}} \cdot \dot{\Phi}_2 \tag{9.7}$$

$$F'_{\text{p}} = (X'_{\text{shunt}} + X_{\text{shunt}}) \cdot \dot{\Phi}_{\text{M}} - X_{\text{shunt}} \cdot \dot{\Phi}_{\text{M}-1} \tag{9.8}$$

where X is the "magnetic" reactance equal to $1/(\omega \cdot P)$ with ω standing for the angular frequency of the primary current I_{p}. For the divisions in between with the index $1 < m < M$, the relations comply to

$$F'_{\text{p}} = 2 \cdot X_{\text{shunt}} \cdot \dot{\Phi}_{\text{m}} - X_{\text{shunt}} \cdot \dot{\Phi}_{\text{m}-1} - X_{\text{shunt}} \cdot \dot{\Phi}_{\text{m}+1} \tag{9.9}$$

equation (9.7) and (9.8) can be reorganized as

$$\dot{\Phi}_2 - \dot{\Phi}_1 = \frac{-F'_{\text{p}} + X'_{\text{shunt}} \cdot \dot{\Phi}_1}{X_{\text{shunt}}} \tag{9.10}$$

$$\dot{\Phi}_{\text{M}} - \dot{\Phi}_{\text{M}-1} = \frac{F'_{\text{p}} - X'_{\text{shunt}} \cdot \dot{\Phi}_{\text{M}}}{X_{\text{shunt}}} \tag{9.11}$$

On one hand, the vertical symmetry of the magnetic structure leads to the fact that $\dot{\Phi}_1 = \dot{\Phi}_{\text{M}}$, which can be substituted into (9.10) and (9.11), thus one can easily find out

$$\dot{\Phi}_2 - \dot{\Phi}_1 = -(\dot{\Phi}_{\text{M}} - \dot{\Phi}_{\text{M}-1}) = \Delta\dot{\Phi}_1 \tag{9.12}$$

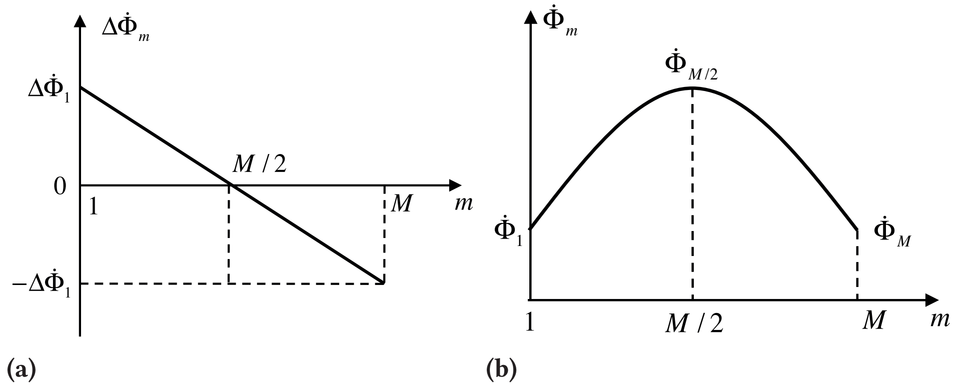

Figure 9.15 (a) Difference between the circulating flux rate of adjacent divisions against the division index; (b) Circulating flux rate of adjacent divisions against the division index.

On the other hand, reformatting equation (9.9) yields the recursive expression

$$\Delta\dot{\Phi}_{\mathrm{m}} - \Delta\dot{\Phi}_{\mathrm{m-1}} = (\dot{\Phi}_{\mathrm{m+1}} - \dot{\Phi}_{\mathrm{m}}) - (\dot{\Phi}_{\mathrm{m}} - \dot{\Phi}_{\mathrm{m-1}}) = -\frac{F_{\mathrm{p}}'}{2 \cdot X_{\mathrm{shunt}}} < 0 \tag{9.13}$$

Combining the equations (9.12) and (9.13) together, the difference between the circulating flux rate of adjacent divisions turns out to be a linear function of the division index which crosses zero at $m = M/2$, as demonstrated in **Fig. 9.15a**. Despite the discrete form, this linear function can be considered as *derivative* of the circulating flux rate $\dot{\Phi}_{\mathrm{m}}$ itself against index m, thus $\dot{\Phi}_{\mathrm{m}}$ turns out to be a second-order polynomial having the maximum at $m = M/2$, as demonstrated in **Fig. 9.15b**. The flux rate $\dot{\Phi}_{\mathrm{s(m)}}$ of the individual secondary windings is constantly biased from the corresponding circulating flux rate $\dot{\Phi}_{\mathrm{m}}$, given as

$$\dot{\Phi}_{\mathrm{s(m)}} = \dot{\Phi}_{\mathrm{m}} + \frac{F_{\mathrm{p}}'}{X_{\mathrm{long}}} \tag{9.14}$$

Therefore $\dot{\Phi}_{\mathrm{s(m)}}$ is also a second-order polynomial and the maximum of which also take place at the secondary winding with index $M/2$, that is at the middle of the primary winding. This reveals the fact that the closer the secondary winding is placed to the centre of the primary winding, the better the flux coupling can be obtained.

After the analysis of the coupling between primary- and secondary windings, the coupling on the secondary side can be demonstrated under the assumption that an AC current I_{s} is flowing on the secondary winding W_{s1}, while all the other secondary windings $W_{\mathrm{s2}} \sim W_{\mathrm{sM}}$ as well as the primary winding are left open, as illustrated in **Fig. 9.16a**. After the same simplification made in the previous analysis case as well as replacing the open windings with short circuit lines, the magnetic circuit becomes the structure shown in **Fig. 9.16b**. The induced flux rates on the secondary windings $\dot{\Phi}_{\mathrm{s1}} \sim \dot{\Phi}_{\mathrm{sM}}$ as well as that flowing on the horizontal permeances $\dot{\Phi}_{\mathrm{h1}} \sim \dot{\Phi}_{\mathrm{h(M-1)}}$ have been denoted in

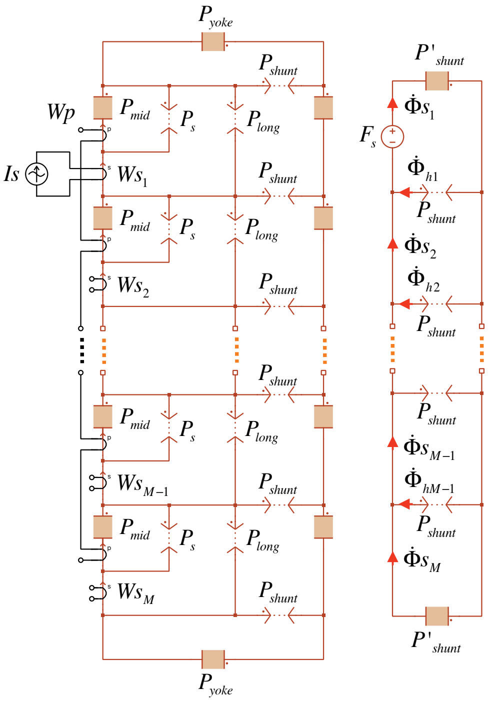

(a) **(b)**

Figure 9.16 Demonstration of the unbalanced coupling II (a) Magnetic circuit of the transformer with current I_s flowing on the secondary winding W_{s1} and other secondary windings as well as the primary winding are left open; (b) Simplified magnetic circuit where the core limb permeances are neglected and the two permeances $\mathscr{P}_{\text{yoke}}$ representing the core yoke are merged into $\mathscr{P}_{\text{shunt}}$ ($\mathscr{P}'_{\text{shunt}}$).

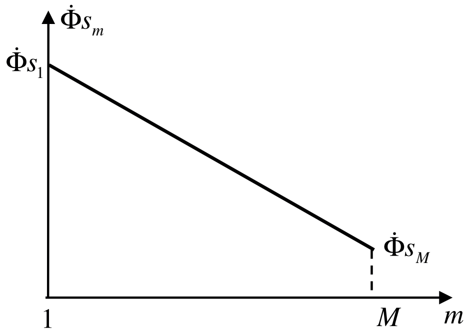

Figure 9.17 Flux rate of secondary windings against the division index.

Fig. 9.16b, following the first Kirchhoff's law yields

$$\dot{\Phi}_{\text{s(m+1)}} = \dot{\Phi}_{\text{s(m)}} - \dot{\Phi}_{\text{h(m)}} \tag{9.15}$$

Since the horizontal flux rates $\dot{\Phi}_{\text{hm}}$ are greater than zero and they have the same value in all the divisions (due to the same horizontal permeance value $\mathscr{P}_{\text{shunt}}$), a linear function can be used to describe the distribution of the secondary winding flux rates $\dot{\Phi}_{\text{h(m)}}$ with respect to the winding index, as demonstrated in **Fig. 9.17**. The relation $\dot{\Phi}_{s(m+1)} < \dot{\Phi}_{s(m)}$ indicates the fact that the closer the secondary winding is located to W_{s1}, the better flux coupling is present. All the phenomenon from the analysis above has been observed from the experimentally measured short-circuit impedance in **Sec. 9.3**.

9.5 Experimental verification with diode rectifiers

In this section, the fidelity of the proposed model in system-level simulation combined with power electronic converters is verified via experimental test. In verification scheme A the primary winding is excited by 115V (RMS), 400Hz sinusoidal voltage generated from programmable AC source 61700 of Chroma, while five secondary windings W_{s1}, W_{s6}, W_{s7}, W_{s8} and W_{s9} are connected to five totally identical full bridge rectifiers supplying constant resistive loads of $R_L = 15\Omega$, filtered by DC capacitors of $C_{dc} = 3mF$, as depicted in **Fig. 9.18**.

The system level simulation model has been established in PLECS/Simulink complying to the experimental setup, using the same transformer model discussed in **Sec. 9.3**, as **Fig. 9.19** demonstrates. For

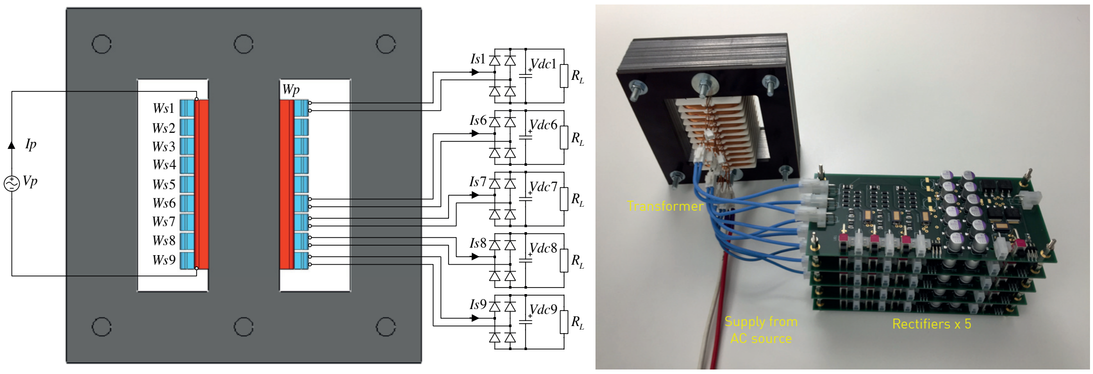

(a) (b)

Figure 9.18 Schematic and photo of the system-level test setup with five diode rectifiers connected (configured for verification scheme A with secondary windings W_{s1}, $W_{s6} \sim W_{s9}$ connected to rectifiers)

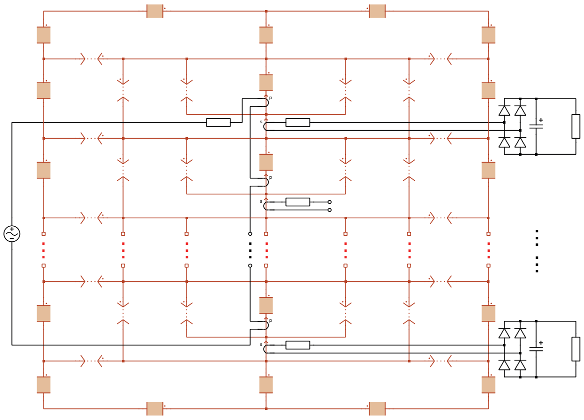

Figure 9.19 System-level simulation model with diode rectifiers connected

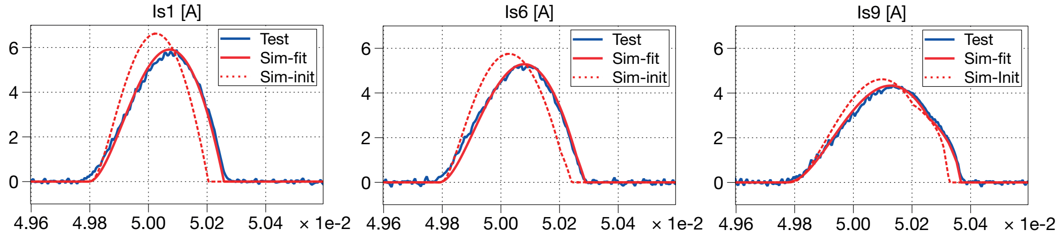

Figure 9.20 Comparison of secondary currents in verification scheme A between measurement and simulation (solid curve), additionally to simulation result obtained with initial permeance values (dashed curve)

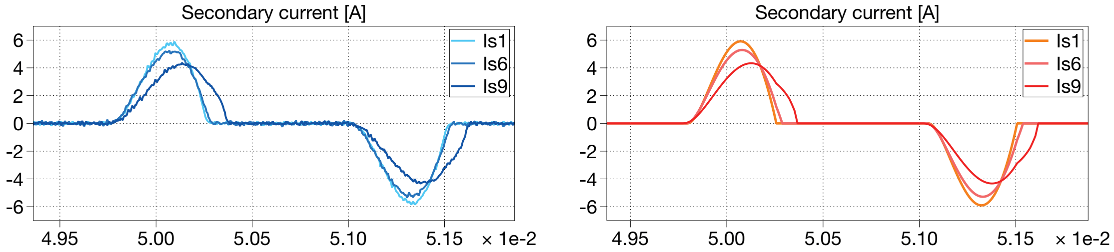

(a) **(b)**

Figure 9.21 Secondary winding currents in verification scheme A, with primary winding supplied, secondary windings $W_{\mathrm{s}1}$, $W_{\mathrm{s}6} \sim W_{\mathrm{s}9}$ connected to rectifiers, (a) Test measurement (b) PLECS/Simulink simulation

the sake of fast system-level simulation, all the rectifier diodes are modeled as ideal switch in series connection with constant resistor, which represents the linearized forward characteristic obtained from manufacturer's data sheet. The secondary windings which are unconnected in the test setup are left as open circuit in the simulation model. The grid side voltage is modeled simply as an ideal sinusoidal voltage source without internal impedance, which corresponds to the terminal behavior of the programmable AC source.

In **Fig. 9.20** the simulated current on secondary windings $W_{\mathrm{s}1}$, $W_{\mathrm{s}6}$ and $W_{\mathrm{s}9}$ after parameter fitting and the ones directly using initial values obtained from equation (3) till (5) are compared to measurements from the experimental setup. The simulation result after parameter fitting is significantly closer to measurement than that with initial values. In **Tab. 9.6** quantitative comparison of the current RMS values is made, where the simulated result after parameter fitting presents a maximum error of only 1.3%, while the ones using initial values has 8.0%. This indicates that the fitting process which takes real measurement as reference is able to significantly reduce the error of the model.

Table 9.6 RMS value of the secondary winding currents from measurement and simulation in verification scheme A [A]

Secondary RMS current	$I_{\mathrm{s}1}$	$I_{\mathrm{s}6}$	$I_{\mathrm{s}9}$
Measured from experimental setup	2.40	2.24	2.00
Simulated with fitted $\mathscr{P}_{\mathrm{s}}$, $\mathscr{P}_{\mathrm{long}}$, $\mathscr{P}_{\mathrm{shunt}}$	2.43	2.26	2.01
Simulated with initial $\mathscr{P}_{\mathrm{s}}$, $\mathscr{P}_{\mathrm{long}}$, $\mathscr{P}_{\mathrm{shunt}}$	2.59	2.37	2.10

Further in **Fig. 9.21** the current of the three secondary windings are displayed in the same plot and compared between measurement and simulation. Please note that although all the rectifiers are identically constructed and loaded, the current flowing on secondary winding W_{s9} however, is significantly lower in amplitude than that on W_{s1}, also with obvious phase shift. In comparison, the current on W_{s5} closely resembles to that on W_{s1}. The measured current on the other two secondary windings W_{s7} and W_{s8} are located just between I_{s5} and I_{s9} (not included into **Fig. 9.21**). This unbalance can be ascribed to the winding-position-related leakage flux coupling, which has been accurately captured by the proposed transformer model. Moreover, the magnetic circuit model allows to observe the flux distribution among the individual permeances, **Fig. 9.22** demonstrates the simulated magnetic flux flowing through the leakage permeances of the type II magnetic circuit divisions belonging to W_{s1}, W_{s6} and W_{s9}, where strong unbalance is present.

In verification scheme B, the first rectifier remains its connection to the secondary winding W_{s1}, while the other four are shifted for one secondary winding upwards, that is, reconnected to the secondary windings $W_{s5} \sim W_{s8}$. The current on the secondary windings W_{s1}, W_{s5} and W_{s8} are compared again between measurement and simulation in **Fig. 9.23** and **Fig. 9.24**. Here the difference between secondary winding currents becomes smaller, in comparison to verification scheme A. Should the four rectifiers be shifted further upwards, the shape of secondary currents becomes nearly identical, (**Fig. 9.25** and **Fig. 9.26**). Again the simulation model is able to capture the same behavior of the experimental setup.

The results presented above demonstrate that the proposed model has the potential to reproduce the issues related to the unbalanced leakage flux distribution in system-level dynamic simulation. If customized to individual magnetic structures, this type of model may help engineers with improvement of control algorithm or proper selection of electrical components to compensate affects from the magnetic unbalance. Taking the verification case presented in this chapter as example, since the rectifier input current is directly related to the ripple current of the DC-link capacitor, which strongly

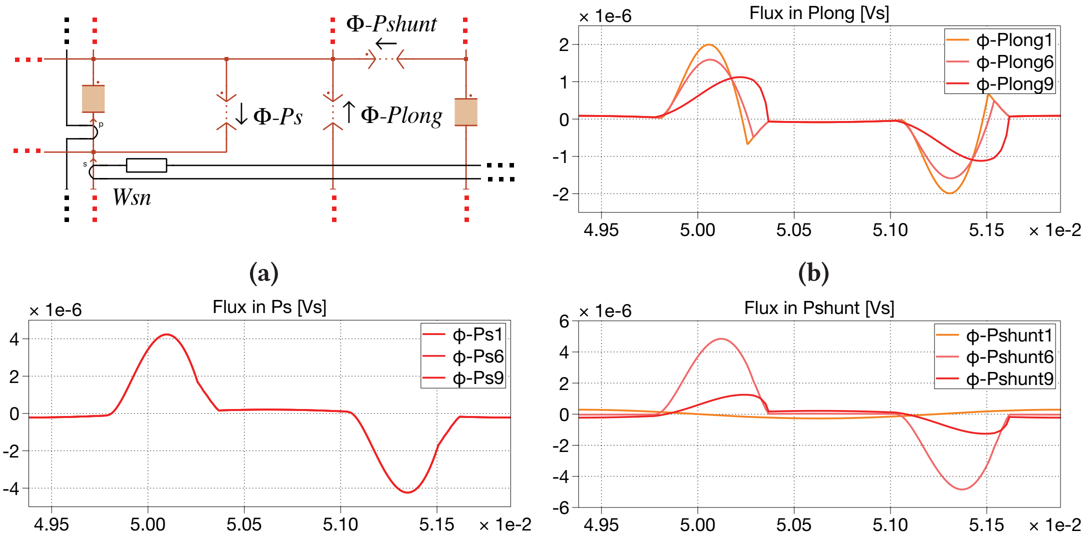

(a) (b)

(c) (d)

Figure 9.22 Simulated flux in the magnetic circuit divisions including secondary windings W_{s1}, W_{s6} and W_{s9} (a) Illustration of flux measurement positions in each magnetic circuit division (b) Simulated flux on $\mathscr{P}_{\mathrm{long}}$ (c) Simulated flux on $\mathscr{P}_{\mathrm{s}}$ (d) Simulated flux on $\mathscr{P}_{\mathrm{shunt}}$

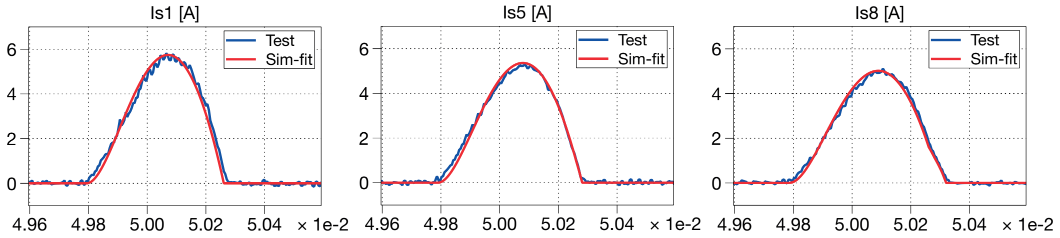

Figure 9.23 Comparison of secondary currents in verification scheme B between measurement and simulation

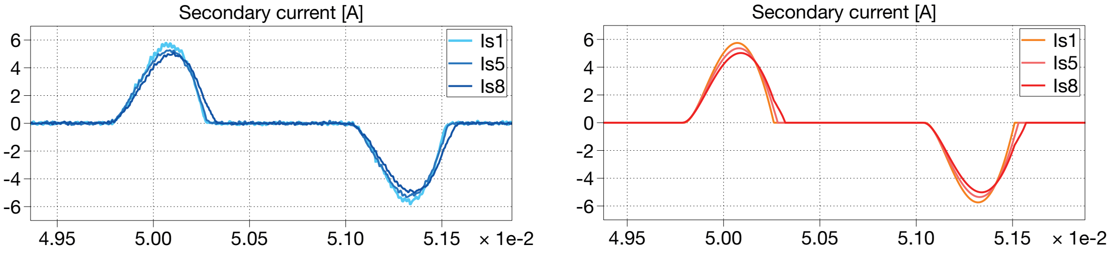

(a) **(b)**

Figure 9.24 Secondary winding currents in verification scheme B, with primary winding supplied, secondary windings W_{s1}, $W_{s5} \sim W_{s8}$ connected to rectifiers, (a) Test measurement (b) PLECS/Simulink simulation

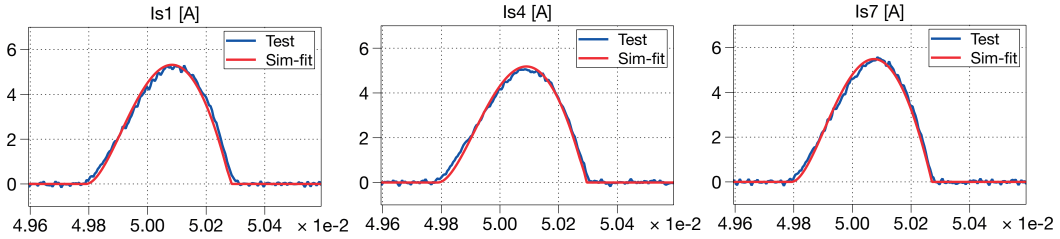

Figure 9.25 Comparison of secondary currents in verification scheme C between measurement and simulation

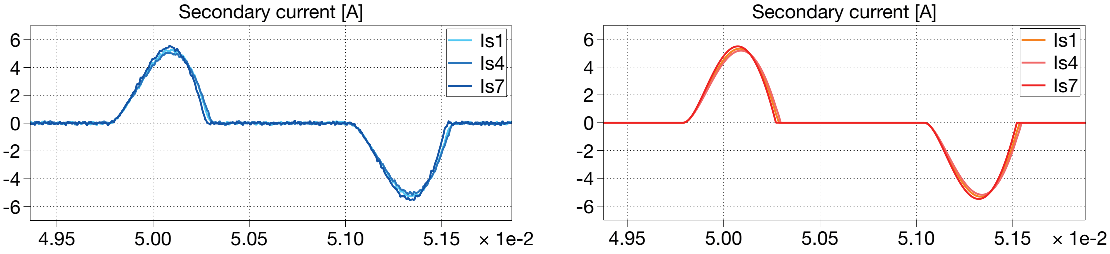

(a) **(b)**

Figure 9.26 Secondary winding currents in verification scheme C, with primary winding supplied, secondary windings W_{s1}, $W_{s4} \sim W_{s7}$ connected to rectifiers, (a) Test measurement (b) PLECS/Simulink simulation

affect the capacitors' lifetime [84]. In practice it is desired to identify the ripple current in converter design-phase to select proper type of capacitors [85], for which the system-level simulation of the whole converter with the proposed transformer model integrated would provide a good reference.

9.6 Summary

This chapter has demonstrated the modeling of single-phase multi-winding transformer using permeance-capacitance based magnetic circuit. The proposed model has the potential to reproduce circuit issues related to the unbalance in leakage flux coupling when integrated into system-level simulation combined with power converters. Via making use of information about the repetitive and symmetrical geometry, the parameter identification process of the leakage flux path can be done from only a few experimental tests. The result from the proposed model shows good match to the hardware test, under a plenty of short-circuit schemes and in operation combined with power electronic converters. With the proposed model, effects that arise from the unbalanced leakage flux path could potentially identified during the design phase of the power converters. **Chap. 10** extends this approach to 3-phase phase-shifted transformers in commercial medium voltage drive application with different winding configurations.

10

Model of leakage flux for 3-phase multi-winding transformer

In this chapter, the magnetic circuit model of leakage flux coupling proposed in the ***Chap. 9*** *is extended to three phase MV transformers with phase-shift winding configuration, which is applied in commercial drive systems.*

10.1 Literature review

Phase-shift transformers are widely used in medium voltage AC to AC converter systems to interface the power grid. These types of transformers usually have multiple secondary winding groups supplying line-commutated rectifiers. They are configured to be star-, delta-, or mixed connections which generate different phase-shift angles. In order to achieve optimal harmonic cancellation of the grid current on the primary winding side, the phase-shift angles referenced to the primary phase voltage are usually chosen as [86]

$$\theta = 60^\circ \cdot (K - 1)/N - 30^\circ \tag{10.1}$$

where N is the total number of secondary winding groups, and $K = 1 \ldots N$ the index of the secondary winding groups. Among the MV converter systems using phase-shift transformers, one typical topology, the cascaded H-bridge (CHB) converter, patented by Robicon Corporation [82] has become popular in medium voltage (MV) drive applications. CHB converter has the advantages such as good fault-tolerance ability [87], and in particular, simplicity and rather low cost due to the ability to realize medium voltage drive using low voltage semiconductors. This type of converter is composed of multiple power cells as depicted in **Fig. 10.1**. Each power cell consists of a three-phase diode rectifier and a single-phase H-bridge inverter. The phase-shift transformer is used to provide isolated AC voltage sources for each of the rectifiers. In order to improve the harmonic content of the voltage and reduce the switching frequency on the inverter output, high number of power cells are desired so that the phase-shift transformer usually has a large number of secondary windings. In such a kind of transformer, non-identical position of the individual windings may lead to different leakage flux coupling, which gives rise to unbalanced short-circuit impedances [71]. This unbalance is directly reflected in the dynamic behavior of the converter system, especially the current flowing out of the secondary winding groups, which directly determines the winding loss and the selection of the rectifier diodes including their thermal system design. Moreover, the ripple current of the DC-link

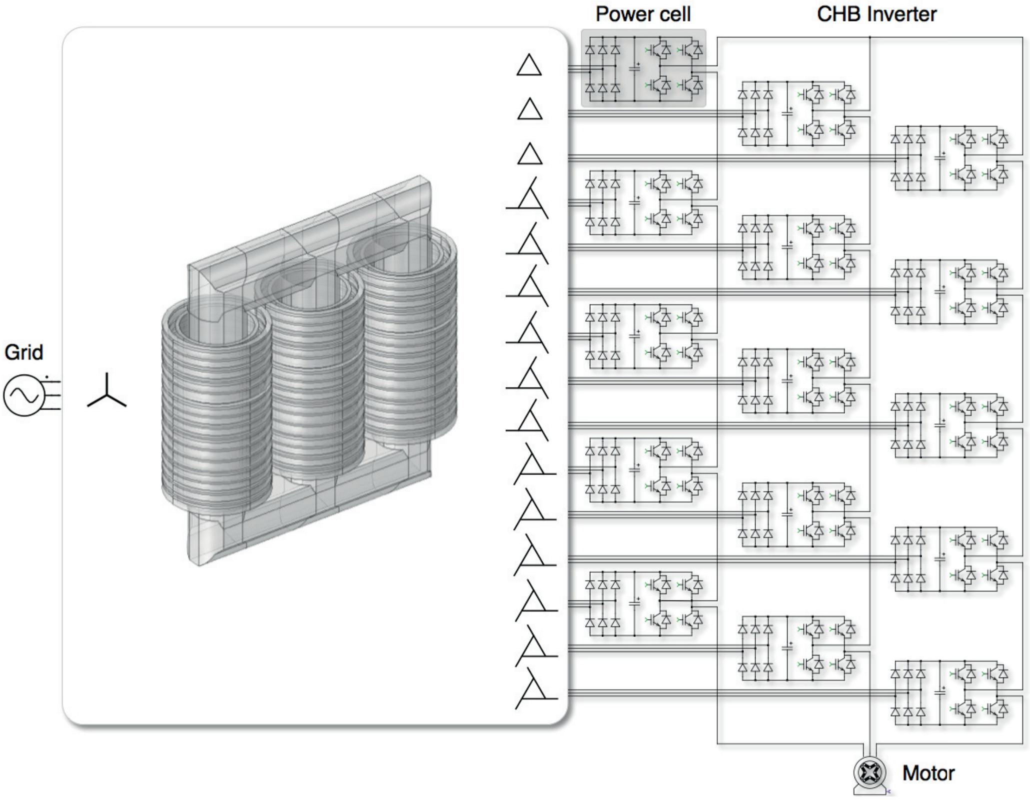

Figure 10.1 Typical topology of cascaded H-bridge converters in MV drive application.

capacitors is also affected. The analysis made in [85] demonstrated that the leakage inductance of the phase-shift transformer has direct contribution to the ripple current of the DC-link capacitors in CHB converters, which highly affects the capacitors' lifetime [84].

Using accurate transformer models which can be combined with power electronic circuit for system-level dynamic simulation, the potentially negative effect of the unbalance can be evaluated conveniently. From the simulation results, the appropriate components can be selected for the converter system, also the control algorithm and protection method can be optimized.

In comparison to the single phase structure discussed in **Chap. 9**, this chapter is extended for the phase shift transformer in the following aspects:

- The methodology of modeling the leakage magnetic flux path is extended to three-phase case of the phase-shift transformers in CHB converters, the fidelity of which is verified on a real transformer from a commercial product.
- In this chapter, the geometry non-idealities of extra gap between some of the secondary windings and unaligned primary winding position are covered, which exist in the reality due to design insulation coordination.
- The intuitive representation of complex phase-shift winding configuration using gyrator structure in permeance-based magnetic circuit is demonstrated, which was not covered by the single-phase case.

In **Sec. 10.2**, model with ideally balanced leakage flux path is established including the representation of complex winding configuration. Afterwards in **Sec. 10.3**, the improved model with unbalanced coupling is described, followed by the experimental verification via short-circuit tests in **Sec. 10.4** and connection to diode rectifiers in 10.5. Finally in **Sec. 10.6** the application of the proposed model in system-level simulation of the whole power converter system is demonstrated, and the result is compared to that from the model with ideally balanced leakage flux coupling.

10.2 Model with ideally balanced leakage flux

An available phase-shift transformer from a commercial MV drive system supplying a CHB converter is taken as a study case. The modeling is carried out only based on the nameplate data and the measurable geometrical- and electrical characteristics, since the detailed internal design specification of this transformer is not provided by the manufacturer. The rated parameters from the nameplate are listed in **Tab. 10.1**.

Table 10.1 Rated parameters of the MV phase-shift transformer

Parameter	Value	Parameter	Value
Apparent power	1 MVA	Primary current	96.2 A
Frequency	50 Hz	Secondary voltage	710 V
Primary voltage	6.3 kV	Secondary current	54.2 A

The geometrical structure of the transformer has been depicted in **Fig. 10.2a**, which is composed of a

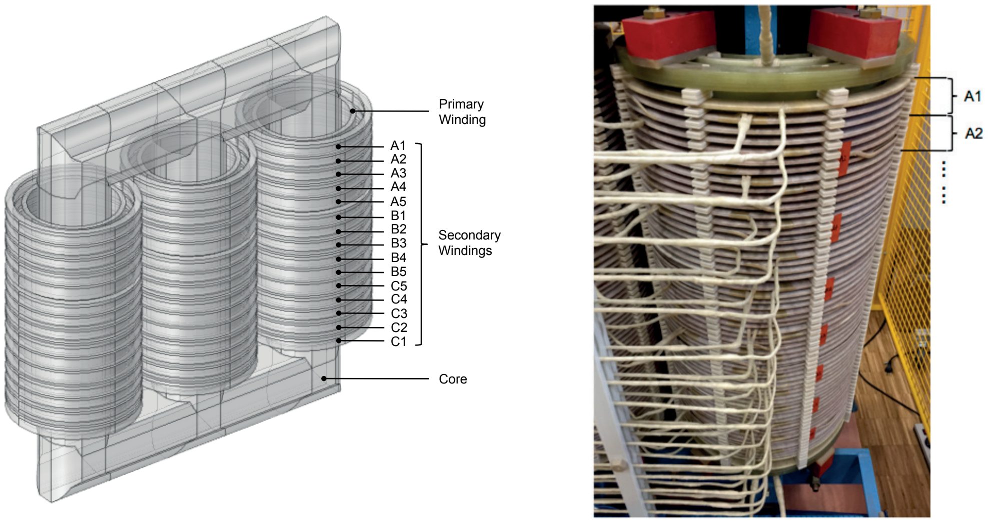

(a)

(b)

Figure 10.2 Structure of the phase-shift transformer with one primary- (W_{p}) and 15 secondary windings ($W_{\mathrm{s,A1}}...W_{\mathrm{s,A5}}$, $W_{\mathrm{s,B1}}...W_{\mathrm{s,B5}}$, $W_{\mathrm{s,C5}}...W_{\mathrm{s,C1}}$): (a) 3-D draft; (b) Photo of the secondary windings belonging to the input phase “w”.

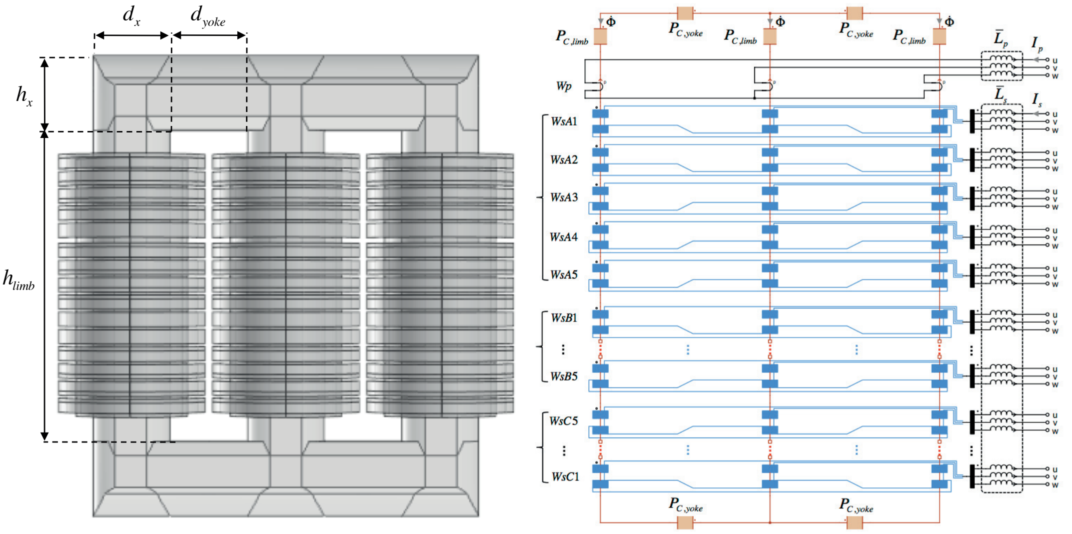

(a) **(b)**

Figure 10.3 (a) Core geometry of the transformer; (b) Model of the transformer including magnetic- and electrical circuit with ideally balanced leakage inductances.

three-limb laminated core, one primary winding and 15 secondary windings. The secondary windings are stacked vertically in succession and wound concentrically around the long primary winding on each of the three legs, they are divided into three groups denoted by A, B and C. Within each of the three groups, the secondary windings numbered with 1~5 are made up of multiple electrically isolated sub-windings that are connected in different configurations to get the desired phase shifts. The basic model can be established as shown in **Fig. 10.3b**. The three-leg iron core is modeled as magnetic circuit in an intuitive way, the permeance blocks $\mathscr{P}_{\text{C,limb}}$ represent the three limbs, while $\mathscr{P}_{\text{C,yoke}}$ represent the yokes together with the corners. The permeance values can be calculated using the formula introduced by [63] with the geometrical parameters of the transformer core (marked in **Fig. 10.3a**).

$$\mathscr{P}_{\text{C,limb}} = \mu_{\text{C}} \cdot \frac{A_{\text{C}}}{h_{\text{limb}}} \tag{10.2}$$

$$\mathscr{P}_{\text{C,yoke}} = \mu_{\text{C}} \cdot \frac{A_{\text{C}}}{h_{\text{yoke}} + (h_{\text{x}} + dx) \cdot \pi/4} \tag{10.3}$$

where μ_{c} is the permeability of the core material and A_{c} the cross-section area of the core limb and yoke. These informations are usually directly available, either from the datasheet of the manufacturer or via measurement of geometry.

The gyrator structure demonstrated in **Fig. 10.4** is adopted to represent the windings of the transformer, which serves as interface between the magnetic- and electrical circuit. The primary winding W_{p} is modeled as three simple gyrator blocks, which are star-connected in the electrical circuit. Each

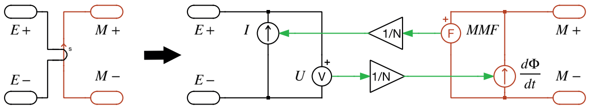

Figure 10.4 Gyrator structure of the winding component

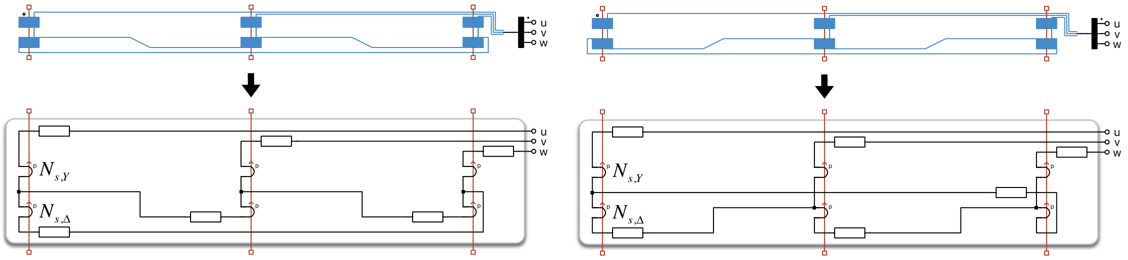

(a) **(b)**

Figure 10.5 Magnetic- and electrical circuit model of the secondary winding (a) with positive phase shift; (b) with negative phase shift.

secondary winding is composed of six gyrator blocks with interconnection in the electrical circuit, as depicted in **Fig. 10.5**, which represent the star- (turns number $N_{\mathrm{s,Y}}$) and delta part (turns number $N_{\mathrm{s},\Delta}$) of the mixed connection. The gyrator representation significantly facilitates the modeling thanks to the intuitive geometrical relation to the real transformer, without the need of deriving a complex electrical equivalent. $N_{\mathrm{s,Y}}$ and $N_{\mathrm{s},\Delta}$ of all the secondary windings can be counted from the real transformer directly, which account for different phase-shift angles referring to the primary side, as has been listed in **Tab. 10.2**.

Table 10.2 Phase-shift and turns number of the secondary windings

	$W_{\mathrm{s,A1(B1,C1)}}$	$W_{\mathrm{s,A2(B2,C2)}}$	$W_{\mathrm{s,A3(B3,C3)}}$	$W_{\mathrm{s,A4(B4,C4)}}$	$W_{\mathrm{s,A5(B5,C5)}}$
Angle	$+18^\circ$	$+6^\circ$	-6°	-18°	-30°
$N_{\mathrm{s,Y}}$	15	30	30	15	0
$N_{\mathrm{s},\Delta}$	40	13	13	40	64

Please note that the winding resistance is series connected in the electrical part of the circuit, for star- and delta part of the winding. The resistance value R_{w} can be approximated as

$$R_{\mathrm{w}} = \rho_{\mathrm{cu}} \cdot l_{\mathrm{w}} / A_{\mathrm{w}} \tag{10.4}$$

where ρ_{cu} is the resistivity of copper, $_{\mathrm{w}}$ is the conductor length of the star- or delta part of the winding, and A_{w} is the conductor cross-section area. l_{w} and A_{w} can be directly obtained from the real transformer.

The magnetic circuit together with the winding components have covered the main magnetic flux path which is constrained inside the iron core. The interface behavior on the winding terminals is equivalent to the conventional electrical circuit model using coupled inductors. The leakage flux path however, is still missing. In order to introduce the leakage flux path into the circuit, one conventional way is to connect electrical inductors $\overline{L}_{\mathrm{p}}$ and $\overline{L}_{\mathrm{s}}$ in series with the winding terminals, which represent the leakage inductance of the primary and secondary windings, as shown in **Fig. 10.3b**. For simplification, the same inductance value $\overline{L}_{\mathrm{s}}$ can be assigned to the inductors connected to the secondary windings. $\overline{L}_{\mathrm{p}}$ and $\overline{L}_{\mathrm{s}}$ are given using the equations below, as an approximation.

$$\overline{L}_{\mathrm{p}} = L_{\mathrm{k,Test}}/2 \tag{10.5}$$

$$\overline{L}_{\mathrm{s}} = (L_{\mathrm{k,Test}}/2) \cdot 15 \cdot (710/6300)^2 \tag{10.6}$$

L_{k} is the equivalent inductance looking into the primary winding, which is measured from the test scheme with the primary winding supplied and all the secondary windings short-circuit at the same time. 6300 V and 710 V are the nominal voltage (**Tab. 10.1**) of the transformer's primary and secondary side. Here it is assumed that the leakage flux path of the individual windings are identical and totally decoupled from each other. This assumption, which is usually made in practice and make the ideal model rather simple, is however not representative enough of the real transformer. In reality, the windings are not only linked via the flux path inside the iron core, but also via the leakage flux path through the air. The strength of the air-path linkage between the windings is strongly influenced by the relative positioning, this will result in unbalanced leakage inductance looking into the individual windings. In the following sections of this chapter, this unbalance is demonstrated in experimental test, and the modeling's approach covering the unbalance in leakage flux path is introduced.

10.3 Proposed model with unbalanced leakage flux

In the case of phase shift transformer, the model of unbalanced leakage flux path is established by extending the magnetic circuit of the ideal model with leakage permeances, instead of connecting identical inductors in the electrical circuit. Similar to the single-phase prototype transformer which was discussed in **Chap. 9**, here the primary winding is also distributed over the length of the core limbs, while the secondary windings are stacked vertically in succession. Recall that the modeling's approach proposed by **Chap. 9** requires that the secondary windings have repetitive structure, so that only a few number of permeance values are required to parametrize the leakage flux path. This requirement is fullfilled in the phase-shift transformer as well. As marked in **Fig. 10.2b**, one single phase of each secondary windings is composed of four conductor bundles (in **Fig. 10.2a** they are displayed as one solid block), the overall height and radius of the four bundles together are approximately identical between different secondary windings. In this sense, the modeling of the phase-shift transformer using permeance-capacitor based magnetic circuit can be carried out in a similar way as **Chap. 9**.

To derive the magnetic circuit model, the geometry of the transformer is separated into divisions along the vertical axis. Fifteen divisions of type 1 have been defined, the position of which are highlighted in **Fig. 10.6a** in blue color divided by dashed lines. All of this type of divisions have the same height equal to $h_{\mathrm{Div1}} = 49mm$, each one includes one section of the three core limbs, one complete secondary

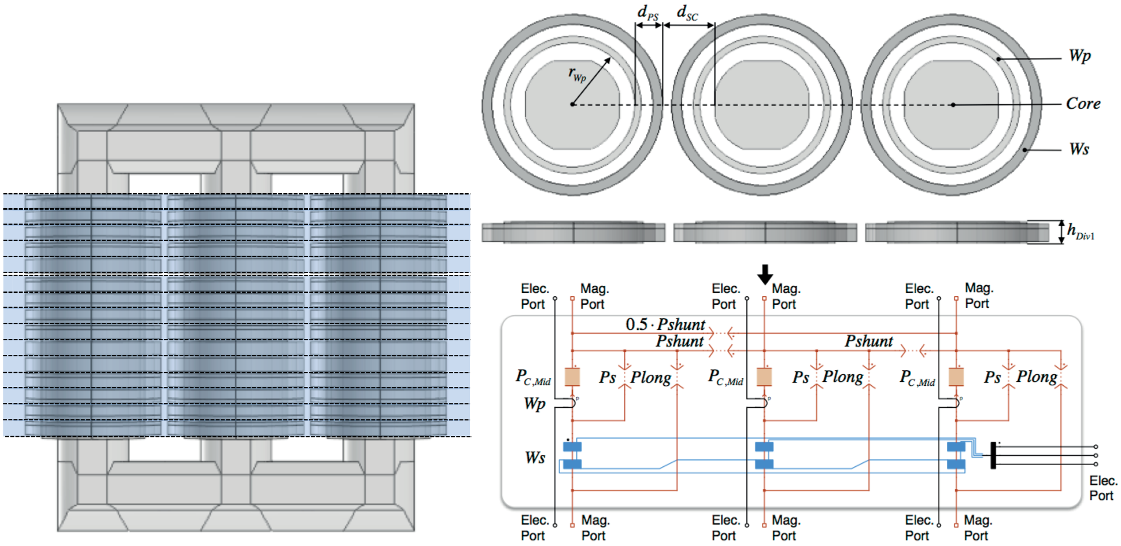

(a) (b)

Figure 10.6 Divisions of type 1 (a) Position in the transformer; (b) Cross section and permeance magnetic circuit with the flux path of the core and air.

winding, and one section of the primary winding of three phases. The division contains the secondary winding $W_{s,A3}$ is taken out from the transformer geometry as an example, the magnetic circuit of which shown in **Fig. 10.6b** is established resembling the physical geometry slice (above the magnetic circuit in the same figure, view from the top and front). This magnetic circuit inherits the structure proposed by [25] as an extension into three phase. The three permeance blocks filled with solid color represent flux path inside the transformer core, the value of which can be calculated as

$$\mathscr{P}_{\mathrm{C,Mid}} = \mu_{\mathrm{C}} \cdot A_{\mathrm{C}} / h_{\mathrm{Div1}} \tag{10.7}$$

Compared to the ideal model described in **Sec. 10.2**, the core permeances $\mathscr{P}_{\mathrm{C,limb}}$ representing the whole limb in **Fig. 10.3b** are now distributed into different divisions. Besides the core permeances, the other permeance blocks $\mathscr{P}_{\mathrm{s}}$, $\mathscr{P}_{\mathrm{long}}$ and $\mathscr{P}_{\mathrm{shunt}}$ represent the leakage flux path through the air, following the definition made in **Sec. 9.4**. They can be parametrized using only a few number of experimental tests, which is discussed later. Thanks to the approximately identical geometry, the magnetic circuit of all 15 divisions can share the same permeance values $\mathscr{P}_{\mathrm{c1}}$, $\mathscr{P}_{\mathrm{s}}$, $\mathscr{P}_{\mathrm{long}}$ and $\mathscr{P}_{\mathrm{shunt}}$. One should pay attention that, in comparison to the structure of single phase transformer presented in **Fig. 9.14b**, the additional horizontal permeance between the two side limbs stands for the inter-phase leakage flux coupling, the value is one half of the others, that is $0.5 \cdot \mathscr{P}_{\mathrm{shunt}}$. The factor 0.5 is applied due to the fact that the magnetic path length between the two side limbs can be considered to be twice of the one between the middle- and side limb, and the permeance value is

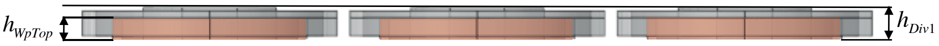

Figure 10.7 Type 1 division including secondary winding W_{sA1} with shorter primary winding section.

inversely proportional to the magnetic path length.

Each phase of the primary winding has $N_\mathrm{p} = 323$ turns in total and the overall height is $h_\mathrm{Wp} = 734mm$. The turns number of the primary winding block distributed in each of the type 1 division (except for the one including W_sA1) can be approximated as the total number of turns multiplied by the ratio between the height of division and the height of the whole primary winding.

$$N_\mathrm{p,Div1} = N_\mathrm{p} \cdot h_\mathrm{Div1}/h_\mathrm{Wp} = 21.6 \tag{10.8}$$

Special attention needs to be paid on the geometrical asymmetries, which was not covered by the **Chap. 9** and is discussed in the following part of this section:

The first kind of asymmetry is the unaligned vertical position of the primary winding with respect to the secondary windings, which is firstly reflected in the division containing W_sA1 located on the very top of all other secondary windings. As shown in **Fig. 10.7**, the primary winding section in this division spans from the bottom only up to $h_\mathrm{Wp,Top} = 32.5mm$, which is lower than the total height of the whole division h_Div1. Following the same idea of equation (10.8), the primary winding component in this division should be calculated as:

$$N_\mathrm{p,Div1Top} = N_\mathrm{p} \cdot h_\mathrm{WpTop}/h_\mathrm{Wp} = 14.3 \tag{10.9}$$

In this way, $N_\mathrm{p,Div1Top}$ becomes lower than $N_\mathrm{p,Div1}$.

Attached to the type 1 division containing the secondary winding W_sC1, one division of type 2 is defined as highlighted in **Fig. 10.8a**, where the primary winding is partly out of the vertical range of

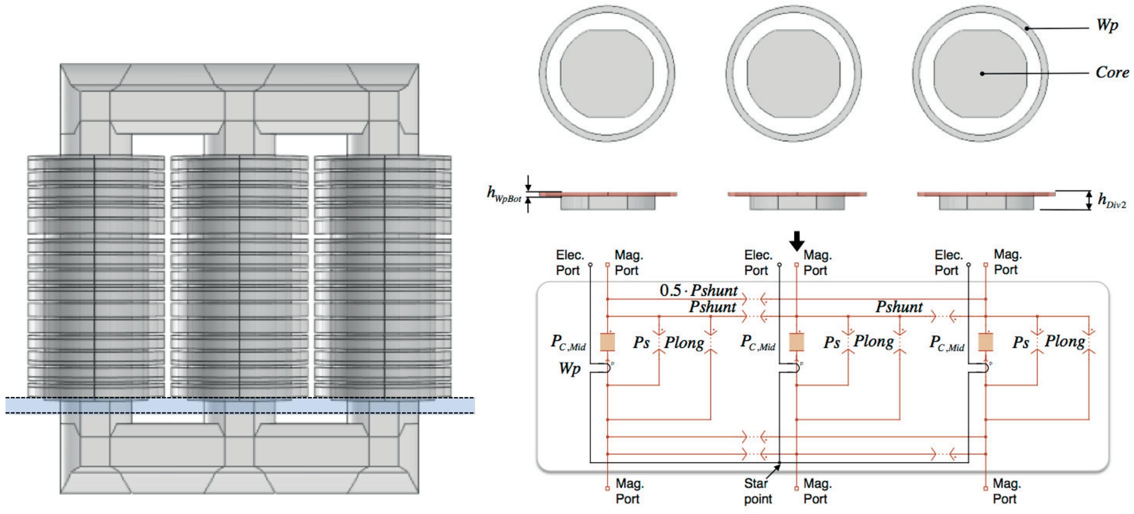

(a) (b)

Figure 10.8 Divisions of type 2 (a) Position in the complete transformer; (b) Cross section and permeance magnetic circuit with the flux path of the core and air.

the secondary windings. The magnetic circuit of this division is demonstrated in **Fig. 10.8b**, which has similar structure as that in **Fig. 10.6b**, except for the absence of secondary winding. The height h_{Div2} of this section is selected to be equal to that of the division type 1, so that the permance blocks representing the core and leakage flux path have the same value as in division type 1. In the real transformer, the three phases of the primary winding are in star connection and the start point is located at the bottom, thus the low-side electrical port of the three primary winding components in this division are connected together. Similar to the type 1 division including W_{sA1}, here the height of the primary winding section h_{WpBot} is also significantly lower than the division height h_{Div2}. Therefore the turns number of the primary winding block in this division should be calculated proportional to the height as well.

$$N_{\text{p,Div2Bot}} = N_{\text{p}} \cdot h_{\text{WpBot}}/h_{\text{Wp}} = 3.3 \tag{10.10}$$

The second kind of asymmetry is reflected on the gaps between the windings, which are defined to comply with dielectric requirements. The windings belonging to the same output phases (A, B or C) are placed close to each other, with a small gap in between. The windings in output phase “C” are arranged up-side-down in comparison to phase “A” and “B”, so that W_{sB5} and W_{sC5} locate directly next to each other. Since the output terminal of the power cells supplied by W_{sB5} and W_{sC5} are both connected to the star point of the load, the voltage stress between these two secondary windings is the same as that inside one output phase, so that the same gap can be applied. In comparison, W_{sA5} has to be kept far away from W_{sB1} due to large voltage stress which can be as high as five times of the DC-link voltage, therefore larger gap has been inserted between them. In order to capture the influence of this excessive gap, one extra division of type 3 is defined between W_{sA5} and W_{sB1}, as highlighted in **Fig. 10.9b**. The height of this extra gap division is equal to $h_{\text{Div3}} = 8mm$ and the magnetic circuit model is depicted in **Fig. 10.9b**. Similar to the division of type 2, the magnetic circuit of the gap division only contain primary winding blocks. One should pay attention that the height of

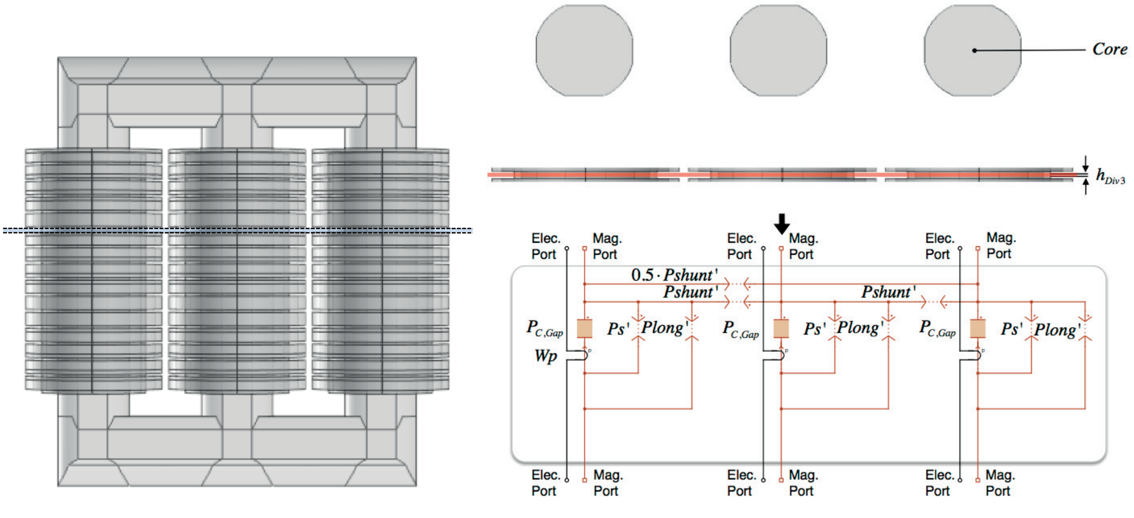

(a) **(b)**

Figure 10.9 Divisions of type 3 (a) Position in the complete transformer; (b) Cross section and permeance magnetic circuit with the flux path of the core and air.

this division is not the same as type 1 and 2, so that the permeance values $\mathscr{P}_{\mathrm{C,Mid}}$, $\mathscr{P}_{\mathrm{s}}$, $\mathscr{P}_{\mathrm{long}}$ and $\mathscr{P}_{\mathrm{shunt}}$ can not be applied here directly. Considering the fact that the leakage permeance value is also proportional to the cross-section area and inverse proportional to the magnetic path length, $\mathscr{P}'_{\mathrm{s}}$, $\mathscr{P}'_{\mathrm{long}}$ and $\mathscr{P}'_{\mathrm{shunt}}$ can be approximated as scaling of $\mathscr{P}_{\mathrm{s}}$, $\mathscr{P}_{\mathrm{long}}$ and $\mathscr{P}_{\mathrm{shunt}}$ about the geometry. The vertical permeance values $\mathscr{P}'_{\mathrm{s}}$ and $\mathscr{P}'_{\mathrm{long}}$ are "inversely" proportional to the division height, while $\mathscr{P}'_{\mathrm{shunt}}$ is proportional to the division height.

$$\mathscr{P}'_{\mathrm{s}} = \mathscr{P}_{\mathrm{s}} \cdot h_{\mathrm{Div1}}/h_{\mathrm{Div3}} \tag{10.11}$$

$$\mathscr{P}'_{\mathrm{long}} = \mathscr{P}_{\mathrm{long}} \cdot h_{\mathrm{Div1}}/h_{\mathrm{Div3}} \tag{10.12}$$

$$\mathscr{P}'_{\mathrm{shunt}} = \mathscr{P}_{\mathrm{shunt}} \cdot \frac{(h_{\mathrm{Div1}} + h_{\mathrm{Div3}})}{2 \cdot h_{\mathrm{Div1}}} \tag{10.13}$$

Please note that $\mathscr{P}'_{\mathrm{shunt}}$ includes the horizontal leakage flux path of not only the gap but also one half of the adjacent type 1 divisions. $\mathscr{P}'_{\mathrm{shunt}}$ instead of $\mathscr{P}_{\mathrm{shunt}}$ should be also applied to the horizontal leakage permeance block in the type 1 division which is directly below the gap division containing W_{sB1}. Besides the leakage permeances, the core permeance value $\mathscr{P}_{\mathrm{C,Gap}}$ in division type 3 can be easily calculated making use of material and geometry information as

$$\mathscr{P}_{\mathrm{C,Gap}} = \mu_{\mathrm{C}} \cdot A_{\mathrm{C}}/h_{\mathrm{Div3}} \tag{10.14}$$

Moreover, the turns number of the primary winding block inside this division should be scaled as well, similar to the treatment in the division type 2.

$$N_{\mathrm{p,Div3}} = N_{\mathrm{p}} \cdot h_{\mathrm{Div3}}/h_{\mathrm{Wp}} = 3.5 \tag{10.15}$$

The modeling of the rest of the transformer is demonstrated in **Fig. 10.10**, including the core yoke, the top and bottom part of the limbs. In comparison to the divisions of type 1, since no winding is present in this part of the transformer and the permeability of the main flux path inside the core is much more dominant than that of the leakage flux path through the air, the leakage permeances can be neglected. The permeance values of the core blocks here can be calculated using material and geometrical information directly, in the similar way as equation (10.7). Between these core blocks, the divisions of type 1, 2 and 3 are stacked vertically in succession, and connected via the magnetic- and electrical ports. This yields the complete circuit model of the transformer, where the electrical terminals of the primary- (with three input phases *u*, *v*, *w*) and the secondary windings can be connected to external circuit, as **Fig. 10.10** demonstrates.

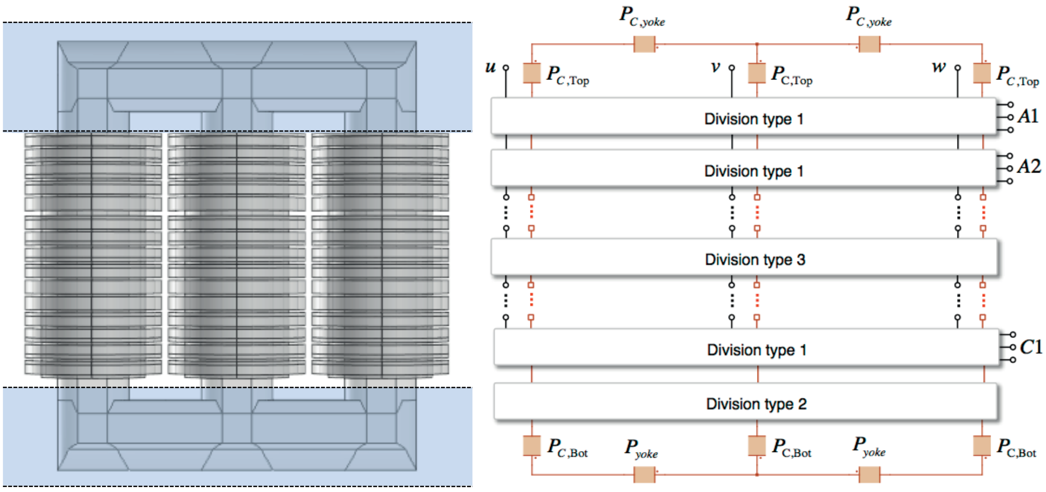

(a) (b)

Figure 10.10 Rest of the transformer geometry outside the winding area (a) Position in the complete transformer; (b) Cross section and permeance magnetic circuit with the flux path of the core and air.

Up to this stage, the core permeance and winding resistances have been determined using geometry and material information explicitly, while the value of the leakage permeances still remain undefined. There are only three parameters $\mathscr{P}_{\mathrm{s}}$, $\mathscr{P}_{\mathrm{long}}$ and $\mathscr{P}_{\mathrm{shunt}}$ needed to characterise the whole leakage flux path, which are present in the divisions of type 1, 2, 3. As has been discussed in the previous section, it is difficult to accurately define the geometry of the leakage flux path through the air, therefore a few short-circuit tests are carried out to identify the three unknown parameters, in which one single winding is supplied by voltage source and selected other windings are short-circuited. Instead of enumerating all the supply-short combinations, only five short-circuit test schemes are needed for the parameter identification which carry sufficient information about coupling between the windings, as recommended by the **Chap. 9**.

At first, the equivalent impedance looking into the supplied winding on phase "u" (**Fig. 10.10**) is calculated as the peak phase voltage divided by the peak phase current, which is essentially the modulus of the complex impedance, as listed in **Tab. 10.3**:

Table 10.3 Test schemes for leakage permeance parameter fitting of the MV phase shift transformer

	Supply	**Short**	**Fit to**
1	W_{p}	W_{sA1}	$Z_{\mathrm{k1,Test}} = \hat{V}_{\mathrm{p}}/\hat{I}_{\mathrm{p}}/(2\pi f)$
2	W_{p}	W_{sB3}	$Z_{\mathrm{k2,Test}} = \hat{V}_{\mathrm{p}}/\hat{I}_{\mathrm{p}}/(2\pi f)$
3	W_{sA1}	W_{sA2}	$Z_{\mathrm{k3,Test}} = \hat{V}_{\mathrm{sA1}}/\hat{I}_{\mathrm{sA1}}/(2\pi f)$
4	W_{sA1}	W_{sC1}	$Z_{\mathrm{k4,Test}} = \hat{V}_{\mathrm{sA1}}/\hat{I}_{\mathrm{sA1}}/(2\pi f)$
5	W_{p}	All W_{s}	$Z_{\mathrm{k5,Test}} = \hat{V}_{\mathrm{p}}/\hat{I}_{\mathrm{p}}/(2\pi f)$

After that, the leakage permeance values of the circuit model are fitted to minimize a quadratic objective function, which is the square-summation of the error between the short-circuit inductances from measurement and the one obtained from magnetic circuit simulation of the aforementioned five short-circuit schemes, given by the equation below:

$$f_{\mathrm{obj}} = \sum_{\mathrm{i=1}}^{5} (\frac{Z_{\mathrm{ki,Test}} - Z_{\mathrm{ki,Sim}}}{Z_{\mathrm{ki,Test}}})^2 \tag{10.16}$$

In high power MV transformers, inductive part in the measured short-circuit impedance is usually dominant over the resistive part, due to the less magnetic coupling as a result of the large spacing between windings, which is the case in the phase-shift transformer studied in this chapter. Therefore the amplitude of the impedance can be directly taken for parameter fitting, without extracting out the inductive component, which is different than the case of low voltage prototype transformer discussed in **Chap. 9**. Commonly used gradient based- or evolutionary fitting algorithms can be applied to find out the leakage permeance values, iteratively. Generally the fitting process can be carried out in a way demonstrated in **Fig. 10.11**. On one side, after receiving the leakage permeance values $\mathscr{P}_{\mathrm{s}}$, $\mathscr{P}_{\mathrm{long}}$, $\mathscr{P}_{\mathrm{shunt}}$ provided by the fitting algorithm before each objective function evaluation, five magnetic circuit models of the transformer which are configured complying to each of the five test schemes specified by **Tab. 10.3** are simulated in time-domain, one after each other. The simulated time-domain waveforms of winding voltage and current are converted into amplitude, so as to calculate the equivalent impedance values and yields the output of the objective function defined by equation (10.16). On the other side, the fitting algorithm retrieves the output of objective function from the last evaluation, adjusts the $\mathscr{P}_{\mathrm{s}}$, $\mathscr{P}_{\mathrm{long}}$, $\mathscr{P}_{\mathrm{shunt}}$ values and brings them into the next objective function evaluation.

Initial values need to be assigned in order to make the algorithm better converge, which for the phase-shift transformer can be calculated as below. In certain circumstances the fitting algorithm may have difficulty in convergence if $\mathscr{P}_{\mathrm{long0}}$ is exactly equal to zero, instead a small value of e.g. 10^{-7} can be chosen.

$$\mathscr{P}_{\mathrm{s0}} = \frac{\mu_0 (2 r_{\mathrm{Wp}}) d_{\mathrm{PS}}}{h_{\mathrm{Div1}}} \tag{10.17}$$

$$\mathscr{P}_{\mathrm{long0}} = 0 \tag{10.18}$$

$$\mathscr{P}_{\mathrm{shunt0}} = \frac{\mu_0 (2 r_{\mathrm{Wp}}) h_{\mathrm{Div1}}}{d_{\mathrm{SC}}} \tag{10.19}$$

The geometrical parameters r_{Wp}, d_{PS} and d_{SC} have been defined in **Fig. 10.6b**. Despite of the repetitive structure, thanks to which the whole leakage flux path can be characterized by only three permeance values, strong unbalance of short-circuit impedances will still take place, which will be discussed in the following sections.

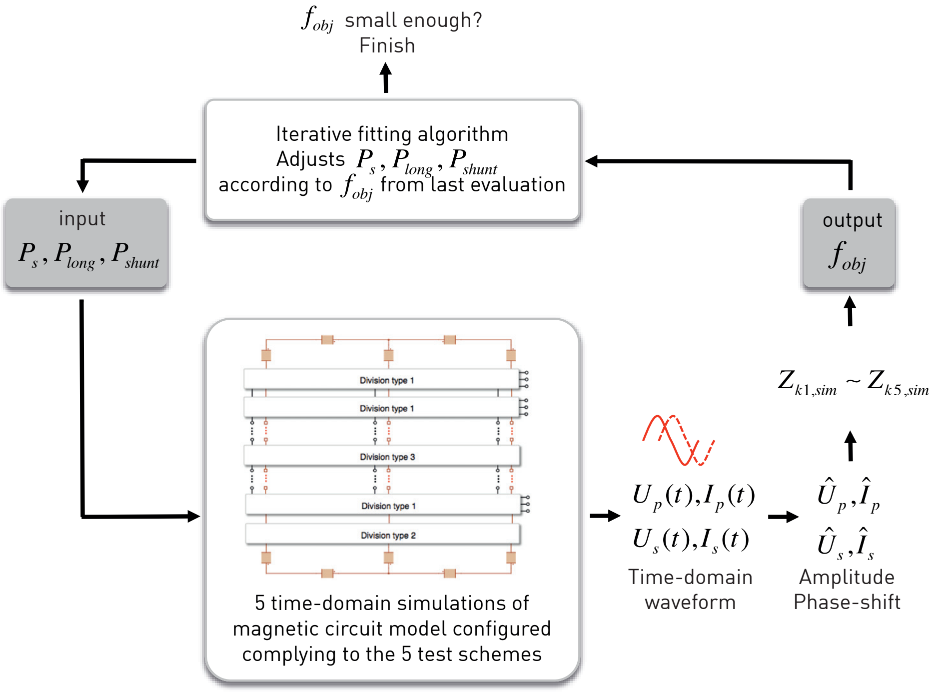

Figure 10.11 Generalized fitting process of the leakage permeance values, where the magnetic circuit model is simulated to for calculating the output of the objective function for the fitting algorithm.

10.4 Experimental verification with short circuit test

For verification of the proposed modeling's approach, the aforementioned MV phase-shift transformer was experimentally measured. In order to carry out the five short-circuit schemes for model parameter identification and further schemes for validation, a test setup is established as shown in **Fig. 10.12a**, which is composed of the following functional units:

- Connection to the 50 Hz power grid with 400 V line-to-line RMS voltage
- A variac to generate adjustable sinusoidal voltage source
- Two power analyzers to measure the winding voltage and current

After the five impedance values listed in **Tab. 10.3** have been obtained, the magnetic circuit models with the structure described in the last section is built up in the system-level simulation software PLECS (Blockset version) in combination with MATLAB/Simulink. Sinusoidal voltage sources are connected to the winding terminals to emulate the variac output in the test setup. Prior to leakage parameter identification, the permeances representing the iron core have been parametrized directly from geometry and material characteristic. Since the transformer is designed to operate far away from saturation, so that the nonlinearity of the core material has little affect on the measured short-circuit inductances, constant permeability has been assigned to the core permeances. The circuit model which is configured complying to test scheme 1 with the source applied to the primary winding W_p and secondary winding W_{sA1} shorted is demonstrated in **Fig. 10.12b**, while the ones for the other four test schemes are established in a similar way.

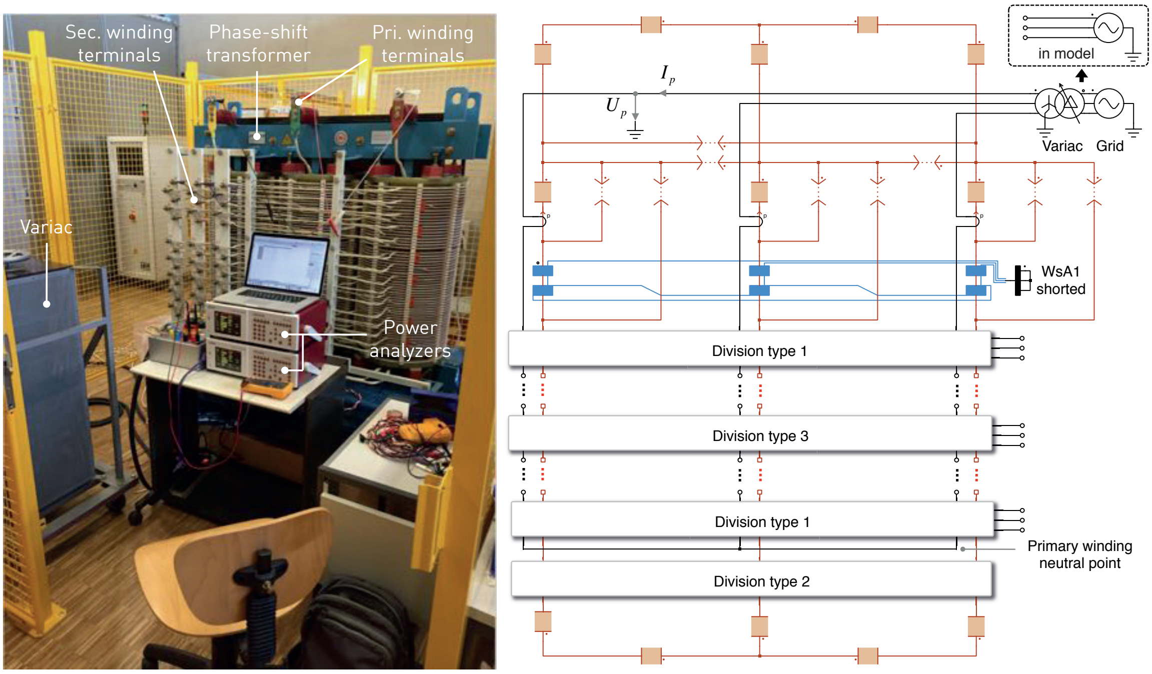

(a) **(b)**

Figure 10.12 (a) Short-circuit test setup for the phase-shift transformer, with voltage and current on the supplied winding measured; (b) Magnetic circuit model in PLECS for parameter fitting and verification (test scheme with primary winding supplied and secondary winding W_{sA1} shorted).

For parameter identification, the "fminsearch" fitting algorithm provided by MATLAB (referred as unconstrained nonlinear optimization) is adopted. The setup of the fitting algorithm including writing the customised objective function is carried out in a similar way as has been discussed in **Sec. 9.2**. The initial permeance values calculated using equations (10.17) till (10.19) and the ones obtained after parameter fitting using "fminsearch" algorithm are compared in **Tab. 10.4**.

Table 10.4 Leakage permeance values fitted to the measurements for the phase shift transformer [H]

	$\mathscr{P}_{\text{s}}$	$\mathscr{P}_{\text{long}}$	$\mathscr{P}_{\text{shunt}}$
Initial value	$490 \cdot 10^{-9}$	$100 \cdot 10^{-9}$	$101 \cdot 10^{-9}$
After fitting	$1156 \cdot 10^{-9}$	$111 \cdot 10^{-9}$	$146 \cdot 10^{-9}$

In the first group of verification schemes, the source is connected to the primary winding, meanwhile one single secondary winding is shorted. The short-circuit impedances looking into the primary winding with different secondary windings shorted are compared between measurement and magnetic circuit model in **Fig. 10.13**. Although all the secondary windings have approximately the same geometrical dimension and parameterized by repetitive permeance network, the resulted short-circuit impedances however, are unbalanced, due to difference in vertical position with respect to the primary winding. The U-shape curve reveals the fact that the more centralized the secondary winding is located with respect to the primary winding, the stronger is the coupling and thus the lower the short-circuit inductance will be, which has proved the analysis made in the **Sec. 9.4**. This U-shape

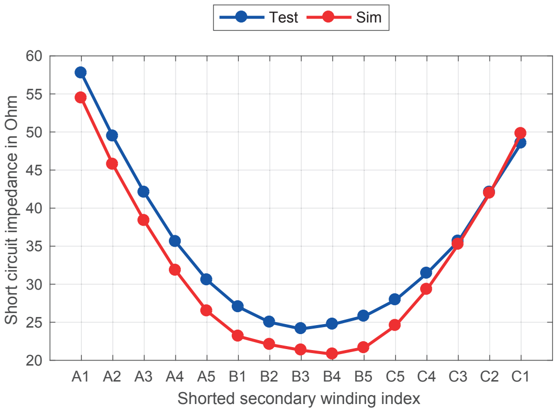

Figure 10.13 Short circuit impedances with W_{p} supplied and different single W_{s} shorted.

curve of short-circuit impedance can be considered to be the reciprocal of the flux curve in **Fig. 9.15b**, or in other words, vertically inversed.

Please note that higher impedance is present with the very top secondary winding W_{sA1} shorted than that with the very bottom W_{sC1} shorted, which reflects the effect of the unaligned vertical position of the primary winding with respect to the secondary windings (demonstrated **Fig. 10.7**), this effect has been captured by the model thanks to the turns number adjustment of the primary winding block and the insertion of a type 2 division in the magnetic circuit, as has been discussed in **Sec. 10.3**.

The short-circuit impedances in **Fig. 10.13** are obtained making use of the current on phase “u” of the primary winding, in both measurement and simulation. Besides that we have also measured the currents of the other two phases, and the comparison to simulation result in the case with W_{sA1} and W_{sB3} shorted are presented in **Tab. 10.5** and 10.6 (rows denoted by “Simulation with $0.5 \cdot \mathscr{P}_{\mathrm{shunt}}$”). Between the currents from different phases, only slight unbalance can be observed. The good match between measurement and simulation indicates that the inter-phase leakage flux coupling is also well captured, thanks to the permeance $0.5 \cdot \mathscr{P}_{\mathrm{shunt}}$ inserted between the two side

Table 10.5 Comparison of three-phase primary winding currents, with W_{p} supplied and W_{sA1} shorted

RMS current	$I_{\mathrm{p,u}}$ **[A]**	$I_{\mathrm{p,v}}$ **[A]**	$I_{\mathrm{p,w}}$ **[A]**
Measurement	4.0	3.2	3.9
Simulation with $0.5 \cdot \mathscr{P}_{\mathrm{shunt}}$	4.2	3.1	4.1
Simulation without $0.5 \cdot \mathscr{P}_{\mathrm{shunt}}$	7.0	3.1	6.4

Table 10.6 Comparison of three-phase primary winding currents, with W_{p} supplied and W_{sB3} shorted

RMS current	$I_{\mathrm{p,u}}$ **[A]**	$I_{\mathrm{p,v}}$ **[A]**	$I_{\mathrm{p,w}}$ **[A]**
Measurement	9.6	8.8	9.2
Simulation with $0.5 \cdot \mathscr{P}_{\mathrm{shunt}}$	10.8	8.7	9.8
Simulation without $0.5 \cdot \mathscr{P}_{\mathrm{shunt}}$	13.9	8.7	11.2

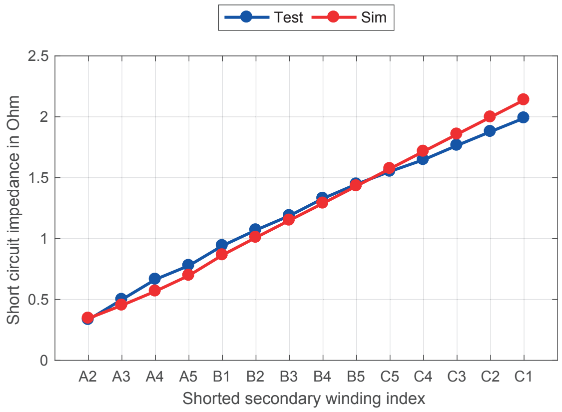

Figure 10.14 Short circuit impedances with W_{sA1} supplied and one of the other W_{s} shorted.

limbs, as demonstrated in **Fig. 9.14b**. If the leakage flux coupling between the two side limbs is neglected in the model by removing the $0.5 \cdot \mathscr{P}_{\mathrm{shunt}}$ permeance, the simulated three-phase currents become strongly unbalanced, the currents on phase "u" and "w" (on side legs) exhibits significant error compared to the measurement, as has also been included in **Tab. 10.5** and 10.6 (rows denoted by "Simulation without $0.5 \cdot \mathscr{P}_{\mathrm{shunt}}$"). In the single-phase case discussed in [25], however, since no winding is present on the side limbs, the permeance $0.5 \cdot \mathscr{P}_{\mathrm{shunt}}$ was not needed.

In the second group of verification schemes, the secondary winding W_{sA1} on the very top is supplied, meanwhile another secondary winding is shorted. The resulted impedances looking into W_{sA1} are shown in **Fig. 10.14** with different other secondary windings shorted. This shape of impedance curve is also correlated to the analysis made in the **Sec. 9.4** that the further the secondary windings are located from each other, the weaker is the leakage flux coupling in between, which can be regarded as the vertical mirror of the flux curve presented in **Fig. 9.17**. From the result comparison one can see that not only the points used for parameter identification (short W_{sA1}, W_{sB3} in **Fig. 10.13** and short W_{sA2}, W_{sC1} in **Fig. 10.14**), but also the impedance values of the other verification points match well between the proposed magnetic circuit model (built in PLECS/Simulink) and test result. The maximum error is 16.1% in **Fig. 10.13** and 14.7% in **Fig. 10.14**. If the same short circuit tests are applied to the ideal model described in **Sec. 10.2**, the simulated short circuit impedances are constant 23.7Ω and 0.59Ω for the two verification schemes, which does not match the unbalance measured from experimental setup.

Table 10.7 Winding currents on phase "u" (RMS value) with primary winding supplied, two secondary windings W_{sA1} and W_{sA2} shorted at the same time

	V_{p} [V]	I_{p} [A]	I_{sA1} [A]	I_{sA2} [A]
PLECS	232	5.12	18.2	26.3
Test	232	4.80	16.3	24.8
Error		6.6%	11.7%	6.0%

In the third group of verification schemes, the primary winding is supplied with other two secondary windings shorted at the same time. The short-circuit combination together with the short circuit

Table 10.8 Windings currents on phase "u" (RMS value) with primary winding supplied, two secondary windings W_{sA1} and W_{sC1} shorted at the same time

	V_{p} [V]	I_{p} [A]	I_{sA1} [A]	I_{sC1} [A]
PLECS	76.2	4.88	19.3	20.6
Test	76.2	4.33	17.4	19.9
Error		12.7%	10.9%	3.5%

currents are listed in **Tab. 10.7** and **Tab. 10.8**. Good match between magnetic circuit model and the measurement is present here as well with maximum error of 12.7 %.

The fourth verification scheme is the same as the fifth test scheme for parameter identification, where the primary winding is supplied by 133 V line-to-line (RMS) voltage and all the secondary windings are shorted at the same time. Here the current on each of the secondary windings is measured, and compared between test measurement and simulation in **Fig. 10.15**. Obvious unbalance is present on

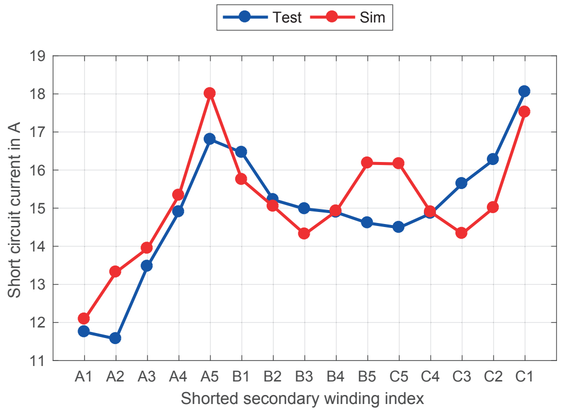

Figure 10.15 Short circuit currents with W_{p} supplied and all of the W_{s} shorted at the same time.

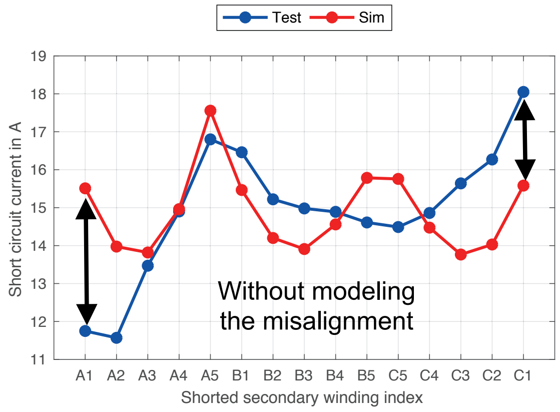

Figure 10.16 Short circuit currents with W_{p} supplied and all of the W_{s} shorted at the same time, neglecting the vertical position misalignment between primary- and secondary windings in the model.

the secondary winding currents and the simulation model is able to reproduce it with good accuracy, the maximum error is 15.1%. The influence of the vertically shifted primary winding with respect to the secondary windings, which has been discussed in the modeling of the type 1 division with W_{sA1} and the type 2 division, can be observed here. This result in significantly reduced current on W_{sA1} and increased current on W_{sC1}, in comparison to the other secondary windings. However, if we neglect this misalignment in geometry by removing the division type 2 and set the primary winding turns number of the very top type 1 division to be identical as the others, the current of W_{sA1} and W_{sC1} becomes nearly equal to each other, which result in obvious discrepancy to the measurement, as demonstrated in **Fig. 10.16**. Again in the single phase case discussed in **Chap. 9**, this misalignment did not exist in the prototype transformer and thus was not included in the model.

Moreover, the extra gap between W_{sA5} and W_{sB1} is showing its influence on the secondary current distribution, which boosts the current on W_{sA5} obviously. This effect has been captured by the model as well, thanks to the insertion of a gap division (**Fig. 10.9**) in the magnetic circuit.

10.5 Experimental verification with diode rectifiers

In this section, the fidelity of the proposed transformer model with connection to power electronic converters is verified. Due to lack of access to a CHB converter power hardware in the original MV application, the experimental test is conducted in combination with low-voltage (LV) diode rectifiers, which are designed to support experimental investigations.. Considering the fact that the leakage fluxes flow through the air, whose magnetic characteristic is linear and independent of the excitation amplitude, the LV setup should be also able to capture the unbalance in leakage flux coupling that originally take place in MV operation.

The schematic and hardware configuration of the verification setup is demonstrated in **Fig. 10.17**: The primary winding is supplied by $50Hz$ balanced three-phase AC voltage generated by the grid emulator from Chroma (type 61700), while the secondary windings are connected to 15 identical three-phase diode rectifiers. Each rectifier is equipped with a $150\mu F$ capacitor on the DC side. In order to observe the influence exclusively from the unbalanced leakage flux coupling and simplify overall test setup, the DC output terminals of all rectifiers are connected in parallel on one load resistor of $R_{load} = 4.5\Omega$, so that all rectifiers share the same output DC voltage. Due to the dominant leakage flux path of the secondary windings and line frequency excitation ($50Hz$), the effect of the stray inductance and capacitance of the long cables connecting the transformer and the rectifiers can be neglected.

The line-to-line RMS voltage of the AC source is configured to be $104V$, which result in a output DC voltage of $15V$ after rectification. The system level simulation model (the magnetic circuit of the divisions are hidden in encapsulated blocks) shown in **Fig. 10.17a** has been established in PLECS/Simulink, which includes the transformer model discussed in the previous section. For the sake of fast system-level simulation, all the rectifier diodes are modeled as ideal components. The other parameters of the simulation model (e.g. load resistance) are configured complying with the test hardware.

In **Fig. 10.18a**, the AC current (phase "u") on the secondary windings W_{sA1}, W_{sB1} and W_{sC1} from measurement and simulation are displayed in two separate plots, respectively. Although these three

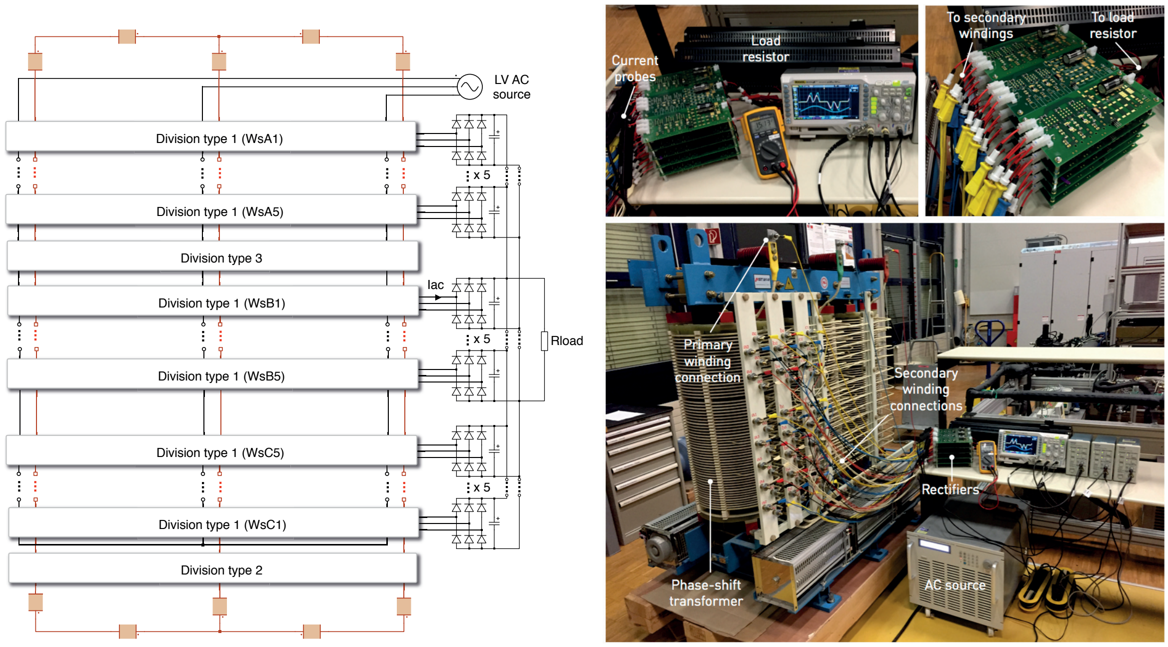

(a) **(b)**

Figure 10.17 Verification setup with the primary winding of the transformer supplied by AC source, and secondary windings feeding 15 diode rectifiers connected to a common resistive load: (a) Schematic and system-level simulation model; (b) Hardware configuration.

windings have exactly the same turns number configuration and the DC voltage for their rectifiers are also identical, the measured AC current on W_{sB1}, however, has significantly higher amplitude than that on W_{sA1} and W_{sC1} (blue curves). This unbalance can be ascribed to the nonidentical leakage flux coupling to the primary winding, as the consequence of the different vertical position of these windings, as shown in **Fig. 10.18b**. This unbalance has been well captured by the simulation model (red-orange curves), thanks to the proposed approaching in representing the leakage flux path. A finer comparison between measurement and simulation has been made in **Fig. 10.19a** for the AC currents on W_{sA1}, W_{sB1} and W_{sC1}, respectively, where the simulation result exhibits only slight discrepancy to the measurement. The maximum error of the RMS value is 8% on W_{sC1}.

If the part of transformer model is replaced by the one with ideally balanced secondary leakage inductance introduced in **Sec. 10.2**, the current waveforms on W_{sA1}, W_{sB1} and W_{sC1} becomes exactly the same, as shown in **Fig. 10.19b**. Without taking into account the unbalanced leakage flux coupling, the simulated current waveforms from the ideal model exhibits significant discrepancy on both amplitude and phase, in comparison to the measurement. The maximum error of the RMS value turns out to be 26.8% on the very-top secondary winding W_{A1}.

Different from the secondary windings W_{sA1}, W_{sB1} and W_{sC1}, the vertical positions of W_{sA5}, W_{sB5} and W_{sC5} (same turns number configuration) are closer to each other (**Fig. 10.20b**) on the transformer core, which makes the AC currents better balanced among these three windings, as the measurement result in **Fig. 10.20a** illustrates. This reduced unbalance can be observed in the simulation result as well. As has been compared in **Fig. 10.21**, the simulation model is still able to reproduces the measurement with good accuracy.

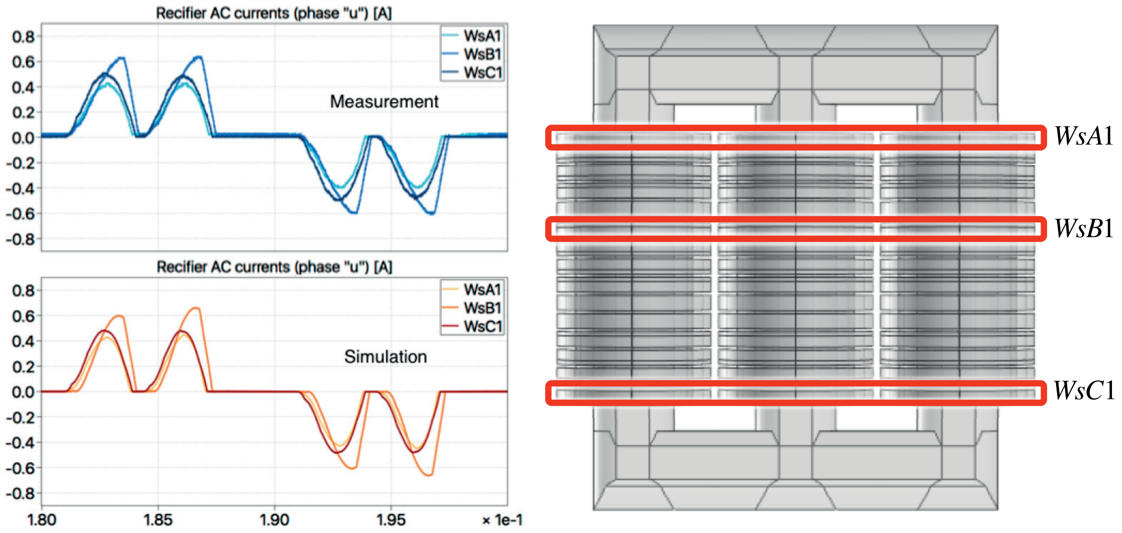

(a) **(b)**

Figure 10.18 (a) Measured and simulated rectifier AC currents on W_{sA1}, W_{sB1} and W_{sC1} (phase "u"); (b) Position of the secondary windings W_{sA1}, W_{sB1} and W_{sC1} on the transformer core.

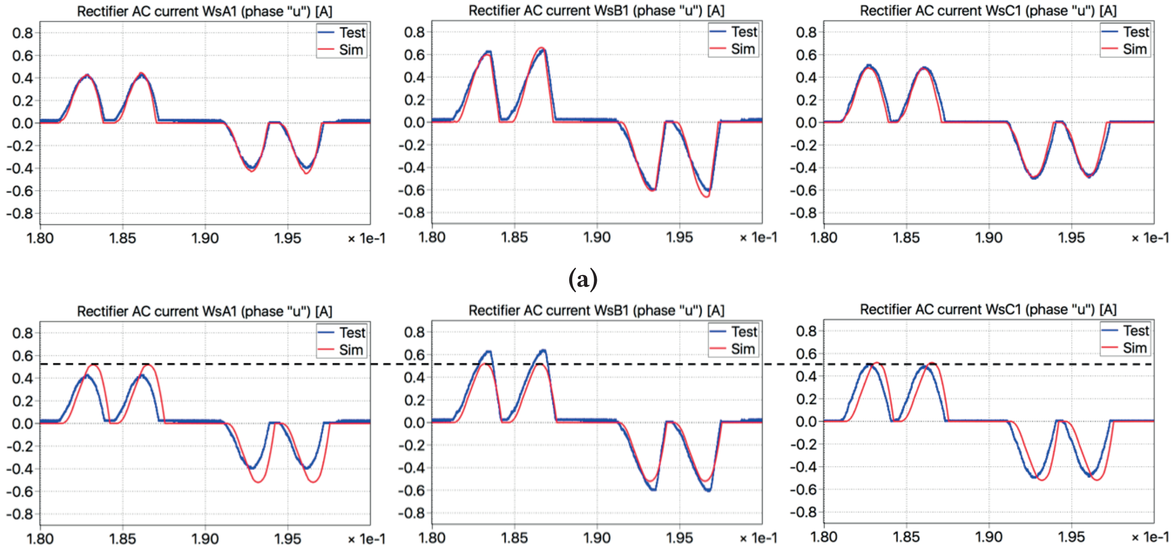

(a)

(b)

Figure 10.19 Comparison between measured and simulated currents on W_{sA1}, W_{sB1} and W_{sC1} (phase "u") (a) using proposed model with unbalanced leakage flux coupling; (b) using ideally balanced leakage inductance model.

Finally, the comparison of the AC currents' RMS value on all the secondary windings are presented in **Fig. 10.22**, strong unbalance can be observed. Please note that if the DC outputs of the rectifiers are isolated from each other, as is the case in the CHB converters, the unbalance present in the rectifier AC current of individual secondary windings will directly lead to unbalanced ripple current on the individual DC-link capacitors, as will be discussed in the next section. Since ripple current is directly related to the lifetime of the capacitors[84], this unbalance will make some of the capacitors age faster

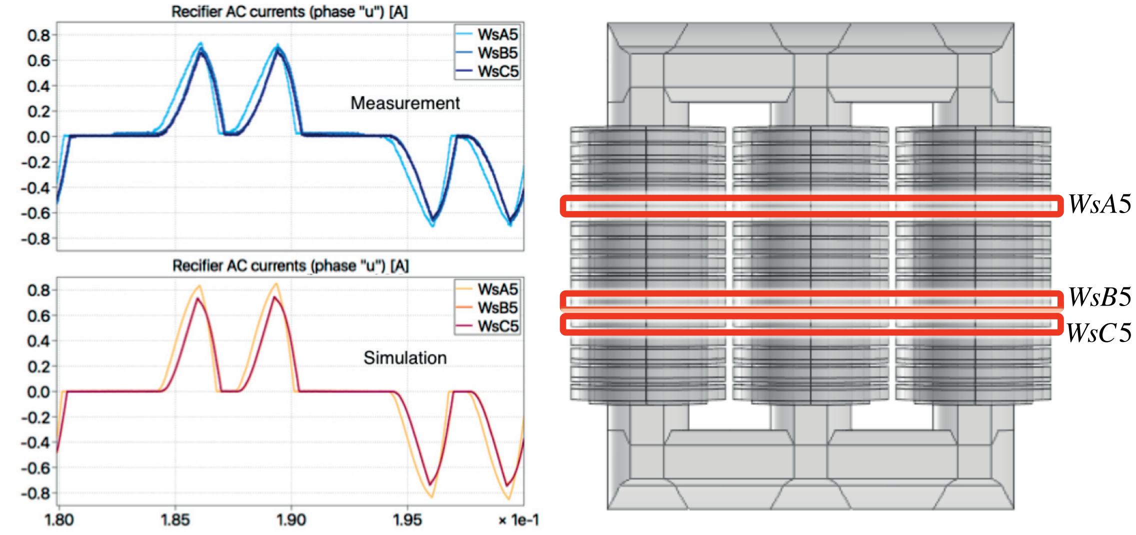

(a) **(b)**

Figure 10.20 (a) Measured and simulated rectifier AC currents on W_{sA5}, W_{sB5} and W_{sC5} (phase "u"), where the currents on W_{sB5} and W_{sC5} nearly overlap with each other; (b) Position of the secondary windings W_{sA5}, W_{sB5} and W_{sC5} on the transformer core.

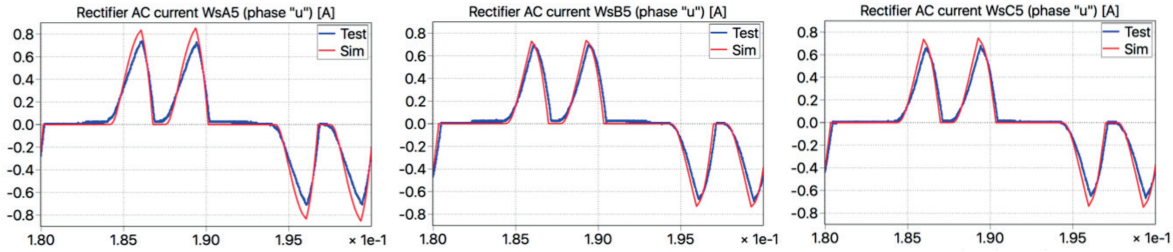

Figure 10.21 Comparison between measured and simulated secondary winding currents on W_{sA5}, W_{sB5} and W_{sC5} (phase "u").

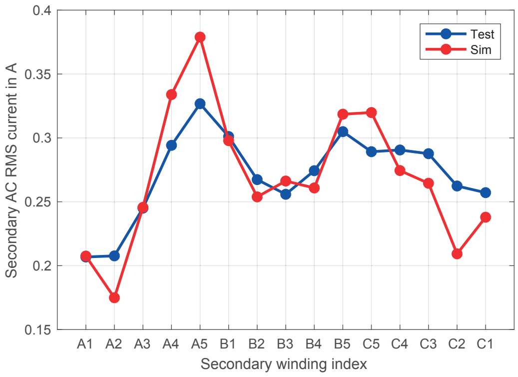

Figure 10.22 Comparison of the AC currents' RMS value among all secondary windings between test measurement and simulation

than the other and thus potentially add up to the difficulty in arranging a maintenance plan.

10.6 Performance in system level simulation

After the magnetic circuit model of the transformer has been verified by the short circuit test results and that with diode rectifier connection, further evaluations are carried out in system level simulation environment under MV excitation. Comparison is made between the simulated performance with balanced and the identified unbalanced leakage parameters.

In the first evaluation scheme, the primary winding is supplied by three-phase 50Hz sinusoidal voltage source which emulates the MV grid connection. The line-to-line RMS voltage is equal to 6.3 kV and the grid internal impedance is neglected. All secondary windings are connected to identical full-bridge diode rectifiers. The output of the diode rectifiers are connected to constant DC voltage sources, the voltage of which are all equally configured to 970 V, the ratio between DC voltage and the primary AC voltage is the same as that of the LV experimental verification setup in the last section. Apart from the connection of the hardware test presented in the previous **Sec. 10.5**, the DC outputs of the rectifiers here are isolated from each other, so that the ripple current of individual DC source can be accessed. The system level simulation model including the transformer is shown in **Fig. 10.23**.

In order to explore the influence from the unbalanced leakage flux path, the transformer model with ideally balanced leakage inductances described in **Sec. 10.2** is also connected to diode rectifiers in the same way as **Fig. 10.23**, for further comparison.

In the upper plots of **Fig. 10.24a** and **Fig. 10.24b**, the simulated AC current I_{ac} of phase "u" (as has been denoted in **Fig. 10.23**) on the secondary windings W_{sA1}, W_{sB1} and W_{sC1} from unideal- and ideal model are compared with each other. In the unideal model, although these three windings have totally the same phase-shift configuration and the same winding geometry, due to the different position

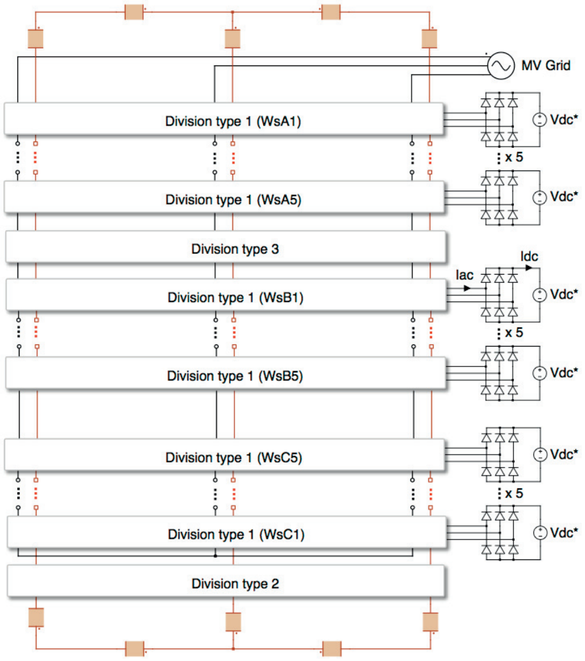

Figure 10.23 System-level simulation model with MV grid as input and diode rectifiers connected to constant DC voltage sources as output.

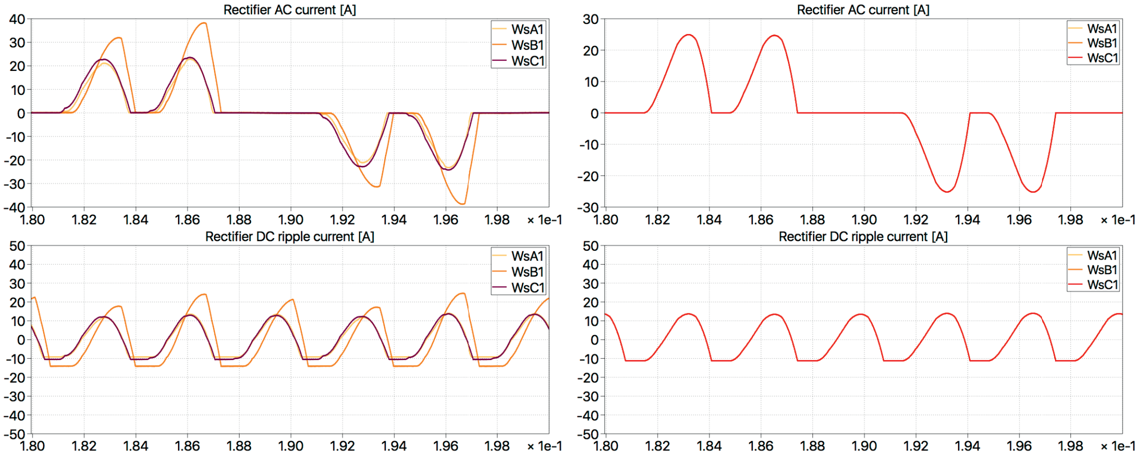

(a) **(b)**

Figure 10.24 Simulated time domain waveform of the rectifier side AC current (phase "u") and DC ripple current on the secondary windings W_{sA1}, W_{sB1} and W_{sC1}, with diode rectifier connected to constant voltage sources, from the model (a) with unideal leakage flux path; (b) with idealized leakage inductances.

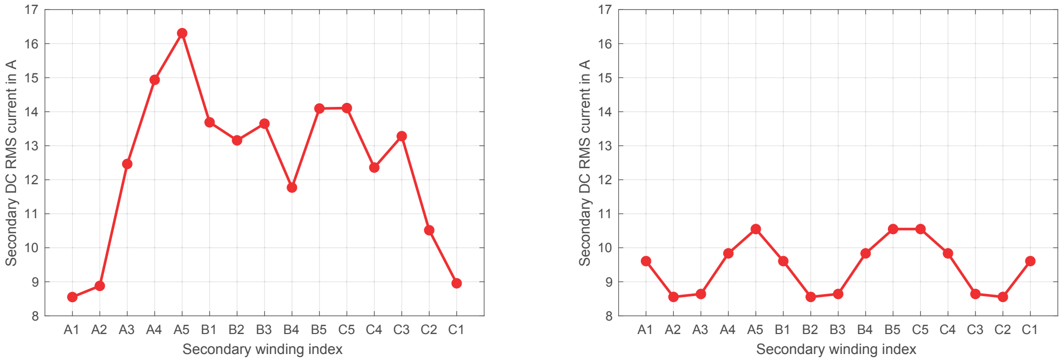

(a) **(b)**

Figure 10.25 Simulated RMS value of the rectifier side DC ripple current on all the secondary windings, with diode rectifier connected to constant voltage sources, from the model (a) with unideal leakage flux path; (b) with idealized leakage inductances.

on the transformer core however, obvious difference can be observed between their AC currents in **Fig. 10.24a**. It is also to be noted that the shape of the AC side current present in **Fig. 10.24a** is essentially a linear scaling of that in **Fig. 10.18a** from the last section, due to the fact that the AC input- and DC output voltage of the MV simulation are scaled up with the same factor from that of the LV experimental setup. After rectification, the ripple currents $\tilde{I}_{dc}$ (with the DC component removed from the DC source current) on the DC side also exhibit noticeable unbalance, as shown in the lower plots from **Fig. 10.24a**. Since the short-circuit impedance from primary winding to the secondary winding W_{sB1} is smaller than that to W_{sA1} or W_{sC1}, as has been demonstrated in **Fig. 10.13**, the DC ripple component on W_{sB1} is higher. In comparison, the simulated current from the ideal model nearly overlap with each other, due to the identical series inductance values $\overline{L}_s$, which is not the case with real transformer.

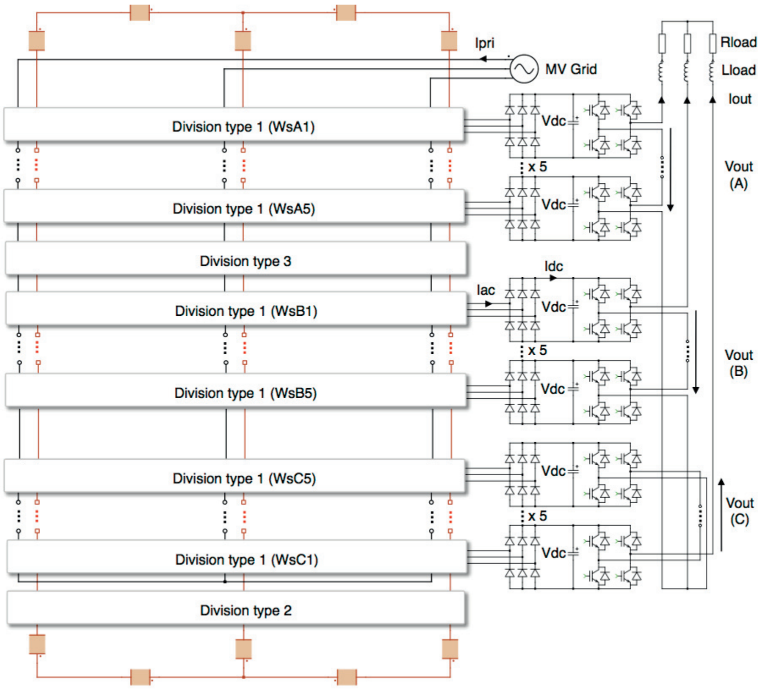

Figure 10.26 System-level simulation model with MV grid as input and complete power cells driving three-phase RL load.

Further in **Fig. 10.25** the RMS value of the DC side ripple current on all the secondary windings are compared between the unideal- and ideal model, and significant unbalance is present in the result of unideal model. The ratio between the highest- and lowest RMS ripple current in the ideal model is 1.24, while in the unideal model it is 1.91.

In the second evaluation scheme, the complete power cells including the diode rectifier, DC-link capacitor and H-bridge IGBT inverter are connected to the secondary windings. The DC link capacitors are configured to be $3mF$. The H-bridges are cascaded in the output phases to drive a three-phase R-L load with resistance $R_{load} = 30\Omega$ and inductance $L_{load} = 10mH$. The complete simulation model with the transformer model including unbalanced leakage flux path is demonstrated in **Fig. 10.26**. The model with idealized leakage inductances is reconfigured in the same way. The H-bridges are controlled in a open-loop way using interleaved carrier PWM modulation of switching frequency $500Hz$ and peak modulation index equal to 1. The simulated primary winding current I_p, multi-level inverter output voltage V_{out} and output current I_{out} from the unideal- and ideal model are shown in **Fig. 10.27a** and **Fig. 10.27b**, respectively. Thanks to the phase-shifted winding configuration, the primary winding currents flowing out of the MV-grid become approximately ideal sinusoidal wave. Slightly higher harmonic component can be observed on the simulated result from the unideal model, as a result of the unbalanced leakage flux paths.

On the inverter output side, the voltage and current waveforms are almost the same between the unideal- and ideal models, due to the fact that the DC-link capacitors have decoupled the voltage source inverter from the transformer unbalance. However on the diode rectifier side of the DC-link capacitors, the simulated ripple current of secondary windings W_{A1}, W_{B1} and W_{C1} from the unideal model shown in **Fig. 10.28a** exhibits even stronger unbalance, in comparison to **Fig. 10.24a**. If

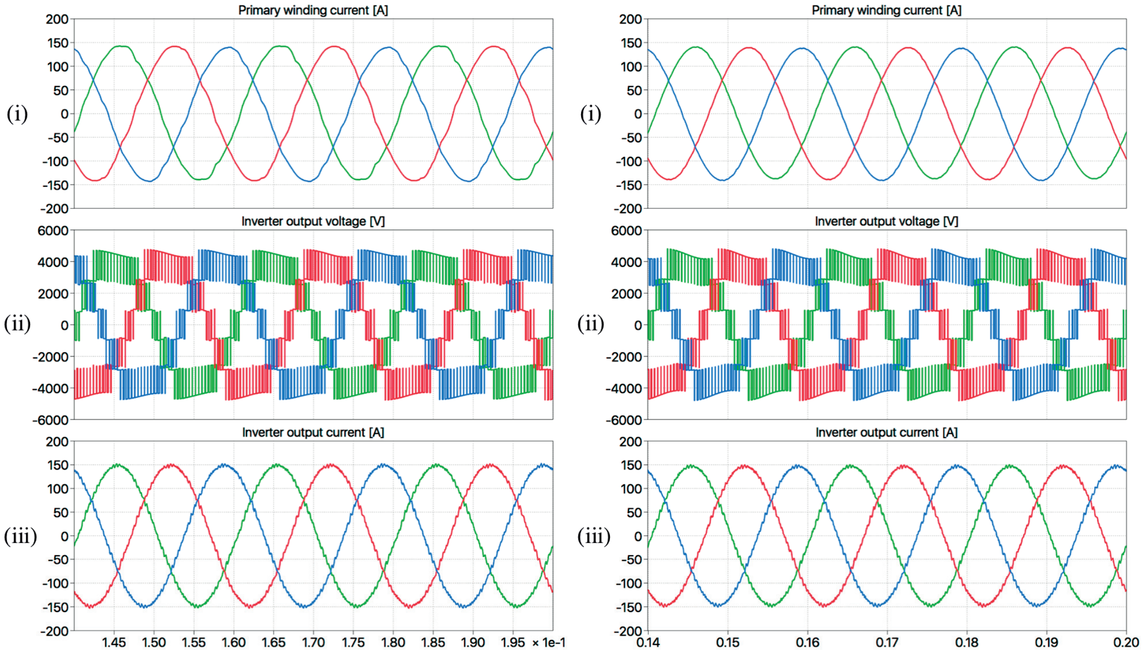

(a) (b)

Figure 10.27 Simulated time domain waveform of the primary current, inverter output voltage and inverter output current from the model using complete power cells (a) with unideal leakage flux path; (b) with idealized leakage inductances.

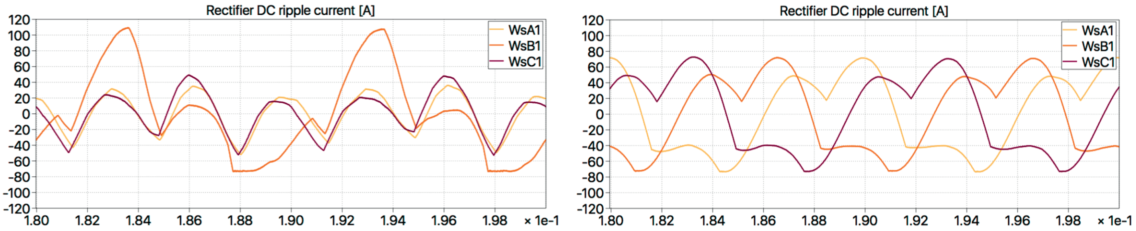

(a) (b)

Figure 10.28 Simulated time domain waveform of the rectifier side DC ripple current on the secondary windings W_{sA1}, W_{sB1} and W_{sC1} from the model using complete power cells (a) with unideal leakage flux path; (b) with idealized leakage inductances.

the RMS ripple current of all the secondary windings are compared together in **Fig. 10.29a**, the ratio between the highest- and lowest value becomes 2.7, which is significantly higher than that in **Fig. 10.25a**. The increased unbalance on rectifier side ripple current can be ascribed to the ripple voltage on the DC-link capacitors (**Fig. 10.30a**), which is not present in the first evaluation case. On the ideal model, however, the ripple currents on the rectifier side are still well balanced as shown in **Fig. 10.28b** and **Fig. 10.29b**.

From the result of unideal model, the current on the secondary windings are significantly different from each other, which makes the rectifier diodes unequally loaded. Besides that, the unbalance on the DC side ripple current lead to different stress on the DC-link capacitors. Making use of the simulation result from the proposed transformer model, one would be able to better predict the stress

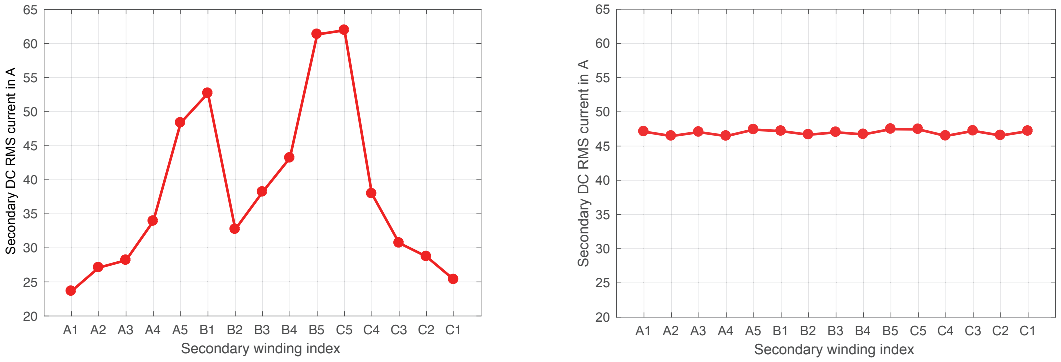

(a) (b)

Figure 10.29 Simulated RMS value of the rectifier side DC ripple current on all the secondary windings from the model using complete power cells (a) with unideal leakage flux path (b) with idealized leakage inductances.

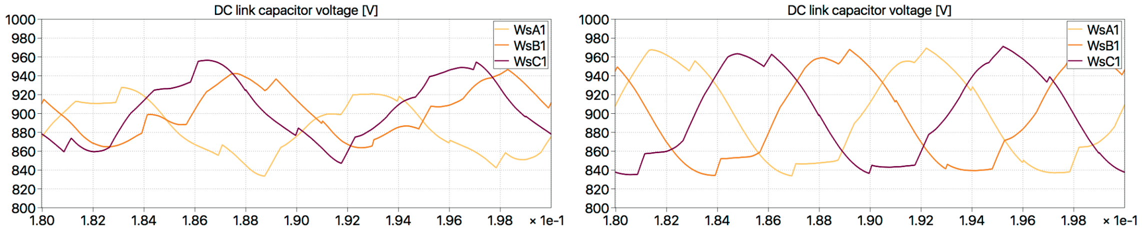

(a) (b)

Figure 10.30 Simulated time domain waveform of the DC link capacitor voltage of the power cells on the secondary windings W_{sA1}, W_{sB1} and W_{sC1} from the model using complete power cells (a) with unideal leakage flux path; (b) with idealized leakage inductances.

on switching devices and passive components, or improve the modulation strategy on the inverter side to compensate the unbalance. This however, can not be achieved using the ideal model with balanced leakage inductances.

10.7 Summary

This chapter has demonstrated the modeling of phase-shift transformer in MV power converter application using permeance-capacitance based magnetic circuit. The proposed model has the potential to reproduce circuit issues related to the unbalance in leakage flux coupling when integrated into system-level simulation combined with power converters. Via making use of information about the repetitive and symmetrical geometry, the parameters of the leakage flux path can be obtained from only a few experimental tests. The result from the proposed model shows good match to the hardware test, under a plenty of short-circuit schemes. In comparison to the conventional model with ideally balanced leakage inductance, the proposed model is able to reproduce effects that arise from the unbalanced leakage flux path. The simulation result may potentially help with component selection and developing the control algorithm of the whole converter system.

11

Summary and future works

The contributions of this thesis are summarized in this chapter regarding the proposed models for core material characteristic and leakage flux coupling. An outlook of the future work is also provided for the possible directions of improvement and extension to the proposed models.

11.1 Summary and contributions

In this thesis, the models of magnetic components which can be seamlessly integrated into system-level circuit simulation are developed. Taking the permeance-capacitance based magnetic circuit as fundamental platform, the magnetic components can be represented in a intuitive way. Magnetic phenomena together with their interaction to the electrical circuit are reflected in the circuit simulation with sufficient insight on the physics. Using the proposed model, the performance of power converter systems can be better evaluated taking into account the non-ideal behavior of the magnetic components. Also the magnetic components design can be optimized with the impact from the external circuit considered.

The model of the frequency-independent core loss arising from static hysteresis effect has been proposed in **Chap. 4** ~ **Chap. 6**. The classical Preisach model was taken as a starting point. According to the experimental results, different materials exhibit significantly different shape of $B-H$ characteristic, which can hardly be covered by the generalized form of the classical Preisach model. To accommodate the $B-H$ characteristic of different materials, the logistic distribution function has been used for the model of ferrite materials in **Chap. 4**, product Preisach model for the silicon steel material in **Chap. 5**, while an explicit representation using the ascending branch of a limiting loop for amorphous- and nanocrystalline alloy. Combining these variations of Preisach model with a reversible component, the static hysteresis loops of popular core materials can be reproduced with good accuracy, which is valid in a wide range of excitation amplitude. Not only the loss-related loop-area is well captured, but also the equivalent permeability which governs the coupling between the magnetic component and the external circuit.

With increasing excitation frequency, the frequency-dependent core loss contributes considerable part to the overall power loss of the magnetic components. In **Chap. 7**, the model extension for relaxation effect of ferrite materials has been presented. Experimental measurements demonstrated that the hysteresis loop area of ferrite material varies significantly, if the zero-voltage period is present in the symmetrical PWM excitation or the duty cycle of asymmetrical PWM is far away from 50 %. This phenomenon can be ascribed to the relaxation effect which has been well captured by the proposed model. In **Chap. 8**, the model of another important loss-related mechanism, eddy current effect which arises from the material conductivity, is presented for metal based core materials. The proposed models for relaxation effect and eddy current effect combined the static hysteresis model, so that both frequency independent and dependent core losses are present in the simulation circuit, and can be separately evaluated.

The core loss models for certain core material can be easily extended to other core geometries other than the toroidal core used for parametrization. For the parameter identification and the fidelity verification of the proposed core loss models, experimental measurements were carried out using the multi-functional test setup constructed during this thesis, whose functionalities and operating modes have been described in **Chap. 3**. The test setup is able to emulate operating conditions including continuous sinusoidal and various PWM excitations that magnetic components experience in real power converter systems.

Beside the characteristic of the magnetic core, the leakage flux path coupling also significantly influence the dynamic behavior of the magnetic components, especially the ones with complex structure. Certain unbalance has been observed by industry partners in the commercial power converter systems, which can be ascribed to the unbalance leakage flux coupling between the transformer windings. In **Chap. 9** and **Chap. 10**, the models of leakage flux coupling in multi-winding structures have been presented, which intuitively represented the leakage flux paths. The unbalances can be captured by the proposed model, whose fidelity is verified with experimental measurements on a single-phase transformer prototype and a three-phase transformer from commercial medium voltage drive system. The proposed model can be expanded to more complex structures, in order to support the power converter designers in modifying the transformer and control engineers in improving the control algorithm, to compensate the negative influence of the unbalance.

11.2 Overall contributions

Magnetic components exhibits nonlinearities when operating in power converter systems. The behavior is significantly influenced by the design specifications, including core material, core geometry and winding placements. In this thesis, the permeance-capacitance based magnetic circuit has been proved to be a versatile platform in modeling magnetic components, to which the design specifications can be conveniently integrated. If the models are properly elaborated for the magnetic phenomena, the non-idealities of magnetic components can be intuitively captured and reflected in the circuit model during time domain simulation. The output of the simulations may help the power converter designers optimize the magnetic components or improve the rest part of the system in terms of component selection and control design. Since optimization methods are not the scope of this thesis, only a simplified workflow is illustrated in **Fig. 11.1** and described below, where the model for the frequency dependent core loss proposed in **Chap. 7** is take as an example:

- (1) At a first step, the required material characteristic under low frequency sinusoidal and high frequency PWM excitation is obtained using a toroidal core sample.
- (2) Secondly, the permeance model is parametrized following the procedure introduced in **Sec. 7.3**.
- (3) The iterative optimization of the magnetic component can be started. In each iteration, a different core geometry and turns number of the windings are chosen.

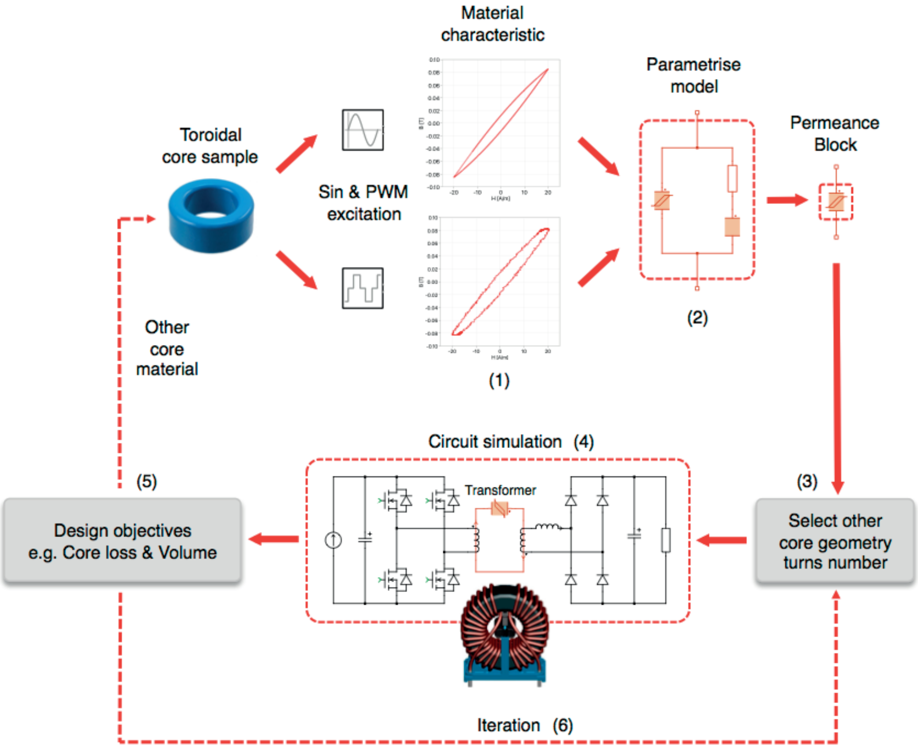

Figure 11.1 Work flow using the proposed model to optimize magnetic component design

- (4) The permeance block is integrated into the circuit simulation environment of the target power converter system and scaled by the core geometry, according to the description in **Sec. 7.4.5**. Also, the winding components are configured with the desired turns numbers. The circuit model is simulated in the time domain and the core loss power is obtained.

- (5) Taking the simulated core loss power and the volume of the selected core in the current iteration, an objective function as trade-off between power loss and volume can be optimized.

- (6) The output of the objective function indicates the direction to change the core geometry and winding turns number. Afterwards the new core geometry and winding turns number are applied to the circuit model in the next iteration.

11.3 Future works

This work has significantly extended the model of magnetic components using permeance-capacitance based magnetic circuit, in the direction of core loss and leakage flux paths. The magnetic phenomenon can be reflected in the time-domain simulation with full coupling to the electrical circuit. Considerable potential of improvement exists, while the work to be carried out in the near future are listed in below:

11.3.1 Improvement of the static hysteresis model with DC bias

In some popular power converter topologies, the magnetic components undertake DC-bias on the $B-H$ plane, in both field strength H and flux density B. In **Chap. 4** ~ **Chap. 6**, the models are parametrized using symmetrical hysteresis loops from experimental measurements. Although the physics-based property of the Preisach model ensures that the minor hysteresis loops with slight DC-bias can be captured with good accuracy, the ones with large DC-bias however, may exhibit significantly discrepancy. To guarantee the accuracy in both symmetrical and biased operating conditions, the proposed static hysteresis models developed in this thesis need to be extended. New parametrization procedure is required to explicitly fit the model to the biased hysteresis loops, if experimental measurements are available.

11.3.2 Improvement of core loss model in high frequency operation

As the switching devices based on silicon carbide and gallium nitride becoming mature regarding reliability and cost for mass production, the switching frequency of power converters is continuously increasing nowadays. For certain low power applications, hundreds of kHz is becoming the main trend and the MHz area is under exploration. Due to the limitation of the test setup established regarding switching speed, excitation voltage and measurement accuracy, the core loss models proposed in this thesis have only been verified under 50 kHz frequency. For higher excitation frequencies above 100 kHz, even the low conductive ferrite materials may exhibits observable eddy current effect, which significantly contributes to the overall power loss together with the relaxation effect. The proposed model in **Chap. 7** is supposed to be extended to cover eddy current loss as well. New parametrization procedure has to be proposed with improved characterization setup.

11.3.3 Winding loss model

The winding losses contributes considerable part to the power loss of the magnetic components, especially with high switching frequencies, where skin effect and proximity effect take place. Skin effect and proximity effect are essentially resulted from the interaction between the electrical current and magnetic field across the winding wires. This could also be potentially represented by the permeance-capacitance based magnetic circuit. Moreover, as has been observed in practice, the presence of air gaps in the magnetic core add up to the winding loss, depending on the way how the windings are installed. To capture these effects, the magnetic circuit representing the core and that covering the winding losses need to be coupled.

Appendices

A

Code of the classical Preisach model

The code for computing the instantaneous permeability of the classical Preisach model, which is written within the C-Script block ”Preisach dB/dH” from Fig. 7.5b, is listed in below. The code is divided into different functional blocks, namely ”Code declaration”, ”Starting function code”, ”Output function code” and ”Update function code”. Detailed description about how these functional blocks are invoked during simulation can be found in the manual of the simulation software PLECS [88] from page 183.

```
/*****************************************************************************************/
/*Code declaration*/
#include <stdlib.h>
#include <math.h>

// Data structure defining the historical turning points
typedef struct
{
   double extremity; // Turning points in history
   int direction; // Direction before turning
} hysteron_t;
static hysteron_t *mHysteronBuffer = NULL; // Stack storage
static int buflen; // Stack size
static long mHysteronIdx = 0; // Actual number of data in the stack
static hysteron_t mHysteronTemp; // Actual operating point

// Zero crossing signals
static double zc_signal[2]; // Actual simulation step
static double zc_signal_pre[2]; // Record of the previous simulation step

// Preisach model parameters
static double mH0 = 0;
static double mSigma = 0;
static double mK = 0;

// Actual permeability
static double dBdH;

// Distribution function of the Preisach model
static double PDF(double aH0 , double aSigma , double aK , double aH)
{
   double pdf;
   double x = (aH - aH0)*aSigma;
   pdf = exp(-x)/pow(1 + exp(-x), 2)*aK;
   return pdf;
}

// Cumulative distribution function of the Preisach model
static double CDF_N(double aH0 , double aSigma , double aK , double aH)
{
   double cdf;
   double x = (-aH - aH0)*aSigma;
```

```
   cdf = -1/(1 + exp(-x))*aK/aSigma;
   return cdf;
}

// Function calculating permeability
static double Permeability(double aH0, double aSigma, double aK, double aHPeak, int aVirgin,
     double aH)
{
   if (aVirgin)
   {
      return 2*PDF(aH0, aSigma, aK, aH)*( CDF_N(aH0, aSigma, aK, aH) - CDF_N(aH0, aSigma, aK
          , -aH) );
   }
   else
   {
      return 2*PDF(aH0, aSigma, aK, aH)*( CDF_N(aH0, aSigma, aK, aH) - CDF_N(aH0, aSigma, aK
          , aHPeak) );
   }
}
/*****************************************************************************************/

/*****************************************************************************************/
/*Start function code*/
// Import external model parameters
mH0 = ParamRealData(0,0);
mSigma = ParamRealData(1,0);
mK = ParamRealData(2,0);

// Allocate memory for the stack storage
mHysteronBuffer = (hysteron_t*) malloc(buflen*sizeof(hysteron_t));

// Initialize the first element in the stack
mHysteronBuffer[mHysteronIdx].extremity = 0.;
mHysteronBuffer[mHysteronIdx].direction = 0;
/*****************************************************************************************/

/*****************************************************************************************/
/*Output Function*/
// Assign actual operating point
mHysteronTemp = mHysteronBuffer[mHysteronIdx];

// Detect direction of movement
if (mHysteronTemp.direction == 0)
{
   if (Input(0) > mHysteronTemp.extremity)
   {
      mHysteronTemp.direction = +1;
   }
   if (Input(0) < mHysteronTemp.extremity)
   {
      mHysteronTemp.direction = -1;
   }
}

// Calculate instantaneous permeability
if (mHysteronTemp.direction > 0) // Positive direction
{
   if (mHysteronIdx > 0)
   {
      dBdH = Permeability(mH0, mSigma, mK, mHysteronBuffer[mHysteronIdx-1].extremity, 0,
          Input(0));
   }
   else // Virgin curve
   {
      dBdH = Permeability(mH0, mSigma, mK, 0., 1, Input(0));
```

```
   }
}
else // Negative direction
{
   if (mHysteronIdx > 0)
   {
      dBdH = Permeability(mH0, mSigma, mK, -mHysteronBuffer[mHysteronIdx-1].extremity, 0, -
          Input(0));
   }
   else // Virgin curve
   {
      dBdH = Permeability(mH0, mSigma, mK, 0., 1, -Input(0));
   }
}

mHysteronTemp.extremity = Input(0); // Update the actual field strength

// Output the instaneous permeability
Output(0) = dBdH;

// Update zero crossing signal and activate zero crossing detection
zc_signal[0] = mHysteronBuffer[mHysteronIdx-2].extremity - Input(0);
zc_signal[1] = Input(1);
ZCSignal(0) = zc_signal[0];
ZCSignal(1) = zc_signal[1];
/*****************************************************************************************/

/*****************************************************************************************/
/*Update function code*/
// If a historical turning point is crosses twice,
// the latest two element in the stack are erased.
if(mHysteronBuffer[mHysteronIdx].direction > 0)
{
   while (mHysteronIdx >= 2 && Input(0) >= mHysteronBuffer[mHysteronIdx-2].extremity)
   {
      mHysteronIdx -= 2;
   }
}
else if (mHysteronBuffer[mHysteronIdx].direction < 0)
{
   while (mHysteronIdx >= 2 && Input(0) <= mHysteronBuffer[mHysteronIdx-2].extremity)
   {
      mHysteronIdx -= 2;
   }
}

// Update the actual element in the stack
mHysteronBuffer[mHysteronIdx] = mHysteronTemp;

// New turning point is pushed into the stack,
// if the excitation changes direction.
if ((zc_signal_pre[1] > 0 && zc_signal[1] <= 0) || (zc_signal_pre[1] < 0 && zc_signal[1] >=
    0))
{
   (mHysteronIdx)++;
   mHysteronBuffer[mHysteronIdx].extremity = mHysteronBuffer[mHysteronIdx-1].extremity;
   mHysteronBuffer[mHysteronIdx].direction = -mHysteronBuffer[mHysteronIdx-1].direction;
}

// Save the zero crossing signal
zc_signal_pre[0] = zc_signal[0];
zc_signal_pre[1] = zc_signal[1];
/*****************************************************************************************/
```

Bibliography

[1] https://www.wikipedia.org,

[2] http://www.edisontechcenter.org,

[3] https://www.electronicsweekly.com/market-sectors/power/cree-licences-gan-power-ip-to-transphorm-2013-08/,

[4] *Datasheet of nlp65 sereis power supply*, Emerson Network Power, Jun. 2008.

[5] J. Sun, “High frequency materials for advanced magnetics”, BsT Frankfurt am Main GmbH, Tech. Rep., Feb. 2017.

[6] http://www.directindustry.com,

[7] “Cast coil dry-type transformers - reliabiility at your hand”, ABB Management Service Ltd., Tech. Rep., 2011.

[8] http://new.abb.com/products/transformers/power/hvdc-converter/hvdc-light-converter-transformers,

[9] “Mf transformer for traction”, STS Induktivitaeten, Tech. Rep.

[10] https://marquemagnetics.com,

[11] https://commons.wikimedia.org,

[12] http://www.psma.com,

[13] https://www.schaffner.com,

[14] J. B. Goodenough, “Summary of losses in magnetic materials”, in *Ieee transactions on magnetics*, vol. 38, 2002, pp. 3398–3408.

[15] J. Allmeling, W. Hammer, and J. Schönberger, “Transient simulation of magnetic circuits using the permeance-capacitance analogy”, in *Control and modeling for power electronics (compel), ieee 13th workshop on*, 2012.

[16] D. Hamill, “Lumped equivalent circuits of magnetic components: The gyrator-capacitor approach”, in *Ieee transactions on power electronics*, vol. 8, 1994, pp. 97–103.

[17] H. Stammberger, *Magnetfeld- und kraftberechnung für strombegrenzende niederspannungs-schaltgeräte*. VDI Verlag, 1995.

[18] R. F. P. Silvester, *Finite elements for electrical engineers*. Cambridge University Press, 1996.

[19] N. M. Abe, J. R. Cardoso, and A. Foggia, “Coupling elelctric circuit and 2d-fem model with dommel’s apporach for transient analysis”, in *Ieee transactions on magnetics*, vol. 34, 1998.

[20] P. Zhou, N. Fu, D. Lin, S. Stanton, and Z. J. Cendes, “Numerical modeling of magnetic devices”, in *Ieee transactions on magnetics*, vol. 40, 2004, pp. 1803–1809.

[21] J. Muehlethaler, J. Biela, J. W. Kolar, and A. E. Ecklebe, “Improved core-loss calculation for magnetic components employed in power electronic systems”, in *Ieee transactions on power electronics*, vol. 27, 2012, pp. 964–973.

[22] D. Tan, J. L. Vollin, and S. M. Cuk, “A practical approach for magnetic core-loss characterization”, in *Ieee transactions on power electronics*, vol. 10, 1995, pp. 124–130.

[23] L. Yan and B. Lehman, “A capacitor modeling method for integrated magnetic components in dc/dc converters”, in *Ieee transactions on power electronics*, vol. 20, 2005, pp. 987–995.

[24] M. Luo and D. Dujic, “Permeance based modelling of the core corners considering magnetic material nonlinearity”, in *Annual conference of the ieee industrial electronics society (iecon)*, 2015, pp. 950–955.

[25] M. Luo, D. Dujic, and J. Allmeling, “Leakage flux modeling of multi-winding transformers for system-level simulations”, in *Ieee transactions on power electronics*, 2017, Early Access.

[26] I. Mayergoyz, *Mathematical models of hysteresis and their applications*. Academic Press, 2003.

[27] F. Liorzou, B. Phelps, and D. L. Atherton, “Macroscopic models of magnetization”, in *Ieee transactions on magnetics*, 418-428, Ed., vol. 36, 2000.

[28] E. D. Torre, *Magnetic hysteresis*. IEEE Press, 1999.

[29] G. Bertotti, F. Fiorillo, and G. P. Soardo, “Dependence of power losses on peak magnetization and magnetization frequency in grain-oriented and non-oriented 3% sife”, in *Ieee transactions on magnetics*, vol. 23, 1985, pp. 3520–3522.

[30] L.-L. Rouve, T. Waeckerle, and A. Kedous-Lebouc, “Application of preisach model to grain oriented steels comparison of different characterizations for the preisach function”, in *Ieee transactions on magnetics*, vol. 31, 1995, pp. 3557–3559.

[31] B. Azzerboni, E. Cardelli, G. Finocchio, and F. L. Foresta, “Remarks about preisach function approximation using lorentzian function and its identification for non-oriented steels”, in *Ieee transactions on magnetics*, vol. 39, 2003, pp. 3028–3030.

[32] M. Luo, D. Dujic, and J. Allmeling, “Modelling hysteresis of soft core materials using permeance-capacitance analogy for transient circuit simulations”, in *European conference on power electronics and applications 2017 (epe, ecce europe)*, 2017.

[33] G. Consolo, G. Finocchio, M. Carpentieri, and B. Azzerboni, “A genetic approach to solve numerical problems in the preisach model identification”, in *Ieee transactions on magnetics*, vol. 42, 2006, pp. 1526–1537.

[34] E. Cardelli, L. Fiorucci, and E. D. Torre, “Identification of the preisach probability functions for soft magnetic materials”, in *Ieee transactions on magnetics*, vol. 37, 2001, pp. 3366–3369.

[35] E. Cardelli, G. Finocchio, and E. Pinzaglia, “Increasing the accuracy of the numerical identification of the modified scalar preisach model”, in *Ieee transactions on magnetics*, vol. 40, 2004, pp. 892–895.

[36] G. Consolo, G. Finocchio, M. Carpentieri, E. Cardelli, and B. Azzerboni, “About identification of scalar preisach functions of soft magnetic materials”, in *Ieee transactions on magnetics*, vol. 42, 2006, pp. 923–926.

[37] D. H. Everett, “A general approach to hysteresis, part 4—an alternative formulation of the domain model”, in *Transactions of the faraday society*, vol. 51, 1955, pp. 1551–1557.

[38] R. M. D. Vecchio, “An efficient procedure for modeling complex hysteresis processes in ferromagnetic materials”, in *Ieee transactions on magnetics*, vol. 16, 1980, pp. 809–811.

[39] S. R. Naidu, “Simulation of the hysteresis phenomenon using preisach’s theory”, in *Iee proceedings*, vol. 137, 1990, pp. 73–79.

[40] J. G. Zhu, S. Y. R. Hui, and V. S. Ramsden, “A dynamic equivalent circuit model for solid magnetic cores for high switching frequency operations”, in *Ieee transactions on power electronics*, vol. 10, 1995, pp. 791–795.

[41] S. Y. R. Hui, J. G. Zhu, and V. S. Ramsden, “A generalized dynamic circuit model of magnetic cores for low- and high- frequency applications - part ii: Circuit model formulation and implementation”, in *Ieee transactions on power electronics*, vol. 11, 1996, pp. 251–259.

[42] J. T. Hsu and K. D. T. Ngo, “A hammerstein-based dynamic model for hysteresis phenomenon”, in *Ieee transactions on power electronics*, vol. 12, 1997, pp. 406–413.

[43] E. D. Torre, J. Oti, and G. Kadar, “Preisach modeling and reversible magnetization”, in *Ieee transactions on magnetics*, vol. 26, 1990, pp. 3052–3058.

[44] C. Perez-Rojas, “Fitting saturation and hysteresis via arctangent funcitons”, in *Ieee power engineering review*, vol. 20, 2000, pp. 55–57.

[45] D. C. Jiles and D. L. Atherton, “Ferromagnetic hysteresis”, in *Ieee transactions on magnetics*, vol. 19, 1983, pp. 2183–2185.

[46] D. C. Jiles, J. B. Thoelke, and M. K. Devine, “Numerial determination of hystereiss parameters for the modeling of magnetic properties using the theory of ferrormangnetic hysteresis”, in *Ieee transactions on magnetics*, vol. 28, 1992, pp. 27–35.

[47] E. Cardelli, E. D. Torre, and E. Pinzaglia, “Identifying the preisach function for soft magnetic materials”, in *Ieee transactions on magnetics*, vol. 39, 2003, pp. 1341–1344.

[48] G. Kadar, “On the preisach function of ferromagnetic hysteresis”, in *Journal of applied physics*, vol. 61, 1987, pp. 4013–4015.

[49] J. Reinert, A. Brockmeyer, and R. W. A. A. D. Doncker, “Calculation of losses in ferro- and ferrimagnetic materials based on the modified steinmetz equation”, in *Ieee transactions on industry applications*, vol. 37, 2001, pp. 1055–1061.

[50] C. R. Sullivan, J. H. Harris, and E. Herbert, “Core loss predictions for general pwm waveforms from a simplified set of measured data”, in *25th annual ieee applied power electronics conference and exposition (apec)*, 2010, pp. 1048–1055.

[51] S. Barg, K. Ammous, H. Mejbri, and A. Ammous, “An improved empirical formulation for magnetic core losses estimation under nonsinusoidal induction”, in *Ieee transactions on power electronics*, vol. 32, 2017, pp. 2146–2154.

[52] V. Basso, “Hysteresis and relaxation effects in magnetic materials”, in *Ieee transactions on magnetics*, vol. 36, 2000, pp. 3176–3181.

[53] A. Abramovitz and S. Ben-Yaakov, “Rgse-based spice model of ferrite core losses”, in *Ieee transactions on power electronics*, vol. 33, 2018, pp. 2825–2831.

[54] M. Luo, D. Dujic, and J. Allmeling, “Modeling frequency independent hysteresis effects of ferrite core materials using permeance-capacitance analogy for system-level circuit simulations”, in *Ieee transactions on power electronics*, 2018, Early Access.

[55] J. van Vlerken and P. G. Blanken, “Lumped modelling of rotary transformers, heads and electronics for helical-scan recording”, in *Ieee transactions on magnetics*, vol. 31, 1995, pp. 1050–1055.

[56] L. Dalessandro, W. G. H. Odendaal, and J. W. Kolar, “Hf characterization and nonlinear modeling of a gapped toroidal magnetic structure”, in *Ieee transactions on power electronics*, vol. 21, 2006, pp. 1167–1175.

[57] Y. Han, G. Cheung, A. Li, C. R. Sullivan, and D. J. Perreault, “Evaluation of magnetic materials for very hight frequency power applications”, in *Ieee transactions on power electronics*, 425-435, Ed., vol. 27, 2012.

[58] M. Mu, Q. Li, D. J. Gilham, F. C. Lee, and K. D. T. Ngo, “New core loss measurement method for high-frequency magnetic materials”, in *Ieee transactions on power electronics*, vol. 29, 2014, pp. 4374–4381.

[59] D. Hou, M. Mu, F. C. Lee, and Q. Li, “New high-frequency core loss measurement method with practial cancellation concept”, in *Ieee transactions on power electronics*, vol. 32, 2017, pp. 2987–2994.

[60] J. Muehlethaler, J. Biela, and J. W. Kolar, “Core losses under dc bias condition based on steinmetz parameters”, in *Ieee transactions on power electronics*, vol. 27, 2012, pp. 953–963.

[61] TDK, “Epcos data book 2013: Ferrites and accesories”, 2013.

[62] http://www.vishay.com/landingpage/extreme/2014/shunt.html,

[63] C. Marxgut, J. Muehlethaler, F. Krismer, and J. W. Kolar, “Multiobjective optimization of ultraflat magnetic components with pcb-integrated core”, in *Ieee transactions on power electronics*, vol. 28, 2013, pp. 3591–3602.

[64] J. A. Martinez and B. A. Mork, “Transformer modeling for low- and mid-frequency transients - a review”, in *Ieee transactions on power delivery*, vol. 20, 2005, pp. 1625–1632.

[65] F. de Leon and A. Semlyen, “Time domain modeling of eddy currrent effects for transformer transients”, in *Ieee transactions on power delivery*, vol. 8, 1993, pp. 271–280.

[66] E. J. Tarasiewicz, A. S. Morched, A. Narang, and E. P. Dick, “Frequency dependent eddy current models for nonlinear iron cores”, in *Ieee transactions on power systems*, vol. 8, 1993, pp. 588–597.

[67] A. Davoudi, P. L. Chapman, J. Jatskevich, and A. Khaligh, “Reduced-order modeling of high-fidelity mangetic equivalent circuits”, in *Ieee transactions on power electronics*, vol. 24, 2009, pp. 2847–2855.

[68] A. Davoudi, P. L. Chapman, J. Jatskevich, and H. Behjati, “Reduced-order modeling of multi-winding power electronic magnetic components”, in *Ieee transactions on power electronics*, vol. 27, 2012, pp. 2220–2226.

[69] P. Holmberg and A. Bergqvist, “Modelling eddy current and hysteresis in a trasnformer laminate”, in *Ieee transactions on magnetics*, vol. 33, 1997, pp. 1306–1309.

[70] P. G. Blanken, “A lumped winding model for use in transformer models for circuit simulation”, in *Ieee transactions on power electronics*, vol. 16, 2001, pp. 445–460.

[71] Z. Zheng, Z. Gao, C. Gu, L. Xu, K. Wang, and Y. Li, “Stability and voltage balance control of a modular converter with multiwinding high-frequency transformer”, in *Ieee transactions on power electronics*, vol. 29, 2014, pp. 4183–4194.

[72] L. Guasch, F. Corcoles, and J. P. L. Sainz, “Effects of symmetrical voltage sags on three-phase three-legged transformers”, in *Ieee transactions on power delivery*, vol. 19, 2004, pp. 875–883.

[73] A. D. Theocharis, J. Milias-Argitis, and T. Zacharias, “Three-phase transformer model including magnetic hysteresis and eddy currents effect”, in *Ieee transactions on power delivery*, vol. 24, 2009, pp. 1284–1294.

[74] P. S. Moses, M. A. S. Masoum, and H. A. Toliyat, “Dynamic modeling of three-phase asymmetric power transformers with magnetic hysteresis: No-load and inrush conditions”, in *Ieee transactions on energy conversion*, vol. 25, 2010, pp. 1040–1047.

[75] J. Cale, S. D. Sudhoff, and L.-Q. Tan, “Accurately modeling ei core inductor using a high-fidelity magnetic equivalent circuit approach”, in *Ieee transactions on magnetics*, vol. 42, 2006, pp. 40–46.

[76] C. Alverez-Marino, F. de Leon, and X. M. Lopez-Fernandez, “Equivalent circuit for the leakage inductance of multiwinding transformers: Unification of terminal and duality models”, in *Ieee transactions on power delivery*, vol. 27, 2012, pp. 353–361.

[77] S. Jazebi and F. de Leon, “Experimentally validated reversible single-phase multiwinding transformer model for the accurate calculation of low-frequency transients”, in *Ieee transactions on power delivery*, vol. 30, 2015, pp. 193–201.

[78] L. Cao and J. Yang, “Linear circuit model of the trhee-phase insulated core transformer power supply”, in *Ieee transactions on nuclear science*, vol. 63, 2016, pp. 288–296.

[79] F. de Leon and J. A. Martinez, “Dual three-winding transformer equivalent circuit matching leakage measurements”, in *Ieee transactions on power delivery*, vol. 24, 2009, pp. 160–168.

[80] M. Lambert, M. Matinez-Duro, J. Mahseredjian, F. de Leon, and F. Sirois, “Transformer leakage flux models for electromagnetic transients: Critical review and validation of a new model”, in *Ieee transactions on power delivery*, vol. 29, 2014, pp. 2180–2188.

[81] M. Lambert, F. Sirois, M. Matinez-Duro, and J. Mahseredjian, “Analytical calculation of leakage inductance for low-frequency transformer modelling”, in *Ieee transactions on power delivery*, vol. 28, 2013, pp. 507–515.

[82] P. W. Hammond, “A new approach to enhance power quality for medium voltage ac drives”, in *Ieee transactions on industry applications*, vol. 33, 1997, pp. 202–208.

[83] E. C. Snelling, *Soft ferrite: Properties and applications*. London Iliffe Books Ltd., 1969.

[84] M. A. Vogelsberger, T. Wiesinger, and H. Ertl, “Life-cycle monitoring and voltage-managing unit for dc-link electrolytic capacitors in pwm converters”, in *Ieee transactions on power electronics*, vol. 26, 2011, pp. 493–503.

[85] L. Sun, Z. Wu, W. Ma, X. Fei, X. Cai, and L. Zhou, “Analysis of the dc-link capacitor current of power cells in cascaded h-bridge inverters for high-voltage drives”, in *Ieee transactions on power electronics*, vol. 29, 2014, pp. 6281–6292.

[86] J. Rodriguez, S. Bernet, B. Wu, J. O. Pontt, and S. Kouro, “Multlevel voltage-source-converter topologies for industrial medium-voltage drives”, in *Ieee transactions on industrial electronics*, vol. 54, 2007, pp. 2930–2945.

[87] J. Rodriguez, P. W. Hammond, J. Pontt, R. Musalem, P. Lezana, and M. J. Escobar, “Operation of a medium-voltage drive under faulty conditions”, in *Ieee transactions on industrial electronics*, vol. 52, 2005, pp. 1080–1085.

[88] *Plecs the simulation platform for power electronic systems - user manual version 4.1.*

Min Luo

PhD candidate in Power Electronics

✉ *mailto:luo@plexim.com*
born 12.15.1986
Chinese

EDUCATION

École Polytechnique Fédérale de Lausanne, Lausanne, Switzerland

2014 – 2018	PhD candidate, *Electrical Engineering Doctoral School*, Power Electronics Laboratory *Dynamic Modeling of Magnetic Components for Circuit Simulation of Power Electronic Systems*

Rheinisch-Westfälische Technische Hochschule Aachen, Aachen, Germany

2009 – 2012	MSc, *Electrical Power Engineering*

Tsinghua University, Beijing, China

2005 – 2009	BSc, *Electrical Engineering*

PROFESSIONAL EXPERIENCE

2012 – 2018	Applications Engineer in Plexim GmbH, Zürich, Switzerland

LANGUAGES

Chinese	Mother tongue
English	Working proficiency
German	Working proficiency